

**The functional role of PI(4,5)P₂ metabolism
at septin-enriched plasmalemmal
microdomains**

A Dissertation

Submitted in Partial Fulfilment of the
Requirements for the Degree of Doctor rerum
naturalium (Dr. rer. nat.)

to the Department of Biology, Chemistry,
Pharmacy
of Freie Universität Berlin

by

GIULIA RUSSO

Berlin, 2023

Supervisor: Prof. Dr. Michael Krauß

Institute: Leibniz-Forschungsinstitut für Molekulare
Pharmakologie (FMP), Berlin

First reviewer: Prof. Dr. Michael Krauß

Second reviewer: Prof. Dr. Volker Haucke

Date of defense: 11th of April 2024

Declaration of Independence

Herewith I certify that I have prepared and written my thesis independently and that I have not used any sources and aids other than those indicated by me.

I also declare that I have not submitted the dissertation in this or any other form to any other institution as a dissertation.

Berlin, December 2023

Acknowledgements

I would like to express my deep gratitude to **Prof. Dr. Michael Krauß**, my research supervisor, for his invaluable guidance over these years. His enthusiasm for science, unstoppable curiosity, and inspiring scientific discussions have been my guiding light throughout this challenging project. I am truly grateful for the wealth of knowledge acquired under his supervision.

Sincere gratitude also goes to **Prof. Dr. Volker Haucke** for providing me with the opportunity to conduct this research work in his excellent laboratory, for his precious support and insightful directions to my project.

Furthermore, I would like to thank **Dr. Martin Lehmann** and **Dr. Christopher Schmied** for their advice and assistance in microscopy and image analysis.

I am very grateful to **Nadja Hümpfer** and **Prof. Dr. Helge Ewers** (Freie Universität Berlin) for their excellent contribution to this project with U-ExM and experiments with NRK cells, and for sharing with us their passion for septins. Being part of the small Berlin-based septin community has been truly enjoyable. I am grateful for the incredible support, inspiring discussions, and for the exchange of knowledge and materials.

I wish to thank **Prof. Dr. Florian Heyd** (Freie Universität Berlin) as well for the precious help with the analysis of the expression of PIPKI γ isoforms.

I extend my acknowledgments to the lab's technicians for their essential work, and especially to **Delia Löwe** for her precious help with cell cycle synchronization, sometimes starting at 5 a.m. Thank you also to **Heike Stephanowitz** (MS-facility), for her important assistance in mass spectrometry analysis.

I would like to thank **Dr. Wen-Ting Lo** and **Dr. Domenico Azarnia Tehran** for patiently sharing their expertise with me since my first days in the lab, and **Dr. Alexander Wallroth** and **Dr. Philipp A. Koch** for introducing me to the CRISPR-Cas9-based technique of genome editing. My gratitude goes also to **Dr. Tania López Hernández** and **Dr. Marijn Kuijpers** for their significant insights, particularly on the ER-PM contact sites project.

I am grateful to my students, **Rebekka Trenkle**, **Andreas Lenk**, **Steffen Restel**, **Nicole Gamburg**, and **Akin Sesver** for trusting me in supervising their internships or theses. Their enthusiasm and valuable contributions, with ideas and experiments, have undeniably enriched my doctoral journey.

A heartfelt thank you to all my past and present colleagues from AG Krauß, AG Haucke, AG Maritzen, and AG Lehmann: **Kerem C. Akkaya, Marietta Bergmann, Svenja Bolz, Caroline Bruns, Gabrielle Capin, Gillian Leigh Dornan, Michael Ebner, Jenny Eichhorst, Paula Samsó Ferré, Uwe Fink, Marine Gil, Hannes Gonschior, Manuel Hessenberger, Lennart Hoffmann, Wonyul Jang, Maria Jäpel, Natalie Kaempf, Mudassar Khan, Gaga Kochlamazashvili, Guan-Ting Liu, Max Lucht, Fabian Lukas, Albert Mackintosh, Marta Maglione, Charles Malek, Tanja Maritzen, Maria Mühlbauer, Phuong Nguyen, Kristine Oevel, Christoph Ott, York Posor, Dymtro Puchkov, Julia Riedlberger, Filiz Sila Rizalar, Dorien Roosen, Linda Sawade, Claudia Schmidt, Kyungyuen Song, Tolga Soykan, Miaomiao Tian, Rozemarijn van der Veen, Dennis Vollweiter, Haibin Wang, Mirjana Weimerschau, Agata Witkowska, Su Yanwei, Klaas Yperman, and Silke Zillmann.** Thank you for creating such a positive, collaborative, and enriching environment in the lab throughout these years. I couldn't have wished for better colleagues. Thank you for your constant support; it really made the difference.

My gratitude goes also to **Alexandra Chylla** and the Sekretariat team for their warm support and commitment to the group's well-being.

At this point, I must acknowledge the source of my strength: **my friends**. Thank you to those colleagues whom I now call friends. Thanks to my friends from all around the world and to my Neapolitan, long-lasting friends. A special thank you goes to my "Pandemonium": my safe harbor, the place I can always fly to.

I am truly privileged to have all of you by my side.

In conclusion, my deepest gratitude goes to the people I wish to dedicate my thesis to: **Vladimir Ugorets** for his outstanding love for septins (and for me), and **my parents**, the pillars of my life

I. Table of Contents

I. Table of Contents	1
II. Abstract	7
III. Zusammenfassung	9
1. Introduction	11
1.1. Mammalian cytokinesis.....	11
1.1.1. From the spindle midzone to the actomyosin ring	11
1.1.2. Ingression of the cleavage furrow and establishment of the anillo-septin subnetwork	13
1.1.3. Abscission	15
1.1.4. <i>In medio stat virtus</i> : functions of the midbody	18
1.1.5. A gap in the middle: the GAP function of centralspindlin.....	21
1.1.6. Origin and function of phosphoinositides during cytokinesis.....	21
1.2. Type I PIP-kinases, a source of diversified PI(4,5)P ₂ pools	24
1.2.1. Overview on the contribution and regulation of type I PIP-kinases	24
1.2.2. The role of PIPKI β during cytokinesis.....	26
1.2.3. PIPKI γ isoforms and their functions	27
1.3. The septin cytoskeleton and its remodeling	30
1.3.1. A variety of septins and septin complexes: a Lego playground for the cell.....	30
1.3.2. Subcellular localization and functions of actin-associated septins.....	33
1.3.3. Subcellular localization and functions of MT-associated septins	36
1.3.4. Septin interactions with phospholipid membranes and distinct phosphoinositides	39
1.4. Aim of this study	41
2. Materials and Methods	42
2.1. Materials	42
2.1.1. Chemicals	42
2.1.2. Solutions and media.....	42
2.1.3. Enzymes and molecular biology kits	46
2.1.4. DNA Oligonucleotides	46
2.1.5. Small interference RNA (siRNA) oligonucleotides.....	48
2.1.6. Plasmids	48
2.1.7. Antibodies	50
2.1.8. Bacterial strains.....	52
2.1.9. Eukaryotic cell lines.....	52
2.1.10. Software and databases.....	53

2.1.11. Macros used for the segmentation of microscopy images	54
2.2. Molecular biology methods.....	55
2.2.1. Extraction of genomic DNA	55
2.2.2. Polymerase chain reaction (PCR).....	55
2.2.3. Agarose gel electrophoresis and DNA purification	57
2.2.4. Restriction digest.....	57
2.2.5. Dephosphorylation of linearized vector DNA.....	57
2.2.6. Ligation of DNA fragments into linearized vectors.....	58
2.2.7. Transformation of chemically competent <i>E. coli</i>	58
2.2.8. Overnight <i>E. coli</i> cultures and purification of plasmid DNA	58
2.2.9. Determination of the concentration and quality of DNA samples.....	59
2.2.10. Sequencing	59
2.2.11. Cloning of the DNA vectors used for CRISPR-Cas9-based genome editing	59
2.3. Biochemistry methods.....	61
2.3.1. Sodium dodecyl sulfate polyacrylamide gel electrophoresis (SDS-PAGE).....	61
2.3.2. Immunoblotting.....	62
2.3.3. Quantification of proteins via Bradford assay	63
2.3.4. Preparation of protein extracts from eukaryotic cells	63
2.3.5. Immunoprecipitation assay	64
2.3.6. Preparation of protein extracts from mouse brains.....	65
2.3.7. Expression and purification of GST-fusion proteins from <i>E. coli</i>	65
2.3.8. Purification of His ₁₀ -tagged PIPK γ -i3 from insect cells	66
2.3.9. GST-pulldown assays	67
2.4. Cell biology methods	68
2.4.1. Mammalian cell culture	68
2.4.2. Transfection of plasmid DNA.....	69
2.4.3. Small interference RNA (siRNA)-mediated gene silencing	70
2.4.4. Generation of stable cell lines	71
2.4.5. Generation of knock-in cell lines	72
2.4.6. Cell cycle synchronization.....	72
2.4.7. Drug treatment.....	73
2.4.8. Immunocytochemistry (ICC)	74
2.4.9. Ultrastructure expansion microscopy (U-ExM)	75
2.4.10. Fluorescence microscopy	76
2.4.11. Image analysis.....	78
2.4.12. Analysis of the expression of PIPK γ isoforms	80

2.4.13. Statistics and reproducibility.....	80
3. Results.....	81
3.1. PIPKI γ controls the organization of anillin and septins at the ICB and is required for successful cytokinesis.....	81
3.1.1. PIPKI β and PIPKI γ are required for furrow ingression, while exclusively PIPKI γ is needed at telophase	81
3.1.2. Depletion of any of the type-I PIP kinases does not cause major changes in total PI(4,5)P ₂ levels at the PM.....	83
3.1.3. PIPKI γ is required for anillin organization and septin enrichment at the ICB.....	84
3.1.4. Depletion of PIPKI γ promotes multinucleation and disrupts prominent septin fibers.	86
3.2. The function of PIPKI γ at late cytokinesis is ascribable to kinase active and septin-binding isoform 5 (PIPKI γ -i5).....	87
3.2.1. PIPKI γ isoform 3 and 5 (PIPKI γ -i3/i5) share a splicing insert responsible for the interaction with septins	87
3.2.2. PIPKI γ -i5 localizes to the ingressed cleavage furrow	90
3.2.3. Selective depletion of PIPKI γ -i3/i5 phenocopies the cytokinetic defects observed upon depletion of PIPKI γ	91
3.2.4. Active and septin-binding PIPKI γ -i5 rescues anillin compactness, SEPT2 accumulation at the cytokinetic bridge and the length of the acetylated tubulin bridge.....	94
3.2.5. Co-depletion of OCRL rescues anillin mislocalization caused by loss of PIPKI γ -i3/i5.....	98
3.3. Septin-associated PIPKI γ -i3/i5 are required to anchor centralspindlin at the midbody.....	100
3.3.1. Depletion of PIPKI γ -i3/i5 affects the accumulation of the centralspindlin component MKLP1 at the midbody.....	100
3.3.2. MKLP1 accumulation at the midbody requires active and septin-binding PIPKI γ -i5 ...	101
3.3.3. Depletion of SEPT2 phenocopies the loss of MKLP1 observed in absence of PIPKI γ -i3/i5	103
3.3.4. Ultrastructure expansion microscopy (U-ExM) confirms defects in centralspindlin accumulation at the midbody upon depletion of PIPKI γ -i3/i5.....	104
3.3.5. Depletion of PIPKI γ -i3/i5 does not impair the formation of a septin double ring at the midbody	105
3.4. PIPKI γ -i3/i5 are dispensable for the synthesis of bulk PI(4,5)P ₂ at the cleavage furrow, but regulate the distribution of PI(4,5)P ₂ at the ICB	107
3.4.1. Depletion of PIPKI γ -i3/i5 does not affect bulk PI(4,5)P ₂ at the furrow.....	107
3.4.2. Depletion of PIPKI γ -i3/i5 alters the distribution of PI(4,5)P ₂ across the ICB.....	109
3.5. PIPKI γ emerges as a novel key regulator of the septin cytoskeleton.....	110
3.5.1. Perinuclear septin fibers derive from the cytokinetic bridge in a PIPKI γ -i3/i5 dependent manner	110
3.5.2. PIPKI γ -i3/i5 regulate the subcellular distribution of septins between MTs and actin filaments	113

3.5.3. Depletion of centralspindlin subunits phenocopies the subcellular relocalization of septins observed upon depletion of PIPKI γ -i3/i5	115
3.5.4. Depletion of PIPKI γ -i3/i5 leads to reduced SEPT6 protein levels	118
3.5.5. Depletion of SEPT6 only partially phenocopies the defects at the cytokinetic bridge observed in absence of PIPKI γ -i3/i5	119
3.5.6. Overexpression of active PIPKI γ -i5 leads to reorganization of septins into rings, independently of its septin binding capability	122
3.6. Supplementary figures	124
4. Discussion	126
4.1. The contribution of type I PIP-kinases to cell division.....	126
4.1.1. Both PIPKI β and PIPKI γ contribute to the ingression of the cleavage furrow.....	126
4.1.2. PIPKI γ plays a unique function at the ICB.....	127
4.1.3. The role of PIPKI γ during telophase is exerted by the septin-binding and catalytically active PIPKI γ -i3/i5 splice variants	129
4.2. Spatiotemporal regulation of PIPKI γ during cell division	130
4.2.1. Putative molecular mechanisms underlying the interaction between PIPKI γ -i3/i5 and septins.....	131
4.2.2. Additional tuning of PIPKI γ activity at the midbody.....	133
4.3. PIPKI γ as a novel regulator of the midbody organelle.....	134
4.3.1. A septin-PIPKI γ -i3/i5 module to localize the synthesis of PI(4,5)P ₂ at the midbody and locally retain centralspindlin	134
4.3.2. PIPKI γ may contribute to abscission by orchestrating vesicle delivery to the midbody	137
4.3.3. Putative mechanisms underlying the redistribution of PI(4,5)P ₂ across the midbody in absence of PIPKI γ -i3/i5	140
4.3.4. Putative mechanisms underlying the morphological changes of the ICB in absence of PIPKI γ -i3/i5.....	142
4.4. PIPKI γ regulates the subcellular localization of septins	143
4.4.1. PIPKI γ -i3/i5 promote the localization of septins to bridge MTs.....	143
4.4.2. The PIPKI γ -i3/i5-dependent relocalization of septins to bridge MTs may regulate the length of the cytokinetic bridge	145
4.4.3. Via septins, PIPKI γ may provide daughter cells with instructions on how to organize their cytoskeleton.....	146
4.5. Putative mechanisms underlying the PIPKI γ -dependent translocation of septins to bridge MTs	149
4.5.1. Centralspindlin promotes spatial proximity between furrow membrane and bridge MTs	149
4.5.2. PTMs may modulate the affinity of septins for bridge MTs.....	150
4.5.3. Rho GTPases contribute to cytoskeletal remodeling during cytokinesis and beyond .	151

4.6. Working model.....	155
4.7. Are septins PI(4,5)P ₂ effectors?.....	157
4.7.1. The co-depletion of OCRL with PIPK1 γ -i3/i5 did not rescue septin relocalization to bridge MTs	157
4.7.2. Septins mostly “shape” PI(4,5)P ₂ pools rather than acting as effectors	158
4.8. Peculiar function of the SEPT6 paralogue during cytokinesis.....	160
4.8.1. Hypothesized mechanism of SEPT6-specific downregulation upon depletion of PIPK1 γ	160
4.8.2. SEPT6 plays a role outside of the septin-PIPK1 γ -i3/i5 module during cytokinesis	161
4.9. Conclusions and outlook	164
5. Bibliography.....	166
6. Appendix A: putative role of septin-binding PIPK1γ isoforms in ER-PM contact sites	191
6.1. Introduction	191
6.1.1. Store-operated Ca ²⁺ entry (SOCE)	191
6.1.2. The extended synaptotagmins (E-Syts).....	193
6.1.3. The role of septins during SOCE.....	195
6.1.4. The role of PI(4,5)P ₂ during SOCE.....	198
6.1.5. Aim of this study	200
6.2. Results	201
6.2.1. E-Syt1-dependent contact sites insert between cortical septin and actin filaments, and actin may regulate their dynamics.....	201
6.2.2. The recruitment of E-Syt1 to the PM may occur at membrane microdomains with a “poor” content of PI(4,5)P ₂	205
6.2.3. PIPK1 γ -i5 negatively regulates the recruitment of E-Syt1 to the PM	206
6.2.4. Distinct PIPK1 γ Isoforms may differentially modulate E-Syt1 dynamics via direct binding of the E-Syt1 C2E domain	208
6.2.5. Confocal imaging reveals colocalization between TG-induced E-Syt1 puncta and PI(4,5)P ₂	211
6.2.6. A putative pool of PI(4,5)P ₂ synthesized at the ER may compete with the binding of E-Syt1 to the PM.....	212
6.2.7. Generation and analysis of a genome-engineered knock-in cell line expressing eGFP-E-Syt1 from its endogenous locus.....	215
6.3. Discussion.....	218
6.3.1. The formation and dissociation of E-Syt1-mediated contact sites may occur at different plasmalemmal microdomains characterized by low and high PI(4,5)P ₂ content, respectively	218
6.3.2. Putative role of the interaction of E-Syt1 with PIPK1 γ	220
6.3.3. The ER as a putative source of PI(4,5)P ₂	221
6.3.4. Experimental considerations and limitations of this study.....	223

7. Appendix B.....	225
7.1. Abbreviations.....	225
7.2. List of Figures and Tables.....	230
7.3. Publications	233
7.4. Curriculum Vitae	Error! Bookmark not defined.

II. Abstract

The process of cytokinesis ultimately results in the partitioning of a mother cell into two daughter cells. Cytokinesis is initiated through the formation of an actomyosin ring at the equatorial plane of the mother cell, which drives the ingression of a cleavage furrow. At this stage, the scaffolding protein anillin stabilizes the actomyosin ring, and recruits septins. Once the ingression of the cleavage furrow is completed, the furrow membrane anchors to the bundled microtubules of the cytokinetic bridge. This is achieved through the centralspindlin complex, which resides at the nascent midbody organelle. Subsequently, anillin and septins further regulate the maturation of an intercellular bridge (ICB), which will ultimately be resolved by the abscission machinery.

The phospholipid phosphatidylinositol 4,5-bisphosphate [PI(4,5)P₂] plays a crucial role in mammalian cytokinesis. It is essential for the anillin-dependent stabilization of the actomyosin ring at the cleavage furrow, and it is required for the centralspindlin-dependent tethering of bridge microtubules to the plasma membrane. Nevertheless, the molecular mechanisms orchestrating PI(4,5)P₂ synthesis in space and time during cytokinesis have remained elusive so far.

In this study we investigated the contribution of type I PIP-kinases (phosphatidylinositol-4-phosphate 5-kinases) to the progression of cytokinesis and unveiled a crucial role for PIPK1 γ at the ICB. We found that septins interact with a common splice insert of PIPK1 γ isoforms 3 and 5 (PIPK1 γ -i3/i5), and that both septins and PIPK1 γ form a complex with centralspindlin. SiRNA-mediated depletion of PIPK1 γ -i3/i5 resulted in the loss of septin association with ICB microtubules, scattering of anillin away from the ICB, reduction of centralspindlin at the midbody, and a shorter cytokinetic bridge. Notably, these defects were rescued by wild-type PIPK1 γ , but not by septin binding-deficient or catalytically inactive mutants. These data support a model wherein septins recruit specific PIPK1 γ isoforms to the nascent midbody and, at this locale, PIPK1 γ -i3/i5 synthesize a pool of PI(4,5)P₂ required for maintaining anillin, centralspindlin, and septins in place.

Super-resolution analysis via ultrastructure-expansion microscopy further confirmed the above-mentioned defects at cytokinetic bridges in cells depleted of PIPK1 γ -i3/i5. Furthermore, live cell imaging of endogenously tagged eGFP-SEPT6 revealed that the hindered association of septins with microtubules observed at cytokinesis

persisted within the daughter cells. Notably, siRNA-mediated depletion of centralspindlin phenocopied the loss of septin association to microtubules in non-mitotic cells, pointing towards a role of centralspindlin in coordinating the translocation of septins to bridge microtubules and, thereby, the inheritance of microtubule-associated septin fibers by daughter cells.

Taken together, our findings establish septin-associated PIPKI γ isoforms as novel regulators of late cytokinesis and demonstrate that both septins and PIPKI γ are essential during midbody assembly and maturation.

III. Zusammenfassung

Der Prozess der Zytokinese führt letztendlich zur Teilung einer Mutterzelle in zwei Tochterzellen. Die Teilung wird durch die Bildung eines Aktomyosin-Rings initiiert, der an der Äquatorialebene der Mutterzelle assembliert wird, und der die Ausbildung einer Teilungsfurche vermittelt. In diesem Stadium wird auch das Gerüstprotein Anillin rekrutiert, das den Aktomyosin-Ring stabilisiert, und zeitgleich die Rekrutierung von Septinen vermittelt. Sobald die Ausbildung der Teilungsfurche abgeschlossen ist, muss die Plasmamembran der eingestülpten Furche an den gebündelten Mikrotubuli der zytokinetischen Brücke verankert werden. Dies wird durch den sog. Centralspindlin-Komplex ermöglicht, der an der entstehenden Midbody-Organelle konzentriert ist. Anschließend regulieren Anillin und Septine die weitere Reifung der interzellulären Brücke (IZB), die letztlich durch die Abschnürungsmaschinerie aufgelöst wird.

Das Phospholipid Phosphatidylinositol 4,5-Bisphosphat [PI(4,5)P₂] spielt eine entscheidende Rolle während der Säugetier-Zytokinese. Es ist unerlässlich für die Anillin-abhängige Stabilisierung des Aktomyosin-Rings an der Teilungsfurche, und wird für die Centralspindlin-abhängige Adhäsion von IZB-Mikrotubuli an der Plasmamembran benötigt. Die molekularen Mechanismen, die die Synthese von PI(4,5)P₂ während der Zytokinese räumlich und zeitlich orchestrieren, sind bisher weitgehend unerforscht geblieben.

In dieser Studie haben wir den Beitrag der Typ-I-PIP-Kinasen (Phosphatidylinositol-4-Phosphat 5-Kinasen) zur Zytokinese untersucht, und eine entscheidende Rolle von PIPK1 γ an der IZB aufgedeckt. Unsere Analysen belegen eindrücklich, dass Septine mit PIPK1 γ Isoformen 3 und 5 (PIPK1 γ -i3/i5) über ein gemeinsames Splice-Insert interagieren, und dass sowohl Septine als auch PIPK1 γ einen Komplex mit Centralspindlin bilden. Die siRNA-vermittelte Depletion von PIPK1 γ -i3/i5 verhindert die Assoziation von Septinen mit den Mikrotubuli der IZB, führt zum Verlust von Anillin an der IZB, erschwert die Akkumulation von Centralspindlin am Midbody, und bewirkt eine Verkürzung der zytokinetischen Brücke. Interessanterweise konnten diese Defekte durch Transfektion einer wildtypischen PIPK1 γ aufgehoben werden, jedoch nicht durch Mutanten, die nicht an Septine binden können, oder die katalytisch inaktiv sind. Diese Daten unterstützen ein Modell, nach dem Septine spezifische PIPK1 γ -Isoformen zum entstehenden Midbody rekrutieren, um dort die

Bildung eines Pools von PI(4,5)P₂ zu vermitteln, der für die korrekte Verankerung von Anillin, Centralspindlin und Septinen erforderlich ist.

Super-Resolution-Analysen mittels Ultrastruktur-Expansions-Mikroskopie bestätigten die oben genannten Defekte an der zytokinetischen Brücke in Abwesenheit von den PIPK γ -i3/i5. Die Lebendzell-Mikroskopie von endogen markiertem eGFP-SEPT6 zeigte darüber hinaus, dass die gestörte Assoziation von Septinen mit Mikrotubuli während der Zytokinese auch nach abgeschlossener Zellteilung in den Tochterzellen weiter besteht.

Bemerkenswerterweise führte die siRNA-vermittelte Depletion von Centralspindlin zu einem Verlust der Septin-Assoziation mit Mikrotubuli auch in nicht-mitotischen Zellen, was auf eine Rolle von Centralspindlin bei der Koordination der Translokation von Septinen auf Brücken-Mikrotubuli schließen lässt, und somit auf die Möglichkeit hinweist, dass Mikrotubuli-assoziierte Septinfasern auf Tochterzellen „vererbt“ werden.

Zusammenfassend etablieren unsere Ergebnisse Septin-assoziierte PIPK γ -Isoformen als neue Regulatoren der späten Zytokinese, und belegen, dass sowohl Septine, als auch assoziierte Kinase-Isoformen für die Entstehung und Reifung des Midbodys essentiell sind.

1. Introduction

1.1. Mammalian cytokinesis

The process of cytokinesis results in the physical separation of a mother cell into two daughter cells. This process starts at anaphase when the mitotic spindle, a microtubule-based supramolecular structure, provides a spatial cue for the assembly of a membrane-bound actomyosin ring (Glotzer, 2009; Piekny *et al*, 2005). Contractions of this ring cause the ingression of a cleavage furrow at the cell equator (Cheffings *et al*, 2016). The cleavage furrow subsequently matures into an intercellular bridge (ICB), bearing in its middle a dense organelle named the midbody (Mierzwa & Gerlich, 2014). This organelle anchors the ingressed cleavage furrow to the underlying cytoskeleton and thereby provides a spatiotemporal cue to initiate the final step of abscission (Lekomtsev *et al*, 2012; Mierzwa & Gerlich, 2014). Cytokinesis is a highly regulated process, whose failure may result in tumorigenesis (Sagona & Stenmark, 2010). Phosphoinositides comprise a group of phospholipids that, among other functions, play key regulatory roles in coordinating cytoskeletal remodeling during cytokinesis (Russo & Krauss, 2021; Cauvin & Echard, 2015; Gulluni *et al*, 2022).

The following sections will describe the stages of cytokinesis, with a special focus on the role of the anillin and septins (anillo-septin) subnetwork and on the midbody organelle in orchestrating the final steps of ICB maturation and abscission. Furthermore, the source and regulatory role of phosphoinositides in organizing the anillo-septin subnetwork and midbody organelle will be highlighted.

1.1.1. From the spindle midzone to the actomyosin ring

The mitotic spindle is a highly dynamic structure, which specifies the cleavage plane of dividing cells and initiates the signaling cascade required to assemble the actomyosin ring (Yüce *et al*, 2005; Barisic *et al*, 2021). At metaphase, the mitotic spindle consists of different subsets of microtubules (MTs) emanating from the two poles of the spindle (Glotzer, 2009). Between the poles, the plus ends of kinetochore MTs are attached to chromosomes, while the plus ends of interpolar MTs partially interdigitate. The astral MTs link the spindle poles to the cell cortex (Glotzer, 2009). At the onset of anaphase, the kinetochore MTs depolymerize, and the interpolar

MTs slide and grow so that the chromosomes segregate, while the mitotic spindle elongates (**fig.1-1-A**) (Barisic *et al*, 2021; Lera-Ramirez *et al*, 2022).

At this point, several factors are relieved from mitotic inhibition (through the removal of inhibitory CDKs-dependent phosphorylations) so that they can promote MTs bundling, and the assembly of the spindle midzone (Holder *et al*, 2019). PRC1 (protein regulator of cytokinesis 1) is essential for MTs bundling and, once activated, binds to the kinesin motor KIF4A and translocates along the mitotic spindle toward the plus ends of interdigitating MTs (Zhu *et al*, 2006). At this site, PRC1 dimers oligomerize and crosslink antiparallel MTs (Zhu *et al*, 2006). The assembly of the midzone further requires the centralspindlin complex. This complex is a heterotetramer consisting of two subunits of the motor protein MKLP1 (mitotic kinesin-like protein 1, also called KIF23) and of two subunits of the GTPase-activating protein (GAP) MgcRacGAP (also called CYK4), (Pavicic-Kaltenbrunner Visnja *et al*, 2007). Upon activation, centralspindlin translocates to the midzone, powered by the motor activity of MKLP1 (Mishima *et al*, 2004). This process contributes to MTs bundling and initiates the signaling cascade required for the assembly of the actomyosin ring (**fig. 1-1**). Specifically, MgcRacGAP binds to and recruits the Rho guanine nucleotide exchange factor (GEF) ECT2 (epithelial cell transforming sequence 2), which in turn activates RhoA at the equatorial plane of the cell cortex (**fig. 1-1-B**) (Yüce *et al*, 2005). The local activation of RhoA at the plasma membrane (PM) overlaying the midzone depends on the ability of ECT2 to associate with plasmalemmal PI(4,5)P₂ (phosphatidylinositol-4,5-bisphosphate) through a pleckstrin homology (PH) domain and a polybasic cluster at its C-terminus (Kotýnková *et al*, 2016; Su *et al*, 2011). MgcRacGAP also possess a membrane binding domain; however, in human cells, it is dispensable for the cortical activation of Rho A, as well as for furrow constriction (Basant *et al*, 2015).

Active RhoA triggers the assembly and initial contraction of the actomyosin ring by regulating several pathways (**fig. 1-1-B**). RhoA-GTP induces the polymerization of linear actin by activating Diaphanous-related formins, such as mDia2 (Watanabe *et al*, 2007). Additionally, RhoA activates ROCK (Rho-associated coiled-coiled-containing kinase), which in turn phosphorylates and activates myosin II (Piekny *et al*, 2005). Rho-A also recruits CIT-K (citron kinase) (Piekny *et al*, 2005); however, it remains unclear whether also this kinase participates to the phosphorylation of myosin II (as elaborated in paragraph 1.1.4) (Watanabe *et al*, 2013; Gai *et al*, 2011).

Active myosin II associates with actin and initiates the contraction of the actomyosin ring (Matsumura, 2005; Piekny *et al*, 2005). In addition to actin and myosin, the contractile machinery contains several actin crosslinking proteins, like the adaptor protein anillin and septins, as described in the next paragraph.

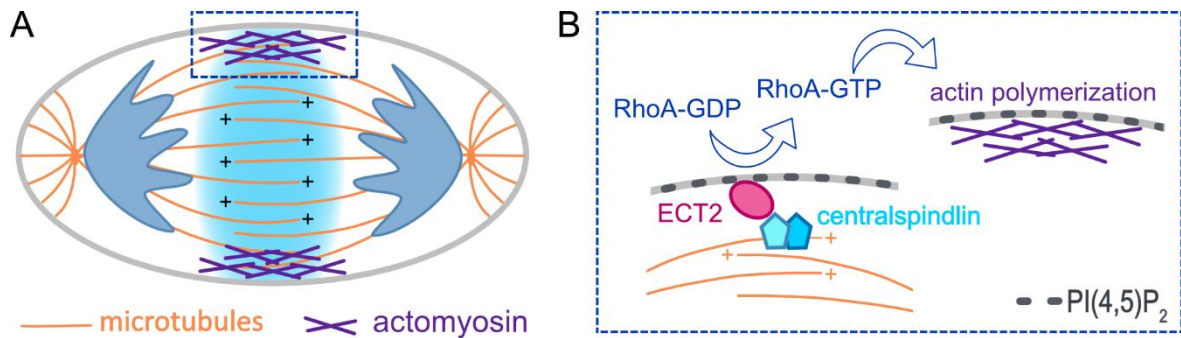


Figure 1-1. Positioning of the actomyosin ring. (A) Representation of a cell at anaphase. The actomyosin ring (violet criss-cross pattern) assembles at the equatorial cortex outlying the midzone (turquoise shadow). **(B)** Inset describing how the spindle midzone provides the spatial cue for the positioning of the contractile machinery. Centralspindlin (turquoise pentagons) accumulates at the plus ends of interpolar MTs and there recruits ECT2 (pink oval). ECT2 associates with the overlaying PM via the binding of PI(4,5)P₂ (dashed dark grey line) and activates RhoA. RhoA-GTP in turn triggers the local assembly of the actomyosin ring through several pathways.

1.1.2. Ingression of the cleavage furrow and establishment of the anillo-septin subnetwork

The contraction of the actomyosin ring is primarily driven by the motor activity of myosin II in combination with localized depolymerization of actin (Cheffings *et al*, 2016). While contracting, the actomyosin ring pulls the PM toward the cell interior, thereby generating a cleavage furrow (**fig. 1-2-A**). However, to allow for the formation of a symmetric invagination, the actomyosin ring must remain attached to the PM within the equatorial plane of the cell (Liu *et al*, 2012).

The adaptor protein anillin plays an important role in this regard. Anillin is a multidomain protein that interacts with several components of the furrow (Piekny & Maddox, 2010). The N-terminal domains interact with non-muscle myosin II, F-actin, mDia2 and CIT-K (Straight *et al*, 2004; Watanabe *et al*, 2010; Gai *et al*, 2011). The C-terminal PH and anillin homology (AH) domains display cooperative binding to plasmalemmal PI(4,5)P₂, while additionally interacting with septins and GTP-loaded RhoA, respectively (Liu *et al*, 2012; Sun *et al*, 2015; Piekny & Glotzer, 2008). The recruitment of anillin to the forming cleavage furrow is initiated at anaphase and requires a synergetic interaction of anillin with active RhoA and PI(4,5)P₂ (Liu *et al*, 2012; Piekny & Glotzer, 2008; Sun *et al*, 2015). Owing to its multidomain nature,

anillin spatially regulates and links together different components of the actomyosin ring, while at the same time it anchors the contractile machinery to the PM (Liu *et al*, 2012; Piekny & Glotzer, 2008; Schiel *et al*, 2013). In line with this role, depletion of anillin does not affect the assembly and initial contraction of the actomyosin ring, but it causes severe oscillation of the cleavage furrow (Liu *et al*, 2012; Piekny & Glotzer, 2008).

While the cleavage furrow ingresses, the antiparallel MTs at the center of the spindle progressively bundle. Once the constriction has completed, daughter cells remain connected through a tube of PM (~1.5 to 2 μm in diameter), the ICB, which surrounds an array of tightly bundled antiparallel MTs: the cytokinetic bridge (or acetylated tubulin bridge) (Mierzwa & Gerlich, 2014; Fededa & Gerlich, 2012; Wang *et al*, 2019). The portion of interdigitating MTs deriving from the midzone becomes confined in a bulge at the center of the ICB, named the midbody organelle (for an overview, **fig. 1-2-A-B** and **fig. 1-3-A**) (Johannes A.G. Rhodin, 1974).

The biogenesis of the ICB relies also on another group of cytoskeletal and PI(4,5)P₂-binding proteins, septins (described in section 1.3). Septins are recruited to the cleavage furrow by anillin at the onset of constriction (**fig. 1-2-A**), however their role at this early stage remains unclear (Liu *et al*, 2012). Joo and colleagues proposes that SEPT2 acts as a molecular scaffold that brings CIT-K and ROCK in proximity to myosin II and thereby promotes phosphorylation and full activation of the latter (Joo *et al*, 2007). Other studies instead report that when endogenous anillin is replaced by a chimera incapable of septin binding, cells still assemble a functional actomyosin ring and the cleavage furrow ingresses symmetrically (Liu *et al*, 2012; Renshaw *et al*, 2014). Nevertheless, cells which fail to recruit septins exhibit several post-furrow defects (Renshaw *et al*, 2014). Indeed, although the initial large scale ingression (tens of micrometers) of the furrow is driven mainly by the actomyosin ring, the septin and anillin subnetwork, often referred as “anillo-septin”, becomes essential for the elongation and thinning of the newly formed ICB (Carim *et al*, 2020). 3D-SIM analysis of HeLa cells revealed that, as the ICB emerges, anillin and septins organize in a collar consisting of an array of curved filaments encircling the cytokinetic bridge at the inner face of the PM (**fig.1-2-B**) (Renshaw *et al*, 2014; Panagiotou *et al*, 2022).

How the anillo-septin system contributes to the maturation of the ICB is not yet fully understood. Sequential addition of anillo-septin rings may promote the elongation

of the ICB. Regarding the narrowing, Carim and colleagues suggested that, as the tension builds in the constricting furrow, anillin disengages from the actomyosin ring and, together with septins, gradually sequesters membrane microdomains. Then, as actomyosin-bound membrane microdomains converge toward each other, anillo-septin-bound microdomains are extruded from the furrow (**fig.1-2-C**). As a consequence, the ICB thins and the actomyosin ring progressively disassembles (Carim *et al*, 2020; Amine *et al*, 2013). In support of this hypothesis, membrane tubules containing anillin and septins, shredded from the ICB, have been visualized in mammalian and *Drosophila* cells (Renshaw *et al*, 2014; Amine *et al*, 2013).

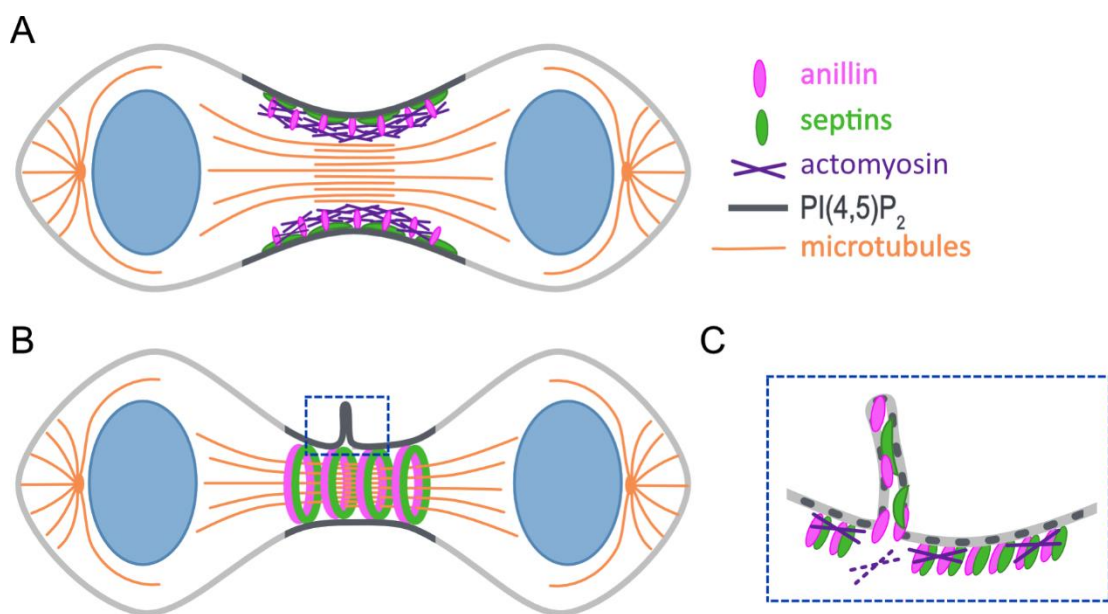


Figure 1-2. Cleavage furrow Ingression. (A) Representation of a cell at anaphase displaying a cleavage furrow. The actomyosin ring (violet criss-cross pattern) initiates the ingress, while the adaptor protein anillin (pink) anchors the contractile machinery to the PM and recruits septins (green). **(B)** Representation of a cell at the onset of telophase displaying an ICB. After the large-scale ingress of the furrow, anillin and septins (anillo-septin) organize into an array of circular filaments and promote the elongation and thinning of the ICB (as revealed by super-resolution analysis in Renshaw *et al.*, 2014). **(C)** Inset representing the extrusion of a membrane tubule from the ICB. This process is mediated by the anillo-septin and contributes to the ICB narrowing and disassembly of actomyosin. PI(4,5)P₂ (dark grey line in A and B) progressively increases at the ICB, but it is also likely lost, together with anillin and septins, during tubules extrusion (dark grey dashed line in C).

1.1.3. Abscission

At telophase, when the ICB has partially matured and the midbody bulge emerges, anillin and septins appear to switch roles, with the latter dictating the localization of the anillo-septin subnetwork (Russo & Krauss, 2021). Indeed, besides localizing to the midbody, anillin reorganizes with septins into a double ring flanking the midbody, and this step requires the interaction with septins (**fig. 1-3-A**) (Renshaw *et al*, 2014;

Panagiotou *et al*, 2022). These sites of ring formation represent two novel sites of constriction, where also a secondary actomyosin ring is formed to further constrict the ICB to a diameter of 200-300 nm. One of these constriction sites will eventually evolve into the site of abscission (Wang *et al*, 2019).

Abscission is primarily mediated by the endosomal sorting complex required for transport (ESCRT), whose assembly is initiated at the midbody (**fig.1-3-C**) (Addi *et al*, 2018). Precisely, the centralspindlin-interacting protein, CEP55, recruits TSG101 (a subunit of the ESCRT-I complex) and the adaptor protein ALIX (Hyung *et al*, 2008). These proteins act in parallel pathways to recruit ESCRT-III (Christ *et al*, 2016; Addi *et al*, 2020). When ESCRT-III appears at the midbody, the septin double ring has mostly faded but still partially overlaps with CHMP4B, the filament forming subunit of ESCRTIII that also organizes in a double ring at the midbody (Karasmanis *et al*, 2019). By the time septin rings have disassembled, CHMP4B extends in a spiral from one of the two sides of the midbody toward the closer constriction site and, together with other ESCRT-III subunits and associated factors, mediates membrane constriction and fission (**fig. 1-3-C**) (Mierzwa *et al*, 2017; Goliand *et al*, 2018; Pfitzner *et al*, 2020).

Interestingly, depletion of SEPT9, or replacement of anillin with a chimera incapable of septin binding, affects the translocation of ESCRT-III to the abscission site. This suggests the involvement of the anillo-septin subnetwork in the final step of cytokinesis (Renshaw *et al*, 2014; Karasmanis *et al*, 2019). Karasmanis and colleagues demonstrated that a direct interaction between SEPT9 and TSG101 is required to initiate the ESCRT-I dependent recruitment of ESCRT-III (Karasmanis *et al*, 2019). Thus, the septin double ring appears to provide a spatial cue for the assembly of the ESCRT machinery in proximity of the future abscission site (Karasmanis *et al*, 2019).

Abscission is facilitated also by a conspicuous delivery of recycling endosomes to the ICB from telophase on (Schiel *et al*, 2013; Gromley *et al*, 2005; Frémont & Echard, 2018). These vesicles move along the spindle MTs and tether in proximity of the midbody via the exocyst complex (Gromley *et al*, 2005). Localized fusion events contribute to the disassembly of cortical actin and promote further thinning of the future abscission site to a diameter of 100-200 nm (Dambournet *et al*, 2011; Schiel *et al*, 2012).

Interestingly, SEPT9 is also required for the midbody localization of the exocyst complex (Estey *et al*, 2010). Hence, SEPT9 contributes to abscission in multiple ways. Accordingly, upon depletion of SEPT9, nascent daughter cells fail to abscise and remain connected until the ICB regresses or breaks (Estey *et al*, 2010, 2013). Interestingly, depletion of SEPT9 does not compromise the generation and maturation of the ICB (Estey *et al*, 2010; Renshaw *et al*, 2014; Panagiotou *et al*, 2022). This is not the case of other septin paralogues, such as SEPT2, 7 or 11, whose depletion causes defects already at telophase (Estey *et al*, 2010). These data suggest that SEPT9 is dispensable for the functioning of the anillo-septin subnetwork at stages that precede late telophase. Considering the ability of septins to arrange in both octameric (with SEPT9) and hexameric (without SEPT9) units (paragraph 1.3.1), it could be that SEPT9 is excluded from the initial anillo-septin system (Mostowy & Cossart, 2012). In this regard, the recent work from Panagiotou and colleagues suggests the existence of two types of septin filaments at the ICB: SEPT9-containing and SEPT11-containing filaments, where exclusively the latter interacts directly with anillin (Panagiotou *et al*, 2022). SEPT9-containing filaments are recruited instead indirectly to the ICB via the interaction between anillin and CIN85, and are subsequently stabilized by hexameric-based septin filaments at the constriction sites (Panagiotou *et al*, 2022).

To finally accomplish the partitioning of daughter cells, the ESCRT-dependent membrane remodeling is tightly coordinated with severing and bucking-induced breakage of MTs bundles at the site of abscission, and with F-actin clearance at the ICB (McNally & Roll-Mecak, 2018; Schiel *et al*, 2013; Addi *et al*, 2018).

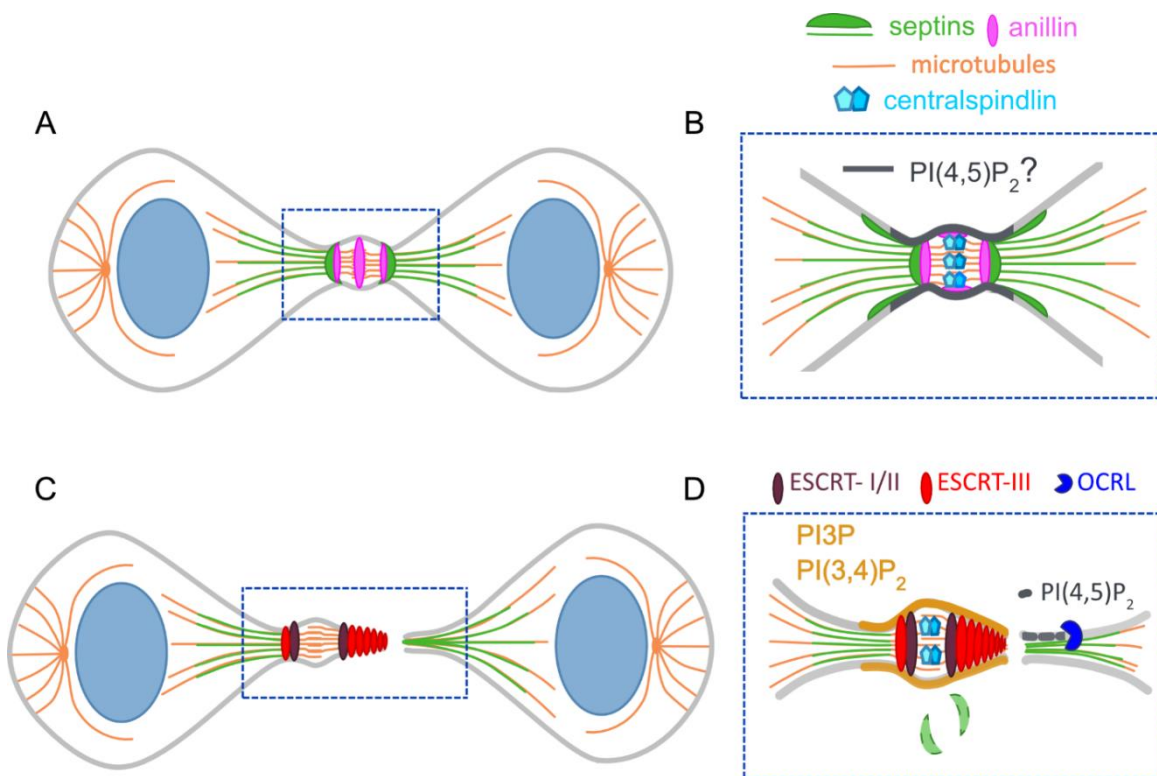


Figure 1-3. Midbody maturation and abscission. (A) From telophase on, daughter cells are connected through an ICB harboring in its middle the midbody organelle. At this stage, septins (green) dictate the reorganization of anillo-septin into a double ring flanking the midbody, and provide a spatial cue for the subsequent recruitment of the ESCRT-III machinery. (B) Inset representing the midbody. Centralspindlin (turquoise) accumulates at the plus-ends of interdigitating MTs and associates with the overlaying PM, where also anillin (pink) transiently localizes. Septins localize together with anillin at the double ring and distribute outside of the midbody at the PM and on bridge MTs. A pool of PI(4,5)P₂ (dark grey line) is likely required for midbody integrity. (C) Abscission. ESCRT-I/II (brown) and ALIX (not shown) recruit in parallel ESCRT-III (red) which arrives almost concomitantly with the septin double ring disappearance from the midbody. ESCRT-III complex polymerizes into a membrane-bound helices that extend toward the abscission site and further constrict the ICB until scission. (D) Phosphoinositide remodeling prior to abscission. The hydrolysis of PI(4,5)P₂ (dark grey dashed line) by OCRL supports the removal of F-actin from the ICB, while the synthesis of PI(3,4)P₂ at the midbody cortex and the delivery of PI(3)P-rich endosomes to the midbody (orange line for both) facilitate the assembly of the ESCRT-III machinery.

1.1.4. *In medio stat virtus*: functions of the midbody

The midbody appears as a bulge at the center of the candy-shaped constricted furrow (fig. 1-3-A-B). More precisely, it is the portion of the ICB that encapsulates the bundled interdigitating MTs deriving from the midzone, and that consists of a dense protein matrix (Mierzwa & Gerlich, 2014; Hu *et al*, 2012a; Fededa & Gerlich, 2012). As the spindle midzone plays a crucial role in initiating furrow constriction, the midbody orchestrates the final steps of cytokinesis.

One function of the midbody is to anchor the MTs array of the cytokinetic bridge to the PM (fig. 1-4) (Mierzwa & Gerlich, 2014). This is primarily mediated by the centralspindlin complex, which, upon completion of furrowing, accumulates at the

overlapping MTs plus ends at the center of the midbody (Hu *et al*, 2012a). While the motor protein MKLP1 binds MTs, MgcRacGAP possesses a C1 domain that binds PI(4)P and PI(4,5)P₂ at the overlaying PM (**fig. 1-4-A**) (Lekomtsev *et al*, 2012). Interestingly, in mammalian cells depletion or mutation of the C1 domain does not impair the assembly of the midzone or furrowing *per se*, but causes furrow retraction and cytokinesis failure (Lekomtsev *et al*, 2012). Therefore, the membrane tethering property of centralspindlin is dispensable at the spindle midzone but becomes essential once the midbody is formed to signal that cytokinesis can proceed toward abscission. MKLP1 also provides tethering since it interacts with the active and membrane-associated small GTPase ARF6 (ADP-ribosylation factor 6) (**fig.1-4-B**) (Makyio *et al.*, 2012).

Also anillin is present at the midbody cortex. In *Drosophila*, anillin interacts directly with MgcRacGAP, however this interaction has not been shown in mammalian cells (D'Avino *et al.*, 2008; Gregory *et al.*, 2008). Nevertheless, anillin binds CIT-K, which also concentrates at the midbody in a Rho A- and kinesin KIF14-dependent manner (B. Mierzwa & Gerlich, 2014). CIT-K links the cortex-associated anillin to MTs via the binding of KIF14, which in turn interacts with the MT-associated PRC1 (**fig.1-4-C**) (Gai *et al.*, 2011; Gruneberg *et al.*, 2006; S. Watanabe *et al.*, 2013). This function is independent of the CIT-K enzymatic activity but is essential for a successful cytokinesis. Indeed, depletion of CIT-K in HeLa and primary cells causes regression of the ICB (Gai *et al.*, 2011; S. Watanabe *et al.*, 2013). This suggests that CIT-K may contribute in a minor way to the activation of myosin II at anaphase but, as the ICB forms, it becomes an essential scaffold at the midbody.

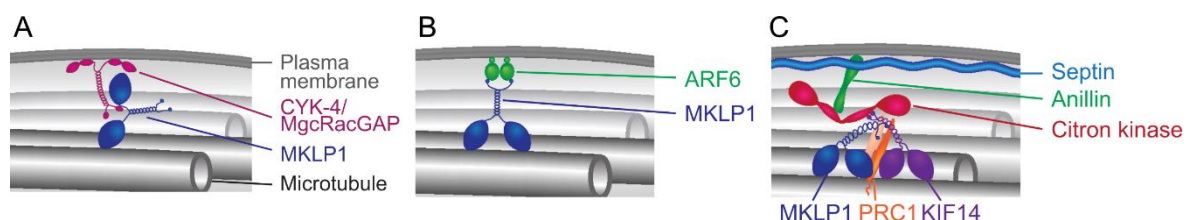


Figure 1-4. The anchoring function of the midbody. Several mechanisms account for the anchoring of bridge MTs to the PM at the midbody. **(A)** Centralspindlin MgcRacGAP subunits interact with plasmalemmal PI(4,5)P₂ while being in a complex with the two MT-associated MKLP1 subunits. **(B)** From telophase on, MKLP1 dimers interact with two molecules of membrane-bound ARF6. **(C)** Anillin binds plasmalemmal PI(4,5)P₂ and CIT-K. CIT-K interacts with the MT-associated kinesin KIF14, which in turn forms a complex with MKLP1 and PRC1. Although septins are depicted in the panel, their presence at the midbody is only transient. Modified from B. Mierzwa & Gerlich, 2014.

Besides its anchoring function, the midbody serves as a crossroad of several pathways that ultimately lead to abscission (Mierzwa & Gerlich, 2014). Firstly, MKLP1 recruits the adaptor protein CEP55, thereby initiating the local assembly of the ESCRT machinery, as described in paragraph 1.1.3 (Hyung *et al*, 2008). Secondly, together with exocyst, centralspindlin participates in the tethering of recycling endosomes that are delivered to the ICB (**fig. 1-5**). This is mediated by the effector protein FIP3 (Rab11 family-interacting protein 3), which localizes on Rab11-positive vesicles and binds directly to MgcRacGAP, and indirectly to MKLP1 through the interaction with ARF6 (Fielding *et al*, 2005; Takahashi *et al*, 2011; Simon *et al*, 2008).

FIP3/Rab11-positive recycling endosomes carry p50RhoGAP, a GAP for RhoA (Schiel *et al*, 2012). Hence, the local accumulation and fusion of these vesicles promotes inactivation of RhoA, and consecutively the disassembly of cortical actin in proximity of the future abscission site (Schiel *et al*, 2013, 2012; Frémont & Echard, 2018). The cascade of events leading to abscission is not only tightly regulated in space, but also in time. Indeed, centralspindlin becomes available to FIP3-positive endosomes only at telophase. FIP3 binds MgcRacGAP at the same site as ECT2. Thus, this interaction can take place only upon ECT2 relocation to the nucleus (Simon *et al*, 2008). ARF6, on the other side, initially localizes in proximity of the cleavage furrow, and only at telophase translocates to the midbody (Takahashi *et al*, 2011; Schweitzer & D'Souza-Schorey, 2002).

The exocyst-mediated tethering and subsequent bulk fusion of post-Golgi derived vesicles near the midbody also contributes to cortical actin destabilization and thinning of the ICB prior to abscission (Gromley *et al*, 2005).

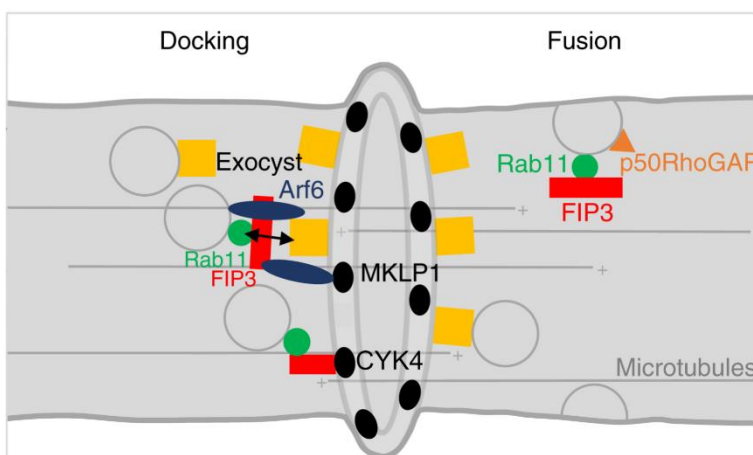


Figure 1-5. The midbody is a docking station for recycling endosomes. Example of vesicle docking and fusion at the midbody. Midbody-localized exocyst (yellow), ARF6 (dark blue) and MgcRacGAP (CYK4, black) tether Rab11-FIP3 (green-red) endosomes which subsequently fuse in proximity of the midbody. Fusion of FIP3-Rab11 endosomes contributes to the narrowing of the ICB and to the downregulation of RhoA through the delivery of

p50RhoGAP. Both processes are required for successful cytokinesis. Modified from Frémont & Echard, 2018.

1.1.5. A gap in the middle: the GAP function of centralspindlin

The centralspindlin subunit MgcRacGAP possesses GAP activity, which is required to complete cytokinesis (Hirose *et al*, 2001; Canman *et al*, 2008; Bastos *et al*, 2012). However, its target is under debate (Wadsworth, 2021). Initial data point toward RhoA, which forms complex with centralspindlin and the RhoGEF ECT2 at anaphase (Miller & Bement, 2009; Piekny *et al*, 2005). This was suggested to result in a constant cycling of RhoA between the GTP and GDP bound state, a condition supposedly needed to maintain its activity at the cell equator (Miller & Bement, 2009). However, in vitro studies demonstrated that MgcRacGAP has low catalytic activity toward RhoA, and has greater activity toward Rac1 and Cdc42 (Jantsch-Plunger *et al*, 2000; Touré *et al*, 1998; Kawashima *et al*, 2000). Accordingly, a growing body of literature now supports a role of MgcRacGAP in downregulating Rac1 from anaphase on (Zhuravlev *et al*, 2017; Canman *et al*, 2008; Bastos *et al*, 2012; Wadsworth, 2021; Chircop, 2014). Consistently, low Rac1 activity at the midzone, as visualized for instance by FRET-based activity probes (Yoshizaki *et al*, 2003), is required to prevent actin branching and the formation of focal adhesions (Bastos *et al*, 2012). Both processes would otherwise restrain furrow constriction and flexibility within the ICB.

Oceguera-Yanez and colleagues have shown that MgcRacGAP also acts toward Cdc42 at prometaphase (Oceguera-Yanez *et al*, 2005). At metaphase, the GAP activity of centralspindlin is inhibited by the interaction with PRC1 (Ban *et al*, 2004). At this stage, Cdc42 activity increases and is required at the mitotic spindle to regulate the bi-oriented attachment of kinetochores to spindle MTs (Yasuda *et al*, 2004; Chircop, 2014; Oceguera-Yanez *et al*, 2005). Following metaphase, Cdc42 activity decreases again (Yoshizaki *et al*, 2003). Interestingly, MgcRacGAP is phosphorylated by aurora B kinase at the midbody, and in vitro studies have shown that this modification releases MgcRacGAP from the inhibitory interaction with PRC1 (Ban *et al*, 2004; Minoshima *et al*, 2003). It is therefore plausible that centralspindlin contributes also to a subsequent downregulation of Cdc42 at the ICB.

1.1.6. Origin and function of phosphoinositides during cytokinesis

Phosphoinositides (PIs) are signaling lipids originating from the reversible phosphorylation of the myo-inositol head group of phosphatidylinositol at hydroxyl

positions 3, 4 and 5 (Balla, 2013). They localize at the cytoplasmic leaflet of cellular membranes, where they insert the two acyl chains and expose the hydrophilic head to the cytoplasm (Balla, 2013). Although PIs represent less than 1% of the total cellular lipids, they play important functions in membrane dynamics and cytoskeletal remodeling, and participate also in cytokinesis (Posor *et al*, 2022; Echard, 2012).

PI(4,5)P₂ is abundant at the PM and, at anaphase, serves the anchoring of the centralspindlin-bound ECT2 to the equatorial plane of the cell cortex. ECT2 thereby aids the local activation of RhoA (**fig. 1-1**) (Yüce *et al*, 2005). Overexpression of PI(4,5)P₂-binding protein domains revealed that at this stage PI(4,5)P₂ is homogeneously distributed at the PM. However, it becomes ~4,5 fold concentrated at the furrow from initial ingression to full constriction (**fig. 1-2**) (Abe *et al.*, 2012; Field *et al.*, 2005; Liu *et al.*, 2012). It is, therefore, likely that PI(4,5)P₂ is synthesized *de novo* at the cleavage furrow. This might be supported by active RhoA, which could recruit and stimulate a type I PIP-kinase (phosphatidylinositol-4-phosphate 5-kinase) to locally increase PI(4,5)P₂ concentration (paragraph 1.2.1) (Emoto *et al*, 2005; Santarius *et al*, 2006). In support of this hypothesis, PIPKI β distributes homogeneously at the PM during interphase and accumulates at the cleavage furrow at late anaphase/early telophase in mammalian CHO cells (as described in paragraph 1.2.2) (Emoto *et al*, 2005). Of note, type I PIP-kinases, Skittles kinase and Its3, have also been visualized at the cleavage furrow of *Drosophila* S2 cells and at the septum of the yeast *S. pombe*, respectively (Roubinet *et al*, 2011; Zhang *et al*, 2000).

Several approaches have been used to manipulate PI(4,5)P₂ levels at the cleavage furrow, for instance the overexpression of PI(4,5)P₂-sequestering or hydrolyzing domains, injection of PI(4,5)P₂-specific antibodies, or overexpression of kinase-dead PIPKI β . All of these approaches led to cytokinesis failure and multinucleation but, interestingly, did not affect the assembly and initial contraction of the actomyosin ring (Liu *et al*, 2012; Field *et al*, 2005; Emoto *et al*, 2005; Abe *et al*, 2012; Echard, 2012). This reflects a prevalent role for PI(4,5)P₂ after the formation of the furrow, where the local increase of this phosphoinositide aids the stabilization and anillin-dependent anchoring of the contractile machinery to the PM (**fig. 1-2-A**) (Liu *et al*, 2012; Field *et al*, 2005; Echard, 2012). Of note, several actin regulators known to localize to the contractile ring are also binding PI(4,5)P₂ (Cheffings *et al*, 2016).

Multiple lines of evidence suggest that PI(4,5)P₂ is also required at the midbody, after closure of the furrow (**fig. 1-3-B**) (Cauvin & Echard, 2015). For example, the anchoring of bundled MTs to the PM depends on the PI(4,5)P₂-binding ability of MgcRacGAP (Lekomtsev *et al*, 2012). A local pool of PI(4,5)P₂ may also facilitate the targeting of the exocyst complex to the midbody, while additional synthesis of PI(4,5)P₂ on vesicles about to fuse seems necessary for their exocyst-mediated tethering to the PM (He *et al*, 2007; Maib & Murray, 2022). Furthermore, as the actomyosin ring thins out, PI(4,5)P₂ may help to retain anillin at the midbody, and guide the reorganization of the anillo-septin at the ICB (**fig. 1-2-B** and **fig. 1-3-A-B**) (paragraph 1.3.4). Of note, at telophase, active ARF6 interacts with MKLP1 and accumulates at the midbody, and may thus contribute to maintaining a high concentration of PI(4,5)P₂ by recruiting and locally activating a type I PIP-kinase (paragraph 1.2.1) (van den Bout & Divecha, 2009; Makyio *et al*, 2012). The septin double ring may then act as a diffusion barrier and help to concentrate PI(4,5)P₂ at the midbody (Katja Schmidt & Benjamin J. Nichols, 2004; Pacheco *et al*, 2023).

Prior to abscission, a remodeling of phosphoinositides takes place at the ICB (**fig. 1-3-D**). As PI(4,5)P₂ stimulates F-actin polymerization and inhibits the F-actin severing protein cofilin (Saarikangas *et al*, 2010) it needs to be degraded to clear F-actin from the abscission site (F-actin may act as a physical barrier to vesicle fusion and ESCRT-III mediated membrane constriction) (Cauvin & Echard, 2015). This process is carried out by the PI(4,5)P₂-5-phosphatase OCRL (oculo-cerebro-renal-syndrome of Lowe), which is targeted to the abscission site by active Rab35 (Frémont & Echard, 2018; Dambournet *et al*, 2011). Furthermore, at late telophase, PI3K-C2 α localizes at the midbody and synthesizes PI(3,4)P₂ which enhances the recruitment of the ESCRT-II subunit VPS36 (Gulluni *et al*, 2022). The latter contributes to the ALIX-independent cascade of ESCRT-III recruitment to the midbody (paragraph 1.1.3) (Christ *et al*, 2016). It is possible that the PI(4)P originating from the dephosphorylation of PI(4,5)P₂ by OCRL fuels the synthesis of PI(3,4)P₂ in a PM-based PI conversion process that precedes abscission.

The assembly of the ESCRT-III complex relies also on PI(3)P (Nezis *et al*, 2010). PI(3)P-positive recycling endosomes accumulate at the midbody and recruit the PI(3)P-binding centrosomal protein FYVE-CENT and its binding partner TTC19 (tetratricopeptide repeat domain 19). TTC19 in turn interacts with CHMP4B and possibly regulates ESCRT-III oligomerization (Sagona *et al*, 2010). Accordingly, the

class III PI-3-kinase VPS34 also localizes to the ICB (possibly at the levels of endosomes) and its depletion, or depletion of its accessory subunit Beclin1, causes defects in cytokinesis (Sagona *et al*, 2010; Thoresen *et al*, 2010).

1.2. Type I PIP-kinases, a source of diversified PI(4,5)P₂ pools

Cellular PI(4,5)P₂ can be synthesized through different routes. The major one consists of the phosphorylation of PI(4)P at the D-5 position of the inositol ring by type I PIP-kinases (Choi *et al*, 2015). This group of enzymes belongs to the family of phosphatidylinositol phosphate kinases (PIP-kinases) together with type II and type III PIP-kinases, with whom they share a conserved catalytic core domain (Balla, 2013). At the C-terminus of the core domain resides the activation loop that confers substrate specificity, and, in type I PIP-kinases, contributes to the targeting to the PM (Doughman *et al*, 2003). Type II PIP-kinases synthesize PI(4,5)P₂ as well, however they use as substrate PI(5)P, which is a less abundant lipid. Moreover, based on their low catalytic activity it has been proposed that some of them rather only act as scaffolds (Bulley *et al*, 2015). The type III PIP-kinase, also called PIKfyve in mammals, phosphorylates PI(3)P into PI(3,5)P₂ (Balla, 2013).

The following paragraphs of this section will describe the regulatory mechanisms governing the localized activity of type I PIP-kinases, and the involvement of PIPKI β during cytokinesis. Furthermore, PIPKI γ isoforms and key functions will be introduced.

1.2.1. Overview on the contribution and regulation of type I PIP-kinases

The type I PIP-kinase subfamily (PIPKIs) comprises three isozymes: PIPKI α , β and γ , and PIPKI γ exists in different isoforms (Balla, 2013). For clarity, reference to PIPKI α and β follows the nomenclature of human variants. PIPKI α and β knock-out mice live to adulthood, albeit they display functional defects in specific cell types, namely mast cells and platelets (Sasaki *et al*, 2005; Wang *et al*, 2008). Regarding PIPKI γ , two independent knock-out mice have been described. One study reports embryonal lethality due to cardiovascular and neural tube closure defects, while the

other describes postnatal death due to generalized neuronal deficits (Wang *et al*, 2007; Di Paolo *et al*, 2004). Indeed, PIPKI γ is the major source of PI(4,5)P₂ required for clathrin mediated endocytosis of synaptic vesicles in the brain (Wenk *et al*, 2001). Interestingly, mice lacking PIPKI α and β , but expressing PIPKI γ from a single allele can survive until adulthood (Volpicelli-Daley *et al*, 2010). These data suggest that, contrary to PIPKI γ , PIPKI α and β synthesize PI(4,5)P₂ pools whose absences can be compensated by the activity of other phosphoinositide kinases.

It has been reported that in HeLa cells, the knock-down of any of the PIPKIs results in the increased expression of at least one of the two other isozymes, again implying the existence of compensatory mechanisms (Padrón *et al*, 2003). Additionally, PIPKI β and γ (and possibly also PIPKI α) form homo- and heterodimers, and this property regulates their catalytic activity and targeting to the PM (Lacalle *et al*, 2015). Nonetheless, it is generally agreed that under wild type conditions PIPKI α , β and γ synthesize distinct pools of PI(4,5)P₂ (Balla, 2013).

PIPKIs are involved in a variety of processes including cell migration, membrane trafficking and cytokinesis, where different PIPKI isozymes act in concert or alone, and their contribution can vary according to the tissue and cell type (van den Bout & Divecha, 2009; Tan *et al*, 2015; Russo & Krauss, 2021). During these processes, the spatiotemporal control of PI(4,5)P₂ synthesis is achieved through a strict regulation of PIPKIs activity and localization. The N- and C- termini of PIPKIs vary between isozymes (and their isoforms) and are responsible for the targeting of the kinase to specific subcellular compartments (Choi *et al*, 2015). As highlighted by Choi and colleagues, several PIPKIs interactors and recruiters are PI(4,5)P₂ effectors themselves, and this guarantees a tight link between PI(4,5)P₂ production and usage (**fig.1-6**) (Choi *et al.*, 2015). The localization and activity of PIPKIs is further regulated by the Rho family of GTPases (RhoA, Rac1 and Cdc42) and the ADP-ribosylation factors (ARFs), which act as molecular switches to spatially and temporally control the synthesis of PI(4,5)P₂ on cellular membranes (van den Bout & Divecha, 2009). Rho GTPases modulate PIPKIs activity and link it to actin remodeling (Santarius *et al*, 2006). Additionally, RhoA and Rac1 interact with PIPKIs and contribute to their targeting to specific subcellular compartments (Weernink *et al*, 2004a). For example, in N1E-115 neuroblastoma cells the interaction with Rac1 controls the targeting of PIPKI β to the PM, and thereby the localized synthesis of PI(4,5)P₂ required for neurite retraction (Halstead *et al*, 2010).

Among ARF proteins, ARF1 and ARF6 have been shown to interact with and regulate the activity of PIPKs (van den Bout & Divecha, 2009; Honda *et al*, 1999). ARF6, in particular, controls the phosphoinositide conversion by PIPK1 γ during vesicle trafficking and, possibly, at the PM during the formation of contact sites between ER (endoplasmic reticulum) and PM (Chen *et al*, 2017; Krauss *et al*, 2003; Maib & Murray, 2022). Specifically, on vesicles about to fuse with the PM, ARF6 recruits PIPK1 γ and thereby enables the synthesis of PI(4,5)P₂ required for the exocyst-mediated membrane tethering (Maib & Murray, 2022). At the presynaptic membrane, ARF6-induced PIPK1 γ activity facilitates the assembly of clathrin coated pits (Krauss *et al*, 2003).

Further relevant examples of PIPKs functions and regulation will be described in the following paragraphs.

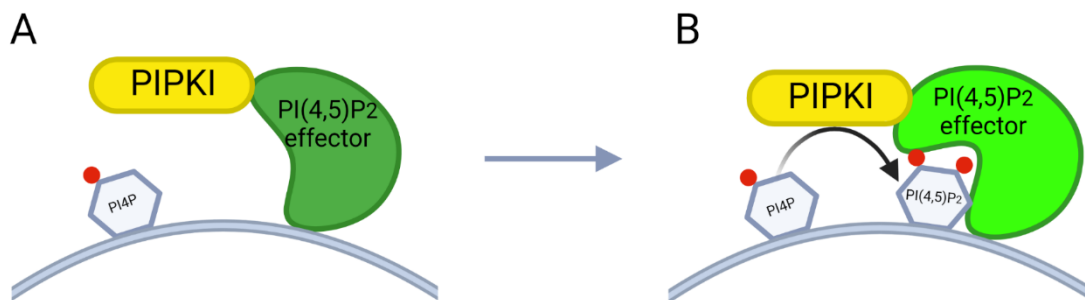


Figure 1-6. The localized synthesis of PI(4,5)P₂ by PIPKs is linked to its usage. (A) PIPKI interacts with -and is recruited by- a PI(4,5)P₂ effector. **(B)** PIPKI synthesizes PI(4,5)P₂ in proximity of the effector which binds PI(4,5)P₂ and undergoes activation (highlighted with lighter green and with a change of shape).

1.2.2. The role of PIPK1 β during cytokinesis

As described in paragraph 1.1.6, PI(4,5)P₂ accumulates at the cleavage furrow of dividing cells and it is required for the maturation of the ICB. Its source remains largely unknown, but some evidence suggests a role for PIPK1 β . PIPK1 β colocalizes with RhoA at the cleavage furrow of dividing CHO cells, and overexpression of a PIPK1 β kinase dead mutant impairs the accumulation of PI(4,5)P₂ at the furrow and leads to an increase in multinucleation (Emoto *et al*, 2005). Based on these data, Emoto and colleagues hypothesize that RhoA may recruit and activate PIPK1 β and thereby couple the local synthesis of PI(4,5)P₂ to furrow constriction (Emoto *et al*, 2005).

In another study, Abe and colleagues show a transbilayer colocalization between PIPK1 β and sphingomyelin (SM)-rich domains (situated at the outer leaflet of the

PM), and propose a role for these domains in the accumulation of PI(4,5)P₂ at the cleavage furrow (Abe *et al*, 2012). Indeed, the removal of SM from the outer leaflet of the PM, via SMase treatment, abolishes the accumulation of PI(4,5)P₂ at the furrow and results in cytokinesis failure of HeLa cells (Abe *et al*, 2012).

Nonetheless, it remains unknown whether other lipid kinases participate to the synthesis of PI(4,5)P₂ during cell division, and which are the mechanisms that define a precise spatial and temporal recruitment of PIPKI β to the cleavage furrow.

1.2.3. PIPKI γ isoforms and their functions

The human gene encoding PIPKI γ gives rise to at least 5 isoforms (PIPKI γ -i1 to PIPKI γ -i5) by alternative splicing, as schematized in **fig. 1-7**. PIPKI γ -i1 is 640 amino acids long and consists of a catalytic core domain flanked by N- and C-terminal sequences (Schill & Anderson, 2009). The sequence of PIPKI γ -i1 is shared by all isoforms, and PIPKI γ -i2 to -5 contain extra C-terminal extensions (from here on referred to as tails), which contribute to the targeting of these isoforms to specific subcellular compartments (Xu *et al*, 2014). PIPKI γ -i1 is predominately found at the PM and is the major contributor to the synthesis of PI(4,5)P₂ utilized upon G-protein coupled receptor activation (Wang *et al*, 2004). PIPKI γ -i2 possesses a C-terminal tail of 28 amino acids that binds the FERM domain of talin (**fig. 1-7**) (Di Paolo *et al.*, 2002). This interaction is responsible for targeting PIPKI γ -i2 to nascent focal adhesions, where the localized synthesis of PI(4,5)P₂ modulates the association of talin with β -integrins and focal adhesions dynamic (Ling *et al*, 2002). The phosphorylation of PIPKI γ -i2 by FAK (focal adhesion kinase), Src kinase, Akt kinase and EGFR (epidermal growth factor receptor) can further regulate the interaction with talin and the lipid kinase activity (Le *et al*, 2015; Ling *et al*, 2002, 2003; Sun *et al*, 2007). Furthermore, the C-terminal tail of PIPKI γ -i2 contains a sorting motif responsible for the direct association with the μ subunit of the protein complex AP1B (Ling *et al*, 2007). Owing to this property, PIPKI γ -i2 acts as a cargo adaptor between E-cadherin and AP1B and is required for the recycling of E-cadherin to the PM (Ling *et al*, 2007; Xiong *et al*, 2012). Accordingly, depletion of PIPKI γ in polarized epithelial cells affects adherent junctions and results in morphological changes and acquisition of a migratory phenotype (Ling *et al*, 2007). Importantly, PIPKI γ -i2 is also highly expressed in the brain, where it plays a crucial role in clathrin mediated

endocytosis of synaptic vesicles (Nakano-Kobayashi *et al*, 2007; Wenk *et al*, 2001). This role is accomplished through the binding of the $\beta 2$ ear of AP2 via the isoform-specific tail, and through the binding of $\mu 2$ via both tail and kinase core domain (Kahlfeldt *et al*, 2010; Bairstow *et al*, 2006; Thieman *et al*, 2009). These interactions serve the recruitment of PIPKI γ -i2 to endocytic sites and the stimulation of its catalytic activity (Kahlfeldt *et al*, 2010; Krauss *et al*, 2006).

The C-terminal tail of PIPKI γ -i3 consists of a 26 amino acid fragment, followed by the 28 amino acid tail of PIPKI γ -i2 (**fig. 1-7**) (Xu *et al*, 2014). During G1/S phase PIPKI γ -i3 has been shown to localize to the centrosome, where it restricts centrioles duplication through the interaction with PLK4 (polo-like kinase 4) (Xu *et al*, 2014). Interestingly, the centrosome-targeting signal of PIPKI γ -i3 is localized at the kinase core domain; it is thus plausible that the C-terminal tail of this isoform helps the exposure of the signal, which remains hidden in other isoforms (Xu *et al*, 2014). It is unclear whether also PIPKI γ -i3 contributes to focal adhesion dynamic, considering the presence of the talin binding fragment at its C-terminus.

PIPKI γ -i4 has a unique C-terminal tail of 60 amino acids (**fig. 1-7**) and is found in the nucleus, however its function there has not been fully determined yet (Choi *et al*, 2015; Schill & Anderson, 2009).

PIPKI γ -i5 tail consists of the 26 amino acids fragment of PIPKI γ -i3, followed by a unique 41 amino acids fragment (**fig. 1-7**) (Schill & Anderson, 2009). The 26 amino acid insert of PIPKI γ -i5 allows the direct binding of SNX5 (sorting nexin 5) on endosomes, where the local production of PI(4,5)P₂ modulates the interaction between SNX5 and Hrs, a component of the ESCRT-0 complex (Sun *et al*, 2013; Schill *et al*, 2014). This interaction prevents Hrs from being ubiquitinated and thereby favors its interaction with EGFR and the consequent sorting of EGFR into lysosomes (Sun *et al*, 2013). In epithelial cells, endosomal PIPKI γ -i5 promotes the lysosomal sorting and degradation of E-cadherin and this process is positively regulated by the Src-dependent phosphorylation of PIPKI γ -i5 at the tyrosine in position 646 (Y646) (Schill *et al*, 2014). This residue is located in the 26 amino acids fragment shared by PIPKI γ -i3 and PIPKI γ -i5 tails. PIPKI γ -i5 also interacts with ATG14 (autophagy related protein 14) at the interphase between endosome and ER, where autophagosomes form (Tan *et al*, 2016). ATG14 binds PI(4,5)P₂, and the localized synthesis of this phosphoinositide promotes the ATG14-Beclin1-VPS34 complex formation and initiation of autophagy (Tan *et al*, 2016; Fan *et al*, 2011).

The presence of a common fragment in the tail of PIPK γ -i3 and i5, suggests the possibility that the localization, regulation, and functions of these two isoforms may partially overlap, although this has not been investigated yet.

In one study, a sixth isoform of PIPK γ (PIPK γ -i6) was amplified from human and rodents tissue cDNA library (Xia *et al*, 2011). This isoform consists of the sequence of PIPK γ -i1 followed by the 26 amino acid fragment common to PIPK γ -i3 and PIPK γ -i5 (**fig. 1-7**) (Xia *et al*, 2011). However, this isoform is not annotated on Ensembl Genome Browser and its role remains unknown; once again, based on its architecture one could hypothesize shared features with PIPK γ -i3 and PIPK γ -i5.

In conclusion, the variable C-terminal tails of PIPK γ isoforms dictate the subcellular localization and function of this lipid kinase. Based on this principle, the discovery of isoform-specific interacting partners may help to identify novel PI(4,5)P₂ pools, and to gain insights in the regulatory mechanisms governing them.

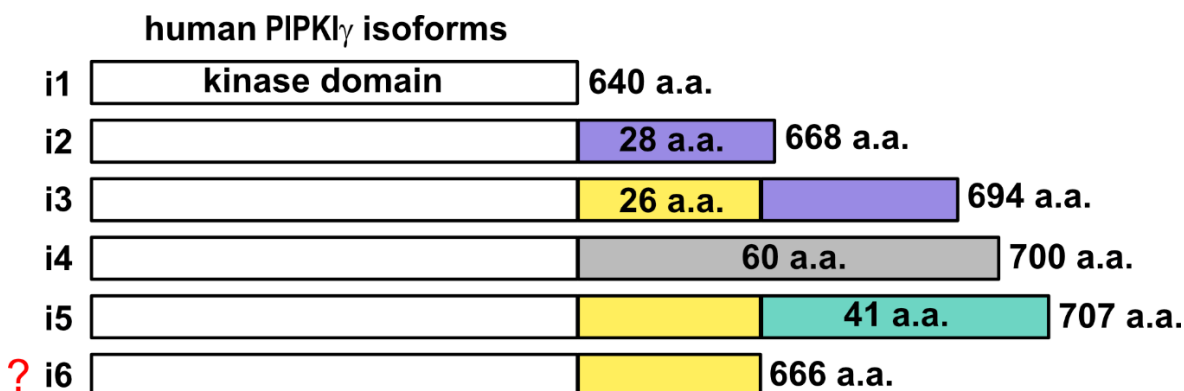


Figure 1-7. Scheme representing the human PIPK γ isoforms. All isoforms share a common sequence (1 to 640 amino acids) containing the kinase core domain. Alternative splicing generates different C-termini. The question mark refers to the putative existence of human PIPK γ -i6. A.a.= amino acids.

1.3. The septin cytoskeleton and its remodeling

As highlighted in section 1.1, septins play a pivotal role during cell division. To fulfill their functions, they must undergo a dramatic remodeling. Upon initial recruitment to the cleavage furrow, they reorganize into a double-ring when the midbody is assembled, and finally redistribute along the acetylated tubulin bridge (Russo & Krauss, 2021; Renshaw *et al*, 2014; Karasmanis *et al*, 2019). Septins play important roles also at interphase or in non-dividing cells and, also in these cases, they display remarkable plasticity in interacting with cellular membranes and other components of the cytoskeleton (Spiliotis & McMurray, 2020). A growing body of literature highlights the relevance of septin subcellular organization in the pathophysiological processes underlying migration and resistance of cancer cells to chemotherapeutic drugs (Poüs *et al*, 2016; Salameh *et al*, 2021; Calvo *et al*, 2015; Targa *et al*, 2019). Hence, understanding the basis of septin remodeling has become of crucial importance. Nevertheless, to date very few mechanisms regulating the septin cytoskeleton are known; interestingly, one of them consists in the interaction with the phosphoinositide PI(4,5)P₂ (Beber *et al*, 2019).

The following paragraphs will describe the organization and functions of mammalian septins and summarize the regulatory mechanisms orchestrating their subcellular remodeling.

1.3.1. A variety of septins and septin complexes: a Lego playground for the cell

Septins are filament-forming cytoskeletal GTP-binding proteins that belong to the superclass of phosphate-binding loop (P-loop) NTPases (Leipe *et al*, 2002). These proteins were initially discovered in the budding yeast *Saccharomyces cerevisiae*, where they promote the formation of a *septum* at the neck between the mother cell and the bud (Hartwell, 1971). In accordance with their role, they were named “septins” by John Pringle (Ford & Pringle, 1991; Haarer & Pringle, 1987). Since their discovery, septins have been identified in all eukaryotes except land plants (Nishihama *et al*, 2011). In mammals there are thirteen septin genes: SEPT1 to SEPT12 and SEPT14, and at least eleven pseudogenes, including the former SEPT13 (now named as pseudogene SEPT7P2) (Ivanov *et al*, 2021). Some septin paralogues are ubiquitously expressed, while others display cell- and tissue-specific expression (Zuvanov *et al*, 2019). Septin complexity is further increased by

alternative splicing that gives rise to a plethora of isoforms (Hilary Russell & Hall, 2011).

Based on sequence homology, septins are divided into four subgroups carrying the names of their founding member: SEPT2 (comprising SEPT1, 2, 4 and 5), SEPT6 (SEPT6, 8, 10, 11, 14), SEPT3 (SEPT3, SEPT9 and SEPT12) and SEPT7 (unique in its subgroup) (Mostowy & Cossart, 2012) (**fig. 1-8-A**). All members of these subgroups share a GTP binding domain (G domain) and a septin unique element (SUE) that is important for filament formation (Cavini *et al*, 2021). On the contrary, the amino- and carboxyl- terminal extensions (NTE and CTE) vary between subgroups. For example, SEPT9 has an alternatively spliced NTE that contains proline-rich domains and repeat motifs that mediate direct interactions with other cytoskeletal components (as described in paragraphs 1.3.2 and 1.3.3) (Spiliotis & Nakos, 2021). Moreover, the NTEs of septins in subgroups 2, 3 and 7 share a polybasic region (adjacent to the N-terminus of the G domain) that is involved in phosphoinositide binding (Zhang *et al*, 1999). Members of the septin 6 subgroup retain only one basic residue in this region and therefore it cannot be classified as polybasic (Cavini *et al*, 2021). On the contrary, septin 6 harbors an amphipathic helix in its CTE that confers the ability to sense micrometer-scale membrane curvature (Cannon *et al*, 2019). Finally, the CTE of septins in subgroups 2, 6 and 7 include coiled coils sequences of variable length that are involved in the stabilization and cross-bridging of filaments (Cavini *et al*, 2021) (**fig. 1-8-A**).

Contrary to other small GTPases, septins are able to polymerize into filaments. The building blocks of a septin filament are palindromic hetero-hexamers and/or hetero-octamers. In these complexes, septin subunits interact with one another through their N- and C- termini or G-domains, creating the so called NC or G interfaces, which alternate along the oligomer (Sirajuddin *et al*, 2007). The prototypical order of the septin subunits in the hexamer and octamer is as follows: 2-6-7-7-6-2 and 2-6-7-3-3-7-6-2, respectively (Mendonça *et al*, 2019; Soroor *et al*, 2021) (**fig. 1-8-B**). Septin hexamers and octamers are able to co-polymerize *in vitro* and they might co-exist within the same filament also *in vivo* (Soroor *et al*, 2021). Due to the palindromic order of the septin oligomers and to the alternation of the NC and G interfaces within them, septin filaments are apolar, contrary to MTs and filamentous actin (Hagiwara *et al*, 2011; Mostowy & Cossart, 2012). Moreover, septin filaments can assemble into high-order structures such as bundles and rings. In this case, the

coiled coils protruding from adjacent filaments mediate the interconnection between adjacent filaments (Leonardo *et al*, 2021).

It has been proposed that any subunit of the prototypical hexamer or octamer can be substituted by another septin belonging to the same subgroup. This theory was proposed by Makoto Kinoshita and it is known as the “Kinoshita hypothesis” (Kinoshita, 2003). Based on this, one can predict 20 and 60 different combinations of hexamers and octamers, respectively. As a consequence, a plethora of septin filaments with distinct identity might be built by the cell to meet different functions. Such a scenario could contribute to the high variability of septin structures and subcellular localizations observed within the cell and between cell types.

Although the Kinoshita hypothesis has been established based on molecular evidence, the existence and biological relevance of different complexes combination have not been established yet (Mendonça *et al*, 2019). Additionally, not all septin paralogues are ubiquitously expressed, and it has been suggested that paralogues with higher correlated expression levels have higher chance to coexist in the same tissue-specific complexes (Ivanov *et al*, 2021). Nevertheless, as mentioned in paragraph 1.1.3, a recent work has described, in the context of cytokinesis, the existence of septin filaments that incorporate either SEPT9 or SEPT11. Both coexist at the ICB but interact differently with anillin (Panagiotou *et al*, 2022) Thus, differences in subunit composition might indeed confer unique functionalities to septin filaments.

As other cytoskeletal structures, assembly and stability of septin filaments depend on nucleoside triphosphate hydrolysis. However, contrary to MTs and actin cables, that are destabilized by the hydrolysis of ATP and GTP respectively, the G interfaces between SEPT7 subunits within the septin filament are significantly stabilized by the presence of GDP (**fig. 1-8-B**) (Sirajuddin *et al*, 2009; Zent & Wittinghofer, 2014). Paralogues belonging to the septin 2, 3 and 7 subgroups present GTPase activity. Instead, members of the septin 6 subgroup are incapable of hydrolyzing GTP; however, the presence of a GTP at the SEPT6-SEPT2 G interface favors the correct pairing of these two paralogues (Zent & Wittinghofer, 2014; Cavini *et al*, 2021; Sirajuddin *et al*, 2009).

Due to a slow GTP turnover, septin filaments are more stable compared to MTs and actin fibers (Spiliotis, 2018; Hu *et al*, 2008; Hagiwara *et al*, 2011). Furthermore, considering the absence of any known septin GAPs and GEFs, their reorganization

possibly relies on posttranslational modifications (PTMs) (Hernández-Rodríguez & Momany, 2012; Spiliotis & McMurray, 2020) and other unknown mechanism.

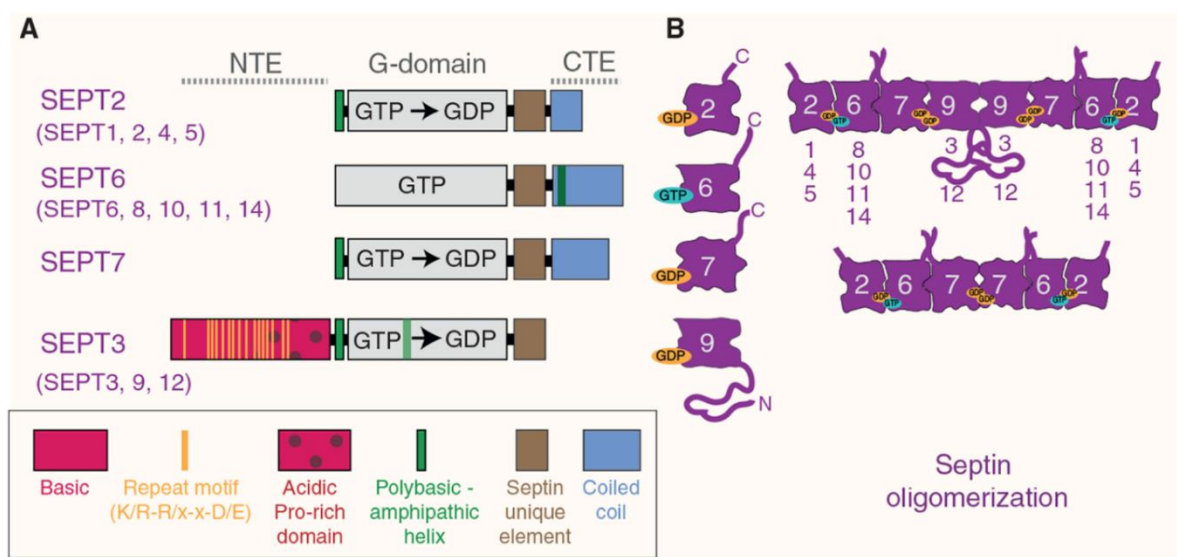


Figure 1-8. Structure and assembly of mammalian septins. (A) Mammalian septin subgroups and representation of conserved and variable sequences among them. (B) Prototypical septin hexamers and octamers. Possible subunit exchange is indicated according to the Kinoshita's hypothesis. Adapted from (Spiliotis & Nakos, 2021).

1.3.2. Subcellular localization and functions of actin-associated septins

So far, among mammalian septin paralogues, only SEPT9 has been proven to directly interact with actin (Spiliotis & Nakos, 2021). Electron microscopy and *in vitro* assays have shown that the purified human isoform 1 of SEPT9 (SEPT9-i1) is able to bind and cross-link F-actin through the basic region of its NTE, which is shared for the most part also by SEPT9-i2 and SEPT9-i3 (Smith *et al*, 2015). Two binding sites of SEPT9 on actin surface are shared by cofilin, hence presence of SEPT9 long isoforms may protect F-actin from severing (Smith *et al*, 2015).

The actin cross-linking activity of septin octamers is required, for instance, at the migratory front (lamella) of renal epithelia (**fig. 1-9**); indeed, disruption of this septin network disorganizes lamellar actin and reduces the half-life of nascent focal adhesions (Dolat *et al*, 2014). Overexpression of α -actinin-1 rescues these phenotypes, hence supporting the idea that SEPT9-containing septin complexes cross-link dorsal stress fibers (connected to focal adhesions) with transversal arcs (Dolat *et al*, 2014).

A recent study has shown that recombinant septin octamers containing the short isoform SEPT9-i5 are also capable of interacting and cross-linking actin filaments *in vitro*, thus suggesting that septin complexes possess additional mode of interaction with actin that do not involve the basic region of SEPT9 long isoforms (Lv *et al*, 2021). Furthermore, although SEPT9-i1 exhibits F-actin cross-linking activity and promotes cell migration, this is not the case of SEPT9-i2, despite it shares most of the SEPT9-i1 NTE. SEPT9-i2 is downregulated in breast tumors and, contrary to SEPT9-i1, when overexpressed, inhibits migration, reorganizes septins into short filaments and causes a loss of sub nuclear actin stress fibers (Verdier-Pinard *et al*, 2017).

These findings indicate that the incorporation of specific SEPT9 isoforms within the septin octamers may drastically affect the actin cytoskeleton.

Association of septins with actin filaments is also mediated by third factors (Kinoshita *et al*, 2002). SEPT2 binds directly myosin II A and scaffolds kinases that di-phosphorylate its light chains, as described in paragraph 1.1.2 in the context of cytokinesis (Joo *et al*, 2007). Presence of septins on stress-fibers and at the actomyosin ring may therefore potentiate actin contractility during interphase or cell division, respectively (**fig. 1-9**, for interphase). Another example of septin-actin bridging factors is the BORG family of Cdc42 effector proteins (Cdc42EPs) that share a 28 amino acid domain (BD3) responsible for the binding of SEPT2-SEPT6-SEPT7 trimers and of SEPT6-SEPT7 dimers (Joberty *et al*, 2001; Sheffield *et al*, 2003). In cancer-associated fibroblasts (CAF) BORG2 is up-regulated and promotes the association of septins with actin stress fibers. This association enables a marked mechano-transduction, possibly by providing support to the contractile actin cytoskeleton (Calvo *et al*, 2015). Moreover, in a recent work conducted on the human hepatocyte line 16 (HHL16), Salameh and colleagues propose a mechanism by which active Cdc42 is required by BORG2 (and possibly by BORG3) to glue septins on actin stress fibers (as depicted in **fig. 1-9**); conversely, the inactivation of Cdc42 is followed by proteasomal degradation of BORGs and consequent translocation of septins from stress fibers to MTs (as in the cell depicted in **fig. 1-10**) (Salameh *et al*, 2021). This switch in subcellular localization of septins has been reported as a possible side effect of paclitaxel treatment, and causes resistance to paclitaxel-based chemotherapeutic drugs, as explained in paragraph 1.3.3 (Salameh *et al*, 2021).

At the cleavage furrow of dividing cells, anillin mediates the interaction between septins and the actomyosin contractile ring, as described in paragraph 1.1.2 (Renshaw *et al*, 2014; Liu *et al*, 2012; Kinoshita *et al*, 2002) (**fig. 1.2**).

Other than crosslinking and stabilizing F-actin, the association between septins and actin has been shown to assist signaling. This is the case of the YAP transcription-co activator that translocates to the nucleus downstream of the previously mentioned septin-mediated mechano-sensing in CAF (Calvo *et al*, 2015). Another example involves the NCK (non- catalytic region of tyrosine kinase) adaptor protein, whose translocation into the nucleus causes loss of actin-stress fibers. The distribution of NCK between the nucleus and the cytoplasm depends on the interaction with the suppressor of cytokine signaling 7 (SOCS7) which, contrary to NCK, possesses nuclear import/export translocation signals. Under steady state conditions, SOCS7 binds SEPT2-SEPT6-SEPT7 complexes and, thus, is retained together with NCK in the cytoplasm. Depletion of septins leads to SOCS7-dependent shuttling of NCK to the nucleus and consequently a loss of stress fibers and cell polarity. The re-introduction of a NCK mutant constitutively retained in the cytoplasm rescues the disintegration of stress fibers in SEPT7 depleted cells (Kremer *et al*, 2007b).

Septins localize also at sites of branched actin. The formation of cell-cell junctions established by vascular-endothelial cadherin (VE-cadherin) is driven by the protrusion of lamellipodia from endothelial cells (Kim & Cooper, 2021, 2018). At these sites, septins accumulate at positively curved membrane tips (**fig. 1-9**), and depletion of SEPT2 causes a reshaping of cells edges into filopodia, and increases gaps between cells (Kim & Cooper, 2021, 2018). In the sensory neurons, SEPT6 promotes the recruitment of cortactin at sites of branched actin patches (Hu *et al*, 2012b). Cortactin, in turn, promotes Arp2/3-mediated actin polymerization and the initiation of filopodia; this process is required for collateral branching in the axon (Hu *et al*, 2012b).

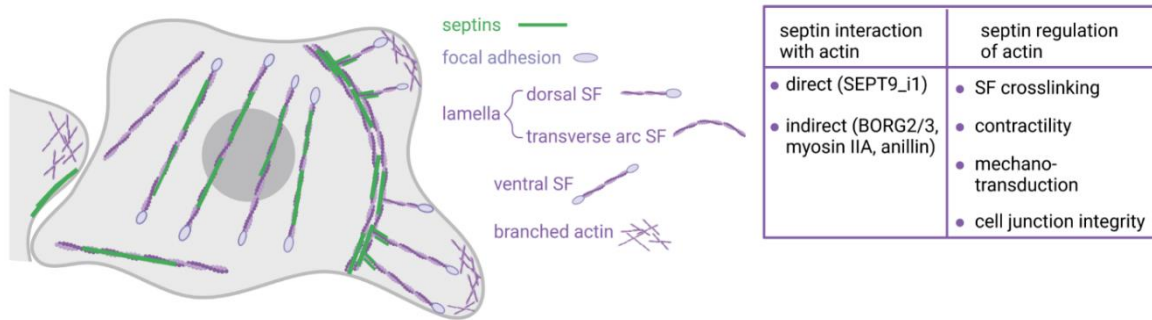


Figure 1-9. Actin-associated septins: subcellular localization and summarized functions. SF: stress fibers.

1.3.3. Subcellular localization and functions of MT-associated septins

Although septins have been initially identified as actin-interacting proteins, a large body of literature indicates numerous processes where septins regulate MTs dynamics, post-translational modifications and interactions with other MT-associated proteins (MAPs) (Spiliotis & Nakos, 2021).

Co-alignment of septin filaments with MTs varies between cell types, and this correlates, at least in part, with expression levels of SEPT9 isoforms, that differ in an alternatively spliced N-terminus (Kuzmić *et al*, 2022). Previous *in vitro* approaches suggested that the repeat motifs (K/R-x-x-E/D and R/K-R-x-E) shared by the NTE of SEPT9 long isoforms (SEPT9-i1, -i2 and -i3) form direct electrostatic interactions with the acidic C-terminal tail of β -tubulin isotype II (Bai *et al*, 2013). However, a recent study refocused the MTs-binding domain (MBD) of SEPT9 within the first 25 amino acids of SEPT9-i1, a region that harbors a motif similar to the MBD of several MAPs, such as MAP2, MAP4 and TAU (Kuzmić *et al*, 2022). According to this new model, the repeat motifs common to the NTE of SEPT9 long isoforms exhibit rather a regulatory role (Kuzmić *et al*, 2022). Tubulin modifications might further modulate the affinity of septins for MTs. For example, in breast cancer cells, the extended tyrosination at the C-terminus of α -tubulin potentiates the association of SEPT9-i1-containing septin octamers to MTs; this condition is associated with resistance to taxol and with poor prognosis (see below) (Froidevaux-Klipfel *et al*, 2015). Studies conducted in neurons suggest that paralogues of the SEPT6 and SEPT7 subgroup also associate with MTs, but it remains unknown whether these interactions are direct or not (Moon *et al*, 2013; Hu *et al*, 2012b).

The interaction of septins with MTs regulates MTs bundling and growth. Negative stain EM and sedimentation assays have proven the ability of SEPT9-i1 to bundle MTs (Bai *et al*, 2013). Moreover, *in vitro* polymerization assays have shown that submicromolar concentrations of SEPT9 homodimers promote MTs growth by recruiting soluble tubulin to the MTs lattice (Nakos *et al*, 2019b). SEPT2-SEPT6-SEPT7 complexes also associate with MTs *in vitro*. However, they do not recruit soluble tubulin, and they affect MTs growth in a concentration-dependent manner (Nakos *et al*, 2019a). These studies suggest that the regulatory role of septin complexes on MTs dynamics might depend on the incorporation of certain septin paralogues (such as SEPT9) into the filament. However, the mode of septin interaction with MTs is still under debate, and *in vitro* data may not necessarily reflect the *in vivo* mechanism. Indeed, Kuzmić and colleagues showed that mutations affecting the ability of SEPT9-i1 to form an octamer, or mutations within the NC termini of SEPT2 that are involved in filaments formation, lead to a loss of colocalization between septins and MTs in a cellular system (Kuzmić *et al*, 2022). Based on these data, the authors propose that only SEPT9-i1-containing septin filaments associate with MTs within the cell (Kuzmić *et al*, 2022).

Additional studies have confirmed the regulatory role of septins on MTs growth. In polarizing epithelial cells, septins capture and bundle perinuclear MTs, and direct MTs growth toward the apical side (**fig. 1-10**) (Bowen *et al*, 2011). Interestingly, live cell imaging has shown that septin filaments promote and steer MTs growth by providing trajectories, along which MTs plus ends move (Bowen *et al*, 2011). In line with their ability to steer MTs growth, septins promote the entry and growth of MTs in membrane protrusions, such as the primary cilium or developing axon collateral branches (**fig. 1-10**) (Ghossoub *et al*, 2013; Hu *et al*, 2012b).

Septins are nowadays considered as “*bona-fide* MT-associated proteins” (Spiliotis & Nakos, 2021) and their interaction with MTs regulates also the binding of other MAPs, and the transport of vesicle along MTs tracks. In epithelial cells, the association of SEPT2 with a subset of polyglutamylated (polyGlu) MTs prevents the binding of MAP4 and defines specific tracks, along which vesicles exiting the *trans*-Golgi network (TGN) travel toward the apical or basolateral membrane polarization (Spiliotis *et al*, 2008). Depletion of SEPT2 causes a loss of vertically oriented polyGlu MTs and impairs cell polarization (Spiliotis *et al*, 2008). Similarly, in HeLa cells SEPT2 counteracts the association of MAP4 with MTs; however, in this case,

it is the cytoplasmic fraction of SEPT2 that sequesters soluble MAP4 (Kremer *et al*, 2005).

Additionally, septins promote and regulate MTs nucleation. At the *cis*-Golgi, SEPT1 scaffolds CEP170 and γ -tubulin, thereby promoting nucleation of Golgi-derived MTs (**fig. 1-10**) (Song *et al*, 2019). At the centrosome, SEPT7 regulates MTs nucleation by forming a complex with the dynactin subunit p150^{glued} and ensuring its local accumulation (**fig.1-10**) (Chen *et al*, 2021). Although in this study SEPT2 and SEPT6 did not colocalize with the centrosomal marker γ -tubulin, the authors could not rule out the involvement of other septin paralogues with which SEPT7 may form a complex (Chen *et al*, 2021). Indeed, depletion of individual septin paralogues, especially SEPT7, which is alone in its subgroup, often leads to septin filaments destabilization (Benoit *et al*, 2023). Consequently, assessing whether a specific phenotype can be attributed to a single paralogue or to the entire filament is challenging.

Septins also modulate tubulin post-translational modifications such as acetylation and polyglutamylolation. In cancer cells, SEPT9-i1-containing octamers associate with MTs and recruit enzymes that elongate and trim the polyglutamate side chains at the C-terminal tails of tubulin (Froidevaux-Klipfel *et al*, 2015). Modified MTs in turn promote the binding of the rescue factor CLIP-70 and of the catastrophe factor MCAK that renders MTs highly dynamic (Froidevaux-Klipfel *et al*, 2015). This mechanism underlies the resistance to the MT-stabilizing drug taxol (paclitaxel-based), observed in several cancer cells (Froidevaux-Klipfel *et al*, 2015). During development of mammalian neurons, SEPT7 provides a scaffold for the recruitment of the histone deacetylase 6 (HDAC6) to α/β -tubulin dimers; this enzyme deacetylates α -tubulin to allow optimal MTs dynamicity required for neuritogenesis (Ageta-Ishihara *et al*, 2013).

During cytokinesis of several cell types, septins coalign with acetylated MTs (see also paragraph 1.3.5) (Russo & Krauss, 2021). Non-sumoylatable septin mutants form aberrant bundles that accumulate at the cytokinetic bridge and cause cytokinetic defects (Ribet *et al*, 2017). This suggests that PTMs may contribute to modulate the interaction of septins with MTs.

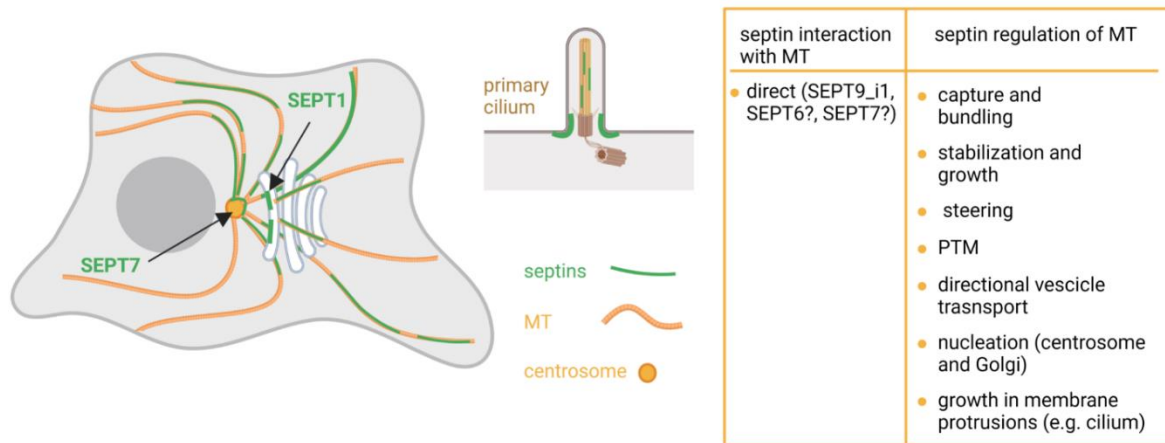


Figure 1-10. MT-associated septins: Subcellular localization and summarized functions. MT: microtubules, PTM: post-translational modifications.

1.3.4. Septin interactions with phospholipid membranes and distinct phosphoinositides

The association of septins with cellular membranes depends on membrane curvature and on lipid composition. Septins interact with select phosphoinositides, namely PI(5)P, PI(4,5)P₂, PI(3,5)P₂ and PI(3,4,5)P₃ through the N-terminal polybasic region shared by members of the septin subgroup 2, 3 and 7 (Cavini *et al*, 2021; Zhang *et al*, 1999; Dolat & Spiliotis, 2016; Akil *et al*, 2016). Liposome sedimentation assays performed with recombinant SEPT4 have shown that the binding of PI(4,5)P₂ takes place at the GDP-bound state, suggesting that this interaction may aid the anchoring of septin heterocomplexes to the PM (Zhang *et al*, 1999). Additionally, Bertin and colleagues have found that the presence of PI(4,5)P₂ on lipid monolayers facilitates the polymerization of yeast septin octamers (0.02mg/mL) into filaments and higher-order structures (Bertin *et al*, 2010a). This was observed already when PI(4,5)P₂ was added at 5% (in weight), a level similar to the one estimated for the PM of *Saccharomyces cerevisiae* (Bertin *et al*, 2010a).

Septins preferentially associate with membrane areas characterized by a micrometer-scale curvature (Woods & Gladfelter, 2021; Bridges *et al*, 2016; Beber *et al*, 2019). At the same time, recombinant mammalian and yeast septins are capable of deforming the surface of PI(4,5)P₂-supplemented GUVs (giant unilamellar vesicles) to generate degrees and types of curvatures which allow the assembly of energetically favorable septin structures (Beber *et al*, 2019; Tanaka-Takiguchi *et al*, 2009). Although in vitro studies with recombinant septins on lipid

bilayers show some discrepancies on which curvature septins may favor (positive or negative), inside the cells septins are often enriched at areas of positively curved PM (curvature described from the cytoplasmic face) (Beber *et al*, 2019; Bridges *et al*, 2016) (**fig. 1-11**). This is the case at the yeast mother-bud neck, at the cleavage furrow of dividing cells, and at the base-neck border of cellular protrusions such as lamellipodia, filopodia, dendritic spines, primary cilia and hyphal branches (Spiliotis & McMurray, 2020; Bridges *et al*, 2016). The Gladfelter lab has shown that the ability of septins to sense membrane curvature relies on an amphipathic helix at the C-terminus of the yeast Cdc12, that is also present in its mammalian orthologue SEPT6 (Cannon *et al*, 2019).

Membrane-associated septins scaffold the recruitment of select binding partners, restrict their diffusion, and influence the organization of other cytoskeletal components in their vicinity (Spiliotis, 2018; Pacheco *et al*, 2023). For example, septins that accumulate at the base-neck border of cellular protrusions can modulate local actin crosslinking and polymerization, and capture and steer MTs growth within the protrusion (**fig. 1-11**). This is the case of SEPT6 and SEPT7 that, during axonal collateral branching, localize at the base of nascent filopodia and promote actin growth and MT entry in the protrusion, respectively (Hu *et al*, 2012b). Moreover, the initial accumulation of septins at specific membrane areas may favor the interaction of septins with the subset of actin filaments and MTs localized nearby, and therefore contribute to the spatial reorganization of septins (Spiliotis, 2018).

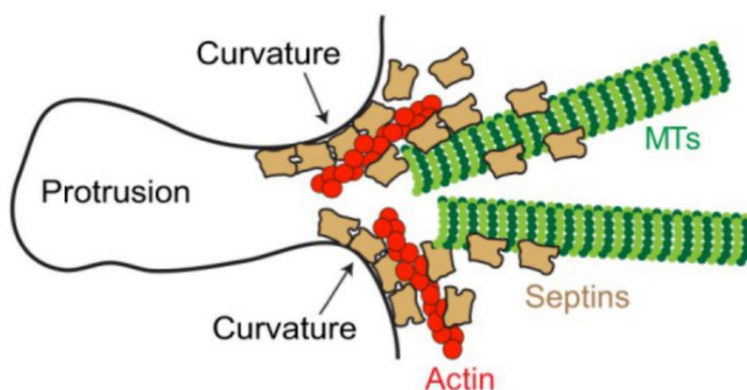


Figure 1-11. Septins at the base-neck border of a cellular protrusion. The accumulation of septins at membrane domains may favor the interaction of septins with proximal actin and MTs, and result in local cytoskeleton remodeling. Adapted from (Spiliotis, 2018).

1.4. Aim of this study

The physical process of cell division initiates during anaphase when a cleavage furrow forms at the equatorial plane of the mother cell. Subsequently, the furrow constricts and elongates to form an ICB. Further thinning of the bridge, down to a diameter of 100-300 nm, precedes the final step of abscission (Wang *et al*, 2019; Mierzwa & Gerlich, 2014). During the reshaping of the PM, the cytoskeleton undergoes profound remodeling. Septins, in particular, are initially recruited to the ingressing furrow, subsequently reorganize into rings flanking the two sides of the midbody, and finally relocate onto MTs bundles along the cytokinetic bridge (Renshaw *et al*, 2014; Karasmanis *et al*, 2019; Russo & Krauss, 2021).

To date, the regulatory mechanisms underlying septin dynamics are largely unknown; however, phosphoinositides, in particular PI(4,5)P₂, take over important functions (Bertin *et al*, 2010b; Tanaka-Takiguchi *et al*, 2009; Beber *et al*, 2019; Zhang *et al*, 1999).

Several studies show that PI(4,5)P₂ is locally enriched at the cleavage furrow and plays a central role in the stabilization of the actomyosin ring, maturation of the ICB and midbody organization (Liu *et al*, 2012; Field *et al*, 2005; Cauvin & Echard, 2015; Lekomtsev *et al*, 2012). These functions are exerted mainly by promoting the recruitment and anchoring to the PM of the anillo-septin subnetwork and centralspindlin complex (Liu *et al*, 2012; Lekomtsev *et al*, 2012). Nevertheless, the source of PI(4,5)P₂ at the furrow and, especially, at the ICB remains poorly understood.

Based on these notions, the aim of this study is to uncover mechanisms of PI(4,5)P₂ production at the cleavage furrow and ICB, and to unravel their potential contribution in the regulation of septin dynamics during cell division.

2. Materials and Methods

2.1. Materials

2.1.1. Chemicals

General chemicals were purchased from Carl Roth, Merck, Sigma-Aldrich, and Invitrogen. The supplier of reagents used in specific applications is indicated in the corresponding method section.

2.1.2. Solutions and media

Solutions and buffers were prepared using ultrapure water (ddH₂O with a resistivity of 18 M Ω * cm at 25 °C), and the pH was adjusted using NaOH or HCl. Solutions used during specific protocols are described in the corresponding method section.

Table 2-1. Solutions and buffers for molecular biology methods

Solution or buffer	Composition
50x Tris-Acetate-EDTA buffer (TAE)	0.2 M Tris 0.1 M Glacial acetic acid 50 mM EDTA pH 8.2-8.4
Lysogeny broth (LB) medium	1 % (w/v) Yeast extract 0.5 % (w/v) NaCl 0.5 % (w/v) Trypton pH 7.4
LB plates	LB medium 15 g/L Agar-agar
2 x YT medium	1.0 % (w/v) Yeast extract 1.6 % (w/v) Trypton 0.5 % (w/v) NaCl pH 7.4
Antibiotics (1000x)	100 mg/mL Ampicillin, sterile filtered 50 mg/mL Kanamycin, sterile filtered

Table 2-2. Solutions and buffers for biochemistry methods

Solution or buffer	Composition
4x SDS stacking gel buffer	0.4 % (w/v) SDS 0.5 M Tris pH 6.8
4x SDS separating gel buffer	0.4 % (w/v) SDS 1.5 M Tris pH 8.8
1x SDS running buffer	25 mM Tris 0.192 M Glycine 0.1% (w/v) SDS pH 8.3
1x Transfer buffer	25 mM Tris 0.192 M Glycine 10 % (v/v) MeOH
Ponceau staining	0.3 % (w/v) Ponceau-S 1 % (v/v) Acetic acid
Ponceau destaining	1 % (v/v) Acetic acid
Coomassie stain	1 g/l Coomassie G250 10 % (v/v) Acetic acid 25 % (v/v) Methanol
Coomassie destain	10 % (v/v) Acetic acid 25 % (v/v) Methanol
Lysis buffer A	20 mM HEPES 100 mM KCl 2 mM MgCl ₂ 1% (v/v) Triton X-100 pH 7.4 supplements: 1 mM phenylmethylsulphonyl fluoride (PMSF) 0.3% (v/v) protease inhibitor cocktail (Sigma-Aldrich) 1% (v/v) Phosphatase Inhibitor Cocktail 2 and 3 (Sigma-Aldrich)
Homogenization buffer	20mM HEPES 320 mM Sucrose pH 7.5 1 tab/10 mL of complete Mini EDTA-free Protease Inhibitor Cocktail (Roche)
2x Bradford solution	17% (v/v) phosphoric acid 10% (v/v) ethanol, 150 µM Brilliant Blue G

Materials and Methods

6x Laemmli SDS sample buffer		For 100 mL
	0.375 M Tris	4.535g
	18 % (w/v) SDS	18g
	30 % (v/v) β -Mercaptoethanol	30 mL
	60 % (v/v) Glycerol	60 mL
	Bromophenol blue	tip of a spatula (do not add H ₂ O) Heat up to 55°C
<hr/>		
Insect cells lysis buffer	50 mM Tris	
	300 mM NaCl	
	2 mM DTT	
	10 mM Imidazole	
	0.5% (v/v) Triton X-100	
	1 mM PMSF	
	1tab/50 mL of complete EDTA-free Protease Inhibitor Cocktail (Roche)	
	pH to 7.5 at 4 °C	
<hr/>		
His-tagged proteins washing buffer	50 mM Tris pH 7.2	
	300 mM NaCl	
	2 mM DTT	
	20 mM Imidazole	
	pH to 7.2 at 4 °C	
<hr/>		
His-tagged proteins elution buffer	50 mM Tris	
	300 mM NaCl	
	2 mM DTT	
	300 mM Imidazole	
	pH to 7.2 at 4 °C	
<hr/>		
His-tagged proteins storing buffer	25 mM Tris	
	300 mM NaCl	
	5 mM DTT	
	50% glycerol	
	pH 7.5 at 4 °C	
<hr/>		
10x Phosphate buffered saline (PBS)	100 mM Na ₂ HPO ₄	
	26.8 mM KCl	
	1.37 M NaCl	
	17.6 mM KH ₂ PO ₄	
	pH 6.8	

Table 2-3. Solutions and buffers for cell biology methods

Solution or buffer	Composition
DMEM (for HeLa M)	Dulbecco's modified Eagle medium, 1 g/L D-glucose (PAN Biotech) Additives: 10 % (v/v) heat-inactivated fetal bovine serum (FBS Gibco) 50 µg/mL penicillin-streptomycin (pen-strep, Gibco). 2mM L-glutamine (Gibco) For stable lines: 1 µg/mL puromycin (Invitrogen)
DMEM (for Hek-293T)	Dulbecco's modified eagles medium, 4,5g/L D-glucose, L-glutamin (Gibco) Additives: 10% (v/v) heat-inactivated FBS (Gibco) 50 µg/mL pen-strep (Gibco)
Imaging buffer	10 mM HEPES 125 mM NaCl 5 mM KCl 1.2 mM MgCl ₂ 1.3 CaCl ₂ 3 mM D-glucose pH 7.4
Matrigel coating solution	5% (v/v) Matrigel (Corning) In Opti-MEM (Thermo Fisher)
4% Paraformaldehyde (PFA)	4% (w/v) PFA 4% (w/v) sucrose In PBS pH 7.4
2% PFA	2% (w/v) PFA 2% (w/v) sucrose In PBS pH 7.4 additive for PI(4,5)P ₂ staining: 1% (v/v) Glutaraldehyde (GA)
Goat serum dilution buffer (GSDB)	20mM HEPES 150 mM NaCl 0.1% Triton X-100 10 % (v/v) normal goat serum pH 7.2
Donkey serum dilution buffer (DSDB)	20 mM HEPES 150 mM NaCl 0.1% Triton X-100 10 % (v/v) normal donkey serum pH 7.2

Washing buffer (for ICC)	20 mM HEPES 150 mM NaCl 0.1% Triton X-100 pH 7.2
0.1x TE (TRIS-EDTA) buffer	1 mM TRIS 0.1 mM EDTA pH 8.0
2x HBS (HEPES buffered saline) buffer	50 mM HEPES 280 mM NaCl 10 mM KCl 1.5 mM Na ₂ HPO ₄ 12 mM dextrose pH 7.05

2.1.3. Enzymes and molecular biology kits

Restriction endonucleases, Phusion polymerase, Taq polymerase, alkaline phosphatase, T4 DNA ligase, along with their respective buffers, were from ThermoFisher Scientific. The kits used for plasmid DNA purification from *E. coli* cultures, DNA purification from agarose gels and PCR reactions, and genomic DNA extraction, were all sourced from Macherey-Nagel. The HiFi DNA Assembly Cloning Kit to clone the donor vectors were purchased from New England Biolabs.

2.1.4. DNA Oligonucleotides

Synthetic DNA oligonucleotides used as primers for polymerase chain reactions (PCRs) or for the generation of single guide RNAs (sgRNAs) were purchased from BioTeZ Berlin-Buch GmbH as lyophilized powder. They were dissolved in DEPC-treated, nuclease free water (Roth) to a stock concentration of 50 µM, and stored at -20 °C.

Table 2-4. List of DNA oligonucleotides used in this study. Primers are named according to the following pattern: amplificate name - restriction site – “Ct” (in case of presence of a stop codon)- forward/reverse. Oligonucleotides used to perform the knock-in (KI) are named as follow: KI- gene to tag – “guide” (if used to generate the sgRNA)/ “eGFP” or “HR” (if used to amplify the eGFP or a homology region) - forward/reverse.

DNA oligonucleotide	Sequence 5´-3´
PIPKI _γ EcoRI for	GATCAgaattcATGGAGCTGGAGGTACCGG
PIPKI _γ -i1 Ct XhoI rev	GATCActcgagTTAAAAGTAGATGTCCGGTGGCG
PIPKI _γ - i3 Ct XhoI rev	GATCActcgagTTATGTGTCGCTCTCGCCGTCGG

PIPKI γ -i5 Ct XhoI rev	GATCActcgagTTACCCAAAGCCCTTCTGG
PIPKI γ -i1 Ct NotI rev	GATCAgcgggccgcTTAAAAGTAGATGTCGGTGGCG
PIPKI γ -i3 Ct NotI rev	GATCAgcgggccgcTTATGTGTGCTCTCGCCGTC
PIPKI γ -i5 Ct NotI rev	GATCAgcgggccgcTTACCCAAAGCCCTTCTGG
PIPKI γ -i3/i5 siRNAs for	TTCACcGAcGGcAGaTACTGGATTTACTCTCCCCGCC
PIPKI γ -i3/i5 siRNAs rev	GGCGGGGAGAGTAAATCCAGTAtCTgCCgTCgGTGAA
PIPKI γ -i3/i5 siRNAs Y646A/W647A for	TTCACcGAcGGcAGagccgcgATTTACTCTCCCCGCC
PIPKI γ -i3/i5 siRNAs Y646A/W647A rev	GGCGGGGAGAGTAAATcgcggctCTgCCgTCgGTGAA
E-Syt1 NotI for	Provided by Prof. Dr. Michael Krauß
E-Syt1 Ct XbaI rev	Provided by Prof. Dr. Michael Krauß
E-Syt1 nt 2935 EcoRI for	Provided by Prof. Dr. Michael Krauß
E-Syt1 nt 3324 Ct Not1 rev	Provided by Prof. Dr. Michael Krauß
E-Syt1 K1018A/R1020A for	GTTGCTACTGCCAGACgcgAACgcaGGCACCAAGAGGAGG
E-Syt1 K1018A/R1020A rev	CCTCCTCTTGGTGCCtgcGTTcgcGTCTGGCAGTAGCAAC
E-Syt1 K1018A/R1020E for	GTTGCTACTGCCAGACgcgAACgagGGCACCAAGAGGAGG
E-Syt1 K1018A/R1020E rev	CCTCCTCTTGGTGCCctcGTTcgcGTCTGGCAGTAGCAAC
E-Syt1 R1052A for	CTGGATGAGGCCAGgcaCGAAAGCTGGATGTCTCT
E-Syt1 R1052A rev	AGAGACATCCAGCTTTcgtGCCTGGGCCTCATCCAG
KI-SEPT6 guide for	CACCGCATCGCTCCTGCGTCCGCCA
KI-SEPT6 guide rev	AAACTGGCGGACGCAGGAGCGATGC
KI-SEPT6 5'HR for	taagctacaacaaggcaaggcttgaccgacGAAGCAGCGTCTCAAGACC TCTAGCC
KI-SEPT6 5'HR rev	gctcacaccggtcatCGCTCCTGCGTCCGCCAGTTCTGCCACGGG
KI-E-SEPT6 eGFP for	gcggacgcaggagcgATGACCGGTGTGAGCAAG
KI-E-SEPT6 eGFP rev	atcggctgctgcatGGATCCCTTGTACAGCTCG
KI-SEPT6 3'HR for	ctgtacaaggatccATGGCAGCGACCGATATAG
KI-SEPT6 3'HR for	tcgaggctgatcagcgggttaaacgggcccCACAGTTTTGGCACACAAG
KI-E-Syt1 guide for	CACCGGCACAATGGAGCGATCTCC
KI-E-Syt1 guide rev	AAACGGAGATCGCTCCATTGTGCC
KI-E-Syt1 5'HR for	taagctacaacaaggcaaggcttgaccgacaattGTGTCCTAGAAGTTCTT CAGGG
KI-E-Syt1 5'HR rev	ctcggccttgctcacCATTGTGCCACCTCTGGG
KI-E-Syt1 eGFP for	agaggtggcacaatgGTGAGCAAGGGCGAGGAGCTG
KI-E-Syt1 eGFP rev	tggagatcgctccatGCGGCCGCACTGTGCTG
KI-E-Syt1 3'HR for	cacagtgggcggccgcATGGAGCGATCTCCAGGAG
KI-E-Syt1 3'HR rev	tcgaggctgatcagcgggttaaacgggcccCGGGGATAAAAGCGAGAA AAG

2.1.5. Small interference RNA (siRNA) oligonucleotides

Single siRNAs were purchased from Sigma-Aldrich as lyophilized powder (**table 2-5**). They were dissolved to a stock concentration of 100 μ M in DEPC-treated, nuclease free, sterile water (Roth), aliquoted, and stored at -80 °C.

Dharmacon On-Target Plus siRNA smart pools were used to silence PIPKI α (L-004780-00-0010), PIPKI β (L-004058-00-0010), MKLP1 (L-004956-00-0005), MgcRacGAP (L-008650-00-0005) and INPP5K (L-017494-01-0005). They were dissolved to a stock concentration of 100 μ M in 1x siRNA buffer (Dharmacon) following manufactures instructions, and stored in small aliquots at -80 °C. All siRNA oligonucleotides used in this study were synthesized with a 3'dTdT-overhang and directed against human mRNA targets.

Table 2-5. List of siRNA oligonucleotides used in this study

Target	Sequence 5'-3'	Additional information
Scrambled (control)	GUAACUGUCGGCUCGUGGU	Scrambled μ 2 (AP2) sequence
PIPKI γ (all isoforms)	GAGGAUCUGCAGCAGAUUA	
PIPKI γ -i3/i5	GGAUGGGAGGUACUGGAUU	Sun et al., 2013
SEPT2	GCCCUUAGAUGUGGCGUUU	Sharma et., 2013
SEPT6	CCUGAAGUCUCUGGACCUAGU	Estay et al., 2010
SEPT7	UAUAUGCUGCACUGAAUGGAA	Estay et al., 2010
SEPT9	GCACGAUAUUGAGGAGAAA	Estay et al., 2010
OCRL	GAAAGGAUCAGUGUCGAUA	Dambournet et al., 2011

2.1.6. Plasmids

The constructs used in this study are listed below (**table 2-6**). The “MK” vector series was generated by Prof. Dr. Michael Krauß. pcHA-MK was the first one and derives from a modification of pcDNA3.1 (+), where the sequence between the NdeI site (located within the CMV promoter) and the EcoRV site (marking the start of the polylinker) was replaced with the corresponding sequence from the pcHA2 vector (#73 in AG Haucke plasmid database). In this and in the other MK vectors, the sequence encoding the tag (HA, mCherry or eGFP) is placed between the KpnI and BamHI sites, and is followed by the same polylinker, thus allowing easy subcloning. For mammalian expression constructs, the coding sequences (CDSs) of human PIPKI γ isoforms and i5 mutants were inserted into pcHA-MK or into pcMCherry-MK, resulting in the expression of N-terminally HA- or mCherry- tagged proteins. The

kinase-dead mutant PIPKI γ -i5 K188A carries the previously described mutation within the kinase core domain (Krauss *et al*, 2006). The mutant deficient in septin binding (PIPKI γ -i5 Δ SB) was generated by mutating Y646 and W647 of human PIPKI γ -i5 into alanine (Y646A/W647A). SiRNA-resistant (siRES) PIPKI γ -i5 and -i5 mutants were created by introducing four silent mutations within the sequence targeted by the siRNA against PIPKI γ -i3/i5 as follows: 5'-CGACGGCAGATACTGGATT-3'.

For viral constructs, PIPKI γ -i5 siRNA resistant wild-type and mutant CDSs were inserted into pLIB-CMV-mCherry-IRES-Puro (#5713 in AG Haucke plasmid database), resulting in the stable expression of N-terminally mCherry-tagged proteins. Instead, the sequence encoding for the fluorescently labeled PH domain of PLC δ 1 (PH δ 1-RFP₆₅₇) was inserted into the pLIB-CMV-IRES-Puro (#4738 in AG Haucke plasmid database).

For bacterial expression constructs, the CDSs of the tail domains (aa 451 to end) of PIPKI γ -i1-i5 and -i5 Δ SB were inserted into pGEX-4T1 (by Prof. Dr. Michael Krauß), allowing for the expression of N-terminally GST-tagged PIPKI γ tails.

The CDS of human E-Syt1, wild type and mutants, were inserted into pcEGFP-MK (or into pcMCherry-MK), resulting into the expression of N-terminally tagged proteins. For bacterial expression, the CDS of the C2E domain (aa 978 to aa 1108) of E-Syt1 (wild-type or mutants), were inserted into pGEX-4T1, allowing for the expression of N-terminally GST-tagged C2E domains.

Table 2-6. List of expression constructs used in this study

Insert	Vector	Restriction sites	Length (amino acids)	Extra information
PIPKI γ -i1	pcHA MK	EcoRI-XhoI	FL	
PIPKI γ -i2	pcHA MK	EcoRI-XhoI	FL	Cloned by MK
PIPKI γ -i3 (siRES)	pcHA MK	EcoRI-XhoI	FL	
PIPKI γ -i5 (siRES)	pcHA MK	EcoRI-XhoI	FL	Cloned by MK
PIPKI γ -i5- Δ SB (siRES)	pcHA MK	EcoRI-XhoI	FL	
PIPKI γ -i5 (siRES)	pcMCherry MK	EcoRI-XhoI	FL	
PIPKI γ -i5- Δ SB (siRES)	pcMCherry MK	EcoRI-XhoI	FL	
PIPKI γ -i5-K188A (siRES)	pcMCherry MK	EcoRI-XhoI	FL	
PIPKI γ -i5 (siRES)	pLIB-CMV-mCherry-IRES-Puro	EcoRI-NotI	FL	

PIPKI γ -i5- Δ SB (siRES)	pLIB-CMV-mCherry-IRES-Puro	EcoRI-NotI	FL	
PIPKI γ -i5-K188A (siRES)	pLIB-CMV-mCherry-IRES-Puro	EcoRI-NotI	FL	
PH δ 1-RFP ₆₅₇ (PLC)	pLIB-CMV-IRES-Puro	EcoRI-NotI		
SEPT5	pc-cmyc6		FL	Cloned by MK
SEPT7	pc-cmyc6		FL	Cloned by MK
SEPT9	pc-cmyc6		FL	Cloned by MK
E-Syt1	pcEGFP-MK	NotI-XbaI	FL	Cloned by Claudia Gras
E-Syt1	pcMCherry-MK	NotI-XbaI	FL	
E-Syt1 K1018A/R1020A	pcEGFP-MK	NotI-XbaI	FL	
E-Syt1 R1052A	pcEGFP-MK	NotI-XbaI	FL	
PH δ 1 (PLC)	pEGFP-N1			Cloned by MK
mCherry-CHUtrophin				Gift from Pietro De Camilli, Yale School of Medicine
PIPKI γ -i1 tail	pGEX-4T-1	EcoRI-XhoI	451-end	Cloned by MK
PIPKI γ -i2 tail	pGEX-4T-1	EcoRI-XhoI	451-end	Cloned by MK
PIPKI γ -i3 tail	pGEX-4T-1	EcoRI-XhoI	451-end	Cloned by MK
PIPKI γ -i4 tail	pGEX-4T-1	EcoRI-XhoI	451-end	Cloned by MK
PIPKI γ -i5 tail	pGEX-4T-1	EcoRI-XhoI	451-end	Cloned by MK
PIPKI γ -i5- Δ SB tail	pGEX-4T-1	EcoRI-XhoI	451-end	Cloned by MK
C2C (E-Syt1)	pGEX-4T-1			Cloned by MK
C2E (E-Syt1)	pGEX-4T-1	EcoRI-NotI	978-1108	Cloned by MK
C2E (E-Syt1) K1018A/R1020A	pGEX-4T-1	EcoRI-NotI	978-1108	
C2E (E-Syt1) K1018A/R1020E	pGEX-4T-1	EcoRI-NotI	978-1108	
C2E (E-Syt1) R1052A	pGEX-4T-1	EcoRI-NotI	978-1108	
C2E (E-Syt1) R1052E	pGEX-4T-1	EcoRI-NotI	978-1108	
PIPKI γ -i3	pFL10His		FL	Cloned by Wen-Ting Lo

2.1.7. Antibodies

The primary and secondary antibodies used in this study are listed in **table 2-7** and **table 2-8**, respectively. Antibodies were stored at -4°C (Santa Cruz and LI-COR) or at -20°C . In the latter case, they were either aliquoted or mixed with 50% (v/v) glycerol to protect against repetitive freeze-thawing cycles. When commercial antibodies were supplemented with glycerol for storage, this is indicated as “1:1” in the tables below, and in this case, the specific dilutions refer to the glycerol-diluted stocks.

Table 2-7. List of primary antibodies used in this study. IF (immunofluorescence), U-ExM (ultrastructure expansion microscopy), WB (western blot). 50% (v/v) dilution into glycerol of the stock is indicated with "1:1".

Antibody	Source	Identifier	IF	U-ExM	WB
Acetylated tubulin (mouse) 1:1	Sigma-Aldrich	T7451	1:1000/ 1:2000		1:4000
α -tubulin (mouse) 1:1	Sigma-Aldrich	T5168	1:500	1:400	1:2000/ 1:4000
HSP70 (mouse) 1:1	Thermo-Fisher	MA3006			1:5000
β -tubulin (mouse)	Sigma-Aldrich	T5293		1:400	
PIPKI α (mouse)	Santa-Cruz	sc-398687			1:100
PIPKI β (mouse)	Santa-Cruz	sc-514169			1:100
PIPKI γ (rabbit)	Home-made				1:500
SEPT2 (rabbit)	Sigma-Aldrich	HPA018481	1:200	1:200	1:500
SEPT5 (mouse)	Santa-Cruz	sc-20040			1:100
SEPT6 (rabbit)	Home-made		1:70		1:250
SEPT7 (rabbit)	Santa-Cruz	sc-20620	1:100		1:500
SEPT7 (rabbit)	TECAN	JP18991	1:250	1:200	
SEPT3 (mouse)	Sigma-Aldrich	WH0055964M3			1:1000
SEPT9 (rabbit)	(Diesenberg <i>et al</i> , 2015)		1:400		1:500
Talin (mouse) 1:1	Sigma-Aldrich	T3287			1:1000
GAPDH (mouse) 1:1	Sigma-Aldrich	G8795			1:10000
Anillin (goat)	Abcam	ab5910	1:50		
c-Myc (mouse)	Hybridoma clone (9E10) obtained from DSHB, purified in house	9E10			1:400
RFP (rabbit) 1:1	Clontech	632496			1:1000
HA (mouse) 1:1	Abcam	ab18181	1:500		
OCRL1 (rabbit) 1:1	Cell Signaling	8797			1:500
PRC1 (mouse)	Thermo-Fisher	MA1-846	1:1000		1:200
CIT-K (mouse)	BD Transduction Laboratories	611377	1:300		1:500
MKLP1 (rabbit)	GeneTex	GTX120875	1:250	1:250	1:500
MgcRacGAP (goat)	Abcam	Ab2270		1:200	
MgcRacGAP (rabbit)	Proteintech	13739-1-AP	1:500		1:500
GFP (mouse) 1:1	Clontech	632381			1:1000
GFP (rabbit) 1:1	Abcam	ab6556	1:1000		
PI(4,5)P ₂ (mouse, IgM) 1:1	Echelon Biosciences	Z-A045	1:400		
Vinculin (mouse) 1:1	Sigma-Aldrich	V9264	1:100		
CHC (mouse)	Hybridoma clone (TD1) obtained from DSHB, purified in house				1:500
E-Syt1 (rabbit)	Home-made				1:200
INPP5K (rabbit)	Thermo-Fisher	PA5-76490			1:1000

Table 2-8. List of secondary antibodies used in this study. IF (immunofluorescence), U-ExM (ultrastructure expansion microscopy), WB (western blot). 50% (v/v) dilution into glycerol of the stock is indicated with 1:1.

Antibody	Conjugate	Source	Identifier	IF	U-ExM	WB
Goat anti rabbit 1:1	Alexa Fluor 488	Thermo-Fisher	A-11034	1:200 or 1:400-PH staining		
Goat anti mouse 1:1	Alexa Fluor 488	Thermo-Fisher	A-11001	1:200		
Goat anti rabbit 1:1	Alexa Fluor 568	Thermo-Fisher	A-11011	1:200		
Goat anti mouse 1:1	Alexa Fluor 568	Thermo-Fisher	A-11004			
Donkey anti goat 1:1	Alexa Fluor 488	Thermo-Fisher	A-11055	1:200	1:250	
Donkey anti rabbit 1:1	Alexa Fluor 647	Thermo-Fisher	A-31573	1:200	1:250	
Donkey anti mouse 1:1	Alexa Fluor 568	Thermo-Fisher	A-10037	1:200	1:250	
Goat anti mouse 1:1	Alexa Fluor 647	Thermo-Fisher	A21236	1:200		
Goat anti mouse (IgM) 1:1	Alexa Fluor 568	Thermo-Fisher	A21043	1:500		
Goat anti mouse 1:1	HRP	Jackson ImmunoResearch	115-035-003			1:2500
Goat anti rabbit 1:1	HRP	Jackson ImmunoResearch	111-035-003			1:2500
Goat anti mouse	IRDye® 800CW	LI-COR	926- 32210			1:5000
Goat anti rabbit	IRDye® 680RD	LI-COR	926-68071			1:5000

2.1.8. Bacterial strains

The TOP10 strain of *E. coli* (Invitrogen) was employed for routine cloning and plasmid propagation. To clone the donor vectors, 5-alpha Competent *E. coli* (NEB) were used. Recombinant proteins were expressed in the *E. coli* BL21-Codon Plus strain (Stratagene), which is optimized for a high-level of protein expression.

2.1.9. Eukaryotic cell lines

The majority of experiments were conducted in HeLa M cells, which are a sub-clone of HeLa cells. HeLa are epithelial-like cells that derive from cervical cancer cells taken in 1951 from Henrietta Lacks. Similar to HeLa, HeLa M cells can be efficiently

transfected and synchronized, rendering them ideal for cytokinesis studies. Furthermore, their flat morphology also makes them well-suited for microscopy-based assays.

Biochemical experiments to assess the interaction between overexpressed proteins were performed in Hek-293T cells, a human embryonic kidney cell line. These cells can be efficiently transfected in large formats and yield a high quantity of proteins. For this reason, they were also chosen to generate viral particles.

NRK-49F are fibroblast-like cells isolated from rat kidney. Contrary to HeLa, they exhibit prominent colocalization of septins with actin stress fibers. For this reason they were employed to test the involvement of actin in the association between PIPKI γ -i3/i5 and septins. HeLa M and Hek-293 T cells were obtained from American Type Culture Collection (ATCC). The genome-edited NRK49F SEPT2-eGFP cell line was generated and cultivated in the laboratory of Prof. Dr. Helge Ewers (Freie Universität Berlin), as described in Banko et al., 2019.

2.1.10. Software and databases

The software and databases used in this study are listed in **table 2-9**.

Table 2-9. List of software and databases used in this study

Name	Source	Application
Fiji (ImageJ)	https://fiji.sc/	Microscopy analysis
Velocity	Perkin Elmer	Control of Zeiss spinning disk microscope
Micromanager v1.4.14	https://micro-manager.org/	Control of epifluorescence/TIRF Imaging (Nikon microscope)
NIS Elements v5.02.01	Nikon	Control of Nikon spinning disk microscope and semi-automated epi imaging
Image Lab	BioRad	WB documentation and analysis
Image Studio Lite v.5.2	LI-COR	WB documentation and analysis
SnapGene	SnapGene	Design of cloning strategy
ApE	Wayne Davis University of Utah	Handling of sequencing data
GraphPad Prism v.9.2	GraphPad	Graphs and Statistics
Adobe Illustrator CS6	Adobe	Figures preparation
Affinity Designer	Affinity	Model drawing
Biorender	https://www.biorender.com/	Model drawing
CRISPOR	http://crispor.tefor.net/	sgRNA design
Ensembl genome browser	https://www.ensembl.org/index.html	Search of genomic, mRNA, and CDS sequences

UniProt	https://www.uniprot.org/	Search of proteins and protein domains sequences
NCBI	https://www.ncbi.nlm.nih.gov/	Bibliography
Mendeley desktop	Mendeley	Bibliography managing

2.1.11. Macros used for the segmentation of microscopy images

To obtain the ROIs outlying the MKLP1, CIT-K and MgcRacGAP dots, an average intensity projection of the z-stack was produced and the desired channel was segmented with the ImageJ macro in **table 2-10**. To obtain the ROIs outlining the acetylated tubulin and PRC1 bridges, the same procedure was used. However, for acetylated tubulin the median radius was set at 10, while for PRC1 at 4. The ImageJ macro in **table 2-11** was instead used to segment MKLP1 and MgcRacGAP channels on images derived from expanded samples. Subsequently, the fluorescence intensity was measured as integrated density within the obtained ROIs on unprocessed average intensity z-projections, after background subtraction. The ROIs outlining the acetylated tubulin and PRC1 bridges were instead analyzed via Feret diameters. To obtain the total number of nuclei (for the quantifications in **fig. 3-1**), the DAPI channel was segmented with the ImageJ macro in **table 2-12**.

Table 2-10. ImageJ macro used for regular confocal images. To be applied on the average intensity z-projection of the interested channel

Macro to segment MKLP1, CIT-K and MgcRacGAP on regular confocal images (ijm)
<pre>run("Median...", "radius=2"); run("Subtract Background...", "rolling=10"); run("Auto Threshold", "method=MaxEntropy white"); run("Make Binary"); setAutoThreshold("Default dark"); run("Analyze Particles...", "add");</pre>

Table 2-11. ImageJ macro used for confocal images derived from expanded samples. To be applied on the average intensity z-projection of the interested channel

Macro to segment MKLP1 and MgcRacGAP on images derived from expanded samples (ijm)
<pre>run("Median...", "radius=2"); run("Subtract Background...", "rolling=20"); run("Auto Threshold", "method=MaxEntropy white"); run("Make Binary"); setAutoThreshold("Default dark"); run("Analyze Particles...", "add");</pre>

Table 2-12. ImageJ macro used to quantify the total amount of nuclei. To be applied on the DAPI channel

Macro to segment the DAPI channel and obtain the total number of nuclei (ijm)
<pre>run("Median...", "radius=5"); setAutoThreshold("Triangle dark"); //run("Threshold..."); setAutoThreshold("Triangle dark"); setOption("BlackBackground", false); run("Convert to Mask"); run("Analyze Particles...", "size=10-20000 show=[Overlay Masks] display exclude add");</pre>

2.2. Molecular biology methods

2.2.1. Extraction of genomic DNA

Genomic DNA (gDNA) was obtained from confluent HeLa M cells seeded on a 6 cm dish. The extraction was performed using the NucleoSpin Tissue kit (Macherey-Nagel) and following manufacturer's protocol. gDNA was subsequently stored at 4°C.

2.2.2. Polymerase chain reaction (PCR)

Polymerase chain reaction (PCR) was employed to amplify DNA fragments from various templates. Plasmid DNA was used as a template for amplifying protein coding sequences (CDSs), which were later inserted into expression vectors during standard cloning procedures. The homology regions (5'HR and 3'HR) to be inserted into the donor vector for the CRISPR-Cas9-based genome editing, were instead

amplified from gDNA. Finally, to identify colonies containing successful ligation products, routine screening of *E.coli* colonies was performed through colony-PCR. Standard PCRs were performed in a volume of 50 μ L containing 1x Phusion GC buffer, 150 μ M of each dNTP, 0.8 μ M of each primer, 50 ng of plasmid DNA, 5% DMSO (when amplifying the CDS of PIPKI γ), and 1 unit of Phusion high fidelity DNA polymerase (Thermo Fisher).

The amplification of the 5' and 3' HR was performed in a volume of 50 μ L containing 1x Phusion GC buffer, 200 μ M of each dNTP, 1 μ M of each primer, 150 ng of gDNA, 3% DMSO, and 1 unit of Phusion polymerase. To generate sufficient material, three 50 μ L reactions were set for each HR.

Colony-PCR were performed in a volume of 20 μ L containing 1x Taq buffer, 80 μ M of each dNTP, 0.4 μ M of each primer, 3 μ L of bacterial culture (derived from a selected colony) and 0.03 units of DreamTaq DNA polymerase (Thermo Fisher). Programs in **table 2-13** were then run in a peqSTAR thermocycler. Step 2 to 4 were repeated for 30 cycles, when plasmid DNA was used as a template and during colony-PCR, or for 40 cycles, when gDNA was used as template. The annealing temperature was chosen based on the melting temperatures of the primers.

Table 2-13. PCR programs

Step	Phusion	Phusion (gDNA)	Taq
1) Initial denaturation	98 °C for 30 sec	98 °C for 3 min	94 °C for 2 min
2) Denaturation	98 °C for 5 sec	98 °C for 30 sec	94 °C for 30 sec
3) Primer annealing	50-68 °C for 20 sec	50-68°C for 30 sec	54 °C for 30 sec
4) Elongation	72°C for 20 sec/Kb	72°C for 20 sec	72 °C for 1 min
5) Final elongation	72°C for 7 min	72°C for 10 min	72 °C for 5 min
6) Storage	4 °C ∞	4 °C ∞	4 °C ∞

To insert one or more point mutations, a forward and a reverse mutagenic primers, annealing to the site of desired mutation were designed. These primers were used in combination with a forward and a reverse primer annealing, respectively, to the start and to the end of the interested DNA fragment. This first round of PCRs generated two amplicons corresponding to the 5' and to the 3' of the sequence of interest, and overlapping at the mutation site. Equimolar amounts of these amplicons were subsequently used as template (to a final 100ng DNA/50 μ L reaction) on a next round of PCR, performed with the forward and reverse primers

annealing to the beginning and to the end of the desired sequence. In both PCR rounds, a standard protocol with Phusion polymerase was used.

2.2.3. Agarose gel electrophoresis and DNA purification

Agarose gels were prepared by dissolving 0.7% to 2% (w/v) agarose (Bio&Sell) in 1x TAE buffer, supplemented with 0.3 µg/mL of UV-absorbing DNA-intercalating agent ethidium bromide (Roth). DNA samples in 1x loading dye (Thermo fisher) were loaded into solidified gels together with the DNALadder (Thermo Fisher), as a standard of DNA fragment size. Electrophoresis was carried out in 1x TAE buffer at 140V for 40 minutes, and UV illumination was subsequently used to visualize separated DNA fragments within the gel. When necessary, the band of interest was cut out from the gel, and DNA was purified using NucleoSpin Gel and PCR Clean-up kit (Macherey-Nagel), according to manufacturer's instructions.

2.2.4. Restriction digest

Digestions with restriction enzymes were performed in 30 µL volumes, using FastDigest enzymes (Thermo Fisher) and their supplied buffer. Isolated PCR products or 1µg (for analysis) or 2.5 µg (for vector backbone preparation) of plasmid DNA were incubated with 1 µL of each enzyme in 1x restriction buffer for 1-2 h at 37°C. Restricted plasmids were subsequently separated on agarose gel and eventually purified as described in section 2.2.3. PCR products were instead directly purified using NucleoSpin Gel and PCR Clean-up kit (Macherey-Nagel), according to manufacturer's instruction.

2.2.5. Dephosphorylation of linearized vector DNA

When plasmid DNA was digested to prepare a backbone for further cloning, the DNA was dephosphorylated by adding 1 unit of alkaline phosphatase (PhastAP, ThermoFisher) to the restriction reaction, 15 minutes before its end. AP hydrolyzes the 5'-phosphates from linear DNA molecules and thereby prevents spontaneous recircularization of plasmids digested by a single enzyme. This strategy was adopted to reduce the number of false positive colonies after transformation of ligation reactions.

2.2.6. Ligation of DNA fragments into linearized vectors

Ligations were performed by combining approximately 20 femtomoles of linearized backbone with a 3- to 7-fold molar excess of DNA insert. Ligations were carried in a volume of 15 μL containing 1x ligase buffer and 1 unit of T4 DNA ligase (Thermo Fisher), and were allowed to incubate overnight at 16°C. Then, 4 μL of ligation reaction were used to transform chemically competent *E.coli*.

2.2.7. Transformation of chemically competent *E.coli*

Chemically competent *E. coli* cells of the TOP10 strain (or BL21 strain, for protein expression purposes) were transformed using the heat shock method. Specifically, 50 μL bacteria aliquots were thawed on ice, supplemented with 4 μL of ligation reaction or 100 ng of plasmid DNA, and incubated for 30 minutes on ice. Then, the cells were heat-shocked in a water bath at 42 °C for 50 seconds, and quickly placed back on ice for an additional 2 minutes. Afterward, bacteria were supplemented with 600 μL of LB medium without antibiotic and shaken for 45 minutes at 37°C. Cells were then pelleted and resuspended into 150 μL of medium before being finally plated on agar dishes containing 100 $\mu\text{g}/\text{mL}$ ampicillin or 50 $\mu\text{g}/\text{mL}$ kanamycin. Dishes were incubated overnight at 37°C or overweekend at room temperature. To eventually perform a colony-PCR, 5 to 10 colonies were picked from the dish with a sterile tip and incubated for 3h at 37°C, shaking at 180 rpm, in 200 μL of LB medium supplemented with antibiotic. 3 μL of these “pre-cultures” were then used to perform a colony-PCR, as described in paragraph 2.2.2.

2.2.8. Overnight *E. coli* cultures and purification of plasmid DNA

Overnight bacteria cultures were set from positive *E. coli* colonies previously screened by colony-PCR, or from bacteria derived from glycerol stock. Bacteria were grown overnight at 37°C, shaking at 180 rpm, in either 5 mL (for “mini-prep”) or 150 mL (for “midi-prep”) of LB medium containing the appropriate antibiotic (100 $\mu\text{g}/\text{mL}$ ampicillin or 50 $\mu\text{g}/\text{mL}$ kanamycin). Of note, when the aim was to purify p-LIB constructs, bacteria were grown at 32°C. Plasmid DNA was purified using the NucleoBond Xtra Mini or Midi kit (Machery-Nagel), according to manufacturer instructions.

2.2.9. Determination of the concentration and quality of DNA samples

The DNA concentration was routinely determined with a NanoDrop ND-1000 (Peqlab). Specifically, by measuring the absorbance of the sample at 260 nm, corresponding to the wavelength of maximum DNA absorption, the instrument was able to provide the DNA concentration, as established by the Beer-Lambert law. Furthermore, to evaluate sample purity and detect eventual contaminants such as proteins, the absorbance ratio between 260 nm and 280 nm, as well as between 260 nm and 230 nm, were routinely measured. An approximate value of 1.8 in the first case, and of 2.0 in the second case, were indicative of good purity.

2.2.10. Sequencing

DNA samples were sequenced by LGC Genomics GmbH using Sanger sequencing method.

2.2.11. Cloning of the DNA vectors used for CRISPR-Cas9-based genome editing

The tagging of endogenous proteins was achieved through the CRISPR-Cas9 technology of genome engineering (Ran *et al*, 2013). This technique was developed based on the discovery that the microbial adaptive immune system, known as “clustered regularly interspaced short palindromic repeats (CRISPR)/CRISPR-associated systems (Cas)”, could be reprogrammed to precisely edit any desired DNA target (Jinek *et al*, 2012). This technology makes use of two vectors: a “guide” and a “donor”. When transfected into the cells, the guide vector expresses the Cas9 endonuclease and a single-guide RNA (sgRNA). The sgRNA forms a complex with the Cas9 and, since it contains a short sequence complementary to a specific genomic locus, it guides the endonuclease to this site. There, Cas9 induces a double-strand break, which will be repaired by the cell via homologous recombination. The donor vector provides readily-available DNA to be used as template during the homologous recombination process and, at the same time, to modify the genomic DNA as desired.

The guide vector was cloned as follow. The CRISPOR tool was used to identify a suitable guide sequence (5'-CATCGCTCCTGCGTCCGCCA-3') for efficiently targeting the start codon of SEPT6. To introduce this sequence into the guide vector,

the forward (5'-CACCGCATCGCTCCTGCGTCCGCCA-3') and reverse (5'-AAACTGGCGGACGCAGGAGCGATGC-3') oligonucleotides were annealed together. The annealing reaction was performed in 20 µL of 1x T4 Ligase buffer containing 2.5 µM of each primer, and was incubated in a peqSTAR thermocycler for 5 minutes at 95°C. Subsequently, the temperature was gradually decreased to 25 °C at a rate of -0.1 °C/s. Meanwhile, the vector px458-pSpCas9(BB)-2A-GFP (Addgene, #48138) was digested with Bpil and dephosphorylated as described in paragraphs 2.2.4 and 2.2.5. The annealed oligonucleotides were ligated into the linearized vector as described in paragraph 2.2.6. Of note, the oligonucleotides were not restricted after annealing, as they were designed so that the annealing product would expose the correct 5' and a 3' overhangs to ligate into the Bpil site.

The donor vector was cloned as follow. pCHA MK was used as a backbone for the generation of the donor vector. Specifically, its expression cassette was exchanged with the CDS of monomeric eGFP inserted between two homology regions (HR) consisting in original genomic sequences of 777 bp upstream the SEPT6 ATG (5'HR) and 896 bp downstream (and including) the SEPT6 ATG (3'HR). The stop codon of eGFP was exchanged with two codons encoding for Gly-Ser as a linker. The designing and cloning of the donor vector was done, respectively, with the NEBuilder assembly tool and NEBuilder HiFi DNA assembly cloning kit, according to the manufacturer instructions. In particular, pCHA MK was digested and dephosphorylated with Apal and Mfel. The homology arms and the eGFP were respectively amplified from HeLa M gDNA and plasmid DNA, as described in paragraph 2.2.2, with the primers designed with the assembly tool, and reported in **table 2-4**. The ligation of PCR products with the linearized backbone was performed following the assembly kit protocol, using 0.05 picomoles of each part. The ligation product was then transformed into NEB 5-alpha Competent *E. coli* provided by the kit, according to manual instructions.

The same strategy was used to tag the N-terminus of E-Syt1. In this case the selected guide was: 5'-GGCACAATGGAGCGATCTCC-3', and was introduced into the guide vector via annealing and ligation of the two oligonucleotides: 5'-CACCGGCACAATGGAGCGATCTCC-3' and 5'-AAACGGAGATCGCTCCATTGTGCC-3'. The expression cassette of pCHA MK was exchanged with the CDS of monomeric eGFP inserted between two genomic sequences consisting of 975 bp upstream the E-Syt1 ATG (5'HR) and 868 bp

downstream (and including) the E-Syt1 ATG (3'HR). The stop codon of eGFP was exchanged with a linker encoding for SGLGSEFDIQHSGGR.

2.3. Biochemistry methods

2.3.1. Sodium dodecyl sulfate polyacrylamide gel electrophoresis (SDS-PAGE)

SDS-PAGE is a method used to separate proteins based on their molecular mass and was performed according to Laemmli (Laemmli, 1970). This technique relies on the use of SDS (sodium dodecyl sulfate), an anionic detergent that disrupts non-covalent interactions within proteins. When used in combination with a reducing agent in the Laemmli sample buffer (and with heat), SDS leads to efficient denaturation of proteins, resulting from the disruptions of their secondary, tertiary, and quaternary structures.

Moreover, SDS associates with proteins in a constant ratio of two SDS molecules for every two amino acids, thereby conferring to proteins a negative charge that is directly proportional to their mass. Consequently, when an electric field is applied during the SDS-PAGE, the negatively charged proteins migrate through the polyacrylamide separating gel toward the anode with a speed that depends on their mass. 3% stacking and 8 to 14% separating polyacrylamide gels were prepared according to **table 2-14**.

All samples prepared for SDS-PAGE were denatured for 5 min at 95°C in Laemmli sample buffer, and were loaded into gel wells with a maximal volume of 25 µL for 15-well pockets and 50 µL for 10-well pockets. The specific amount of proteins loaded varied depending on the type of sample, please refers to the following paragraphs for details. 2-5 µL of PageRuler Plus Protein standard (Thermo Fisher) were loaded in each gel, along with samples. Electrophoresis was performed in 1x SDS running buffer at 120 V until the blue dye front had migrated to the bottom of the gel. Supports and tanks from Mini Protean Tetra Cell System (BioRad) were used to cast the gels and perform the electrophoresis. Gels were subsequently processed for immunoblotting or stained with Coomassie blue, in order to visualize protein bands *in loco*.

Table 2-14. SDS-PAGE recipes

	14%	12%	10%	8%	3%
ddH ₂ O (mL)	2	2.5	3	3.5	1.25
4x separating gel buffer (mL)	1.875	1.875	1.875	1.875	-
4x stacking gel buffer (mL)	-	-	-	-	0.625
30% acrylamide/0.8% bis-acrylamide mixture (mL)	3.5	3	2.5	2	0.33
10% ammonium persulfate (APS) (μL)	75	75	75	75	75
Tetramethylethylenediamin (TEMED) (μL)	7.5	7.5	7.5	7.5	7.5

2.3.2. Immunoblotting

Following SDS-PAGE, proteins were analyzed by immunoblotting (western blot). To this aim, the negatively charged proteins were transferred from polyacrylamide gels to nitrocellulose membranes (Amersham Protran 0.2; GE Healthcare) by applying an electric field in an electroblotting Mini Trans-Blot Cell (BioRad). This transfer was performed at 110V for 90 minutes at 4°C, in 1x transfer buffer. To visualize all transferred proteins, and thereby assess their amount and quality of transfer, membranes were stained with ponceau S for 10 min at RT, washed in 1x acetic acid to remove excessive dye, and subsequently scanned. Ponceau was then removed by washing the membranes in PBS. For chemiluminescence-based detection, membranes were blocked for 1h at RT in a solution of 3% BSA in PBS mixed 1:1 with Intercept (PBS) Protein-Free Blocking Buffer (LI-COR). Primary antibodies were diluted in a solution prepared as for blocking, and were then incubated on membranes for two hours at RT or, preferably, overnight at 4°C.

Membranes were then washed 3 times for 10 minutes with 0.05% Tween-20 in PBS and a fourth time with PBS, and incubated with the HRP-conjugated secondary antibodies diluted in 5% Milk in PBS, for 1h at RT. Membranes were washed again as before, and incubated for 5 minutes in the dark with the HRP substrate Pierce ECL Western Blotting-Substrate (Thermo Fisher Scientific). The resulting chemiluminescence was detected via a ChemiDoc XRS+ (Bio-Rad) controlled by the Image Lab software. The same software was used to evaluate and eventually quantify the resulting western blot bands.

For infrared-based detection (**fig. 3-1-A**, **fig. 3-19-B**, **fig. 3-20-C**, **fig. 3-S2**, and **fig. 6.2-11**), times and temperatures of incubations were as above. However, membranes were blocked in Intercept (PBS) Protein-Free Blocking Buffer, and

primary and IRDye-conjugated secondary antibodies were diluted in Intercept (PBS) buffer mixed 1:1 with 0.1% Tween-20 in PBS. Excess of antibody was removed by washing three times for 10 minutes with 0.1% Tween-20 in PBS and a fourth time with PBS. Membranes were imaged with LI-COR Odyssey Fc imaging system controlled by the Image Studio software (LI-COR Biosciences). The same software was used to evaluate and eventually quantify the resulting western blot bands.

2.3.3. Quantification of proteins via Bradford assay

Protein concentration of different samples was determined using the Bradford protein assay. This assay relies on the absorbance shift of Coomassie brilliant Blue G250 which exists in three forms: cationic (red), neutral (green) and anionic (blue), presenting distinct absorption spectra. When proteins bind to it, it shifts toward the blue form whose absorbance peaks at 595 nm (Bradford, 1976). Therefore, the increase in absorbance at 595 nm (A_{595}) of the Bradford solution (Sigma-Aldrich) (containing Coomassie brilliant Blue G250) is directly proportional to the amount of bound protein, and thus to the protein concentration of the tested sample. In this assay, 1 mL of 1x Bradford solution was mixed with 1 μ L of sample or empty buffer (to be used as blank), quickly vortexed, and left in the dark for 10 minutes. A_{595} was measured using a spectrophotometer (BioPhotometer Plus, Eppendorf), and the protein concentration was derived from a standard curve covering the range of 1 μ g to 10 μ g of BSA, prepared for each new batch of Bradford solution.

2.3.4. Preparation of protein extracts from eukaryotic cells

Cells were harvested via trypsinization (paragraph 2.4.1) and centrifuged for 5 min at 300 x *g*. The resulting pellets were washed by resuspending them in 1 mL of PBS, and were then transferred to Eppendorf tubes. After another round of centrifugation, the PBS was aspirated, and the cell pellets were placed on ice for lysis. Lysis was carried out for 15 minutes in ice-cold lysis buffer A supplemented with 0.3% (v/v) protease inhibitor cocktail (Sigma-Aldrich) and 1 mM PMSF. Cells harvested from 6-well plates were lysed in 50 μ L of lysis buffer A, whereas cells harvested from 10 or 15 cm dishes required bigger volumes, as described in paragraph 2.3.5. Lysates were then cleared by centrifugation at 17000 x *g* for 15 minutes at 4°C, and the protein concentration was determined using the Bradford assay (paragraph 2.3.3). If the lysates were not intended for further experiments, they were denatured in 1x

Laemmli sample buffer for 5 minutes at 95°C, and then stored at -20°C or analyzed directly. For each sample, 10-30 µg of proteins were resolved by SDS-PAGE and analyzed by western blot.

2.3.5. Immunoprecipitation assay

To assess the binding between overexpressed PIPK1 γ -i5 and overexpressed septins, the immunoprecipitation (IP) assay was set as follows. Hek-293T cells seeded in 10 cm petri dishes were transfected at 70% confluency with 5 µg of plasmid encoding mCherry-PIPK1 γ , or mCherry alone, and 5 µg of myc-tagged SEPT5, SEPT6, or SEPT9, using the calcium phosphate method (paragraph 2.4.2). 24 h later cells were trypsinized, washed once with PBS, transferred to Eppendorf tubes and lysed on ice for 15 minutes in 700 µL of ice-cold lysis buffer A supplemented with 0.3% (v/v) protease inhibitor cocktail (Sigma-Aldrich), 1 mM PMSF, and phosphatase inhibitors cocktails 2 and 3 (Sigma-Aldrich). Lysates were cleared by centrifugation at 17000 x g for 15 minutes at 4°C. Of the resulting supernatants (containing 2 – 4 mg of proteins, depending on the experiment), 50 µL were kept as input, while the other 600 µL were supplemented with 15 µL of RFP-Trap magnetic particles (ChromoTek), and incubated for 2.5 h at 4°C on a rotating wheel. Beads were washed three times with 1 mL of ice-cold lysis buffer A, and a fourth time with 1 mL of ice-cold lysis buffer without detergent. After the final wash, all buffer was removed using a Hamilton syringe. Finally, proteins bound to the beads were eluted by boiling in 60 µL of 1x Laemmli sample buffer for 5 minutes at 95 °C. The eluate was recovered with the Hamilton syringe and eventually stored at -20 °C. Half of the eluate was analyzed by SDS-PAGE and immunoblot at a time. The input was kept on ice throughout the duration of the IP and finally denatured in 1x Laemmli sample buffer for 5 minutes at 95°C, along with IP samples.

The IP experiments with HeLa M cells in **fig. 3-12** and **fig. 3-S2-A** were performed as follow (please note **fig. 3-12** is a courtesy of Prof. Dr. Michael Krauß). Synchronization was performed as described in paragraph 2.4.6. To ensure comparable amounts, cells to be synchronized at cytokinesis were cultured in a larger scale compare to those destined to S-phase or left asynchronous (e.g. 15 cm dish vs. 10 cm dish). Cells at cytokinesis were harvested by gentle pipetting, while the others via trypsinization. Cell pellets were washed once with PBS, and lysed as described for Hek-293T, in a volume of 700-900 mL depending on the pellet size.

Upon centrifugation at 17000 x *g* for 15 minutes at 4°C, the protein concentration of lysates was quantified with Bradford assay and equalized among samples adding extra lysis buffer A (+supplements) when necessary. Equal volumes of lysate (600-800 µL containing 3-5 mg of proteins, depending on the experiment) were used for IP and supplemented with 3-5 µg of rabbit-anti-human control or of rabbit-anti-SEPT2 antibody and with 60 µL of A/G agarose beads (Pierce™), pre-washed twice in lysis buffer A. Samples were then incubated at 4°C for 4 h on a rotating wheel. Notably, the antibody was not pre-bound to the beads to minimize hindrance in its binding to the epitopes. Afterward, beads were washed four times in 1mL of ice-cold lysis buffer A and once in 1mL of ice-cold lysis buffer A devoid of detergent, using brief centrifugations in a tabletop centrifuge. After the final wash, all buffer was removed using a Hamilton syringe. Finally, proteins bound to the beads were eluted by boiling in 90 µL of 1x Laemmli sample buffer for 5 minutes at 95 °C. The eluate was recovered with the Hamilton syringe and eventually stored at -20 °C. Half or a third of the eluate was analyzed by SDS-PAGE and immunoblot at a time. Inputs were prepared as described for Hek-293T cells.

2.3.6. Preparation of protein extracts from mouse brains

Mouse brains were homogenized in homogenization buffer containing complete EDTA-free protease inhibitor cocktail (Roche). Specifically, half a brain was considered per pull-down, and 1.5 mL of buffer was added per brain in the homogenization tube. Brains were subjected to 10 strokes at 900 rpm with a glass-Teflon homogenizer. Afterward, the homogenate was centrifuged at 1000 x *g* for 15 minutes at 4°C. The resulting supernatant was recovered and supplemented with 1% Triton X-100, 100 mM KCl, 2 mM MgCl₂, and then kept on ice for 10 minutes. Afterward, the lysate was cleared by centrifugation at 17000 x *g* for 15 min at 4°C and by ultracentrifugation at 178000 x *g* for 15 min at 4°C. The supernatant was recovered, quantified via Bradford assay and used right away for pull-down assays (described in paragraph 2.3.9).

2.3.7. Expression and purification of GST-fusion proteins from *E. coli*

E. coli of the BL21 strain were used to express glutathione-S-transferase (GST)-fused PIPKI_γ tails, E-Syt1-C2E domains or GST alone (to be used as control). To

this aim, overnight cultures of BL21 transformed with pGEX-4T-1 expression constructs were diluted 1:10 in 0.5-1L of 2x YT medium containing ampicillin. Cultures were grown to an OD₆₀₀ of 0.8, corresponding to the beginning of the logarithmic phase of bacterial growth. At this point, protein expression was induced by addition of isopropyl thio- β -D-galactoside to a concentration of 0.5 mM. Induced cultures were incubated for 5h at 22°C shaking at 200 rpm. Bacteria were then harvested by centrifugation at 4000 x g for 15 minutes at 4°C. The pellets were resuspended in 20 mL of PBS per 500 mL of culture and eventually stored at -20°C. To purify the GST-fused proteins, bacteria were thawed on ice and brought to a final volume of 30 mL by adding extra ice-cold PBS. Samples were supplemented with 1mM PMSF, 4U/ μ L of cyanase and 1 mg/mL of lysozyme, and left on ice for 15 min. Then, samples were supplemented with 1% Triton X-100 and sonicated on ice (2 minutes: 1 second pulse on, 6 seconds pulse off, with a SONOPLUS from Bandelin). Lysates were subsequently cleared by centrifugation at 50000 x g for 15 minutes at 4°C. 500 μ L of glutathion-coupled beads (GE-Healthcare) were added to each supernatant and rotated end-over-end for 2 h at 4°C. Beads were then washed three times with 20 mL of ice-cold 0.1% Triton X-100 in PBS and twice with 20 mL of ice-cold PBS, by centrifugation at 4°C for 3 min at 1000 x g (acceleration at 9, deceleration at 6) and finally resuspended in 500 μ L of ice-cold PBS and transferred to Eppendorf tubes. Amount and quality of purified proteins were estimated with Bradford assay and SDS-PAGE followed by Coomassie staining. Proteins were stored at 4°C and used for pulldown experiments within 24h.

2.3.8. Purification of His₁₀-tagged PIPK γ -i3 from insect cells

His₁₀-tagged PIPK γ -i3 was expressed in *Sf21* insect cells using SF900-II serum-free media (ThermoFisher). In brief, 800 mL of *Sf21* cells were grown to a density of $1.5-2 \times 10^6$ cells per ml, and infected with 8 ml of baculovirus encoding His₁₀-tagged PIPK γ -i3. Cells were subsequently harvested when their viability dropped below 90%, and cell pellets were stored at -20°C. Dr. Wen-Ting Lo conducted the cloning of PIPK γ -i3 into a pFL10His vector and the subsequent generation of the baculovirus. The cultivation and infection of insect cells were carried out together with Dr. Wen-Ting Lo.

To purify His₁₀- PIPK γ -i3, an insect cell pellet deriving from 50 mL of culture was thawed on ice and resuspended in 15 mL of ice-cold lysing buffer. Cells were then

sonicated on ice using a SONOPLUS from Bandelin (30 seconds: 1 second pulse on, 5 seconds pulse off). Lysate was subsequently cleared by centrifugation at 17000 x *g* for 10 minutes at 4°C. The supernatant was recovered and incubated with 160 µL of His Nickel-NTA agarose beads (Sigma) for 1 h at 4°C on a rotating wheel. Beads were then washed four times with 5mL of ice-cold washing buffer by centrifuging at 1000 x *g* for 2 minutes at 4°C. After the final wash, all buffer was removed using a Hamilton syringe and the beads were resuspended in 200 µL of ice-cold elution buffer. The beads were pelleted again by centrifugation at 1000 x *g* for 2 minutes at 4°C, and the eluate was finally collected with the Hamilton syringe. The eluate was dialyzed overnight at 4°C against the storing buffer. The concentration of His₁₀-PIPKI_γ-i3 was obtained by measuring its absorbance at 280 nm (*A*₂₈₀) at the spectrophotometer (BioPhotometer Plus, Eppendorf), and by applying the Lambert-Beer equation as follow: $c = \frac{A_{280}}{\epsilon * l}$. In this equation, *c* is the desired concentration expressed in mol*L⁻¹ (M), ϵ is the molar absorption coefficient of the protein (for His₁₀-PIPKI_γ-i3 is 56040 M⁻¹*cm⁻¹), and *l* is the length of the light path across the sample, which for a cuvette is 1cm. The purified protein was either used immediately, or divided into aliquots, snap-frozen in liquid nitrogen and stored at -80 °C until usage.

2.3.9. GST-pulldown assays

GST pulldowns from mouse brains lysate were performed by incubating 1 mL of brain protein extract (containing 10-14 mg of proteins, depending on the experiment) with 50-70 µg of each beads-bound GST- protein (or GST alone) for 3 h at 4°C on a rotating wheel. Samples were subsequently washed four times with 1 mL of ice-cold lysis buffer A and once in 1 mL of ice-cold lysis buffer A devoid of detergent using brief centrifugations in a tabletop centrifuge. After the final wash, all buffer was removed using a Hamilton syringe. Proteins bound to the beads were then eluted by boiling in 100 µL of 1x Laemmli sample buffer for 5 minutes at 95 °C. The eluate was recovered with the Hamilton syringe and eventually stored at -20 °C. A third of the eluate was analyzed by SDS-PAGE and immunoblot at a time. Input was prepared by keeping a small portion of brain lysate on ice throughout the duration of the pull-down and it was denatured in 1x Laemmli sample buffer for 5 minutes at 95°C, along with pull-down samples.

To assess the direct binding of the C2E domain with PIPKI γ -i3, 10 μ g of His₁₀-PIPKI γ -i3 were incubated with 28 μ g of beads-bound GST-C2E (or GST) in 200 μ L of lysis buffer A, supplemented with PMSF and PIC, for 1 h at 4°C on a rotating wheel. Beads were subsequently washed three times with 250 μ L of ice-cold lysis buffer A and once with 250 μ L of ice-cold lysis buffer A devoid of detergent, using brief centrifugations in a tabletop centrifuge. After the final wash, all buffer was removed using a Hamilton syringe. Proteins bound to the beads were then eluted by boiling in 40 μ L of 1x Laemmli sample buffer for 5 minutes at 95 °C. The eluate was recovered with the Hamilton syringe and eventually stored at -20 °C. Half of the eluate was analyzed by SDS-PAGE and immunoblot at a time. The Input was prepared by denaturing few micrograms of His₁₀-PIPKI γ -i3 in 1x Laemmli sample buffer for 5 minutes at 95°C, along with pull-down samples.

2.4. Cell biology methods

2.4.1. Mammalian cell culture

HeLa M and Hek-293T were obtained from American Type Culture Collection (ATCC), and not used beyond passage 30 from original derivation. The genome-edited NRK49F SEPT2-eGFP knock-in cell line has been described previously (Banko *et al*, 2019). HeLa M cells were cultured in Dulbecco's modified Eagle's medium (DMEM) containing 1 g/L D-glucose and phenol red (except for live cell imaging) (PAN Biotech), supplemented with 10% (vol/vol) heat-inactivated fetal bovine serum (FBS, Gibco), 2 mM L-glutamine (Gibco), 50 μ g/mL penicillin-streptomycin (Pen-Strep, Gibco). Stably transfected HeLa cells were generated by viral transduction, and maintained under constant selection pressure by additionally supplementing the above described medium with 1 μ g/mL puromycin (Invitrogen). Hek-293T were cultured in DMEM containing 4,5 g/L D-glucose, phenol red, L-glutamin (Gibco), supplemented with 10% FBS and 50 μ g/mL pen-strep. NRK49F-SEPT2-eGFP cells were cultured by Nadja Hümpfer in DMEM containing 4,5 g/L D-glucose (Gibco), supplemented with 10% FBS and 2 mM L-glutamine. All cell lines were cultured at 37 °C and 5% of CO₂, and regularly tested for mycoplasma contaminations.

Cells were passaged every 2-4 days and reseeded at a dilution of 1:3 to 1:20. For detaching, cells were washed with Dulbecco's phosphate buffered saline (DPBS, Gibco) and trypsinized with one volume of TrypLE™ Express Enzym (Gibco, e.g. 1mL for a 10 cm dish and 0.2 mL for a 6 well plate), for 5 min at 37 °C. Resuspension was done by gentle pipetting in 10 volume of full culture medium. Cells were frozen in full culture medium supplemented with extra FBS (to 20% v/v) and 5% v/v DMSO and stored at -80 °C for a maximum of 2 weeks. Subsequently, cells were transferred into liquid nitrogen. Freshly thawed cells were passaged at least twice before being use for an experiment.

2.4.2. Transfection of plasmid DNA

Transfection of HeLa M was performed with JetPRIME (Polyplus), according to manufacturer instructions. Cells were seeded on day 1 to be transfected in full medium, on day 2. The ratio between µg of DNA and µL of reagent used was always 1:2. For the overexpression of PIPKI γ isoforms, cells were seeded on matrigel (from Corning)-coated glass coverslips (18 mm diameter) in a 12-well plate and transfected at 60% confluency with 0.5 µg of DNA per well. For TIRF imaging, cells were seeded on matrigel-coated glass coverslips (24 mm of diameter) in a 6-well plate and transfected at 40% confluency with 1 µg of fluorescently labeled-E-Syt1 construct, eventually in combination with 1 µg of CHUtrophin-mCherry, PH- δ 1-eGFP or mCherry-PIPKI γ -i5 construct. For the experiment in **fig. 6.2-8**, cells were seeded on matrigel-coated glass coverslips (18 mm diameter) in a 12 well plate and transfected at 60% confluency with 0.5 µg of eGFP-E-Syt1 construct, per well. In all of these cases, the medium was exchanged after 6 hours of transfection and the cells were processed on day 3, or later as for the generation of the eGFP-SEPT6 knock-in cell line, whose details are in paragraph 2.4.5.

Transfection of NRK49F-SEPT2-eGFP was performed by Nadja Hümpfer with Lipofectamin 3000 (Thermo-Fisher), following the manufacturer's instructions. Cells were seeded on glass coverslips in a 6-well plate and transfected on the following day. 2 µg of plasmid were used per well, and the cells were used for experiments 48 h post transfection.

For immunoprecipitation assays or virus production, Hek-293T cells were transfected using calcium phosphate. For this, cells were seeded in 10 cm dishes and transfected at 70% confluency. Specifically, plasmid DNA was mixed with 0.12

M CaCl₂ in 0,1x TE buffer and incubated for 5 min at room temperature. The same volume of 2x HBS was added drop-wise while vortexing at low speed, in order to allow the formation of DNA-calcium-phosphate precipitates. After 20 min of incubation at room temperature, the DNA solution (1mL for a 10 cm dish) was added to the cells. For the IP assay cells were transfected with 10 µg of DNA (paragraph 2.3.5 for details), while for the generation of viruses cell were transfected with 30 µg of DNA (paragraph 2.4.4). All buffers were sterile-filtered prior to use.

2.4.3. Small interference RNA (siRNA)-mediated gene silencing

SiRNA-mediated gene silencing was performed with JetPRIME reagent. Specifically, to silence PIPKI α , PIPKI β , PIPKI γ and PIPKI γ -i3/i5, two rounds of 48h knock-down with 50 nM siRNA were performed as follows. On day 1, 0.045 *10⁶ HeLa M (parental, knock-in or stable lines) were seeded in a 2 cm plate (generally from a 6-well plate) in full medium. Meanwhile, 1 µL of siRNA (100 µM stock solution) was mixed with 4 µL of JetPRIME reagent in 200 µL of JetPRIME buffer and added to the cells still in suspension, to reach a final volume of 2mL in the well. On day 2, cells were washed three times with DPBS and the medium was exchanged. On day 3, a second round of knock-down was performed. For western blot analysis, 0.045 *10⁶ cells were reseeded in a 2 cm plate and treated as the first round. For ICC and U-ExM, 0.06*10⁶ and 0.09*10⁶ cells per well were seeded, respectively, on matrigel-coated glass coverslips in a 12-well plate and supplemented with 100 µL of JetPRIME buffer containing pre-mixed 0,5 µL of siRNA (100 µM stock) and 2 µL of JetPRIME (to reach a final volume of 1mL in the well). For live-cell imaging of eGFP-SEPT6, the second round of knock-down was performed in matrigel-coated 8 well glass-bottom slides (ibidi). In this case, 0.02*10⁶ cells were seeded per well and supplemented with 25 µL of jetPRIME buffer containing pre-mixed 0,125 µL of siRNA (100 µM stock) and 0.5 µL of JetPRIME; the final volume per well was 250 µL.

On day 4, cells were washed three times with DPBS and the medium was exchanged (in case of synchronization, thymidine was added). On day 5, the cells were ready to be lysed, fixed or imaged.

Silencing of septins was achieved with one round of 48h knock-down with 100 nM siRNA. JetPRIME reagent was doubled accordingly, while the volume of the jetPRIME buffer was kept to 1/10 of the final volume in the well.

For the co-depletion of PIPK1 γ -i3/i5 and OCRL, two rounds of knock-down were performed with 50 nM siPIPK1 γ -i3/i5 + 50 nM siOCRL. In the same experiment, the single depletions of PIPK1 γ -i3/i5 and OCRL were performed with 50 nM targeting siRNA + 50nM siControl, while control cells were treated with 100 nM siControl at each round. JetPRIME reagent was doubled accordingly and the volume of JetPRIME was kept to 1/10 of the final volume in the well.

For the depletion of INPP5K, one round of 72h knock-down with 100nM siRNA was performed. Specifically, on day 1, 0.045×10^6 HeLa M cells were seeded per well in a 6-well plate and supplemented with 200 μ L of JetPRIME buffer containing pre-mixed 2 μ L of siRNA (100 μ M stock) and 8 μ L of JetPRIME (the final volume in the well was 2 mL). On day 2, cells were washed three times with DPBS, trypsinized and reseeded at a dilution of 1:2 on matrigel-coated glass coverslips (24 mm), to be transfected on day 3 and imaged on day 4. For western blot analysis cells were re-seeded on plastic.

2.4.4. Generation of stable cell lines

Stable cell lines were obtained by transducing HeLa M cells with retroviral particles carrying the transgene of interest within a pLIB-CMV-IRES-Puro vector. In this vector, the desired transgene is under the transcriptional control of the CMV promoter, and is separated from a sequence encoding for puromycin N-acetyltransferase (providing resistance to puromycin) by an internal ribosome entry site (IRES). Therefore, successful viral transduction and subsequent integration of the expression cassette into the host cell genome results into the expression of the transgene and into the acquisition of puromycin resistance. This, in turn, allows for the positive antibiotic selection of cells that stably express the desired transgene.

To generate the retroviruses, Hek-293T cells were seeded into 10 cm dishes and transfected at 70% confluency with a mix of plasmids consisting of 10,5 μ g packaging pCIG3.NB, 4,5 μ g envelope pMD2.G and 15 μ g retroviral vector pLIB-CMV-IRES-Puro, encoding for the transgene of interest. After 24h the medium was changed and reduced by 20% to start concentrating the virus. 72h post transfection the medium was collected and stored at 4 °C, while the cells received fresh medium which was collected once again after 96h post transfection. Harvested medium was pooled and centrifuged for 5 min at 1000 x g and subsequently concentrated by

centrifugation at 5000 x *g* for 25 min at 4 °C in Amicon Ultra-15 (100 kDa) tubes. Viruses were then stored at 4 °C to be used within a week.

To perform the transduction, 1/3 of the concentrate virus volume was added to a 5 cm plate of 60% confluent HeLa M (parental or knock-in). After 72h, the medium was exchanged and supplemented with 1 µg/mL of puromycin in order to select the cells expressing the protein of interest. Stable cells were subsequently propagated under puromycin selection.

2.4.5. Generation of knock-in cell lines

The strategy used for the CRISPR-Cas9-based genome editing of HeLa M cells was designed based on (Ran *et al*, 2013). Specifically, a guide and a donor vector were cloned, as described in paragraph 2.2.11. These two vectors were designed so that the guide plasmid encoded for a single guide RNA able to bring the Cas9 endonuclease in proximity of the SEPT6 or E-Syt1 starting codon. There, a double strand DNA break would eventually be repaired by homologues recombination, using the HRs of the donor vector and thereby resulting in the fusion of eGFP to the SEPT6 or E-Syt1 gene.

To this aim, HeLa M cells were seeded in a 10 cm dish, and transfected at 70% confluency with 2,5 µg of guide vector and 7,5 µg of donor vector as described in paragraph 2.4.2. The guide vector px458-pSpCas9(BB)-2A-GFP encoded for Cas9 fused to eGFP and thus allowed for the selection of successfully transfected cells. Accordingly, after 72h, eGFP-expressing HeLa M were sorted in 96-well plates at the density of 1 cell per well, using fluorescence-activated single cell sorter (BD FACSAria). Colonies were expanded and tested for the expression of eGFP-SEPT6 or eGFP-E-Syt1 by automated live cell imaging and western blot. The generation and validation of the eGFP-SEP6 knock-in cell line was done by Steffen Restel in the ambit of his bachelor thesis, under our supervision.

2.4.6. Cell cycle synchronization

The protocol used in this study was optimized in order to synchronize HeLa M cells at late cytokinesis. This was achieved through the use of thymidine (Sigma-Aldrich) first and nocodazole (Sigma-Aldrich) after, in order to impose an initial block at S-phase and a subsequent block at prometaphase.

Specifically, when thymidine is present in excess it is quickly converted into deoxythymidine triphosphate (dTTP) via the thymidine salvage pathway (Ligasová & Koberna, 2021). dTTPs acts as an allosteric inhibitor of the enzyme ribonucleotide reductase during the conversion of cytidine diphosphate (CDP) into dCDP, a precursor of dCTP (Ligasová & Koberna, 2021; Bjursell & Reichard, 1973). This, in turn, results into an imbalanced deoxynucleotides pool and consequent inhibition of DNA synthesis. Nocodazole, instead, as an inhibitor of microtubules polymerization, can be used in small quantities to reversibly pause the assembly of the mitotic spindle, and thereby the progression through metaphase.

For microscopy-based assays, 2 mM thymidine was applied in full medium to stall the cells (seeded on matrigel-coated glass coverslips/ ibidi slides) at S-phase. After 24h, thymidine was removed by 4 washes of 1 minute each with DPBS, and the cells were allowed to proceed through the cell cycle for 7,5h in fresh medium. Then, 20ng/mL of nocodazole were added to the medium in order to impair the formation of the mitotic spindle and thereby impose a second block at prometaphase. 4h later, the cells were carefully washed 4 times for 1 minute with full medium and were finally allowed to proceed to telophase for an extra 1.5 h, before fixation. For live cell imaging, the nocodazole block was omitted and the recording was initiated 7,5 h after the thymidine washout.

For immunoprecipitation assays, the nocodazole block was applied overnight by supplementing the medium with 40 ng/mL of nocodazole. The following day, cells stalled at prometaphase were collected by mitotic-shake off and were washed 4 times in full medium by centrifugating for 5 minutes at 300 x *g*. Cells were then re-plated in full medium, and allowed to proceed to telophase for an extra 1,5h before lysis. Importantly, DPBS and culture medium were pre-warmed to 37°C, and the time that the cells spent outside the incubator was minimized as much as possible throughout the synchronization.

2.4.7. Drug treatment

For the treatment with Latrunculin A, cells were washed with DPBS and subsequently incubated for 10 minutes at 37°C with 5 µM latrunculin A (or DMSO) in DMEM medium without supplements. To block endocytosis, cells were washed with DPBS and subsequently incubated for 30 minutes at 37°C with 80 µM dynasore, or 30 µM pitstop 2, or DMSO, in DMEM medium without supplements.

After the treatment, cells were either fixed, or the medium was exchanged with the imaging buffer and the cells were immediately imaged via TIRF microscope.

The treatment of NRK49F-SEPT2-eGFP with cytochalasin D was performed by Nadja Hümper. In this case, the cells were incubated for 30 minutes at 37°C with 5 µM of cytochalasin D in full medium.

2.4.8. Immunocytochemistry (ICC)

HeLa M cells (parental, knock-in or stable lines) seeded on matrigel-coated glass coverslips were fixed with 4% PFA or with 2% PFA (for septin immunostainings) for 15 minutes at RT and subsequently washed three times with PBS. Cells were permeabilized with washing buffer for 15 minutes and then blocked with goat serum dilution buffer (GSDB) for 20 minutes. Incubation with primary antibodies, diluted in GSDB, was carried at RT for 1 h, and the excess of antibody was removed with three washes of 10 minutes each with washing buffer. Cells were subsequently incubated with Alexa-Fluor-coupled secondary antibodies diluted in GSDB for 1 h at RT, and washed again three times for 10 minutes with washing buffer. Finally, coverslips were incubated for 5 minutes with 1 µg/mL of DAPI (Life Technologies) in PBS and mounted on microscope glass slides with Immu-Mount (Thermo-Fisher). In case of anillin staining, performed with a primary antibody raised in goat, goat serum was replaced with donkey serum throughout the protocol, and secondary donkey antibodies were used (see **table 2-8**). To stain F-actin, Alexa 647-coupled phalloidin (Invitrogen) was used as a probe and was applied at a 1:70 dilution in GSDB along with secondary antibodies.

To stain SEPT2 in **fig. 6.2-1**, cells were first incubated for 180 seconds at 37°C with 1 µM thapsigargin (TG) in imaging buffer, and subsequently fixed with 4% PFA for 15 minutes at RT. The rest of the staining was conducted as described above, until the three washes following the secondary antibody incubation. After that, the cells were fixed once more with 4% PFA for 5 minutes at RT, washed three times with PBS, and stored in PBS at 4°C. The imaging with the TIRF microscope was conducted within 24h. In this case, since the coverslips had to be placed into an imaging chamber, cells were preventively seeded on matrigel-coated coverslips having a diameter of 24 mm.

For the staining of plasmalemmal PI(4,5)P₂ with the purified pleckstrin homology (PH) domain, cells seeded on matrigel-coated coverslips were fixed with 2% PFA +

1% Glutaraldehyde (GA) for 20 minutes at RT. Excess of fixative was quenched by three washes of 5 minutes each with 50 mM NH₄Cl in PBS. Permeabilization and blocking were performed concomitantly with a first round of incubation with 0.25 µg/mL of GFP-PH-PLCδ1 in 0.5% saponin, 1% BSA in PBS for 30 minutes at RT. Subsequently, cells were incubated (without washing in between) again with 0.25 µg/mL of GFP-PH-PLCδ1 diluted in 1% BSA in PBS for 30 min at RT. After that, coverslips were washed three times with PBS and incubated with primary antibody (rabbit-anti-GFP, Abcam) in 1% BSA, 10% GS in PBS for 1h at RT. Excess of antibody was removed by three washes of 5 minutes each with PBS. The secondary antibody (AlexaFluor488-coupled goat-anti-rabbit) was diluted in 1% BSA, 10% GS in PBS and incubated at RT for 30 minutes. Excess of antibody was removed with four washes of 5 minutes each with PBS, the latter supplemented with 1 µg/mL of DAPI, before mounting.

For the staining of PI(4,5)P₂ with antibody at the intercellular bridge, cells seeded on matrigel-coated coverslips were fixed with 2% PFA +1% GA for 20 minutes at RT. The excess of fixative was quenched with three washes of 5 minutes each with 50 mM NH₄Cl in PBS. Subsequently, cells were permeabilized in 0,5% saponin, 1%BSA in PBS for 30 minutes at RT. Primary antibodies (mouse-anti-PI(4,5)P₂, Echelon-Z + rabbit-anti-MgcRacGAP, Proteintech) were diluted in 1% BSA, 10% GS in PBS and centrifuged for 5 minutes at 17000g at 4 °C to remove precipitates, and then incubated with coverslips for 2h at RT. Excess of antibodies was removed by three washes of 5 minutes each with PBS. Secondary antibodies (AlexaFluor568-coupled goat-anti-mouse IgM and AlexaFluor488-coupled goat-anti-rabbit) were also diluted in 1% BSA, 10% GS in PBS and centrifuged for 5 minutes at 17000 x g at 4 °C before incubation with coverslips for 1h at RT. Coverslips were subsequently washed 3 times for 10 minutes with PBS, additionally incubated for 5 minutes with PBS supplemented with 1 µg/mL of DAPI, and finally mounted.

PI(4,5)P₂ in **fig. 6.2-8** was stained as described above. However, prior to fixation, cells were incubated for 200 seconds at 37°C with 1 µM TG in imaging buffer.

2.4.9. Ultrastructure expansion microscopy (U-ExM)

To overcome the challenge of antibody penetration within the densely packed midbody organelle during conventional indirect immunofluorescence, we took

advantage of U-ExM in collaboration with Nadja Hümpfer and Prof Dr. Helge Ewers (Freie Universität Berlin).

This technique enables the physical expansion of the sample prior to immunocytochemistry, in order to facilitate the antibody penetration into the specimen and, at the same time, obtaining a magnification of the latter.

The sample magnification is achieved through subsequent steps of polymerization, denaturation and expansion. To allow polymerization, after a regular fixation, the sample is incubated in a solution containing PFA and a high concentration of acrylamide (AA). The PFA reacts with the N-termini and side chains of several amino acids, while the AA binds to these modified residues and prevent intra and inter protein cross-linking. Acrylamide-bound proteins can then participate in the following free-radical polymerization step, initiated in presence of TEMED and APS. In this way, the proteins of the sample become part of a gel. The jellified specimen is then subjected to denaturation and immersion into pure water to allow expansion (Gambarotto *et al*, 2021). Antibody labelling is performed subsequently, and therefore the process of magnification does not involve the epitope-antibody complex.

For this study, the gelation and 4 times isotropic expansion of the samples was performed by Nadja Hümpfer, according to Gambarotto et al., 2019, 2021. Gels were subsequently stained with primary antibodies diluted in 2% BSA in PBS for 3h at 37°C. The excess of antibody was then removed by three washes of 20 minutes each with 0.1% Tween20 in PBS under agitation. The incubation with secondary antibodies was carried out in 2% BSA in PBS for 2,5h at 37°C. Gels were washed again as before, and twice for 30 minutes at RT in milliQ water, to be finally stored overnight at 4 °C in milliQ water. Imaging was performed the day after, with a confocal microscopy.

2.4.10. Fluorescence microscopy

To obtain high resolution of subcellular structures, immunostained HeLa M cells were routinely imaged with a Zeiss confocal spinning disk microscope (Yokogawa CSU22, Hamamatsu EMCCD camera), using a 60x immersion oil objective (1.4 NA). 12 images were acquired per condition, per experiment.

For each image of cytokinetic cells, a stack of 21 pictures within the z-plane (z-stack), with a spacing of 0.2µm was acquired. For cells at interphase, a z-stack of

15 pictures with the same spacing was acquired. Cells stained with purified PH domain (**fig. 3-2-A**) or expressing the PH domain (**fig. 3-17-A**) were imaged within a single z-plane by focusing on the plasma membrane. EGFP-SEPT6 knock-in cells in **fig. 3-21-A** were imaged within a single z-plane by focusing on prominent septin filaments.

For the experiment in **fig. 3-1** semi-automated epi-fluorescent imaging was conducted with a Nikon Eclipse Ti microscope (illumination: CoolLED, pE4000; prime95B sCMOS camera) operated by NIS-Elements software, using a 20x air objective (0.75 NA). Tile scans of $1.3\mu\text{m}^2$ were produced by stitching together images automatically acquired around a chosen point. Four tile scans were acquired per condition, per experiment.

Epi-fluorescent pictures of HeLa M cells transfected with PIPK1 γ isoforms (**fig. 3-5-C**) or treated with siRNA against indicated PIPKs (**fig. 3-4-A** and **fig. 3-9-A**) were acquired with the same microscope, using a 40x immersion oil objective (1.3 NA). 12 images were acquired per condition, per experiment.

Live cell imaging of eGFP-SEPT6 cells was performed on a spinning disk Nikon Eclipse Ti microscope (Yokogawa CSU-X1 and EMCCD Camera), operated by NIS-Elements software, with a 40x air objective (0.75 NA). For this experiment cells were seeded on matrigel-coated 8-well chamber slides (ibidi). Imaging was initiated 7.5h after thymidine release, and was carried overnight, with a frame rate of 10 minutes. Cells were kept in full medium (without phenol red) at 37°C and 5% CO₂, and pictures were acquired within a single z-plane that was set at the beginning by focusing on septin fibers of pre-mitotic cells, and kept by an autofocus system. This experiment was repeated three times, and in each experiment 5 positions were imaged per condition.

NRK49F SEPT2-eGFP cells and gels for U-ExM were imaged with an Olympus spinning disk microscope (Yokogawa CSU-X1, Hamamatsu C11440 camera), using a 60x immersion oil objective (1.42 NA). Specifically, cells in **fig. 3-6** were imaged by Nadja Humpfer and a 10 picture z-stack with a spacing of 0.3 μm was acquired. During U-ExM imaging (performed together with Nadja Humpfer), for each image a 21 pictures z-stack with a spacing of 1 μm was acquired, and 20 images were acquired per condition, per experiment.

Total internal reflection (TIRF) microscopy was used to visualize eGFP-E-Syt1 at the plasma membrane. During TIRF, the laser beam is angled to match the critical

angle for total internal reflection at the boundary between a glass (coverslip) and an aqueous medium (sample). Hence, when the laser strikes this boundary, it is entirely reflected back into the glass. However, this process generates an electromagnetic field, called the evanescent wave, at the solid-liquid interface. This evanescent wave shares the same frequency as the excitation light, but its intensity decreases exponentially with distance from the glass surface. As a result, only fluorophores located within approximately 200 nanometers from the coverslip are excited. In a cellular context, this allows the specific excitation of the plasma membrane and of its immediate cytoplasmic surroundings; hence, it is suitable for the selective visualization of plasma membrane contact sites. TIRF imaging was performed using a Nikon Eclipse Ti equipped with a custom-built solid state laser setup and Andor sCMOS camera, operated by open-source ImageJ-based Micromanager software. Cells were imaged at 37°C with a 60x TIRF-objective (1.49 NA) and a Nikon PerfectFocus autofocus system. Cells were seeded on 24 mm coverslips which, at the moment of imaging, were rinsed with DPBS and placed in the imaging chamber with 500 µL of imaging buffer. After the first frame, extra 500 µL of imaging buffer, containing 2 µM of TG, were carefully added to the cells. Images were acquired every 10 seconds for 10 minutes at a 50% laser intensity, with an exposure time within the range of 15-30 milliseconds.

2.4.11. Image analysis

The processing and analysis of images was performed with the open-source software Fiji (ImageJ) on original tiff files.

Quantifications depicted in **fig. 3-1-D-G** were performed by identifying and manually counting mitotic cells displaying a mitotic spindle or a cytokinetic bridge, as schematized in **fig. 3-1-C**. This number was then divided by the total number of nuclei, identified via a macro (**table 2-12**) and serving as the total number of cells in the picture.

The qualitative assessment of anillin was conducted on maximum intensity projections of the z-stacks.

For measuring the intensity of MKLP1 dots, average intensity projections of the z-stacks were generated and the MKLP1 channel was segmented as described in **table 2-10**, in order to obtain regions of interest (ROIs) outlaying the MKLP1 dots. Subsequently, the fluorescence intensity of MKLP1 was measured as integrated

density within the obtained ROIs on unprocessed average intensity z-projections, after background subtraction. The intensities of CIT-K and MgcRacGAP dots were measured the same way. A similar analysis was performed on expanded samples (**table 2-11**).

For measuring the sizes of the acetylated tubulin bridges, average intensity projections of the z-stacks were generated, and the acetylated tubulin channel was segmented as described in paragraph 2.1.11 in order to obtain ROIs outlaying the bridges. The length and width of the acetylated tubulin bridges were then measured, respectively, as maximum and minimum Feret diameter of the identified ROIs. The length of the PRC1 bridge was measured the same way (paragraph 2.1.11).

Septin enrichment at the cytokinetic bridge was determined by dividing the intensity of SEPT2 in a ROI outlining the acetylated tubulin (or PRC1) bridge by the intensity of SEPT2 in a ROI outlining the whole dividing cell (drawn by hand). Also in this case, the measurements were carried out on average intensity z-projections, after background subtraction.

The intensity of PI(4,5)P₂ per cell area in **fig. 3-2** was measured as mean grey value of the GFP-PH-PLC δ 1 fluorescence in the ROI outlining single cells (drawn by hand), after background subtraction. The percentage of PI(4,5)P₂ at the cleavage furrow in **fig. 3-17** was determined by dividing the intensity of the expressed PH domain in a ROI covering the cleavage furrow by the intensity of the domain in a ROI covering the plasmalemma of the whole dividing cell, both drawn by hand. These quantifications were performed on confocal images acquired within a single z-plane by focusing on the PM.

The intensity line scan analysis as depicted in **fig. 3-6-B-C** and **fig. 3-24-B-C** were performed on the maximum intensity projection of the z-stack. The intensity line scan analysis as depicted in **fig. 3-18** was performed on confocal images acquired within a z-plane at the middle of the bridge. The intensity line scan analysis as depicted in **fig. 6.2-5** was performed on TIRF images.

The percentage of multinucleated cells in **fig. 3-4** and **fig. 3-9**, and the percentage of midbodies displaying septin rings in **fig. 3-16-D-E** were obtained by manual counting.

The pearson's coefficients in **fig. 3-21-B-C** were measured with the JACoP plugin (ImageJ) on confocal images acquired within a single z-plane by focusing on prominent septins structures.

For TIRF experiments, the change in fluorescence overtime was measured by the Time Series Analyzer plugin (ImageJ) within hand-drawn ROIs outlying single cells. For all displayed images brightness and contrast were adjusted equally for different conditions, unless otherwise stated.

2.4.12. Analysis of the expression of PIPKI γ isoforms

Cells treated with siRNA control or against PIPKI γ -i3/i5 were collected in TRIzol (Thermo Fisher), snap frozen in liquid nitrogen and stored at -80°C until further processing by Prof. Dr. Florian Heyd (Freie Universität Berlin) as follows. Reverse transcriptase (RT)-PCRs were performed as described previously (Preußner *et al*, 2017). Briefly, 1 μ g of RNA was used with isoform-specific reverse primers for the RT-reaction, and the subsequent PCR was performed with a ³²P-labeled forward primer. Products were separated by denaturing PAGE and quantified using a Phosphoimager (Typhoon 9200, GE Healthcare) and ImageQuantTL software. The sequence of the primers used for PCR and the resulting sizes of the amplicons were as follows: Common PIPKI γ forward: GCGCCCGCCACCGACATCTAC; PIPKI γ -i1-3 reverse: CATCTCCCGAGCTCTGGGCCTC (i1=125 nt, i2=210 nt, i3=290 nt); PIPKI γ -i4 reverse: GAGACCAGGACGCGCACAAACCAG (i4 = 154 nt); PIPKI γ -i5 reverse: CAGACACTGAGCTTCCGGCCGG (v5 = 195 nt).

2.4.13. Statistics and reproducibility

All data (except **fig. 3-23-F-G**, **fig. 3-S5** and figures in the Appendix), were derived from at least three independent experiments and are presented as means \pm standard deviation (SD). GraphPad Prism version 9.2 software was used for statistical analysis. Unpaired two-tailed t-test was applied to compare two groups. One-way ANOVA followed by Dunnett's multiple comparison test was used to compare more than one experimental group to a control group. When the control group was set to 1 by normalization, one sample two-tailed t-test was applied for comparing one or more experimental groups to control. The level of significance is indicated in the figures by asterisks (*P < 0.05; **P < 0.01; ***P < 0.001; ****P < 0.0001), and detailed in the figure legends as exact P value.

3. Results

3.1. PIPKI γ controls the organization of anillin and septins at the ICB and is required for successful cytokinesis

3.1.1. PIPKI β and PIPKI γ are required for furrow ingression, while exclusively PIPKI γ is needed at telophase

Synthesis of specific PIs is tightly regulated through the spatiotemporally controlled recruitment of the respective lipid kinases to distinct subcellular compartments (Choi *et al*, 2015). To date, only PIPKI β has been visualized at the cleavage furrow, and has therefore been proposed to drive PI(4,5)P₂ synthesis during cell division (Emoto *et al*, 2005). PIPKI β belongs to type-I PIP kinases, a class of enzymes that uses PI(4)P as substrate and provides the major pools of PI(4,5)P₂ in mammalian cells. This class includes also the isozymes PIPKI α and PIPKI γ (Balla, 2013).

To assess whether also these other type-I PIP kinases play a role in cell division, PIPKI α , β or γ were selectively depleted by siRNA-mediated knock-down (**fig. 3-1-A**). Cells were then fixed and stained for acetylated-tubulin, which marks the mitotic spindle before and at the onset of furrow ingression, and the cytokinetic bridge at the end of furrow ingression (see scheme in **fig. 3-1-C**). Samples were then analyzed by semi-automated imaging to cover an area of 5.2 μm^2 on each coverslip (representative insets in **fig. 3-1-B**). In agreement with the above mentioned literature, depletion of PIPKI β stalled mitosis in phases that precede the closure of the furrow (metaphase or anaphase) (**fig. 3-1-D**), as indicated by a significant increase in the fraction of cells displaying a mitotic spindle. Interestingly, the same phenotype was observed upon knock-down of PIPKI γ , suggesting a potential redundant function of these two kinases. Importantly, only depletion of PIPKI γ significantly increased (of about two-fold) the fraction of cells displaying an acetylated tubulin bridge (**fig. 3-1-E**). We conclude that PIPKI γ has a specific function from telophase on.

Our analysis also revealed abnormalities such as multipolar spindles or bridges. Again, depletion of PIPKI β or γ caused a significant increase in the fraction of cells that displayed a multipolar spindle (**fig. 3-1-F**), while solely depletion of

PIP $KI\gamma$ caused a significant increase in multipolar bridges (**fig. 3-1-G**). However, these abnormalities account for less than 1% of the complete cell population.

In conclusion, this first mini-screen suggests a potential novel role for PIP $KI\gamma$ at the ingressed furrow, opening the intriguing possibility that a late-stage pool of PI(4,5)P $_2$ synthesized by this enzyme is required to ensure successful cytokinesis.

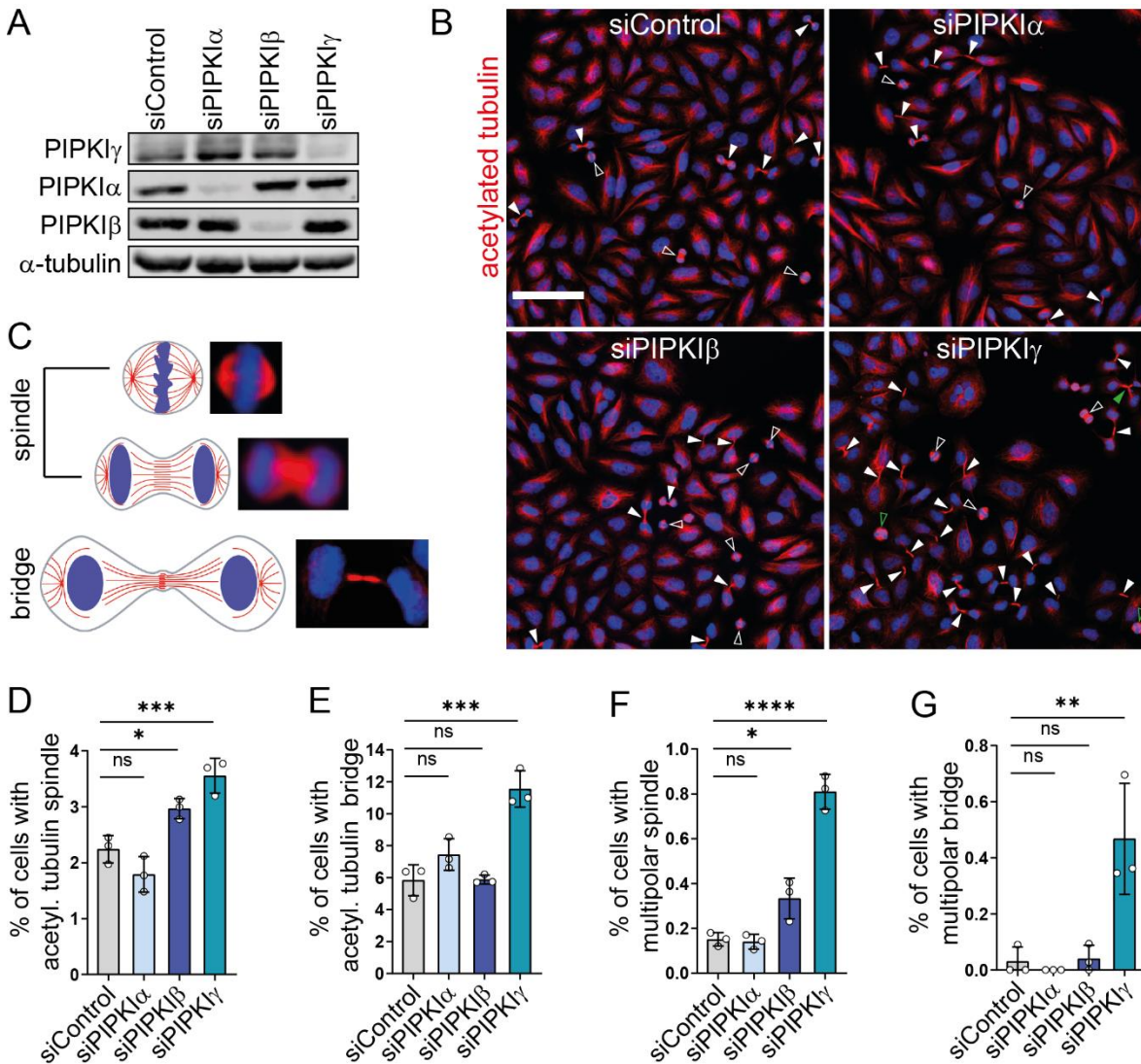


Figure 3-1. Depletion of PIP $KI\beta$ or PIP $KI\gamma$ stalls cells at early stages of mitosis while exclusively PIP $KI\gamma$ is required for mitotic progression after furrow ingression. (A) Western blot analysis of cell lysates upon treatment of HeLa M cells with control siRNA, or with siRNAs targeting PIP $KI\alpha$, β or γ . **(B)** Representative images of HeLa M cells treated with indicated siRNAs and stained for acetylated tubulin and with DAPI. Arrowheads: white contour indicates acetylated tubulin spindles, white fill acetylated tubulin bridges, green contour multipolar spindles, green fill multipolar bridges. Scale bar: 100 μ m. **(C)** Scheme depicting the distribution of acetylated tubulin at different stages of mitosis. Before and at the beginning of furrow ingression acetylated tubulin aligns with the mitotic spindle, at the end of furrow ingression (from telophase on) acetylated tubulin marks the cytokinetic bridge. **(D-G)** Quantifications based on the scheme depicted in C. For each condition and experiment, four coverslips areas of 1.3 μ m 2 were imaged by semi-automated imaging (epifluorescence). **(D-E)** Percentage of cells with an acetylated tubulin spindle **(D)** or bridge **(E)**. **(F-G)** Percentage of cells with a multipolar acetylated tubulin spindle **(F)** or bridge **(G)**. Data are represented as mean \pm SD (n=3) with 2593-4431 cells imaged per condition and experiment.

Statistics: 1way ANOVA, followed by Dunnett's multiple comparison test. Adjusted P values in D: ns $P=0.1723$, $*P=0.0274$, $***P=0.0009$. Adjusted P values in E: ns (siControl vs. siPIPKI α) $P=0.1423$, ns (siControl vs si PIPKI β) $P=0.0007$, $***P=0.0002$. Adjusted P values in F: ns $p=0.9933$, $*p=0.0203$, $***P<0.0001$. Adjusted P values in G: ns (siControl vs. siPIPKI α) $P=0.9701$, ns (siControl vs si PIPKI β) $P=0.9986$, $**P=0.0024$.

3.1.2. Depletion of any of the type-I PIP kinases does not cause major changes in total PI(4,5)P₂ levels at the PM

The mitotic defects observed upon depletion of PIPKI β or PIPKI γ (**fig. 3-1**) could be a consequence of global changes in PI(4,5)P₂ levels. To rule this out we quantified plasmalemmal levels of PI(4,5)P₂ upon knock-down of either isozyme.

Labeling of PI(4,5)P₂ was achieved by the pleckstrin homology (PH) domain of phospholipase C (PLC) δ 1, which specifically interacts with PI(4,5)P₂ (Várnai *et al*, 2002). Cells were then imaged by confocal microscopy, with the focus being kept on the PM (**fig. 3-2-A**). Depletion of either enzyme did not change the intensity of PI(4,5)P₂ labeling (**fig. 3-2-B**). This result is not unexpected because, despite their unique tissue and subcellular localizations, PIPKI α , β and γ are known to be plastic and able to compensate for each other (Balla, 2013). Accordingly, a single copy of the PIPKI γ gene is sufficient to support mouse development to adulthood, even in absence of PIPKI α and β (Volpicelli-Daley *et al*, 2010).

In conclusion, this result suggests that the increase in mitotic cells observed upon knock-down of PIPKI β or γ does not depend on a major decrease of PI(4,5)P₂ at the PM.

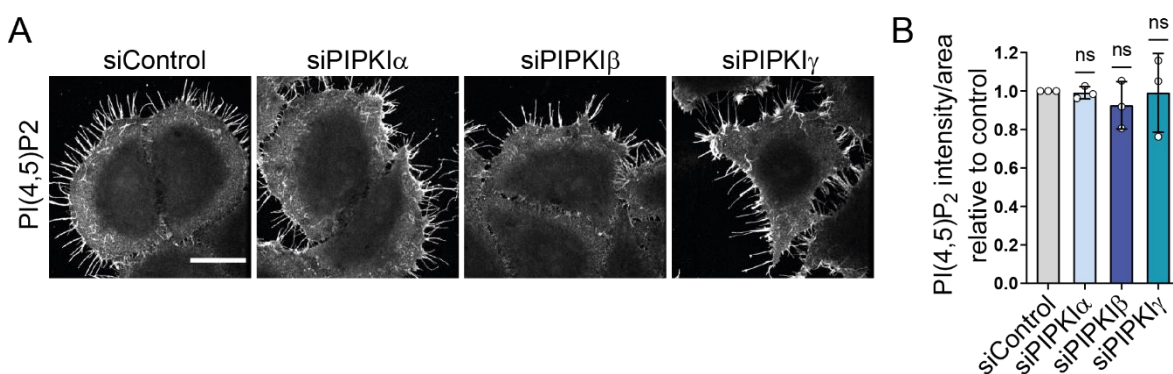


Figure 3-2. Depletion of PIPKI α , β or γ does not cause major changes in plasmalemmal PI(4,5)P₂. (A) Representative confocal images of HeLa M cells treated with the indicated siRNAs, and stained for PI(4,5)P₂ with purified GFP-tagged PH-PLC δ 1 domain; scale bar: 30 μ m. (B) Intensity of PI(4,5)P₂ labeling per cell area, mean \pm SD (n=3) between values normalized to control. ~ 30 cells per condition and experiment were imaged. Statistics: two-tailed one sample t test (hypothetical value 1), siPIPKI α ns $P=0.6580$, siPIPKI β ns $P=0.4034$, siPIPKI γ ns $P=0.9415$.

3.1.3. PIPKI γ is required for anillin organization and septin enrichment at the ICB

Our initial result (**fig. 3-1**) revealed a dual contribution of PIPKI β and PIPKI γ to the ingression of the cleavage furrow, while PIPKI γ emerged as the sole isozyme required for late stages of cytokinesis. To further investigate this unique function, we analyzed the impact of PIPKI γ depletion on the distribution of anillin and septins at the ICB. Anillin is a known effector of plasmalemmal PI(4,5)P₂, which stabilizes the actomyosin ring to allow a symmetric ingression of the furrow, and is ultimately deposited at the midbody and at its sides (Sun *et al*, 2015; Liu *et al*, 2012; Gai *et al*, 2011). Anillin recruits septins, which are able to oligomerize into higher-order structures in a PI(4,5)P₂-dependent manner (Bertin *et al*, 2010b; Zhang *et al*, 1999). Similar to anillin, septins remain concentrated within the ICB and exhibit a distinctive organization that likely depends on a local pool of PI(4,5)P₂, perhaps synthesized by PIPKI γ (see **fig. 1-2-B** and **1-3-B**). In fact, anillin and septins are essential for the maturation of the ICB and later abscission events (Panagiotou *et al*, 2022; Renshaw *et al*, 2014; Karasmanis *et al*, 2019).

To assess the role of type I PIP kinases in anillin/septin organization at late stages of mitosis, cells were depleted of PIPKI α , β or γ , synchronized, fixed at telophase, and immunostained for anillin or SEPT2. Acetylated tubulin was stained in parallel to visualize the cytokinetic bridge. In control cells and in cells depleted of PIPKI α or β , anillin displayed a compact organization at the two sides of the (putative) midbody, while upon loss of PIPKI γ it appeared scattered (**fig. 3-3-A**). Indeed, the percentage of dividing cells displaying compact anillin significantly dropped from 47% in control cells to 16.7% in absence PIPKI γ (**fig. 3-3-B**). Note that the unstained “gap” in the middle of the acetylated tubulin bridge corresponds to the midbody, a densely packed organelle that cannot be penetrated by most antibodies, including the one directed against acetylated tubulin.

Regarding septins, in control cells or upon knock-down of PIPKI α , SEPT2 appeared enriched at the ICB, likely reflecting its successful translocation onto the acetylated MTs of the cytokinetic bridge (**fig. 3-3-C**). Similar observations were made upon knock-down of PIPKI β , although occasionally SEPT2 was also observed at the flanking membrane of the future daughter cells (as in the depicted example). Depletion of PIPKI γ led to a drastic relocation of SEPT2: SEPT2 no longer

concentrated along the cytokinetic bridge but rather appeared enriched at the PM of the forming daughter cells. Consequently, its percentage at the acetylated tubulin bridge was about half of the control (**fig. 3-3-D**).

Together these data point at PIPK1 γ as a novel regulator of anillin and septins at the ICB.

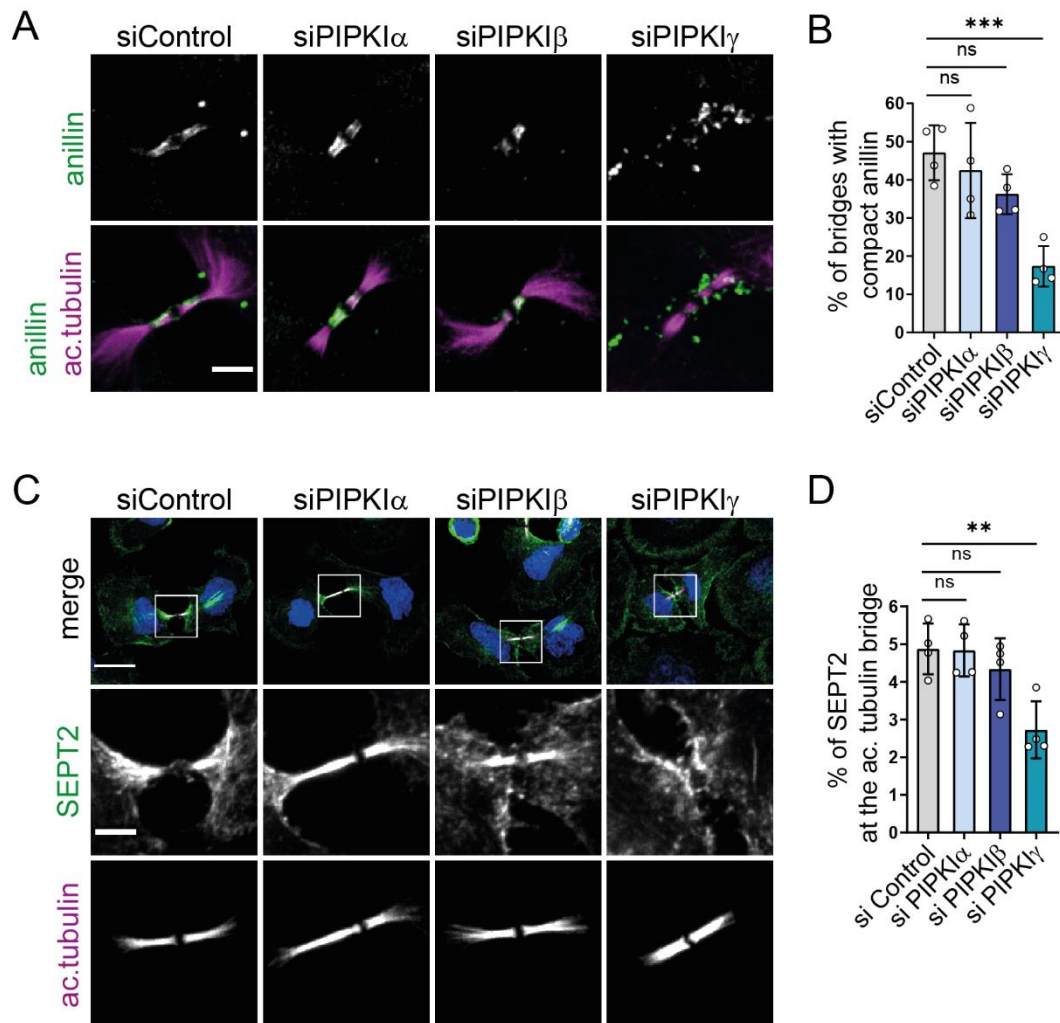
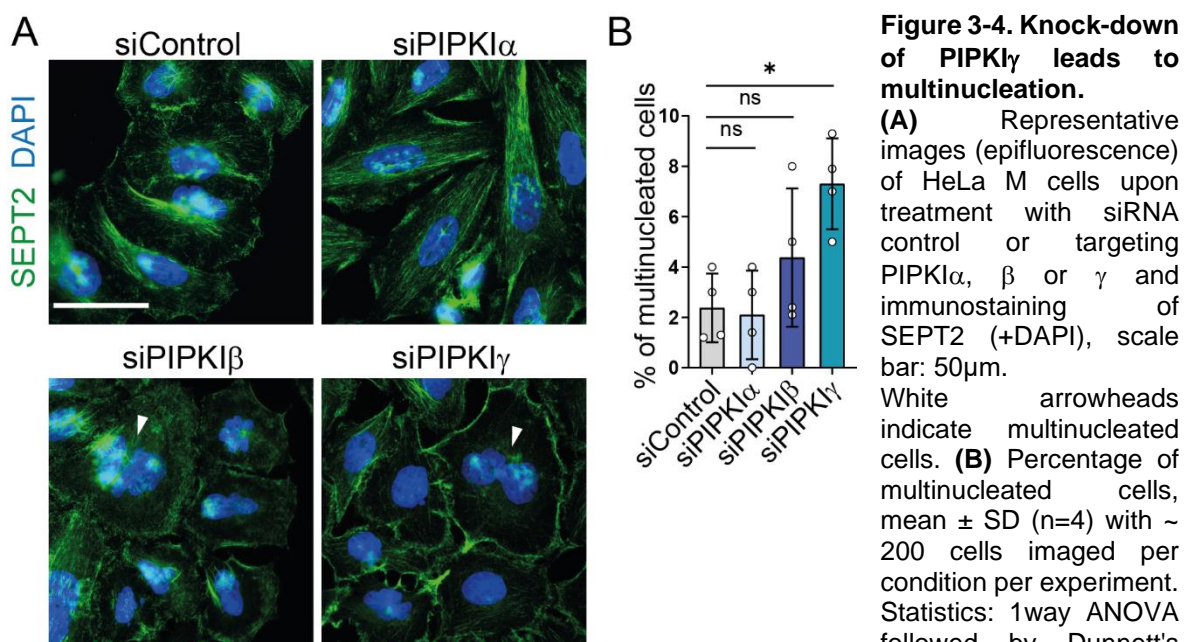


Figure 3-3. Upon knock-down of PIPK1 γ , anillin is scattered and the fraction of SEPT2 at the cytokinetic bridge is reduced. **(A)** Representative confocal images (max. intensity z-projection) of HeLa M cells treated with siRNA control or targeting PIPK1 α , β or γ and immunostained for acetylated tubulin and anillin. Scale bar: 5 μ m. **(B)** Quantification of cytokinetic bridges with compact anillin, mean \pm SD (n=4); between 15 and 30 bridges were imaged per condition and experiment. Statistics: 1way ANOVA followed by Dunnett's multiple comparison test. Adjusted P values: ns (siControl vs. siPIPK1 α) P=0.7600, ns (siControl vs siPIPK1 β) P=0.1914, ***P=0.0006. **(C)** Representative confocal images (max. intensity z-projection) of HeLa M cells treated with siRNA control or targeting PIPK1 α , β or γ and immunostained for acetylated tubulin and SEPT2 (+DAPI). Scale bar of merge: 20 μ m, scale bar of inset: 5 μ m. **(D)** Percentage of total SEPT2 at the acetylated tubulin bridge. Quantifications were performed on average intensity z-projections after background subtraction. Values are represented as mean \pm SD (n=4); between 15 and 30 cytokinetic cells were imaged per condition and experiment. Statistics: 1way ANOVA, followed by Dunnett's multiple comparison test. Adjusted P values: ns (siControl vs. siPIPK1 α) P=0.9996, ns (siControl vs siPIPK1 β) P=0.6167, **P=0.0038.

3.1.4. Depletion of PIPK γ promotes multinucleation and disrupts prominent septin fibers

Loss of septins causes defects in cell division that ultimately result in multinucleation (two-to fourfold increase in case of SEPT2, 6 or 9 depletion) (Estey *et al*, 2010; Spiliotis *et al*, 2005). To test whether similar holds true upon loss of type I PIP-kinases, we assessed the percentage of multinucleated cells upon depletion of PIPK α , β or γ . Strikingly, knock-down of PIPK γ led to a threefold increase in multinucleation (**fig. 3-4-B**), thereby phenocopying the loss of SEPT2, 6 or 9 observed by others and pointing at a role of this kinase in cell division. Depletion of PIPK β increased the fraction of multinucleated cells, though to a lesser extent. This possibly reflects its requirement at early mitotic stages.

In the same experiment, septin distribution was visualized by immunostaining of SEPT2. In absence of PIPK β and γ prominent septin fibers were lost, especially in multinucleated cells (white arrowhead) (**fig. 3-4-A**). This likely reflects a loss of septin association with MTs (see below, paragraph 3.5.2; **fig. 3-20**).



multiple comparison test. Adjusted P values: ns (siControl vs. siPIPK α) P=0.9944, ns (siControl vs. siPIPK β) P=0.3827, *P=0.0113.

3.2. The function of PIPK1 γ at late cytokinesis is ascribable to kinase active and septin-binding isoform 5 (PIPK1 γ -i5)

3.2.1. PIPK1 γ isoform 3 and 5 (PIPK1 γ -i3/i5) share a splicing insert responsible for the interaction with septins

The human gene of PIPK1 γ (PIP5K1C, ensemble: ENSG00000186111) encodes for at least five splice variants (here referred to as i1, i2, i3, i4, i5) (**fig. 3-5-A**). These isoforms share a segment comprised by the first 640 amino acids (white segment, not in scale with the other segments) that harbors the kinase core domain, but display variable C-termini. Different C-termini of PIPK1 γ isoforms ensure recruitment to specific subcellular compartments, and therefore the localized synthesis of PI(4,5)P₂ pools during select cellular events (Schill *et al*, 2014; Xu *et al*, 2014; Di Paolo *et al*, 2002; Sun *et al*, 2013; Kahlfeldt *et al*, 2010).

Interestingly, a mass spectrometry-based screen for proteins that preferentially associate with distinct splice variants revealed septins as major binding partners of PIPK1 γ -i3 (Michael Krauß, data not shown). This isoform-specific interaction could be confirmed by affinity purification experiments from mouse brain lysate, using GST-fused kinase tail variants as baits. Both, PIPK1 γ -i3 and i5 could pull-down different septin paralogues (**fig. 3-5-B**). This result suggests an interaction of the shared stretch of amino acids in the PIPK1 γ -i3/i5 tails (yellow segment in **fig. 3-5-A**) with oligomerized septins. Of note, PIPK1 γ i2 and i3 tails were able to pulldown the focal adhesion protein talin due to another common splice insert (purple segment in **fig. 3-5-A**), in line with previous reports that demonstrated an interaction with the FERM domain of talin (Di Paolo *et al*, 2002; Ling *et al*, 2002).

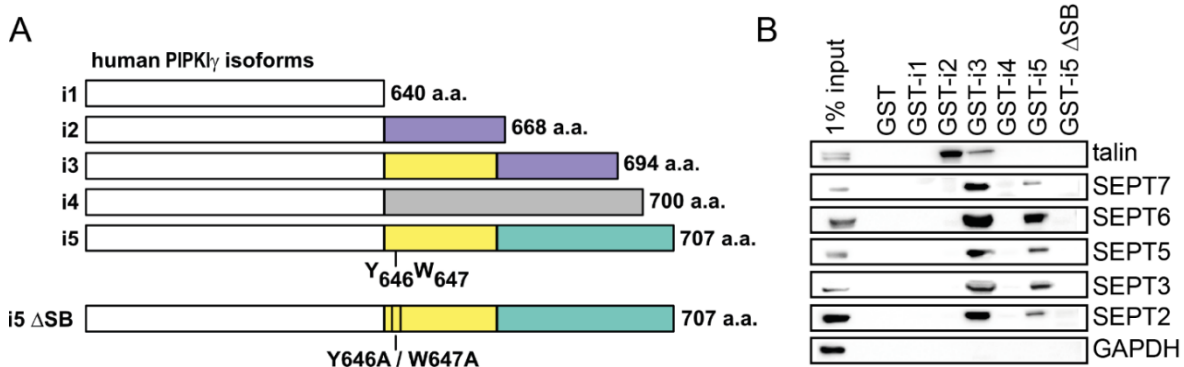
Alanine scanning mutagenesis revealed two aromatic amino acids, Y646 and W647, within the septin-associating splice insert of PIPK1 γ -i3/i5 (aa 646-647, within the yellow segment in **fig. 3-5-A**) that are critical for the interaction with septins (Diploma thesis of Nina Jänsch). Accordingly, a PIPK1 γ -i5 mutant (Y646A/W647A) lost the ability to pull down septins from mouse brain lysates (**fig. 3-5-B**, last lane). We, thus, named this mutant Δ SB (deficient in septin binding).

Interestingly, upon overexpression, HA tagged-PIPK1 γ -i3 and i5, but not i1, i2 or i5 Δ SB, were occasionally found to be organized in filaments that partially overlapped with septin fibers (yellow arrows) (**fig. 3-5-C**). In NRK-49F cells that exhibit

prominent colocalization of septins with actin stress fibers (**fig. 3-6-A**), a colocalization of septins with PIPK γ -i3, i5 and i5 K188A (catalytically inactive mutant) but not i1, i2, i4 or i5 Δ SB was also observed (Nadja Humpfer, not shown). Notably, upon treatment with cytochalasin D, septin filaments crumbled into rings that lost the colocalization with actin but retained the colocalization with PIPK γ i5 and i5 K188A (**fig. 3-6-B-C**, courtesy of Nadja Humpfer). This suggests that the interaction between PIPK γ -i3/i5 and septins is not bridged by actin and is independent of kinase activity.

Immunoprecipitation assays further confirmed the interaction of PIPK γ -i5 with septins. Overexpressed mCherry-PIPK γ -i5 successfully co-immunoprecipitated co-transfected myc-tagged SEPT6 (not shown), 7, 9 or 5, but not endogenous talin, from HEK-293T lysate (**fig. 3-5-D-F**).

Together, these data suggest that PIPK γ -i3/i5 interact with septin oligomers. Septins, in turn, might aid the recruitment of these two isoforms to the ICB.



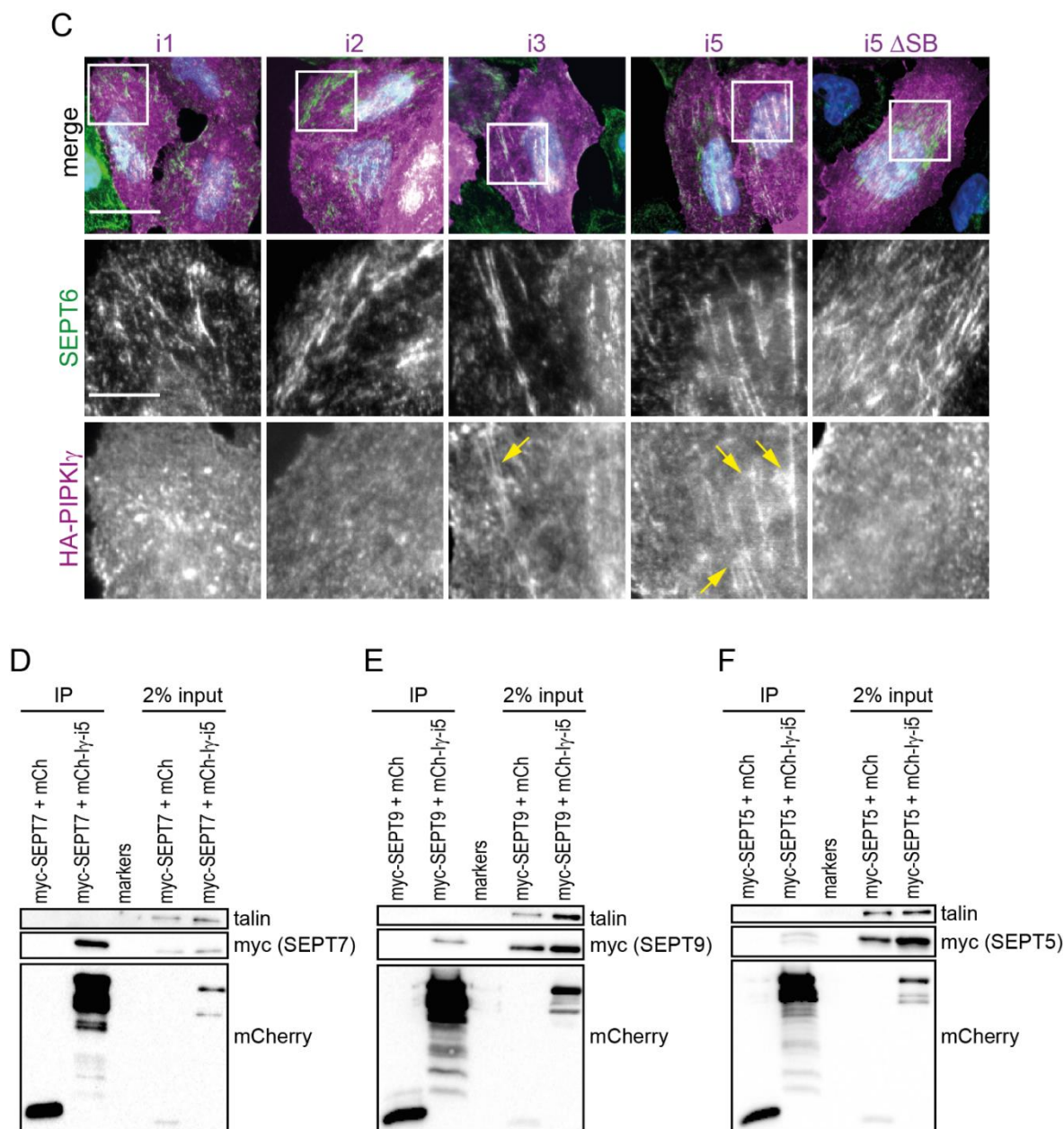


Figure 3-5. PIPK1 γ isoform 3 and 5 (i3/i5) interact with septins through two aromatic amino acids (W646 and Y647) harbored in their common splice insert. (A) Schematic representation of human PIPK1 γ isoforms. Note that the common white insert (harboring the kinase core) is not in scale. i3 and i5 share a splice insert (yellow). I5 Δ SB is a mutant incapable of septin binding, with Y646 and W647 being mutated into alanines; a.a. = amino acids. **(B)** Affinity-purification of septins from mouse brain lysate on GST-fused PIPK1 γ tail variants (a.a. 451 to end). Tails of human PIPK1 γ -i3/i5, but not of PIPK1 γ -i1/i2/i4 or I5 Δ SB, associate with septin paralogues from all subgroups. PIPK1 γ -i2 and i3 interact with talin through a common splice insert (violet segment in A). GAPDH: Glyceraldehyde-3-Phosphate Dehydrogenase. **(C)** Representative epifluorescence images of HeLa M cells demonstrate that overexpressed HA-tagged PIPK1 γ -i3/i5, but not i1/i2 or i5 Δ SB, exhibit a filamentous pattern (yellow arrows) overlapping with endogenous septin fibers (immunostaining of SEPT6 and HA). Scale bar: 30 μ m, scale bar of inset: 10 μ m. Please note that in our hands PIPK1 γ -i4 could not be overexpressed in HeLa M cells. However, according to literature, this isoform displays nuclear localization (Schill & Anderson, 2009). **(D-F)** Western blot analysis showing co-immunoprecipitation of overexpressed myc-tagged SEPT7 **(D)**, SEPT9 **(E)** or SEPT5 **(F)** with overexpressed mCherry-tagged PIPK1 γ -i5 from HEK-293T lysate.

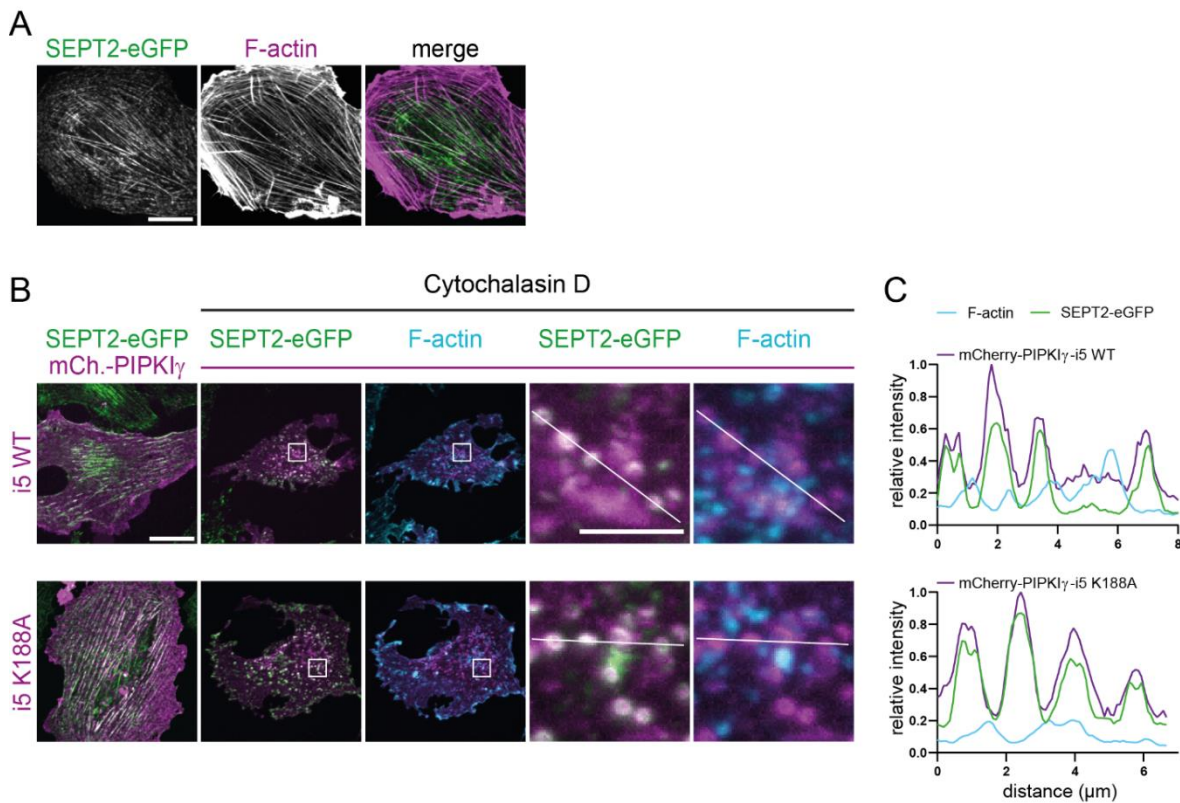


Figure 3-6. PIPKI γ -i5 interacts with septins independently of actin and kinase activity. (A) Representative confocal images showing partial overlap between endogenous SEPT2-eGFP and F-actin in genome-edited NRK49F cells (Banko *et al*, 2019) stained with phalloidin. Scale bar: 20 μm . (B) Representative confocal images (max. intensity z-projection) of genome-edited NRK49F transfected with plasmids encoding human mCherry-tagged PIPKI γ -i5 or PIPKI γ -i5 catalytically inactive mutant (K188A). To disrupt actin filaments, cells were incubated with 5 μM Cytochalasin D. Actin was stained with phalloidin. Scale bar: 20 μm , scale bar of inset: 5 μm . (C) Intensity profiles (normalized to the maximum value, set as 1) of F-actin, SEPT2-eGFP and mCherry-PIPKI γ -i5 wild type or K188A, along a line (shown in B) crossing septin rings that formed upon actin disruption. This figure is a courtesy of Nadja Humpfer.

3.2.2. PIPKI γ -i5 localizes to the ingressed cleavage furrow

Unfortunately, all attempts to generate an antibody that selectively recognizes PIPKI γ -i3/i5 failed. Therefore, in order to visualize PIPKI γ -i5 at low and consistent expression levels, a stable cell line expressing mCherry-PIPKI γ -i5 was generated. This cell line was then used to correlate the distribution of PIPKI γ -i5 with endogenous anillin and SEPT2 at different stages of cell division (**fig. 3-7**).

At anaphase (**fig. 3-7**, upper row), mCherry-PIPKI γ -i5 is homogeneously distributed across the PM, while SEPT2 appears enriched at the equatorial plane and at the poles of the mother cell. Anillin is detected exclusively at the equatorial plane. As the cell constricts between anaphase and telophase (**fig. 3-7**, middle row), mCherry-PIPKI γ -i5 enriches at the cleavage furrow. At telophase, upon closure of the cleavage furrow, mCherry-PIPKI γ -i5 outlines the midbody ring, together with SEPT2

and anillin (**fig. 3-7**, last row). At this stage, anillin is accumulated at the midbody, while SEPT2 starts to translocate to cytokinetic bridge. These data support the hypothesis that PIPK γ -i5 may be recruited by septins to the ingressing cleavage furrow/emerging midbody organelle, to secure the synthesis of a PI(4,5)P $_2$ pool required for post-furrowing events, such as anillin and septin reorganization at the ICB. Similar observations were made in a cell line stably expressing mCherry-PIPK γ -i3. However, the expression of mCherry-PIPK γ -i3 drastically dropped after each passage and therefore data acquired with this cell line are not shown.

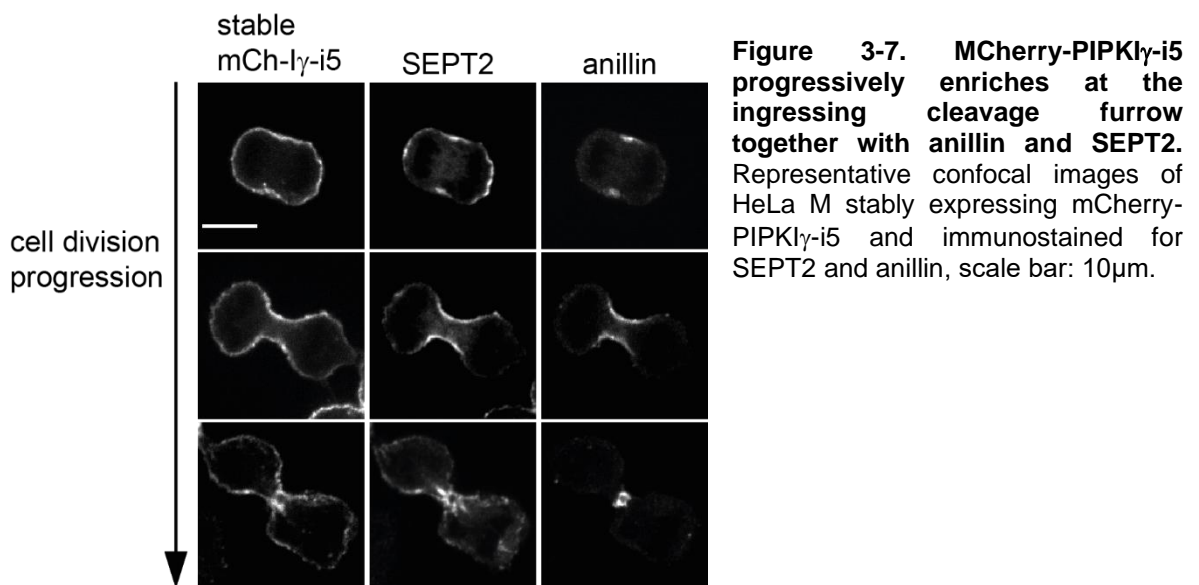


Figure 3-7. MCherry-PIPK γ -i5 progressively enriches at the ingressing cleavage furrow together with anillin and SEPT2. Representative confocal images of HeLa M stably expressing mCherry-PIPK γ -i5 and immunostained for SEPT2 and anillin, scale bar: 10 μ m.

3.2.3. Selective depletion of PIPK γ -i3/i5 phenocopies the cytokinetic defects observed upon depletion of PIPK γ

To test whether the previously described disorganization of anillin and septins at the ICB (**fig. 3-3**) could be ascribed to the septin-binding isoforms of PIPK γ , we selectively depleted PIPK γ -i3/i5.

To achieve this, we first tested the efficiency of a published siRNA targeting the splice insert shared by PIPK γ -i3 and i5 (Sun *et al*, 2013). In collaboration with Prof. Dr. Florian Heyd, we could demonstrate that depletion of PIPK γ -i3/i5 reduced the mRNA levels of i3 and i5 by about 80% (**fig. 3-8-A**) while the expression of the other isoforms (i1/i2/i4) remained unchanged (**fig. 3-8-B**).

Once the efficiency and selectivity of knock-down was established, we assessed the organization of anillin and septins at the ICB.

Upon reduction of PIPKI γ -i3/i5 the percentage of bridges exhibiting compact anillin decreased from 54.7% (control) to 32% (**fig. 3-8-C-D**). Interestingly, through co-labeling of anillin and SEPT6, we could observe that both proteins appeared disorganized, but still colocalized (**fig. 3-8-C**). This suggests that loss of PIPKI γ -i3/i5 did not perturb their interaction. In line with this result, the percentage of SEPT2 at the acetylated tubulin bridge was significantly reduced. Clearly, SEPT2 no longer aligned with MTs along the ICB but rather appeared scattered over a broad area in its proximity (**fig. 3-8-E-F**), similar to what observed upon depletion of all PIPKI γ isoforms (**fig. 3-3-C**). Also SEPT7 and 9 underwent a similar redistribution (data not shown), in line with the hetero-oligomeric nature of septin units assembled into filaments. Depletion of PIPKI γ -i3/i5 also led to disorganization of F-actin that, together with septins, appeared distributed over a wide area at the flanking PMs of the forming daughter cells (**fig. 3-S1**). In control cells instead, F-actin was confined at the two sides of the cytokinetic bridge.

Interestingly, the average length of the acetylated tubulin bridge in control cells was 12.1 μm , while in absence of PIPKI γ -i3/i5 it decreased to 8.9 μm (**fig. 3-8-G**). This small but consistent difference in length could be a consequence of anillin and septin disorganization, in accordance with their role of promoting the maturation and elongation of the ICB (Renshaw *et al*, 2014). Also the MTs bundling factor PRC1, which in control cells interacted and co-aligned with septins (**fig. 3-S2-A-B**), formed a shorter bridge in absence of PIPKI γ -i3/i5 (9.4 μm vs. 6.9 μm) (**fig. 3-S2-C**), thus suggesting a MTs bundling defect within the ICB.

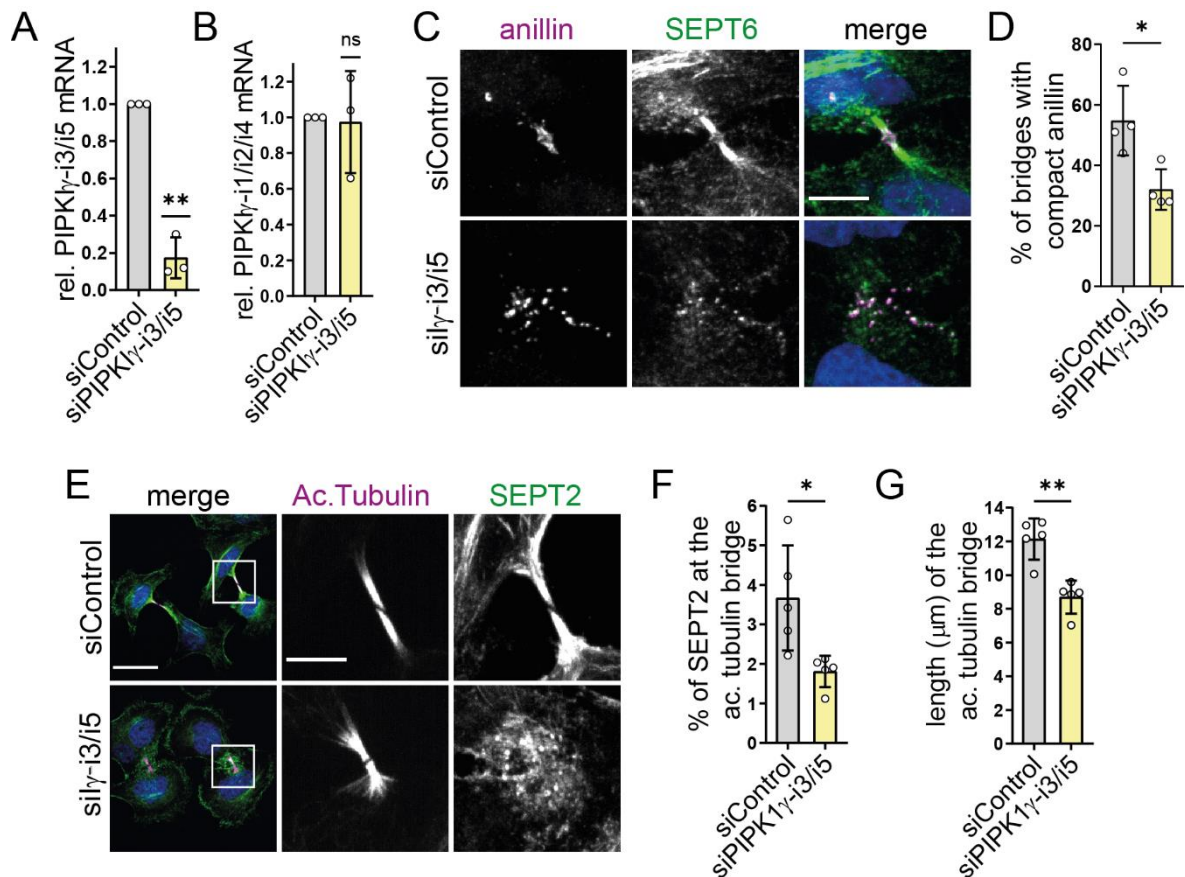
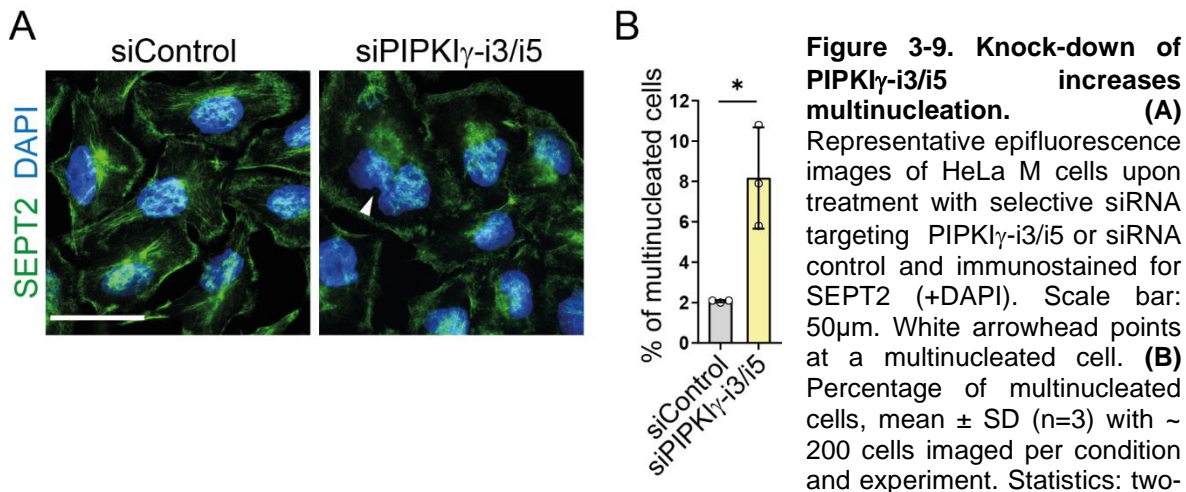


Figure 3-8. Selective knock-down of PIPK γ -i3/i5 affects the organization of anillin and SEPT2, and impairs the elongation of the cytokinetic bridge. (A-B) Expression of PIPK γ isoforms was assessed by radioactive PCRs performed on cDNA synthesized from HeLa M cells treated with siRNA control or targeting the common splicing insert of PIPK γ i3 and i5. Radioactive amplicons were separated and quantified. (A) Expression of PIPK γ -i3+i5 normalized to GAPDH and relative to control. (B) Expression of PIPK γ -i1+i2+i4 normalized to GAPDH and relative to control. (C) Representative confocal images (max. intensity z-projection) of HeLa M cells treated with siRNA control or targeting PIPK γ -i3/i5 and immunostained for anillin and SEPT6 (+DAPI), scale bar: 10 μ m. (D) Quantification of cytokinetic bridges with compact anillin, mean \pm SD (n=4); between 15 and 30 bridges were imaged per condition and experiment. Statistics: two-tailed unpaired t test *P=0.0142. (E) Representative confocal images (max. intensity z-projection) of HeLa M cells treated with siRNA control or targeting PIPK γ -i3/i5 and immunostained for acetylated tubulin and SEPT2 (+DAPI). Scale bar of merge: 30 μ m, scale bar of insets: 10 μ m. (F) Percentage of total SEPT2 at the acetylated tubulin bridge. Quantifications were performed on average intensity z-projections after background subtraction. Data are represented as mean \pm SD (n=5); between 15 and 30 cytokinetic cells were imaged per condition and experiment. Statistics: two-tailed unpaired t test *P=0.0171. (G) Length of the acetylated tubulin bridge was measured as diameter of the ROI delimitating the acetylated tubulin bridge. Data are represented as mean \pm SD (n=5); between 15 and 30 cytokinetic cells were imaged per condition and experiment. Statistics: two-tailed unpaired t test **P=0.0012

Remarkably, depletion of PIPK γ -i3/i5 also caused an increase in multinucleation from 2% (control) to 8.2% (fig.3-9-B). A similar increase was observed upon knock-down of all PIPK γ isoforms (fig.3-4-B) or, according to literature, upon loss of SEPT2, 6 or 9 (Estey *et al*, 2010; Spiliotis *et al*, 2005). Moreover, as observed for the siRNA targeting all PIPK γ isoforms (fig.3-4-A), also in this case the knock-down caused a loss of prominent perinuclear septin fibers (fig.3-9-A).

Together these data demonstrate that the newly identified functions of PIPK1 γ during cytokinesis can be ascribed to its septin binding isoforms PIPK1 γ -i3 and i5, which constitute only a minor fraction of the total pool of PIPK1 γ (Balla, 2013).



tailed unpaired t test *P=0.0136.

3.2.4. Active and septin-binding PIPK1 γ -i5 rescues anillin compactness, SEPT2 accumulation at the cytokinetic bridge and the length of the acetylated tubulin bridge

To corroborate our finding of PIPK1 γ -i3/i5 as novel regulators of late cytokinesis, and to test whether kinase activity and/or septin binding ability are required to carry out this role, rescue experiments were performed. As transient overexpression of PIPK1 γ yielded variable results, and was not well tolerated by cells, we generated cell lines stably expressing mCherry, or mCherry-tagged (siRNA resistant) PIPK1 γ -i5 wild type, K188A (catalytically dead mutant) or Δ SB (septin binding deficient). The cell line expressing mCherry was then treated with siRNA control or targeting PIPK1 γ -i3/i5, while the other lines were treated with siRNA targeting PIPK1 γ -i3/i5. Cells were then synchronized, fixed at telophase and analyzed with regard to the organization of anillin, SEPT2, and the length of the acetylated tubulin bridge. Representative images are shown in **fig. 3-10-A/C**.

Loss of endogenous PIPK1 γ -i3/i5 caused a significant decrease in compact anillin in ICB of cells expressing mCherry (20.9%), mCherry-PIPK1 γ -i5 K188A (29.9%) or mCherry-PIPK1 γ -i5 Δ SB (34.8%). On the contrary, expression of wild type PIPK1 γ -i5 led to 59.8% of bridges displaying compact anillin, a value comparable to control (62%) (**fig.3-10-B**). Based on these results, we drew the following conclusions.

Depletion of PIPKI γ -i3/i5 in presence of mCherry, yielded a similar decrease in anillin compaction as observed in wild type cells (**fig. 3-8-D**), hence excluding the possibility that mCherry alone could attenuate this phenotype. Expression of wild type PIPKI γ -i5 rescued the percentage of bridges displaying compact anillin, thereby proving that the phenotype in question was not an off-target effect of siRNA treatment. Furthermore, the absence of rescue in presence of PIPKI γ -i5 K188A revealed that PIPKI γ does not serve a scaffolding function at the ICB but exerts its role by synthesizing PI(4,5)P₂. Ultimately, since also the PIPKI γ -i5 Δ SB mutant did not rescue anillin compaction, we hypothesize that the interaction between PIPKI γ and septins may serve the anchoring of PIPKI γ splice variants to the ICB and the consequent synthesis of PI(4,5)P₂ at the correct location.

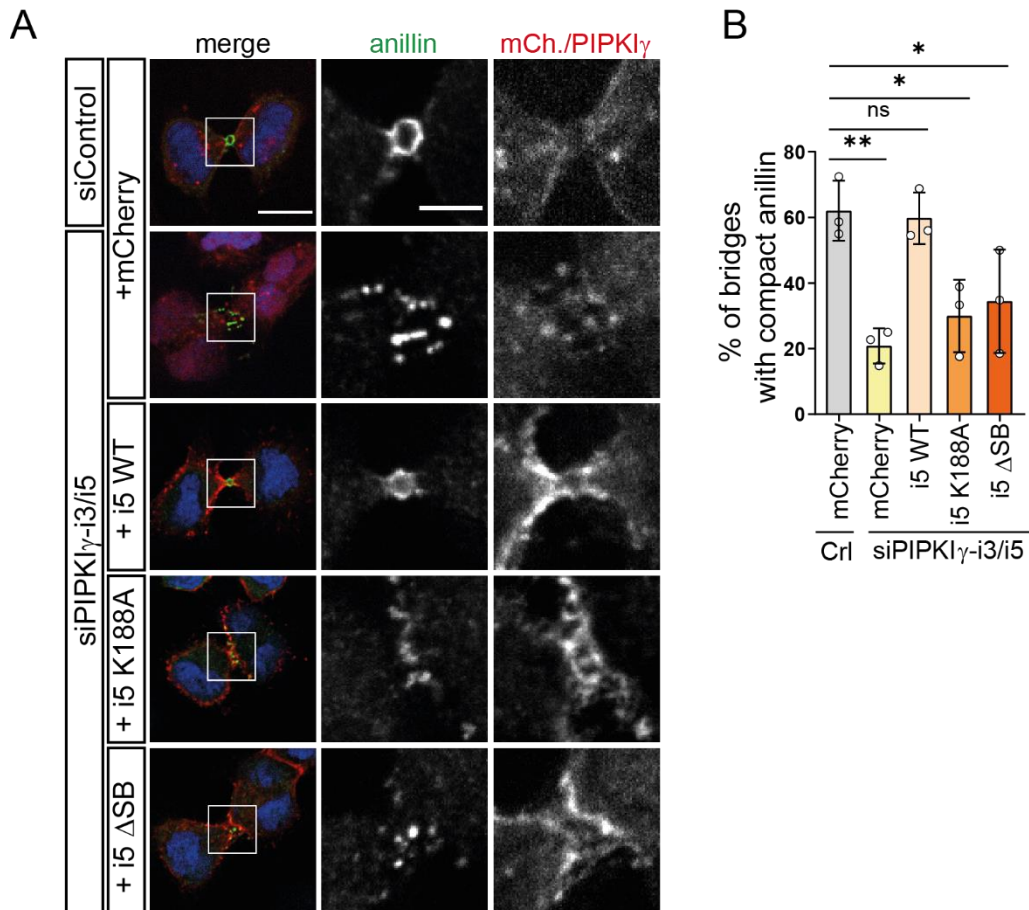
Similar effects were seen with regards to the organization of the septin cytoskeleton. Control cells expressing mCherry displayed 5% of total SEPT2 at the acetylated tubulin bridge (**fig.3-10-D**). Upon knock-down of PIPKI γ -i3/i5, this fraction decreased by half, as observed previously in parental HeLa M cells (**fig. 3-8-F**). The presence of mCherry-PIPKI γ -i5 wild type could rescue this loss (4.3%), while kinase dead or septin binding-deficient kinase variants failed to rescue (2.9%, for both) (**fig. 3-10-D**).

Likewise, expression of mCherry-tagged wild type PIPKI γ -i5, but not of mutant variants, rescued the shortening of the acetylated tubulin bridge observed upon depletion of endogenous PIPKI γ -i3/i5 (**fig. 3-10-E**). Control cells displayed an acetylated tubulin bridge of 12.7 μ m in length that was found significantly shorter upon knock down of PIPKI γ -i3/i5 (9.2 μ m). Cells expressing mCherry-PIPKI γ -i5 wild type exhibited a length of 11.3 μ m, while cells expressing mCherry-PIPKI γ -i5 K188A or Δ SB were only 9.2 μ m or 9.6 μ m in length, respectively (**fig. 3-10-E**).

Fig. 3-10-A/C also show the localization of siRNA resistant mCherry-PIPKI γ i5 variants upon knock-down of PIPKI γ -i3/i5. MCherry-PIPKI γ -i5 wild type concentrated at the bridge, and the bridge itself appeared well constricted around the midbody ring, where also anillin and localized. On the contrary, both, mCherry-PIPKI γ -i5 K188A and Δ SB, appeared distributed over a larger area along the furrow membrane, similar to dispersed SEPT2 or scattered anillin.

In conclusion, PIPKI γ -i5 wild type, but not kinase dead or septin binding-deficient mutants, was able to rescue anillin compactness, localization of SEPT2 on

acetylated MTs and the length of the acetylated tubulin bridge. These results suggest that the regulatory role of PIPK1 γ -i5 during late cytokinesis involves both, the synthesis of PI(4,5)P₂ and the septin binding capability. We hypothesized that the latter is required to confer precise spatiotemporal coordinates to the PIPK1 γ -dependent PI(4,5)P₂ pool at the emerging ICB.



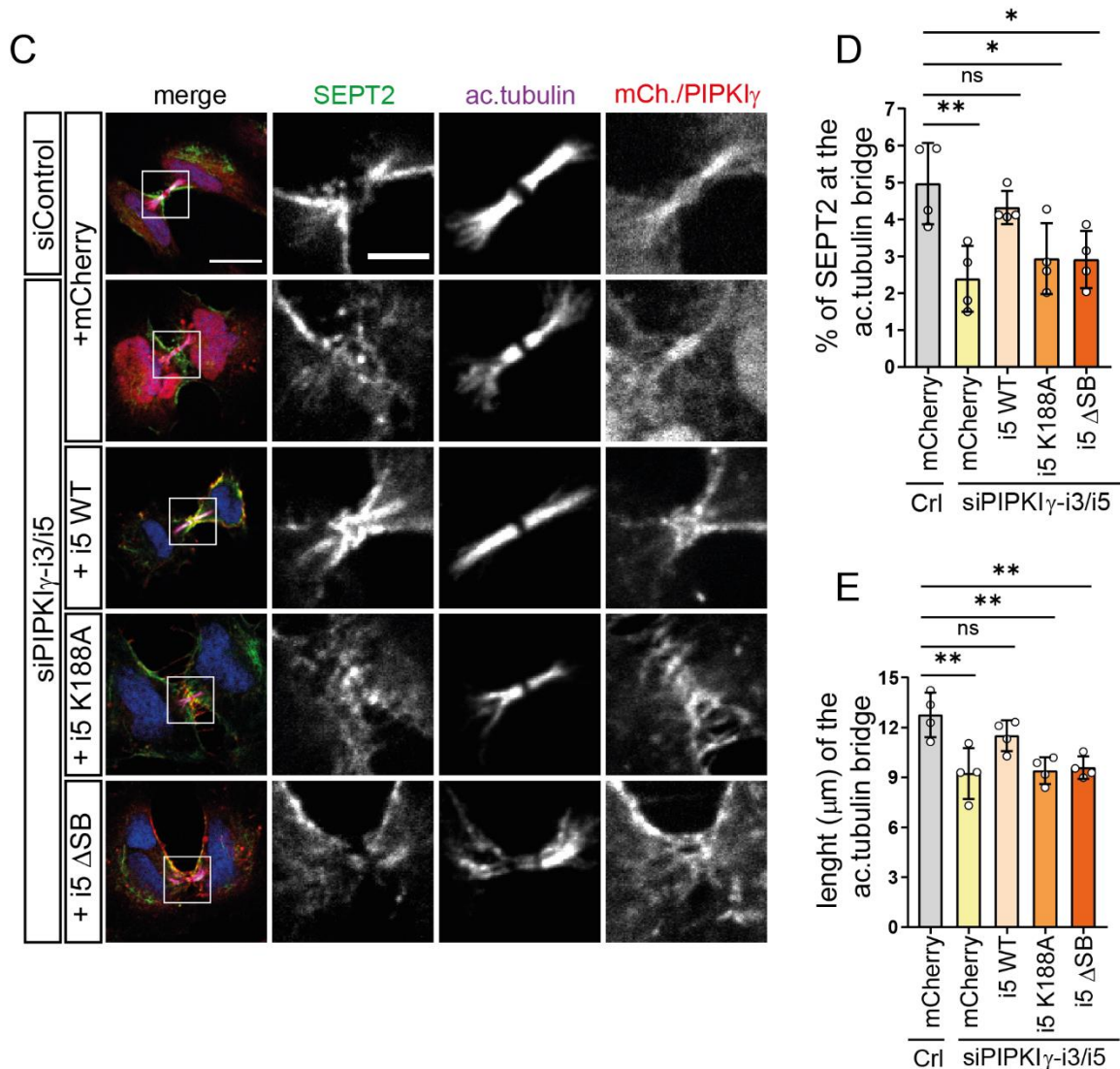


Figure 3-10. PIPK1 γ -i5 wild type, but not kinase dead or septin binding-deficient, rescues anillin compactness, septin accumulation at the bridge and the length of the acetylated tubulin bridge. Knock-down of PIPK1 γ -i3/i5 was performed in HeLa M cells stably expressing mCherry or siRNA resistant mCherry-tagged PIPK1 γ -i5 wild type (WT), kinase dead (K188A) or septin binding-deficient (Δ SB: W646A-Y647A). Resulting phenotypes were compared to those obtained in stable cells expressing mCherry and treated with siRNA control. **(A-B)** Rescue of anillin organization. **(A)** Representative confocal images of cells treated with siRNA control or targeting PIPK1 γ -i3/i5 and immunostained for anillin (+DAPI). Scale bar of merge: 15 μ m, scale bar of inset: 5 μ m. **(B)** Percentage of bridges with compact anillin, mean \pm SD (n=3). 15-30 cytokinetic cells were imaged per condition and experiment. 1way ANOVA followed by Dunnett's multiple comparison test. Adjusted P values: **P=0.0023, ns P= 0.9962, (control vs siPIPK1 γ -i3/i5 + i5 K188A) *P=0.0121, (control vs siPIPK1 γ -i3/i5 + i5 Δ SB) *P=0.0282. **(C-E)** Rescue of SEPT2 accumulation at the bridge and length of the acetylated tubulin bridge. **(C)** Representative confocal images of cells treated with siRNA control or targeting PIPK1 γ -i3/i5 and immunostained for SEPT2, acetylated tubulin (+DAPI). Scale bar of merge: 15 μ m, scale bar of inset: 5 μ m. **(D)** Percentage of total SEPT2 at the acetylated tubulin bridge. Quantifications were performed on average intensity z-projections after background subtraction. **(E)** Length of the acetylated tubulin bridge (max. Feret diameter). Quantifications are represented as mean \pm SD (n=4). 15-30 cytokinetic cells were imaged per condition and experiment. Statistics: 1way ANOVA followed by Dunnett's multiple comparison test. Adjusted P values in D: **P=0.0026, ns P= 0.6814, (control vs siPIPK1 γ -i3/i5 + i5 K188A) *P=0.0156, (control vs siPIPK1 γ -i3/i5 + i5 Δ SB) *P=0.0145. Adjusted P values in E: (control vs siPIPK1 γ + mCherry) **P=0.0015, ns P= 0.3474, (control vs siPIPK1 γ -i3/i5 + i5 K188A) **P=0.0023, (control vs siPIPK1 γ -i3/i5 + i5 Δ SB) **P=0.0036.

3.2.5. Co-depletion of OCRL rescues anillin mislocalization caused by loss of PIPK γ -i3/i5

Our data demonstrate that catalytically active PIPK γ -i5 is required for proper septin organization at the cytokinetic bridge, and for the stable association of anillin at the midbody. To further corroborate that this function is mediated by PI(4,5)P₂ we followed an alternative approach aiming at artificially increasing the levels of PI(4,5)P₂ at the ICB. To this end we depleted OCRL, a 5-phosphatase known to hydrolyze PI(4,5)P₂ upon Rab-35 dependent delivery to the PM of the ICB prior to abscission (Cauvin *et al*, 2016; Dambournet *et al*, 2011). OCRL is required to clear PI(4,5)P₂ from the bridge to facilitate the disassembly of actin filaments and to, thus, prepare for abscission (Dambournet *et al*, 2011). We hypothesized that co-depletion of OCRL with PIPK γ -i3/i5 could restore PI(4,5)P₂ levels, and therefore asked whether it could rescue anillin and SEPT2 organization at telophase.

As depicted in **fig. 3-11-D**, depletion of OCRL by siRNA-mediated knock-down was efficient. Cells were then synchronized, fixed at telophase and immunostained to visualize anillin and SEPT2 (additional immunostaining of PRC1 was used to mark the cytokinetic bridge, not shown) (**fig. 3-11-A**). Knock-down of PIPK γ -i3/i5 reduced the percentage of bridges displaying compact anillin by about half (from 40.7% to 22.7%), as seen before, while co-depletion of OCRL brought this value back to control level (37.7%) (**fig. 3-11-B**). Of note, upon knock-down of OCRL, cells displayed some tendency of increase in compact anillin (48.7%), possibly reflecting increased levels of PI(4,5)P₂ at the bridge that might have hyperstabilized anillin association with the PM (**fig. 3-11-B**).

In case of septins, however, co-depletion of OCRL did not restore SEPT2 levels at the cytokinetic bridge (**fig. 3-11-C**). Although a portion of SEPT2 partially overlapped with “restored” anillin at the midbody, most of it still looked dispersed over a broader area (**fig. 3-11-A**). Additionally, depletion of OCRL alone did not change the localization of SEPT2 compared to control.

This result suggests that in HeLa M septin organization at the bridge is independent of OCRL. A possible explanation could be that OCRL acts downstream and depletes PI(4,5)P₂ at a late stage of cytokinesis, while septin translocation to MTs might be strictly dependent on an earlier pool of PI(4,5)P₂ generated upon furrow constriction. On the contrary, anillin exhibits more plasticity, and its organization might be reversible, according to increased PI(4,5)P₂ availability.

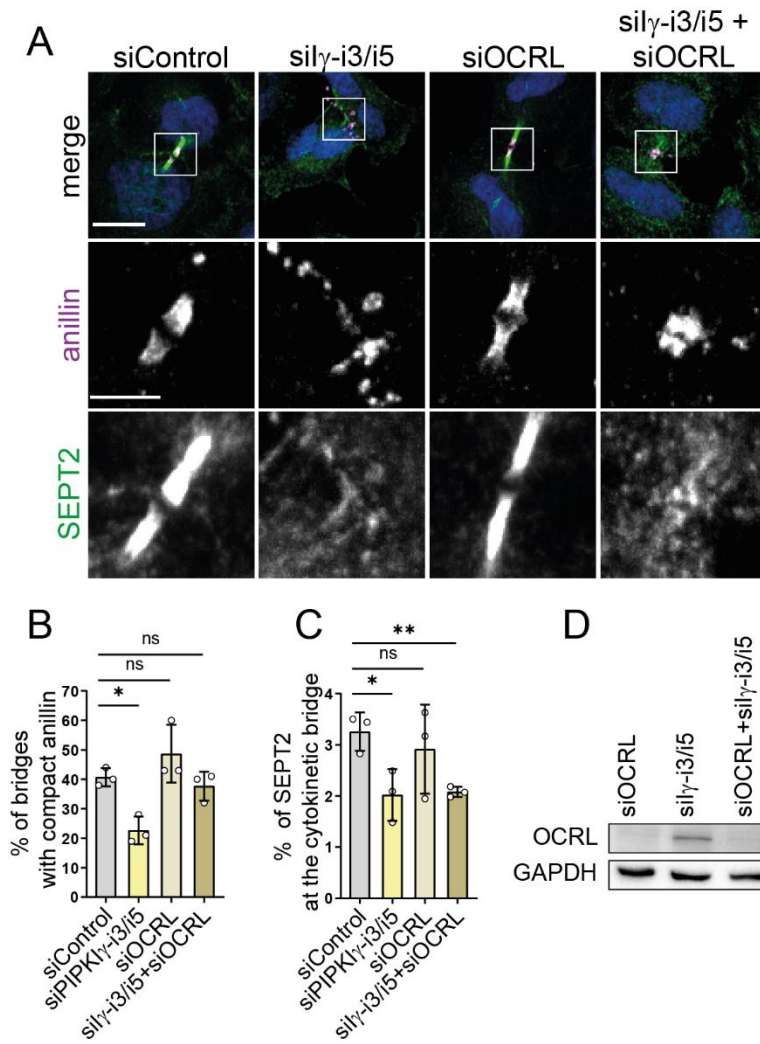


Figure 3-11. Knock-down of OCRL rescues anillin scattering, but not septin enrichment at the bridge, in PIPK γ -i3/i5 depleted cells. (A) Representative confocal images (max. intensity z-projection) of HeLa M upon depletion of PIPK γ -i3/i5, OCRL, or both, and immunostaining of anillin, SEPT2 and of a cytokinetic bridge marker (PRC1, not shown) +DAPI. Scale bar of merge: 15 μ m, scale bar of inset: 5 μ m. **(B)** Quantification of bridges marked by compact anillin, mean \pm SD (n=3); 15-30 cytokinetic cells were imaged per condition and experiment. Statistics: 1way ANOVA followed by Dunnett's multiple comparison test. Adjusted P values: *P=0.0183, (siControl vs siOCRL) ns P= 0.3236, (siControl vs siPIPki γ -i3/i5 + OCRL) ns P=0.8808. **(C)** Percentage of total SEPT2 at the cytokinetic bridge. Quantification was performed on average

intensity z-projections after background subtraction. Mean \pm SD (n=3), between 15 and 30 cytokinetic cells were imaged per condition and experiment. Statistics: two-tailed unpaired t test, *P=0.0274, ns P= 0.5667, **P=0.0063. **(D)** Western blot analysis of cell lysates upon treatment of HeLa M cells with the indicated siRNAs. OCRL: Oculo-Cerebro-Renal syndrome of Lowe, GAPDH: Glyceraldehyde-3-Phosphate Dehydrogenase.

3.3. Septin-associated PIPK1 γ -i3/i5 are required to anchor centralspindlin at the midbody

3.3.1. Depletion of PIPK1 γ -i3/i5 affects the accumulation of the centralspindlin component MKLP1 at the midbody

Upon constriction of the cleavage, furrow PIPK1 γ -i5 localizes to the midbody together with anillin and SEPT2 (**fig. 3-7**). The midbody is a densely packed organelle at the center of the ICB that serves as an anchor between the acetylated tubulin bridge and the PM (Mierzwa & Gerlich, 2014). Tethering between MTs and the midbody PM is achieved by the centralspindlin complex, a heterotetramer formed by two molecules of the kinesin like protein MKLP1 and two molecules of the GAP protein MgcRacGAP. MgcRacGAP contains an atypical C1 domain that binds PI(4)P and PI(4,5)P₂. Notably, mutants defective in phosphoinositide binding do not interfere with early centralspindlin functions (recruitment of Ect2 at anaphase), but lead to poorly understood defects during telophase (Lekomtsev *et al*, 2012).

Interestingly, we found MKLP1, as well as CIT-K (another midbody component) to co-immunoprecipitate with SEPT2 and with PIPK1 γ , hence confirming the localization of the kinase at the midbody (**fig. 3-12-A-B**, a courtesy of Prof. Dr. Michael Krauß). Of note, anillin co-purified only with SEPT2 (**fig. 3-12-A**). This suggests that the interaction between septins and PIPK1 γ is not bridged by anillin.

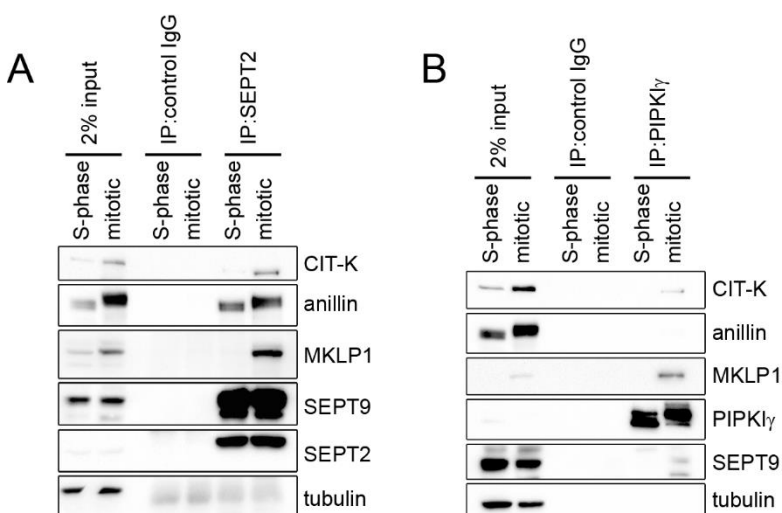


Figure 3-12. Septins and PIPK1 γ form a complex with midbody components.

Western blots analysis showing co-immunoprecipitation of CIT-K, MKLP1 and SEPT9 with SEPT2 (**A**) and PIPK1 γ (**B**) from lysates of synchronized HeLa M. Please note that anillin co-immunoprecipitates with SEPT2 but not with PIPK1 γ . This figure is a courtesy of Prof. Dr. Michael Krauß

Based on the above, we hypothesized that the septin-associated PIPK1 γ -i3/i5 may synthesize a late pool of PI(4,5)P₂ required for the correct organization of the

midbody. To assess that, staining of the centralspindlin component MKLP1 and of CIT-K was performed in control cells and upon knock-down of PIPKI γ -i3/i5 (**fig. 3-13-A**). Depletion of PIPKI γ -i3/i5 did not affect the intensity of CIT-K at the midbody but caused a significant decrease in MKLP1 intensity (**fig. 3-13-B-C**).

Hence, these data revealed a specific defect in the accumulation of the PI(4,5)P₂ effector centralspindlin.

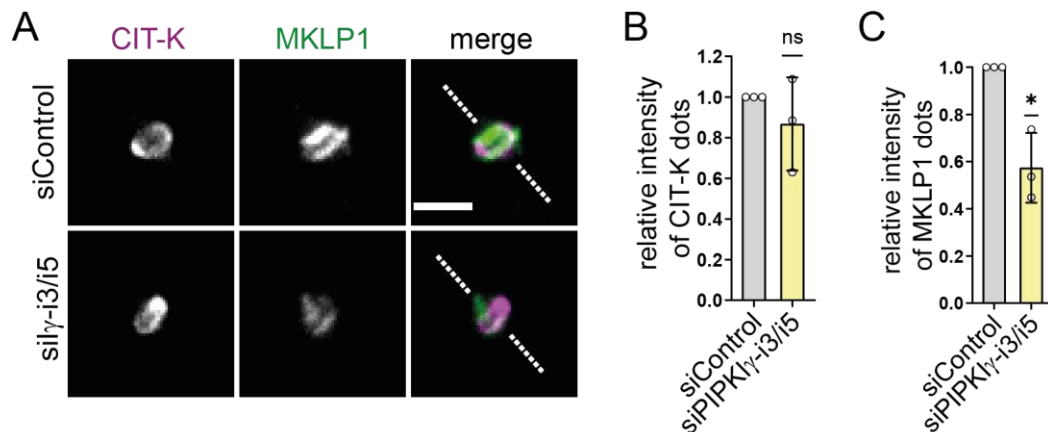


Figure 3-13. Depletion of PIPKI γ -i3/i5 selectively reduces the intensity of the centralspindlin component, MKLP1, at the midbody. (A) Representative confocal images of midbodies upon treatment of HeLa M cells with siRNA control or targeting PIPKI γ -i3/i5, and immunostaining of CIT-K and MKLP1, scale bar: 3 μ m. The dashed line indicates the orientation of the cytokinetic bridge. (B-C) Relative intensity of CIT-K (B) and MKLP1 (C). The quantification was performed on average intensity z-projections after background subtraction. Data are represented as mean \pm SD (n=3) between values normalized to control. 15-30 cytokinetic cells were imaged per condition and experiment. Statistics: two-tailed one sample t test (hypothetical value 1). P value in B: ns P=0.4217, P value in C: *P=0.0214.

3.3.2. MKLP1 accumulation at the midbody requires active and septin-binding PIPKI γ -i5

To confirm the requirement of PIPKI γ -i3/i5 for the accumulation of centralspindlin at the midbody, rescue experiments were performed with the same strategy as described in paragraph 3.2.4. Depletion of PIPKI γ -i3/i5, combined with stable expression of mCherry reduced the relative intensity of MKLP1 by half (0.54) as compared to control (1) (**fig. 3-14-A-B**). This phenotype was partially rescued by the siRNA resistant mCherry-PIPKI γ -i5 wild-type (0.81), but not by PIPKI γ -i5 K188A or Δ SB mutants (0.6 under either condition) (**fig. 3-14-B**). These data confirm the requirement of a catalytically active and septin binding kinase, suggesting a scenario where septins recruit PIPKI γ -i5 (and possibly also -i3) to synthesize a local

pool of PI(4,5)P₂ that maintains centralspindlin at the midbody to ensure anchoring at PM.

Regarding the localization of the kinases (**fig. 3-14-A**), once again PIPK1 γ -i5 wild-type demarcated a well constricted cleavage furrow and localized around the midbody ring and at the two sides. On the contrary, as described in paragraph 3.2.4, PIPK1 γ -i5 mutants distributed over a broader area around the midbody, rich in membrane ruffles or filopodia.

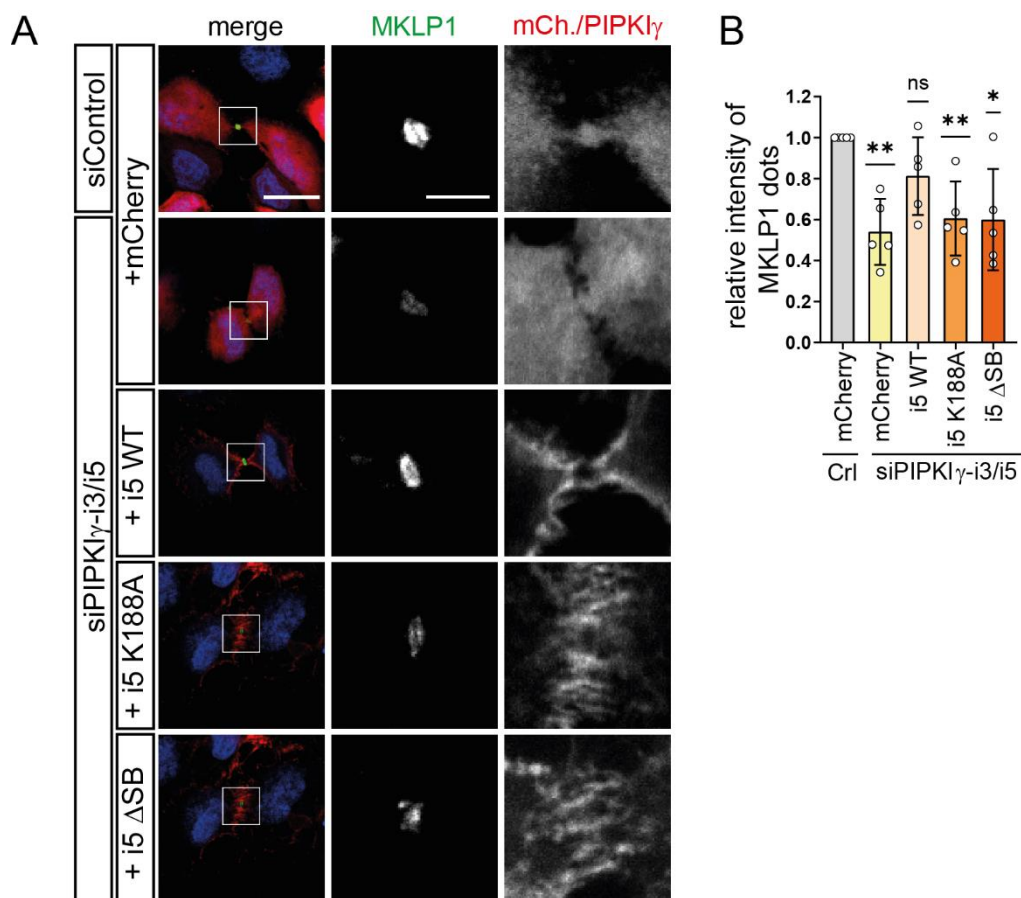


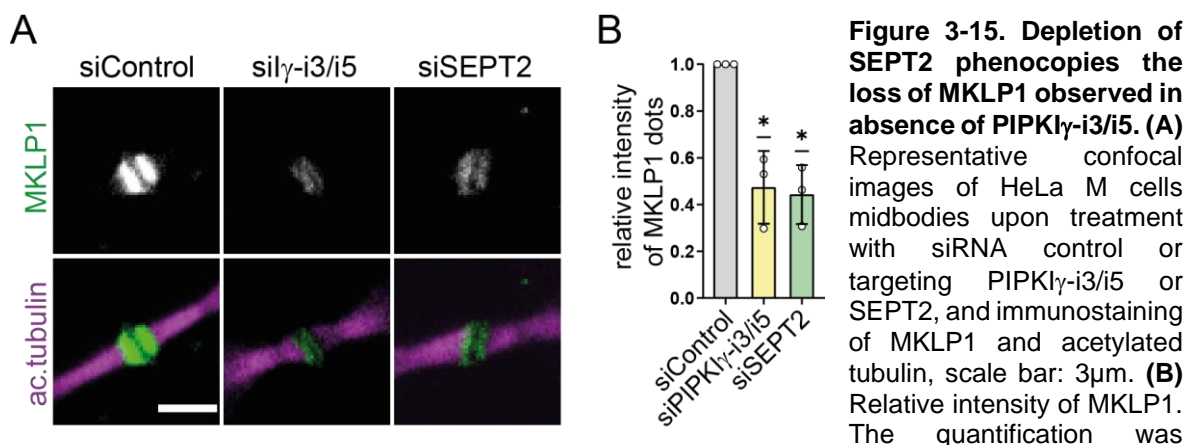
Figure 3-14. PIPK1 γ -i5 wild type, but not kinase dead or septin binding-deficient mutants, rescues MKLP1 accumulation at the midbody. (A) Representative confocal images of HeLa M cells expressing mCherry or mCherry-tagged (siRNA resistant) PIPK1 γ -i5 wild type, kinase dead (K188A) or septin binding deficient (Δ SB) and treated with siRNA control or targeting PIPK1 γ -i3/i5. Cells were immunostained for MKLP1 (+DAPI). Scale bar of merge: 20 μ m, scale bar of inset: 5 μ m. **(B)** Relative intensity of MKLP1. The quantification was performed on average intensity z-projections after background subtraction. Data are represented as mean \pm SD (n=5) between values normalized to control. Between 15 and 30 cytokinetic cells were imaged per condition and experiment. Statistics: two-tailed one sample t test (hypothetical value: 1), mCherry **P= 0.0031, i5 WT ns P= 0.0909, i5 K188A **P= 0.0081, i5 Δ SB *P= 0.0224.

3.3.3. Depletion of SEPT2 phenocopies the loss of MKLP1 observed in absence of PIPKI γ -i3/i5

PIPKI γ -i5 Δ SB failed to rescue the loss of MKLP1 at the ingressed furrow upon knock-down of PIPKI γ -i3/i5. The interaction of PIPKI γ -i3/i5 with septins could, thus, be required to recruit and maintain the kinase in proximity of the forming midbody, as soon as the furrow completes ingression. If this were the case, absence of septins should affect MKLP1 accumulation at the furrow. Indeed, depletion of SEPT2 reduced the relative intensity of MKLP1 at the midbody by half (from 1 to 0.44), a value comparable to the one obtained upon knock down of PIPKI γ -i3/i5 (0.47) (**fig. 3-15-A-B**).

A similar result was observed upon knock-down of SEPT7 (**fig. 3-S5-A-B**), although in this case few cells could be synchronized at telophase. Indeed, SEPT7 plays a pivotal role for the hetero-oligomerization of septins into filaments and its depletion causes extensive cytokinetic defects, as reported by others (Menon *et al*, 2014; Estey *et al*, 2010).

In conclusion, our data demonstrate a role for the septin cytoskeleton in the organization of the midbody, presumably by ensuring the generation of a local pool of PI(4,5)P₂, through the recruitment of PIPKI γ -i3/i5.



performed on average intensity z-projections after background subtraction. Data are represented as mean \pm SD (n=3) between values normalized to control. 15-30 cytokinetic bridges were imaged per condition and experiment. Statistics: two-tailed one sample t test (hypothetical value 1), siPIPKI γ -i3/i5 *P: 0.0279, siSEPT2 *P: 0.0167

3.3.4. Ultrastructure expansion microscopy (U-ExM) confirms defects in centralspindlin accumulation at the midbody upon depletion of PIPKI γ -i3/i5

The midbody organelle encloses highly bundled MT plus-ends deriving from the spindle midzone. These antiparallel MTs are embedded in a dense protein matrix that is hardly accessible to antibodies (Hu *et al*, 2012a). For this reason, in many cases conventional indirect immunofluorescence techniques fail to fully detect midbody-associated proteins. This results in dark gaps, as observed above in the staining of the acetylated tubulin bridge or of MKLP1.

To be able to gain higher-resolution insights into the structures of the midbody and of the cytokinetic bridge, we performed ultrastructure expansion microscopy (U-ExM) in collaboration with Nadja Hümpfer and Prof. Dr. Helge Ewers (Freie Universität Berlin). This technique is based on a physical magnification of the specimen, and allows super-resolved images with a regular diffraction-limited microscope (Gambiarotto *et al*, 2021). In our case, samples were processed according to Gambiarotto *et al.*, 2019, in order to achieve a 4-times isotropic expansion, which was followed by immunostaining and imaging by a conventional confocal microscope. This approach successfully revealed the presence of MTs and of the centralspindlin complex at the midbody (**fig. 3-16-A**).

In both control and PIPKI γ -i3/i5 knock-down cells, the cytokinetic bridge often had the shape of a candy, where antiparallel MTs formed a dense line at the center of the midbody bulge, and the secondary ingression sites were visible at the two sides of the midbody. MKLP1 and MgcRacGAP overlapped with the antiparallel MTs at the midbody center (**fig. 3-16-A**). This localization was expected, considering that MKLP1 has motor activity and, at the onset of anaphase, migrates toward the plus-ends of the spindle MTs and concentrates the centralspindlin complex at the midzone (Glotzer, 2009).

Knock-down of PIPKI γ -i3/i5 resulted in a shorter cytokinetic bridge, in line with previously described data (see for instance **fig. 3-8-G**), but did not affect centralspindlin localization. However, the intensity of MKLP1 significantly decreased upon kinase depletion (from 1 to 0.67, **fig. 3-16-B**), in agreement with previously shown data (see **fig. 3-13-C**). Remarkably, also the intensity of the PI(4,5)P₂-binding subunit MgcRacGAP was significantly reduced from 1 to 0.56 (**fig. 3-16-C**).

Hence, these U-ExM data allowed us to resolve the localization of the centralspindlin complex and confirmed the requirement of PIPK γ -i3/i5 to accumulate MKLP1 and MgcRacGAP at the midbody.

3.3.5. Depletion of PIPK γ -i3/i5 does not impair the formation of a septin double ring at the midbody

Upon furrow closure, septins relocate away from the cleavage furrow to form a double ring at the two sides flanking the midbody. In addition, a subpopulation of septins associates with the MTs of the cytokinetic bridge at portions distal to the midbody (Karasmanis *et al*, 2019). The molecular mechanism underlying this septin remodeling at telophase is only poorly understood. Based on the findings outlined above we speculated that the presence of PIPK γ -i3/i5 at the midbody, and therefore the local synthesis of PI(4,5)P₂, could sustain the formation of membrane-bound septin rings.

To test this hypothesis, we stained for MTs and septins in expanded samples (**fig. 3-16-D**). In control cells, septins were absent from the midbody and localized to parallel MTs within the cytokinetic bridge (**fig. 3-16-D**). On average, 55% of the bridges displayed a double ring adjacent to the midbody (yellow arrowheads), while in 16% of the bridges only one ring was visible (**fig. 3-16-E**). Upon depletion of PIPK γ -i3/i5, septins failed to localize to the tubulin bridge, and were rather dispersed, confirming previous data obtained with regular confocal imaging (see for instance **fig. 3-8-C/E**). U-ExM further revealed that disorganized septins formed rods (green arrowheads) and rings (red arrowhead), possibly associated with the PM (**fig. 3-16-D**, 4X magnification inset). However, in absence of PIPK γ -i3/i5 no major changes in septin rings organization could be detected. The capability of septins to form double rings at the sides of the midbody was only slightly impaired (42% upon knock-down), resulting in a small increase in bridges displaying only a single ring (28%) (**fig. 3-16-E**). The percentage of bridges with no visible septin rings remained comparable between control and PIPK γ -i3/i5 knock-down (29.5% and 27.3%, respectively). Thus, PIPK γ -i3/i5 is required for septin translocation onto MTs, but does not function as a main regulator of the septin double ring formation. **Fig. 3-16-F**, depicts an example of bridges from cells fixed at a later time point during cytokinesis. In control cells, septins were no longer organized into rings flanking the midbody, and exclusively localized on MTs. Upon knock-down of PIPK γ -i3/i5, the

tubulin bridge appeared once again shorter, largely devoid of septins, and septins themselves were rather dispersed distal to the bridge. Though these data do not allow for a direct correlation between the localization of septins and the PM, it becomes clear that septins formed rods and circles that outlined the shape of daughter cells PMs at the two sides of the constricted furrow.

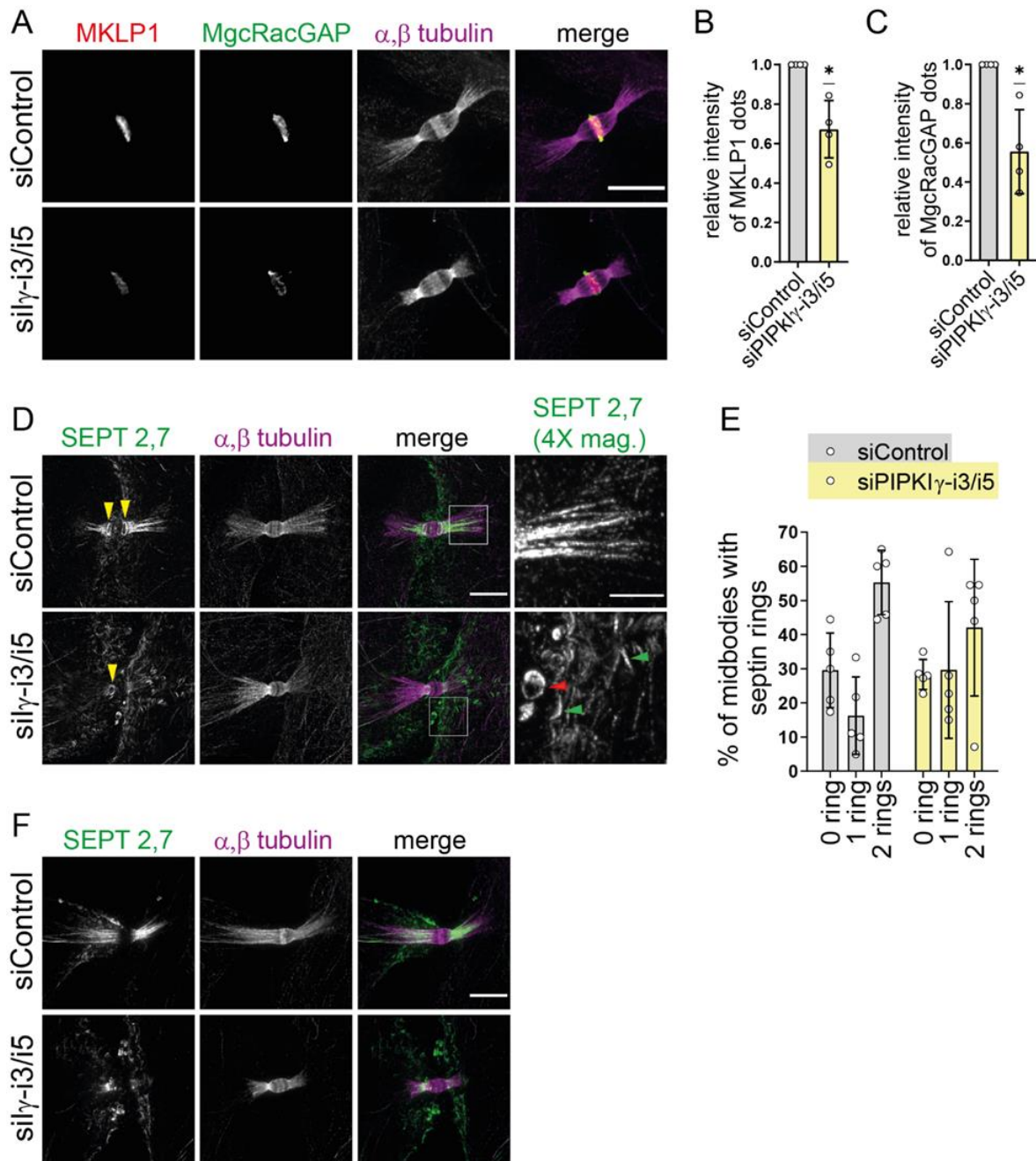


Figure 3-16. Super-resolution of the cytokinetic bridge through ultrastructure expansion microscopy (U-ExM). (A-C) U-ExM confirms a defect in centralspindlin accumulation at the midbody upon depletion of PIPK1 γ -i3/i5. (A) Representative confocal images (max. intensity z-projection) of cytokinetic bridges in specimen derived from expansion microscopy. Cells were treated with siRNA control or targeting PIPK1 γ -i3/i5, fixed, expanded and immunostained for MKLP1, MgcRacGAP, α and β tubulin. Scale bar: 5 μ m. (B) Relative intensity of MKLP1 and (C) MgcRacGAP. The quantification was performed on average intensity z-projections after background subtraction. Data

are represented as mean \pm SD (n=4) between values normalized to control; between 15 and 20 bridges were imaged per condition and experiment. Statistics: two-tailed one sample t test (hypothetical value 1). P values: for MKLP1 *P=0.0203, for MgcRacGAP *P=0.0256. **(D-F)** Depletion of PIPKI γ -i3/i5 affects septin localization on MTs, but not the formation of rings at the two sides of the midbody. **(D)** and **(F)**, representative images of ICBs (two stages of cytokinetic progression) from HeLa M, processed as described in (A) and immunostained for SEPT2 and 7, α and β tubulin. Scale bar: 5 μ m; inset in (D): 1,8 μ m. Yellow arrowheads point at septin rings flanking the midbody. Red and green arrowheads point, respectively, at a small ring or rods formed by disorganized septins upon depletion of PIPKI γ -i3/i5. **(E)** Percentage of midbodies showing zero, one or two septin rings in presence or absence of PIPKI γ -i3/i5. Results are represented as mean \pm SD (n=5); between 15 and 20 bridges were imaged per condition and experiment. To achieve efficient labeling of septins and MTs in expanded samples, SEPT2 was co-stained with SEPT7 and α tubulin was co-stained with β tubulin, respectively.

3.4. PIPKI γ -i3/i5 are dispensable for the synthesis of bulk PI(4,5)P₂ at the cleavage furrow, but regulate the distribution of PI(4,5)P₂ at the ICB

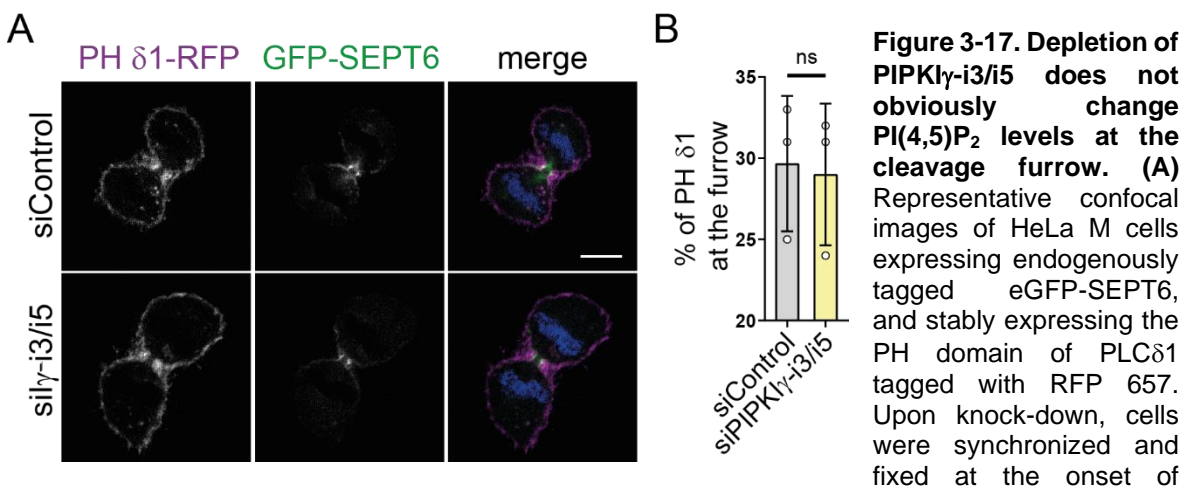
3.4.1. Depletion of PIPKI γ -i3/i5 does not affect bulk PI(4,5)P₂ at the furrow

Our data suggest the requirement of a catalytically active and septin binding PIPKI γ -i5 in the organization of the ICB and midbody. Based on this, depletion of PIPKI γ -i3/i5 should result in a decrease of PI(4,5)P₂ at the cleavage furrow, ideally from the moment on when these isoforms are recruited. According to **fig. 3-7**, PIPKI γ -i5 progressively accumulates at the ingressing furrow to finally outline the midbody ring at telophase. PIPKI γ -i5 recruitment may therefore take place between anaphase and telophase.

In several studies, PI(4,5)P₂ has been indirectly visualized through overexpression of the PH domain of PLC δ 1 (Liu *et al*, 2012; Field *et al*, 2005). In order to quantify the PI(4,5)P₂ levels at the furrow in absence of PIPKI γ -i3/i5, we took advantage of the same probe and stably expressed the domain fused to RFP657 in a eGFP-SEPT6 genome edited cell line (see below). With this strategy, we initially aimed at correlating PI(4,5)P₂ levels with endogenous SEPT6 localization. Unfortunately, however, live cell imaging attempts failed because mitotic cells oscillate between different focal planes, and acquisition of z-stacks resulted in phototoxicity and bleaching. Fixed samples were then preferred and cells were synchronized and fixed at the onset of telophase, when the midbody ring starts to emerge (**fig. 3-17-**

A). In both, control and PIPK γ -i3/i5-depleted cells, about 30% of the PH-PLC δ 1 domain localized at the furrow, revealing no detectable differences between the two conditions (**fig. 3-17-B**). A similar result was obtained upon stable expression of the RFP657-tagged PH-PLC δ 4 domain that exhibits lower affinity to PI(4,5)P $_2$ (Hammond & Balla, 2015) (data not shown). This result could be explained by a wrong guessing of the “time of action” of the PI(4,5)P $_2$ pool synthesized by PIPK γ -i3/i5. However, our data strongly suggest that this pool is essential at the midbody membrane. Indeed, depletion of PIPK γ -i3/i5 affected the accumulation of anillin and centralspindlin at the midbody and the translocation of septins from the cleavage furrow to acetylated MTs flanking the midbody.

Another possible scenario could be the failure of our stable system to reach the emerging midbody membrane due, perhaps, to the crowd of proteins and PI(4,5)P $_2$ -effectors that accumulate within this organelle. Indeed, in **fig. 3-17-A** PH-PLC δ 1 marks a larger membrane area (possibly including filopodia or membrane ruffles) than the midbody ring where PIPK γ -i5 localizes upon furrow ingression (**fig. 3-7**). The enrichment of PI(4,5)P $_2$ detected by the PH-PLC δ 1 may therefore consist of the bulk PI(4,5)P $_2$ synthesized earlier at the cleavage furrow, to which all isoforms of PIPK γ may contribute together with PIPK β (**fig. 3-1** and Emoto et al., 2005).



telophase. Scale bar: 10 μ m. **(B)** Percentage of PH- δ 1 domain at the furrow. Data are represented as mean \pm SD (n=3). 15 - 30 cells were imaged per condition and experiment. Statistics: two-tailed unpaired t test, ns P= 0.8574. ROIs covering the cleavage furrow and the whole plasmalemma were obtained by hand drawing. Of note, in another experiment we used CIT-K as a mask to obtain ROIs outlining exclusively the emerging midbody rings. However, also in this case, the % of the PH- δ 1 at the midbody remained unchanged between conditions (not shown).

3.4.2. Depletion of PIPKI γ -i3/i5 alters the distribution of PI(4,5)P₂ across the ICB

Depletion of PIPKI γ -i3/i5 did not cause a detectable change in PI(4,5)P₂ at the constricted cleavage furrow. We therefore aimed at visualizing PI(4,5)P₂ at the midbody at a later stage, when the ICB has emerged and the bulk PI(4,5)P₂ deriving from the cleavage furrow has supposedly been hydrolyzed or extruded (Renshaw *et al*, 2014; Dambournet *et al*, 2011). Stably expressed PH-PLC δ 1-RFP was poorly enriched at the bridge, resulting in a very dim signal (data not shown). We therefore changed our strategy, and stained for PI(4,5)P₂ with an antibody in control and in PIPKI γ -i3/i5-depleted cells. PI(4,5)P₂ was co-stained with MgcRacGAP, to facilitate detection of the midbody (**fig. 3-18-A**).

In control cells, PI(4,5)P₂ outlined the ICB and was occasionally enriched at the midbody (**fig. 3-18-A**, last two lanes). Upon depletion of PIPKI γ -i3/i5, MgcRacGAP intensity decreased, as expected (in accordance with **figs. 3-13, 3-14, 3-16-A-B**), and PI(4,5)P₂ was distributed over a broader area. More in detail, in kinase-depleted cells the bridge looked wider, and PI(4,5)P₂ was less confined to cortical areas along the ICB. Instead, it was more diffuse, and frequently detected in filopodia in proximity of the bridge. Unfortunately, the marked change of the ICB morphology did not allow us to distinguish between the PI(4,5)P₂ localized at filopodia and the PI(4,5)P₂ at the midbody cortex, where PIPKI γ -i3/i5 presumably function. However, to gain insight in the distribution of PI(4,5)P₂ around the midbody we decided to measure its intensity over a 20 μ m line across the bridge and centered on MgcRaGAP (which was still visible in knock-down samples upon boosting the brightness and contrast). In absence of PIPKI γ -i3/i5 the resulting intensity peaks were broader and further apart than in control cells (**fig. 3-18-B**). This indeed suggests a widening of the bridge at the midbody. Based on this observation we hypothesize that the absence of PIPKI γ -i3/i5 impairs the anchorage of the midbody at the cell cortex.

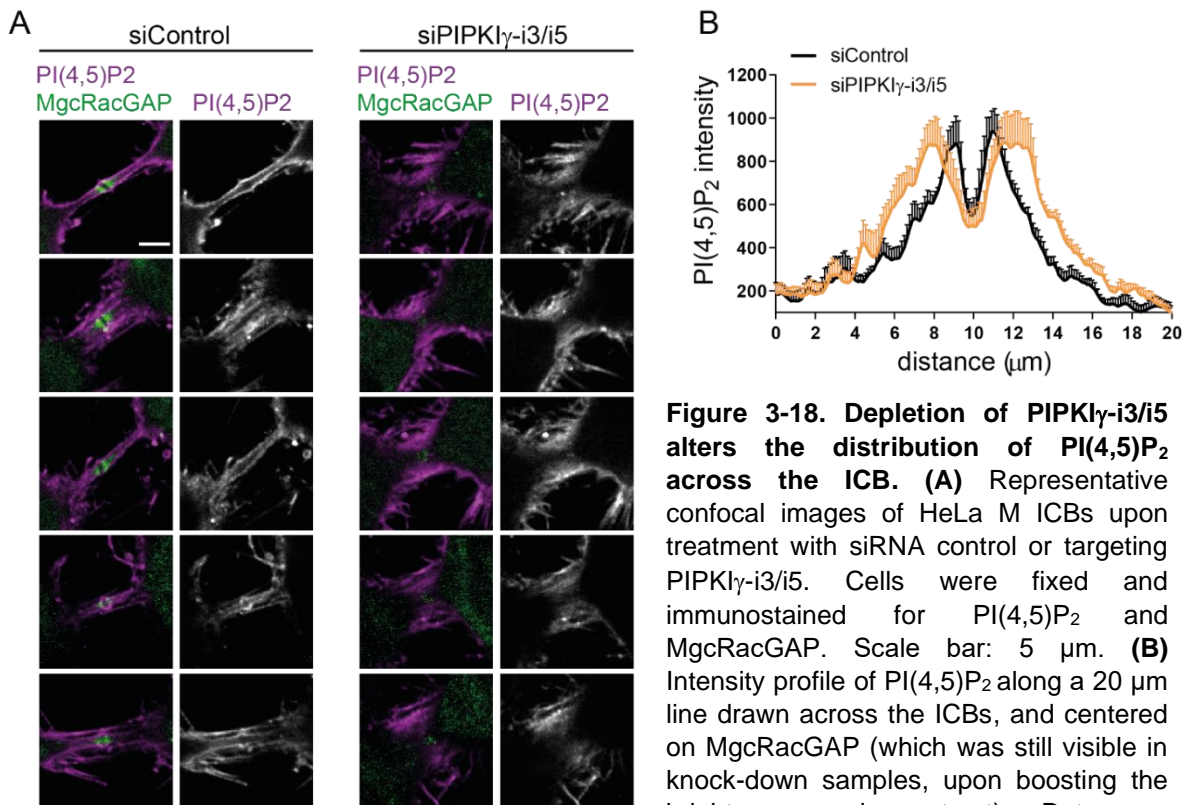


Figure 3-18. Depletion of PIPK 1γ -i3/i5 alters the distribution of PI(4,5)P₂ across the ICB. (A) Representative confocal images of HeLa M ICBs upon treatment with siRNA control or targeting PIPK 1γ -i3/i5. Cells were fixed and immunostained for PI(4,5)P₂ and MgcRacGAP. Scale bar: 5 μm. **(B)** Intensity profile of PI(4,5)P₂ along a 20 μm line drawn across the ICBs, and centered on MgcRacGAP (which was still visible in knock-down samples, upon boosting the brightness and contrast). Data are

represented as mean \pm SEM (n=5). Between 15 and 30 bridges were imaged per condition and experiment.

3.5. PIPK 1γ emerges as a novel key regulator of the septin cytoskeleton

3.5.1. Perinuclear septin fibers derive from the cytokinetic bridge in a PIPK 1γ -i3/i5 dependent manner

Ultrastructure expansion microscopy confirmed a defect in septin localization at the acetylated tubulin bridge in absence of PIPK 1γ -i3/i5 (**fig. 3-16-F-D/F**). Similarly, non-mitotic cells exhibited an altered septin cytoskeleton when depleted of PIPK 1γ or PIPK 1γ -i3/i5 (**fig. 3-4-A** and **fig. 3-9-A**). We therefore hypothesized that the two phenotypes might be interconnected.

To follow septin localization throughout cytokinesis, a knock-in cell line carrying eGFP fused to the N-terminus of endogenous SEPT6 was generated. We chose among the members of the “canonical septin filament” (SEPT2-SEPT6-SEPT7-SEPT9) since antibodies were available that allowed us to confirm their expression and filament-forming capabilities in HeLa M cells (Steffen Restel bachelor thesis).

SEPT6 appeared suitable for genome-editing as all human splice variants share the same N-terminus. Furthermore, contrary to other paralogues, SEPT6 does not play a prominent role during cell division (Joo *et al*, 2007; Spiliotis *et al*, 2005; Menon *et al*, 2014; Estey *et al*, 2010, 2013). Hence, we hypothesized that its tagging would not interfere with cell cycle progression.

Using the CRISPR/Cas9 technology (Ran *et al*, 2013) we inserted a sequence encoding for eGFP and a gly-ser linker right before the start codon of the SEPT6 gene (**fig. 3-19-A**, see Materials and Methods for further details). Screening and characterization of the deriving clonal cell populations was performed by Steffen Restel, whose results are described in his bachelor thesis and therefore not reported here. One heterozygous knock-in clone (#245) was selected as, upon treatment with siRNA against SEPT6, both SEPT6 and eGFP-SEPT6 protein levels decreased (**fig. 3-19-B**). In this cell line eGFP-SEPT6 was successfully incorporated into septin filaments and colocalized with wild type SEPT6 and other septin paralogues (Steffen Restel bachelor thesis).

To visualize and compare septin fibers during cytokinesis, live cell imaging of synchronized cells was performed in control and PIPKI γ -i3/i5-depleted cells. Representative frames are reported in **fig. 3-19-C**. In control cells, eGFP-SEPT6 first accumulated at the cleavage furrow, and then relocated at the cytokinetic bridge (white arrow), where it presumably colocalized with acetylated tubulin. The cytokinetic bridge appeared ~ 30 minutes after completion of furrow ingression, and eGFP-SEPT6 localized there for hours until abscission. After abscission, the daughter cells displayed perinuclear sinuous septin fibers (likely associated with MTs) that seemed to derive from the cytokinetic bridge (red arrowheads).

Upon knock-down of PIPKI γ -i3/i5, eGFP-SEPT6 still localized at the cleavage furrow. However, as division proceeded, it failed to accumulate at the cytokinetic bridge, and the daughter cells lacked the prominent septin fibers observed under control conditions. Occasionally, daughter cells displayed short and straight septin segments, as indicated by yellow arrowheads. Similar observations were made in two other knock-in clones (not shown).

This result suggests that the inheritance of prominent septin fibers possibly requires the association of septins with the cytokinetic bridge. The cytokinetic bridge could act as a “collection point” where septins are gathered through the association with MT bundles and subsequently partitioned between daughter cells. This process is

impaired in absence of PIPK1 γ -i3/i5, possibly due to the failure of septins to translocate onto MTs during cytokinesis.

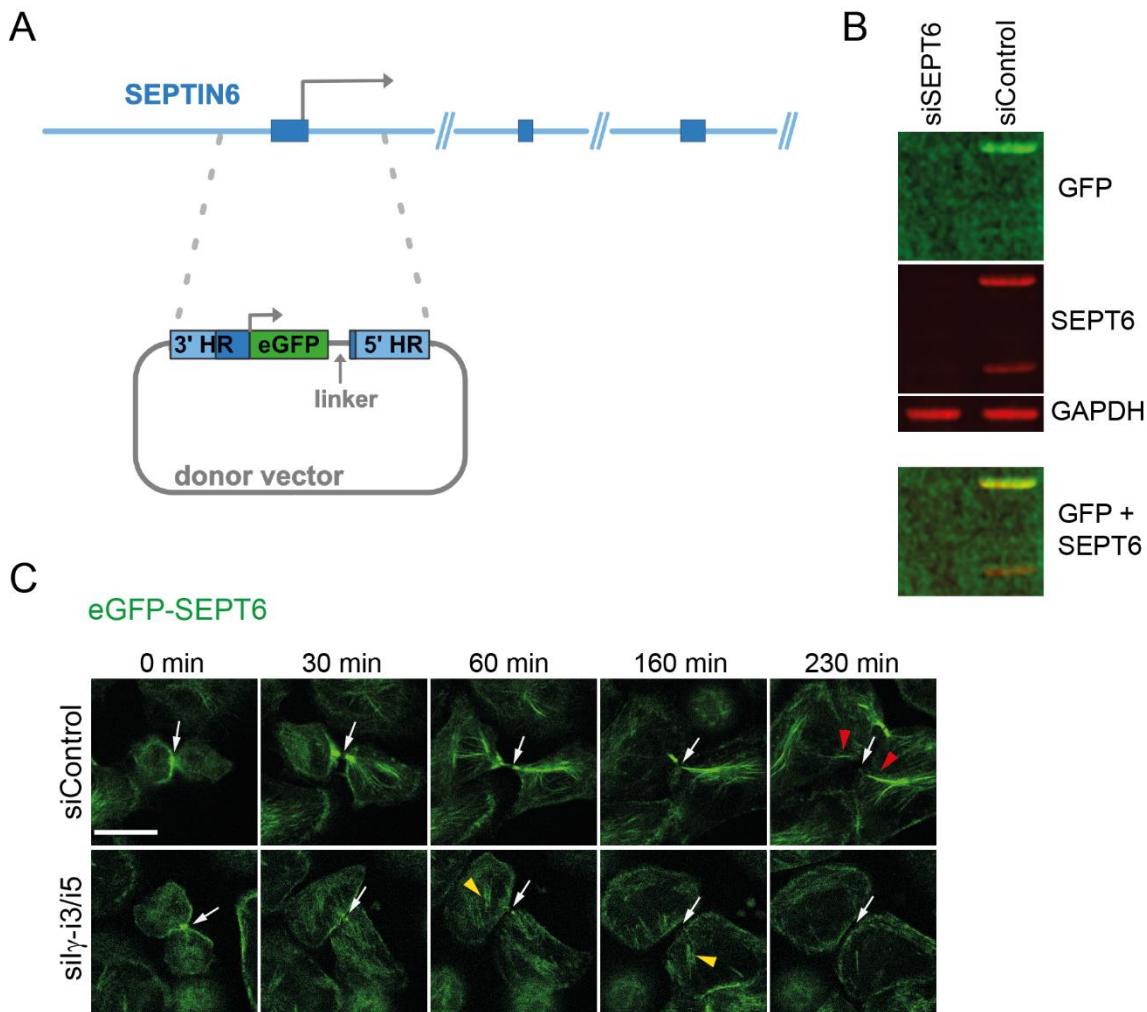


Figure 3-19. Generation and time lapse imaging of an eGFP-SEPT6 knock-in HeLa M cell line throughout cytokinesis. (A) Scheme of the first portion of the SEPT6 gene (blue: exons, light blue: introns) and of the donor vector used to tag the N-terminus of SEPT6 with eGFP via the CRISPR-Cas9 based gene editing. The cDNA sequence of eGFP was inserted between homology regions (HR). The 5' HR anneals with 777 bp of genomic sequence upstream the SEPT6 start codon, while the 3' HR anneals with 896 bp downstream (and including) the start codon. A short linker encoding for gly-ser was inserted between eGFP and the 3'HR. **(B)** Western blot analysis of cell lysates derived from a selected heterozygous knock-in clone (#245) upon treatment with siRNA control or targeting SEPT6. Immunoblot of GFP, SEPT6 and GAPDH (loading control). **(C)** Knock-in clone #245 was treated with siRNA control or targeting PIPK1 γ -i3/i5, synchronized and imaged during cytokinesis by confocal microscopy. Representative frames are shown. Scale bar: 15 μ m. White arrows point at the cleavage furrow/ cytokinetic bridge. Red arrowheads indicate long and sinuous septin fibers visible in control cells. Yellow arrowheads point at short and straight septin segments observed in knock-down cells.

3.5.2. PIPKI γ -i3/i5 regulate the subcellular distribution of septins between MTs and actin filaments

Septins associate with MTs or actin stress-fibers in a cell specific fashion (reviewed in Spiliotis, 2018). Through live confocal imaging of endogenous eGFP-SEPT6, we observed in HeLa M a prevalent pool of sinuous septin fibers that resembled bundled MTs, and in part originated from the cytokinetic bridge. These structures were lost upon depletion of PIPKI γ -i3/i5 (**fig. 3-19-C**).

To see whether these fibers associate with MTs, acetylated tubulin (a marker of bundled MTs, Bulinski et al., 1988) and F-actin were visualized in knock-in cell line #245 upon depletion of PIPKI γ -i3/i5 (**fig. 3-20-A**). In control cells, the sinuous perinuclear septin fibers colocalized with bundled MTs, whereas F-actin showed poor colocalization with septins. In absence of PIPKI γ -i3/i5, however, septin distribution was surprisingly different: they organized in shorter “zig-zag” segments that overlapped with actin stress fibers and showed little overlap with MTs. This observation was not caused by clonal selection, as a similar reorganization was observed in the parental HeLa M cell line (**fig. 3-20-B** and **fig. 3-S3**). Moreover, upon depletion of PIPKI γ -i3/i5, MTs appeared more sparse and buckled (see also **fig. 3-S4**), similarly to what observed by others upon depletion of SEPT2 (Bowen *et al.*, 2011). Accordingly, western blot analysis from cell lysates revealed a tendency of decrease in the fraction of acetylated tubulin over total tubulin upon depletion of PIPKI γ -i3/i5, hence suggesting a defect in MTs stabilization and bundling (**fig. 3-20-C-D**).

The shift of septins from MTs to actin fibers was confirmed also biochemically. Immunoprecipitation of SEPT2 followed by mass-spectrometry analysis showed a loss of interaction with MTs-associated proteins and a gain of interaction with several components of the actin cytoskeleton upon depletion of PIPKI γ -i3/i5 (not shown).

In conclusion, these data show that HeLa M cells display a prominent association of septins with bundled MTs, but, upon depletion of PIPKI γ -i3/i5, the septin cytoskeleton undergoes a profound remodeling and relocates onto actin filaments. This reorganization might be caused, at least in part, by the impaired translocation of septins to MTs upon cleavage furrow closure.

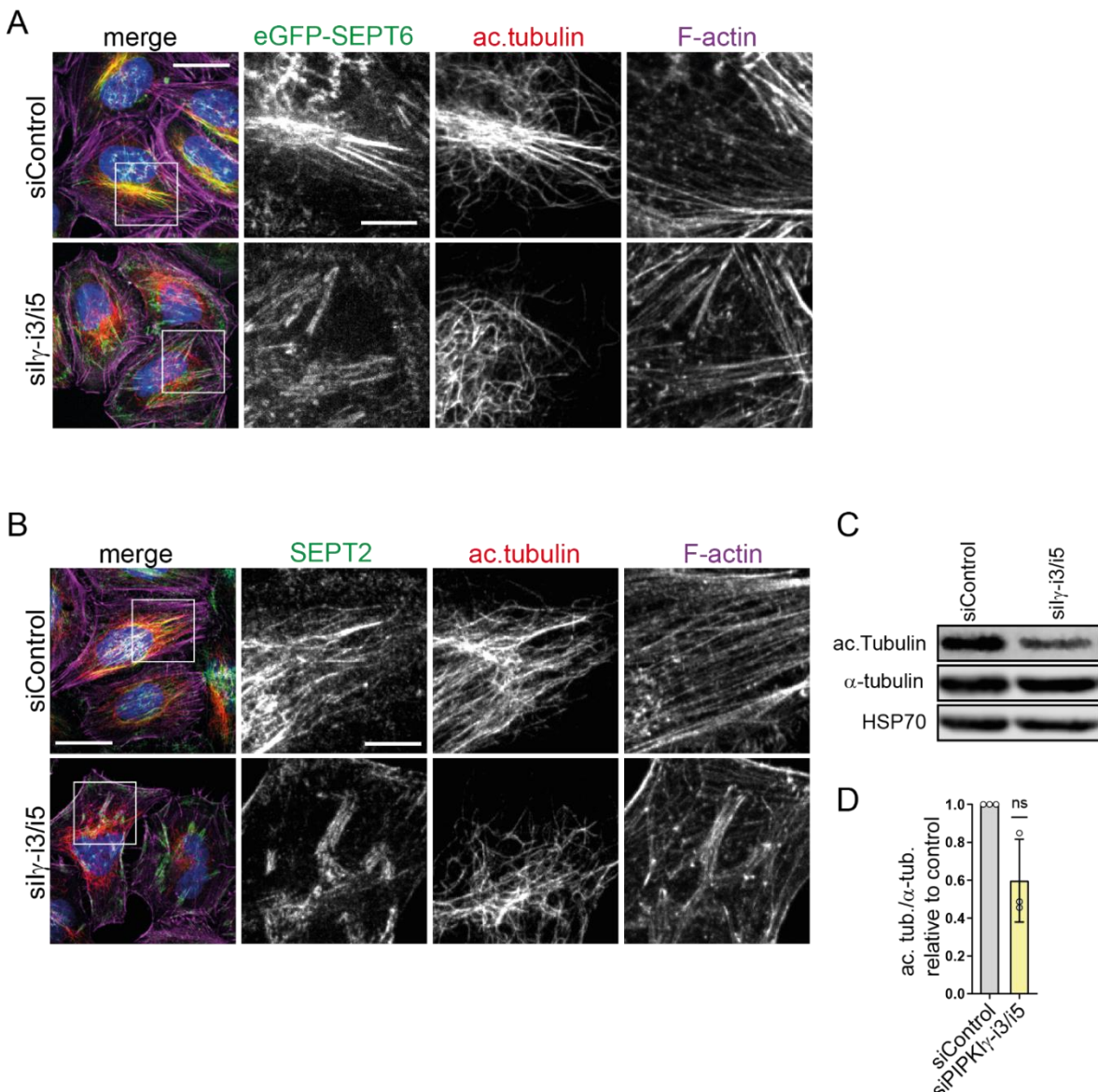


Figure 3-20. Upon knock-down of PIPK1 γ -i3/i5, septins relocate to actin filaments and MT bundling is impaired. (A) Representative confocal images (max. intensity z-projection) of eGFP-SEPT6 knock-in clone #245 upon treatment with control siRNA or siRNA targeting PIPK1 γ -i3/i5. Cells were fixed and stained for acetylated tubulin, F-actin (phalloidin), and with DAPI. Scale bar, 30 μ m; inset, 10 μ m. **(B)** Representative confocal images (max-intensity z-projection) of HeLa M cells, upon treatment with control siRNA or siRNA targeting PIPK1 γ -i3/i5. Cells were fixed and stained for SEPT2, acetylated tubulin, F-actin (phalloidin), and with DAPI. Scale bar, 30 μ m; inset, 10 μ m. **(C)** Representative western blot analysis of acetylated tubulin, α -tubulin and HSP70 (heat shock protein of 70 KDa, used as loading control) from HeLa M cell lysates upon treatment with siRNA control or siRNA targeting PIPK1 γ -i3/i5. **(D)** Ratio between the intensities of acetylated tubulin and α -tubulin bands. Data are represented as mean \pm SD (n=3) between values normalized to control. Statistics: two-tailed one sample t test (hypothetical value: 1), ns P=0.0857.

3.5.3. Depletion of centralspindlin subunits phenocopies the subcellular relocalization of septins observed upon depletion of PIPKI γ -i3/i5

Based on the findings outlined above we hypothesized that the prominent association of septins with MTs in HeLa M cells is established at telophase when, upon furrow closure, septins relocalize from the cleavage furrow onto MTs at the cytokinetic bridge in a PIPKI γ -i3/i5-dependent manner (**fig. 3-8-E** and **fig. 3-19-C**). Loss of PIPKI γ -i3/i5 impairs this process, and consequently prevents the formation of MT-associated septin fibers in non-mitotic cells (**fig. 3-19-C** and **fig. 3-20**).

We found that active PIPKI γ -i5 is required to accumulate centralspindlin at the midbody, likely by providing a local pool of PI(4,5)P₂ (**fig. 3-14**). This is in line with previous studies, which demonstrated that PI(4,5)P₂ is essential to anchor midbody-associated centralspindlin at the PM (Lekomtsev *et al*, 2012). In this scenario, depletion of PIPKI γ -i3/i5 would result in defective centralspindlin anchorage, and increase the distance between MTs and the cell cortex. This would ultimately hamper the translocation of septins onto MTs at the cytokinetic bridge. Accordingly, **fig. 3-18** suggests a wider bridge in absence of PIPKI γ -i3/i5.

To test this hypothesis, we analyzed the colocalization of endogenous eGFP-SEPT6 with acetylated MTs or with F-actin in absence of PIPKI γ -i3/i5, MKLP1 or MgcRacGAP. We used the genome-edited cell line since the fixation conditions to obtain optimal immunostaining of septins and MTs are incompatible. By depleting centralspindlin subunits we aimed at hampering the anchorage of the cytokinetic bridge to the PM at telophase, or at blocking cell division at an earlier stage, in line with the role of centralspindlin at anaphase. In both cases, we expected to destroy the presumed opportunity of septins to translocate onto MTs. As expected, upon depletion of centralspindlin subunits, only few cells reached telophase, hence we focused our studies on non-mitotic cells which often displayed multinucleation, suggesting a failure in cytokinesis.

Although septin filaments appearance and localization varied between cells, cells treated with control siRNA mainly displayed perinuclear sinuous fibers that overlapped with acetylated MTs, while F-actin localized predominantly at the cell periphery (**fig. 3-21-A**). Upon depletion of PIPKI γ -i3/i5, septins reorganized into straight segments co-aligning with actin stress fibers spanning across the cell, and

lost their colocalization with MTs. Knock-down of MKLP1 and MgcRacGAP led to a similar change in the appearance of the septin cytoskeleton. As in absence of *i3/i5*, septins displayed a “zig-zag” pattern, and partially overlapped with actin stress fibers underneath the nucleus (**fig. 3-21-A**).

To obtain a quantitative analysis of the above mentioned septin reorganization, Pearson's correlation coefficients were determined (**fig. 3-21-B-C**). In control cells the Pearson's correlation between eGFP-SEPT6 and acetylated-tubulin was 0.58, indicating a moderate colocalization. Upon depletion of PIPKI γ -*i3/i5*, MKLP1 and MgcRacGAP, this value significantly decreased to 0.37, 0.39 and 0.44, respectively (**fig. 3-21-B**). On the contrary, the Pearson's correlation between eGFP-SEPT6 and F-actin had the opposite trend, starting with 0.14 in control cells and increasing to 0.40, 0.32 and 0.42 in absence of PIPKI γ -*i3/i5*, MKLP1 and MgcRacGAP, respectively (**fig. 3-21-C**).

Although the major remodeling occurred to septins, the appearance of actin and MTs also changed upon depletion of PIPKI γ -*i3/i5*, MKLP1 and MgcRacGAP (**fig. 3-21-A**). In particular, the actin cytoskeleton exhibited an increase in stress fibers (possibly dorsal and ventral, or forming a perinuclear actin cup) extending toward or across the cell center, especially upon depletion of PIPKI γ -*i3/i5*. We confirmed the association of these stress fibers with focal adhesions (**fig. 3-S3**). MTs devoid of septins instead appeared as a tangled web, and the perinuclear bundles were lost in absence of PIPKI γ -*i3/i5* or centralspindlin subunits (**fig. 3-21-A**). More experiment would be required to establish whether and how this reorganization of actin fibers and MTs is linked to septin remodeling.

In conclusion, knock-down of centralspindlin subunits led to a phenocopy of the cytoskeletal remodeling observed in non-mitotic cells depleted of PIPKI γ -*i3/i5*. This result suggests that the loss of septin association with MTs could be caused by the decrease of centralspindlin at the midbody. It remains unknown how centralspindlin coordinates the translocation of septins to MTs. As mentioned before, a possibility could be the anchoring of the cytokinetic bridge to the PM and the providing of a physical vicinity between MTs and cell cortex, where septins initially localize.

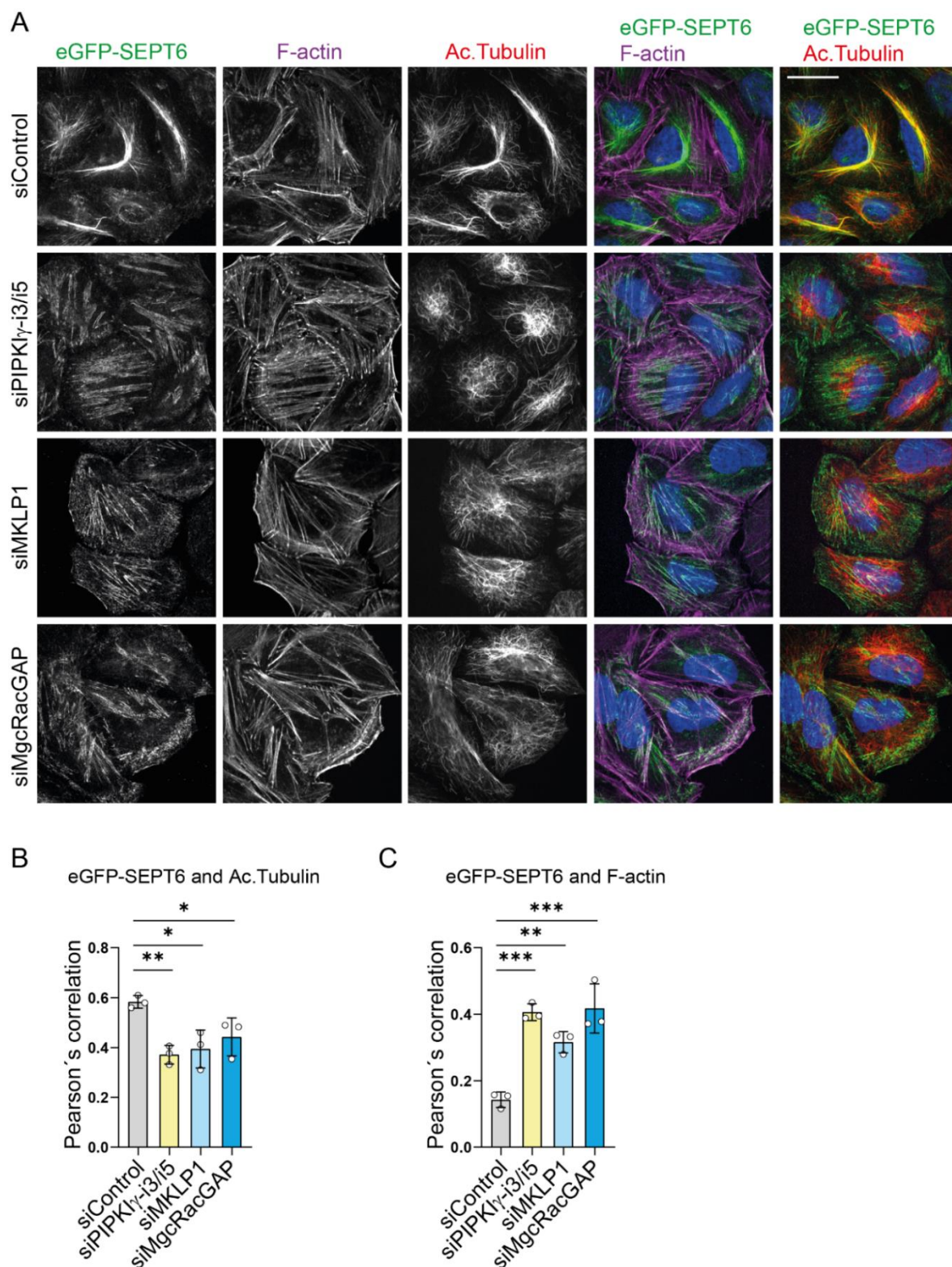


Figure 3-21. Depletion of MKLP1 or MgcRacGAP phenocopies the relocation of eGFP-SEPT6 from MTs to actin stress fibers observed in absence of PIPK1 γ -i3/i5. (A) Representative confocal images of eGFP-SEPT6 knock in cells (#245) treated with siRNA control or targeting PIPK1 γ -i3/i5, MKLP1 or MgcRacGAP, stained with phalloidin and immunostained for acetylated tubulin (+DAPI). (B) Pearson's correlation coefficient between eGFP-SEPT6 and acetylated tubulin. (C) Pearson's correlation coefficient between eGFP-SEPT6 and F-actin. Quantifications were performed with JACoP plugin (Fiji) on confocal images acquired while maintaining the focus on septin structures. Mean \pm SD (n=3); 12 images were analyzed per condition and experiment. Statistics: 1way ANOVA followed by Dunnett's multiple comparison test. Adjusted P values in B: **P=0.0056,

(siControl vs. siMKLP1) *P=0.0107, (siControl vs. siMgcRacGAP) *P=0.0453. Adjusted P values in C: (siControl vs. siPIPKI γ -i3/i5) ***P=0.0002, **P=0.0034, (siControl vs. siMgcRacGAP) ***P=0.0002.

3.5.4. Depletion of PIPKI γ -i3/i5 leads to reduced SEPT6 protein levels

The spatial reorganization of septins during cytokinesis and in interphase, as observed in absence of PIPKI γ -i3/i5, can be also caused by alterations in protein levels of specific septin paralogues. Notably, septin paralogues interact directly and indirectly with other components of the cytoskeleton in a fashion that affects septin localization, MT organization and actin dynamics (reviewed in Spiliotis & Nakos, 2021). We, thus, investigated a potential effect of PIPK I γ -i3/i5 on SEPT2, 6, 7 and 9 protein levels by western-blot analysis of lysates derived from HeLa M cells (parental line) and genome-edited cells (clone #245) (**fig. 3-22-A**). In both cell types, depletion of PIPKI γ -i3/i5 led to a decrease of SEPT6 (or of SEPT6 + eGFP-SEPT6) protein levels to about 0.4 of the corresponding control (**fig. 3-22-B**). Similar observations were made upon treatment with a siRNA that targets all PIPKI γ isoforms (not shown).

This result explains the dimmer eGFP-SEPT6 fluorescence signal we frequently noticed in knock-in cell lines treated with siRNA against PIPKI γ -i3/i5 (compare panels in **fig.3-19-C**). However, the remaining eGFP-SEPT6 translocates onto actin stress fibers as other septins, suggesting that it is still incorporated into filaments (**fig. 3-20** and Steffen Restel bachelor thesis).

Protein levels of SEPT2, 7 and 9 remained unchanged hinting toward a paralogue-specific mechanism. Nevertheless, it is not possible to exclude a change in protein levels of additional septin paralogues, against which antibodies are not available, in particular of other members of the SEPT6 subgroup.

In conclusion, depletion of PIPKI γ -i3/i5 leads to a decrease of SEPT6 protein levels. This could be caused by a change of SEPT6 expression levels, or by a mechanism affecting SEPT6 stability.

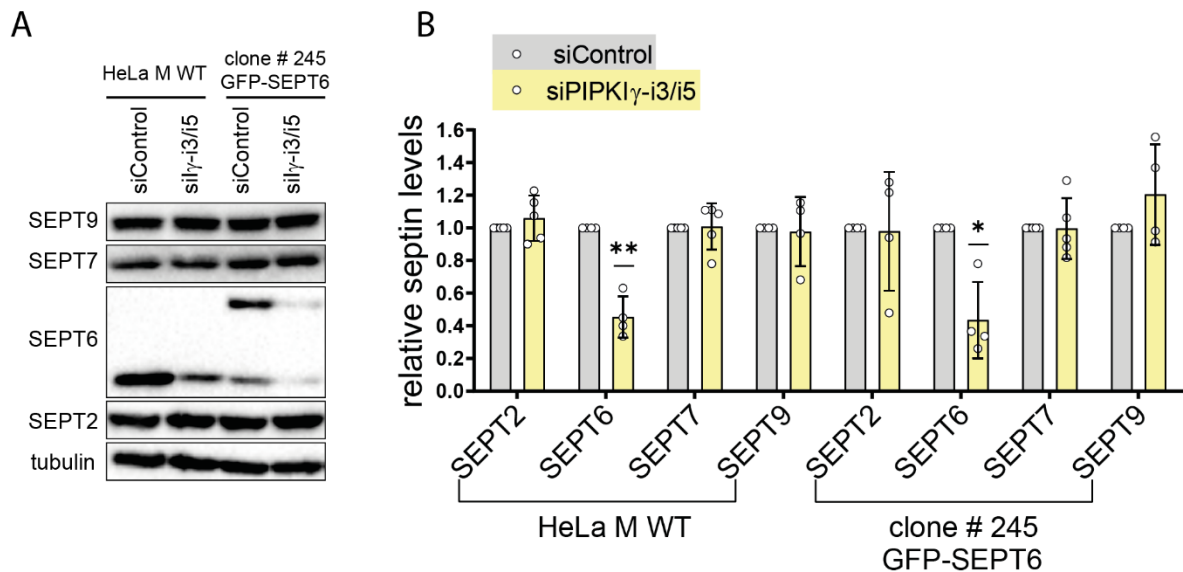


Figure 3-22. SEPT6 protein levels decrease upon knock-down of PIPK1 γ -i3/i5. (A) Representative western blots of septin paralogues derived from lysates of HeLa M cells (wild-type and genome-edited clone #245) upon treatment with control siRNA or targeting PIPK1 γ -i3/i5. **(B)** Quantification of septin levels based on western blots. Each band intensity was normalized to its loading control (α -tubulin). Data are represented as mean \pm SD (n=4 or 5) between values normalized to control (corresponding septin in control treated lysate). Statistics: two-tailed one sample t test (hypothetical value 1). P values for HeLa M (parental): SEPT2 ns P= 0.3958, SEPT6 **P= 0.0033, SEPT7 ns= 0.8937, SEPT9 ns= 0.8414. P values for HeLa M (clone #245): SEPT2 ns P= 0.9157, SEPT6 (sum of wild type and eGFP-tagged) *P= 0.0170, SEPT7 ns= 0.9751, SEPT9 ns P= 0.2750.

3.5.5. Depletion of SEPT6 only partially phenocopies the defects at the cytokinetic bridge observed in absence of PIPK1 γ -i3/i5

Depletion of PIPK1 γ -i3/i5 leads to a decrease of SEPT6 protein levels. This phenotype could be either the cause or the consequence of the septin spatial remodeling, especially of the loss of septin association with MTs, observed in absence of PIPK1 γ -i3/i5. So far, a direct interaction of septins with MTs has only been documented for isoform 1 of SEPT9, which encodes a MT binding domain in its N-terminus (Bai *et al*, 2013; Kuzmić *et al*, 2022). However, a contribution of other septin paralogues cannot be excluded.

We, thus, next evaluated the impact of reduced SEPT6 levels in the organization of the septin cytoskeleton and the appearance of the cytokinetic bridge. Knock-down of SEPT6 led to undetectable levels of SEPT6 by western blot, while knock-down of PIPK1 γ -i3/i5 reduced SEPT6 to about half of the control (**fig. 3-23-A**). Based on this, if absence of SEPT6 were the primary cause of septin disorganization and further cytokinetic defects observed in absence of PIPK1 γ -i3/i5, one would expect stronger phenotypes upon knock-down of SEPT6 as compared to knock-down of the kinase.

Depletion of SEPT6 did not further reduce the percentage of SEPT2 at the acetylated tubulin bridge (**fig. 3-23-C**). Often, indeed, SEPT2 was still spotted at the cytokinetic bridge (indicated by the yellow arrow in **fig.3-23-B**). Furthermore, although depletion of SEPT6 led to a shorter acetylated tubulin bridge compared to control (10.6 μm vs. 12.8 μm , respectively), it did not worsen the phenotype observed in absence of PIPKI γ -i3/i5 (9.8 μm) (**fig.3-23-D**). Interestingly, absence of SEPT6 led to a small but significant increase in the width of the acetylated tubulin bridge compared to control (2.85 μm vs. 2.50 μm , respectively), while depletion of PIPKI γ -i3/i5 did not cause a significant change (2.53 μm) (**fig.3-23-E**). Together these data suggest that the decrease in SEPT6 protein levels is not the primary cause of the defective relocation of septins to bridge MTs and of the shorter cytokinetic bridge observed in absence of PIPKI γ -i3/i5. We further challenged this outcome by assessing MKLP1 levels at the midbody in absence of SEPT6 (**fig. 3-23-F**). Contrary to depletion of PIPKI γ -i3/i5, the knock-down of SEPT6 did not cause a decrease in MKLP1 intensity (**fig. 3-23-G**). Hence, we conclude that the defects observed in absence of PIPKI γ -i3/i5 are not caused by the concomitant decrease of SEPT6 protein levels. Further experiments would be required to unveil the mechanism leading to the downregulation of SEPT6 upon depletion of PIPKI γ -i3/i5.

Fig. 3-23-E suggests a role for SEPT6 in the narrowing of the cytokinetic bridge. Interestingly, depletion of other paralogues, such as SEPT7, did not result in and wider acetylated tubulin bridge (**fig. 3-S5-D**). This, and the fact that SEPT6, contrary to SEPT2 and SEPT7 (**fig. 3-15** and **fig. 3-S5-A-B**), is dispensable for the accumulation of centralspindlin at the cytokinetic bridge, hints toward the intriguing scenario of a SEPT6-specific function during cytokinesis.

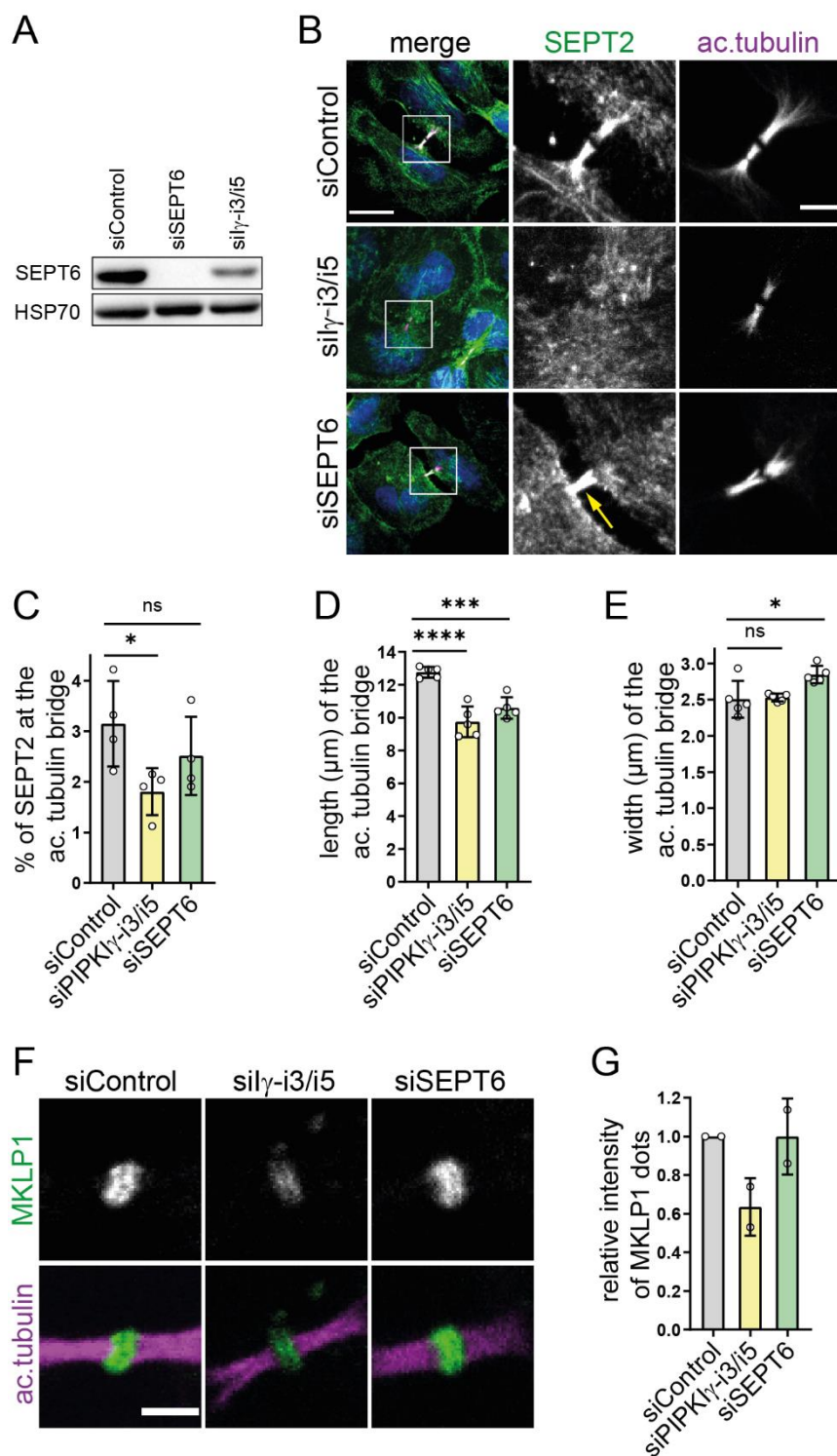


Figure 3-23. Depletion of SEPT6 leads to only a partial phenocopy of PIPKI γ -i3/i5 depletion.

(A) Western blot analysis of SEPT6 levels in HeLa M lysates upon knock-down of SEPT6 or of PIPKI γ -i3/i5.

(B) Representative confocal images (max. intensity z-projection) of HeLa M cells upon knock-down of PIPKI γ -i3/i5 or of SEPT6, and immunostaining of SEPT2 and acetylated tubulin (+DAPI). The yellow arrow points at SEPT2 still enriched at the cytokinetic bridge in absence of SEPT6. Scale bar: 20 μ m; scale bar of the inset: 5 μ m.

(C) Percentage of total SEPT2 at the acetylated tubulin bridge. Quantifications were performed on average intensity z-projections after background subtraction. Values are represented as mean \pm SD (n=4).

(D) Length and (E) width of the acetylated tubulin bridge were measured, respectively, as max. Feret and min. Feret diameter of the ROIs delimiting the acetylated tubulin bridge. Values

are represented as mean \pm SD (n=4). 15-30 cytokinetic cells were imaged per condition and experiment. Statistics: 1way ANOVA followed by Dunnett's multiple comparison test.

Adjusted P values: *P= 0.0459, ns= 0.3832. (F) Representative confocal images of midbodies upon treatment of HeLa M cells with siRNA control or targeting PIPKI γ -i3/i5 or SEPT6 and immunostaining of MKLP1 and acetylated tubulin. Scale bar: 3 μ m.

(G) Relative intensity of MKLP1. The quantification was performed on average intensity z-projections after background subtraction. Data are represented as mean \pm SD (n=2) between values normalized to control. 15-30 cytokinetic cells were imaged per condition and experiment.

are represented as mean \pm SD (n=5). 15-30 cytokinetic cells were imaged per condition and experiment. Statistics: 1way ANOVA followed by Dunnett's multiple comparison test. Adjusted P values for D: ****P<0.0001, *** 0.0006. Adjusted P values for E: ns P= 0.9637, *P= 0.0127. (F) Representative confocal images of midbodies upon treatment of HeLa M cells with siRNA control or targeting PIPKI γ -i3/i5 or SEPT6 and immunostaining of MKLP1 and acetylated tubulin. Scale bar: 3 μ m. (G) Relative intensity of MKLP1. The quantification was performed on average intensity z-projections after background subtraction. Data are represented as mean \pm SD (n=2) between values normalized to control. 15-30 cytokinetic cells were imaged per condition and experiment.

3.5.6. Overexpression of active PIPKI γ -i5 leads to reorganization of septins into rings, independently of its septin binding capability

As outlined above, PIPKI γ -i5 is required to localize septins onto the acetylated tubulin bridge, and this depends on kinase activity, as well as on the enzyme's capability to associate with septins (**fig. 3-10-C-D**). As loss of PIPKI γ -i3/i5 impairs the formation of prominent, MT-associated septin fibers in daughter cells, we speculated that overexpression of PIPKI γ -i5 could result in a gain of such filaments. However, this was not the case. Modest levels of exogenous kinase frequently disrupted septin fibers (not shown). But interestingly, high levels of overexpression led to a re-organization of septins into rings, predominantly residing in the perinuclear area (**fig. 3-24-A**). Rather than the PM, these rings seemed to outline perinuclear vacuoles, where a localized synthesis of PI(4,5)P₂ could recruit septins. More experiments would be required to elucidate the identity of these compartments, however we decided to not pursue this question in this study. Normalized intensity profiles showed partial overlap of the septin rings with overexpressed kinase, and a poor overlap with actin (**fig. 3-24-B-C**). Overexpression of PIPKI γ -i5 Δ SB also caused the formation of septin rings suggesting that this process does not require the interaction between septins and the kinase (**fig. 3-24-D**). However, in the case of PIPKI γ -i5 Δ SB the septin rings appeared slightly more dispersed. Possibly, an initial recruitment of PIPKI γ -i5 wild type by perinuclear septin fibers dictated the localization of PI(4,5)P₂ and the consequent assembly of septin rings at perinuclear sites. By contrast, the mutant incapable of septin binding, PIPKI γ -i5 Δ SB, could synthesize PI(4,5)P₂ over a broader area and consequently yield to septin rings also at the periphery.

When we overexpressed the catalytically inactive enzyme (PIPKI γ -i5 K188A) septin rings did not form, confirming that septin reorganization into rings was the consequence of increased production of PI(4,5)P₂ (**fig. 3-24-D**). Interestingly, PIPKI γ -i5 K188A overexpressed at high levels displayed a dotted pattern and did not colocalize with septin filaments.

Ultimately, upon overexpression of PIPKI γ -i5 the actin cytoskeleton did not undergo a major reorganization, highlighting once more that septins can function independently of actin (**fig. 3-24-D**). Regarding MTs, preliminary observations

revealed an increase in acetylation, but also a change of shape (not shown). More experiments would be required to confirm these findings.

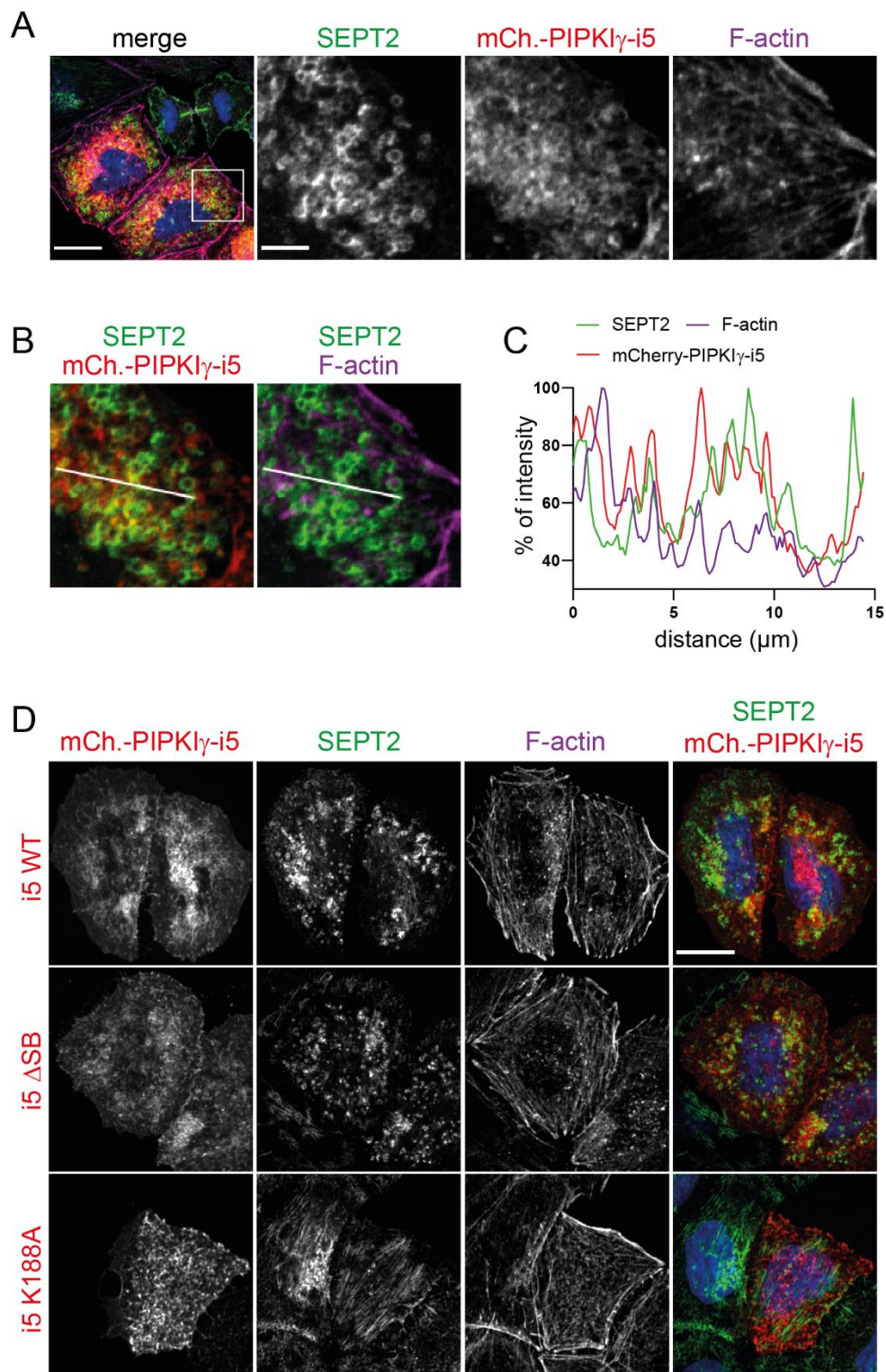


Figure 3-24. Septins reorganize into rings upon high-level overexpression of active PIPK1 γ -i5. **(A)** Representative confocal images (max. intensity z-projection) of HeLa M cells upon high-level overexpression of mCherry-PIPK1 γ -i5. Cells were fixed and stained for SEPT2 and F-actin (phalloidin), +DAPI. Scale bar: 20 μ m, inset: 5 μ m. **(B)** Insets from panel in A, merges between SEPT2 and mCherry-PIPK1 γ -i5, or F-actin. **(C)** Peak-normalized intensity profiles of SEPT2, mCherry-PIPK1 γ -i5 and F-actin along 15 μ m (white line in B). **(D)** Representative confocal images (max. intensity z-projection) upon high-level overexpression of mCherry-PIPK1 γ -i5 wild type, septin

binding-deficient (Δ SB) or kinase-dead (K188A). Active kinase promotes the formation of septin rings, while F-actin is largely unperturbed. Scale bar: 20 μ m.

3.6. Supplementary figures

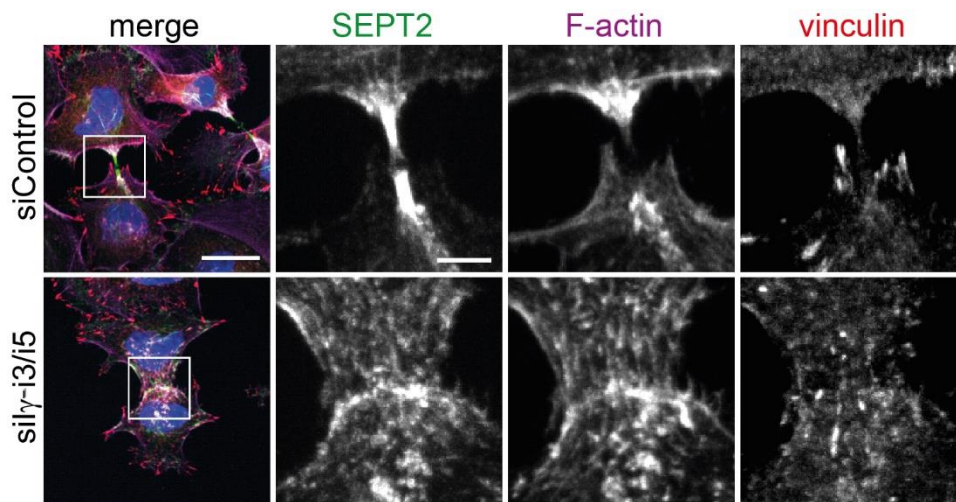


Figure 3-S1. Depletion of PIPK γ -i3/i5 scatters F-actin at the flanking membranes of daughter cells. Representative confocal images (max. intensity z-projection) of HeLa M cells treated with siRNA control or targeting PIPK γ -i3/i5, and stained with SEPT2 and vinculin antibody, and with phalloidin (+DAPI). Scale bar of merge 20 μ m; scale bar of inset: 5 μ m

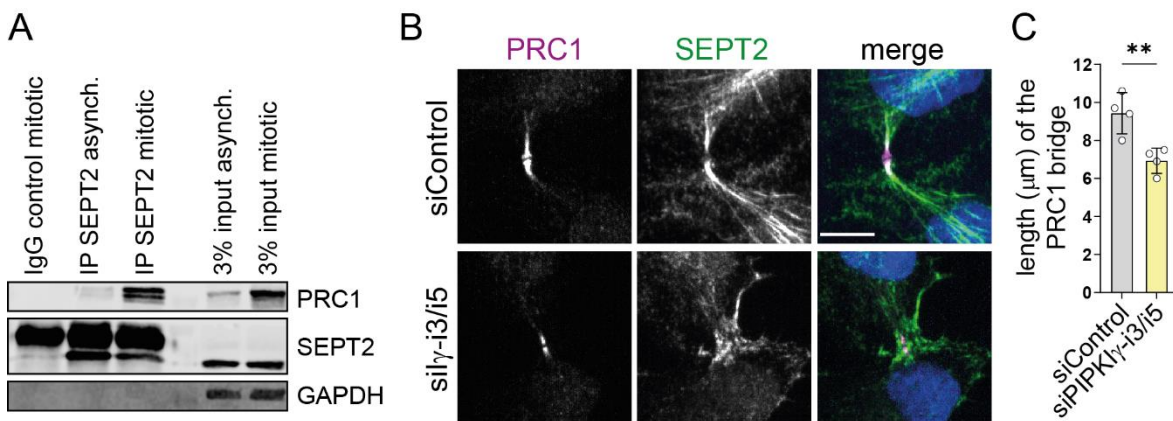


Figure 3-S2. PRC1 interacts with septins during mitosis, and depletion of PIPK γ -i3/i5 affects its distribution along the ICB. (A) Western blot analysis showing co-immunoprecipitation of PRC1 with SEPT2 from lysate of mitotic HeLa M cells. Notably, lysate from cells left asynchronous (“asynch.”) exhibits lower levels of PRC1, which poorly co-immunoprecipitated with SEPT2. (B) Representative confocal images (max. intensity z-projection) of HeLa M cells treated with siRNA control or targeting PIPK γ -i3/i5 and immunostained for PRC1 and SEPT2 (+DAPI). Scale bar: 10 μ m. (C) Length of the PRC1 bridge was measured as max. Feret diameter of the ROI delimitating the PRC1 bridge. Data are represented as mean \pm SD (n=4); between 15 and 30 cytokinetic cells were imaged per condition and experiment. Statistics: two-tailed unpaired t test **P=0.0076.

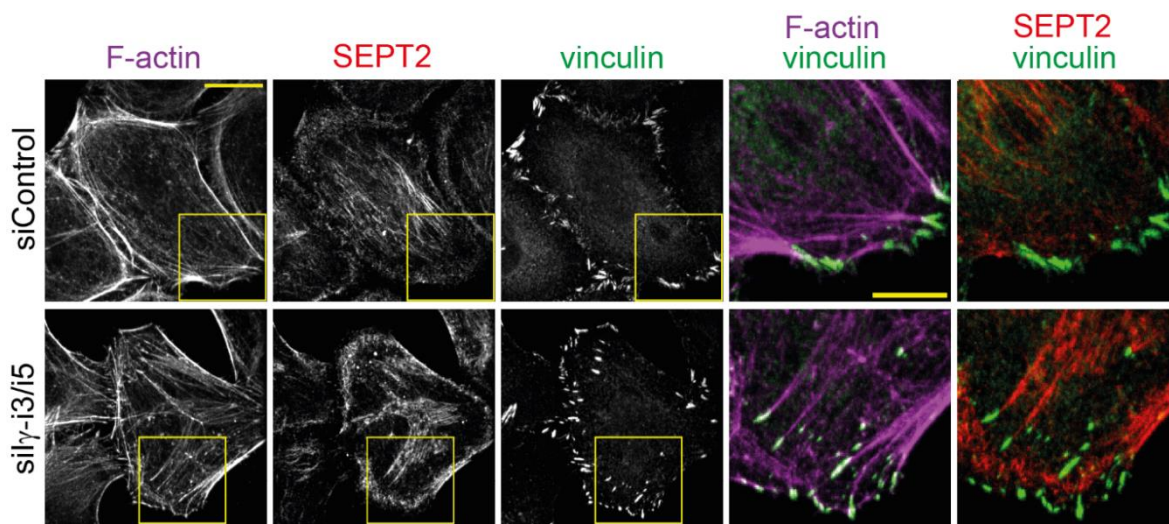


Figure 3-S3. Depletion of PIPK γ -i3/i5 enhances stress fibers across the cell and leads to a redistribution of focal adhesions from the periphery toward the center. Representative confocal images (max. intensity z-projection) of HeLa M cells treated with siRNA control or targeting PIPK γ -i3/i5, and stained with SEPT2 and vinculin antibody, and with phalloidin. Scale bar of merge 20 μ m; scale bar of inset: 10 μ m

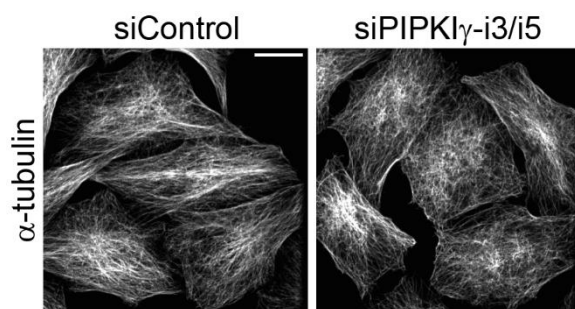


Figure 3-S4. Depletion of PIPK γ -i3/i5 affects MTs organization. Representative confocal images (max. intensity z-projection) of HeLa M cells treated with siRNA control or targeting PIPK γ -i3/i5 and immunostained for α -tubulin. In absence of PIPK γ -i3/i5 MTs become entangled and loose bundling. Scale bar: 20 μ m.

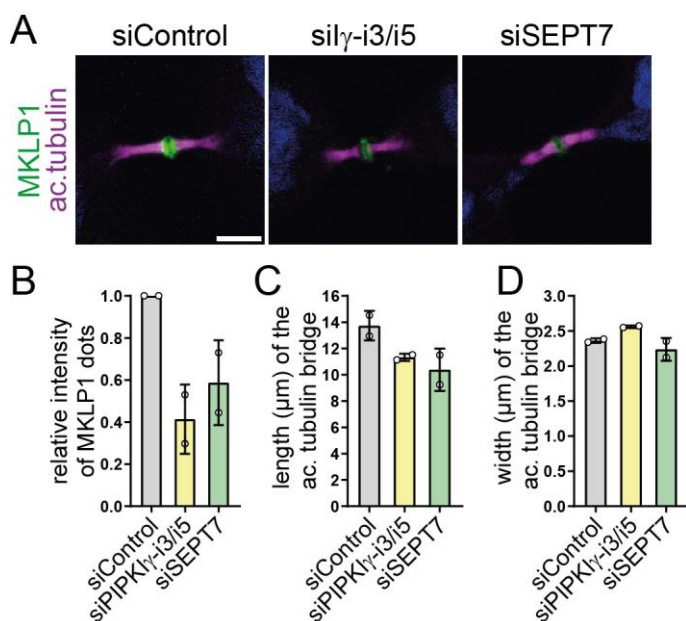


Figure 3-S5. Depletion of SEPT7 phenocopies the loss of MKLP1 and the shortening of the acetylated tubulin bridge. (A) Representative confocal images of cytokinetic bridges upon treatment of HeLaM cells with siRNA control or targeting PIPK γ -i3/i5 or SEPT7 and immunostaining of MKLP1 and acetylated tubulin (+DAPI). Scale bar: 5 μ m. (B) Relative intensity of MKLP1. The quantification was performed on average intensity z-projections after background subtraction. Data are represented as mean \pm SD (n=2) between values normalized to control. 15-30 cytokinetic cells were imaged per condition and experiment. (C) Length and (D) width of the acetylated tubulin bridge were measured, respectively, as max. Feret

and min. Feret diameter of the ROIs delimiting the acetylated tubulin bridge. Values are represented as mean \pm SD (n=2). 15-30 cytokinetic cells were imaged per condition and experiment.

4. Discussion

4.1. The contribution of type I PIP-kinases to cell division

PI(4,5)P₂ builds up at the cleavage furrow and reaches a 4,5 fold increase in concentration by the onset of telophase (Field *et al*, 2005). PI(4,5)P₂ levels at the furrow were manipulated by different approaches, for instance by overexpression of PI(4,5)P₂-sequestering or -hydrolyzing domains, injection of PI(4,5)P₂-specific antibodies, or overexpression of kinase-dead type I PIP-kinases (Field *et al*, 2005; Liu *et al*, 2012; Emoto *et al*, 2005; Abe *et al*, 2012). In all cases, the cleavage furrow displayed marked instability and regressed. This demonstrates that the major role of PI(4,5)P₂ is to anchor the contractile machinery to the PM (Liu *et al*, 2012; Echard, 2012). Nevertheless, the source of this lipid during cell division remained elusive.

Previous studies have shown that type I PIP-kinases are enriched at the cleavage furrow of *Drosophila* S2 cells and at the septum of *S. pombe* (Roubinet *et al*, 2011; Zhang *et al*, 2000). In mammalian cells, Emoto and colleagues have shown that PIPKI β accumulates together with RhoA at the cleavage furrow (Emoto *et al*, 2005). However, this study did not unequivocally reveal a requirement of PIPKI β during cell division, for instance by gene silencing.

By contrast, we assessed the contribution of type I PIP-kinases to the process of cytokinesis by siRNA-mediated depletion of single isozymes, and surprisingly identified PIPKI γ as the major isozyme regulating cell division at late stages.

4.1.1. Both PIPKI β and PIPKI γ contribute to the ingression of the cleavage furrow

To unveil the molecular mechanisms orchestrating PI(4,5)P₂ synthesis during cell division, we selectively depleted each type I PIP-kinase (**fig. 3-1**). We focused on type I PIP-kinases because they are the major source of PI(4,5)P₂ in the cell (Balla, 2013). In fact, among type II PIP-kinases, which also synthesize PI(4,5)P₂, but use PI5P as substrate, only PIPKII α possesses significant catalytic activity, while PIPKII β and PIPKII γ exhibit poor to no activity (Bultsma *et al*, 2010; Bulley *et al*, 2015). Moreover, the total amount of PI(5)P in the cell is only the 0,5 to 2% of PI(4)P (Sarkes & Rameh, 2010), therefore it has been proposed that type II PIP-kinases

function to regulate PI(5)P levels rather than synthesizing PI(4,5)P₂ pools with a precise function (Bulley *et al*, 2015).

Depletion of PIPKI β led to a moderate but significant increase of mitotic cells stalled at a phase that precedes furrow closure (from 2,2% to 3%) (**fig. 3-1-D**), thus supporting the previously proposed role for PIPKI β at the cleavage furrow (Emoto *et al*, 2005; Abe *et al*, 2012). Interestingly, depletion of PIPKI γ led to an even greater increase of early mitotic cells (3,6%), suggesting the contribution of this second isozyme to mediate furrow ingression (**fig. 3-1-D**). Examples of different PIPKI isozymes acting in concert have been previously reported. For instance, PIPKI α and PIPKI γ act in tandem to modulate actin remodeling at the nascent phagocytic cup of macrophages (Mao *et al*, 2009). Moreover, the direct interaction of PIPKI γ with PIPKI β enhances membrane targeting and catalytic activity of the latter (Lacalle *et al*, 2015). Thus, PIPKI β and PIPKI γ may also function as a heterodimeric complex to produce PI(4,5)P₂ at the furrow.

Alternatively, the two isozymes may play a redundant role. Experiments conducted in HeLa showed that knock-down of each PIPKI isozyme causes a change in the expression levels of the other variants (Padrón *et al*, 2003). Interestingly, in our hands, depletion of PIPKI α and PIPKI β led to an increase in PIPKI γ protein levels, but not vice-versa (**fig. 3-1-A**). Thus, in a scenario of functional redundancy between PIPKI β and PIPKI γ at the cleavage furrow, the increase of PIPKI γ protein could help to partially compensate PIPKI β loss, hence explaining the milder phenotype observed upon depletion of PIPKI β compared to depletion of PIPKI γ (**fig. 3-1-D**). Nevertheless, further experiment would be required to clarify the precise contribution of PIPKI β and PIPKI γ at the onset of cell division.

4.1.2. PIPKI γ plays a unique function at the ICB

Interestingly, only depletion of PIPKI γ led to a twofold increase of cells stalled at stages that follow furrow closure (**fig. 3-1-E**), hence pointing at a specific role of this isozyme from telophase on. This result was intriguing since, as outlined in paragraph 1.1.6, several findings suggest the requirement of PI(4,5)P₂ also at the ICB, especially around the midbody. In brief, it is plausible that, as the actomyosin ring progressively disassembles, anillin and/or septins increasingly interact with the PM

by binding to PI(4,5)P₂, and this may underlie their retention at the ICB after cleavage furrow closure.

Presence of PI(4,5)P₂ at the midbody is also required to link the MTs bridge to the PM via the centralspindlin complex (Lekomtsev *et al*, 2012), and for the exocyst-mediated tethering of recycling endosomes (He *et al*, 2007; Maib & Murray, 2022; Frémont & Echard, 2018). Yet, the identification of a possible “late-stage” pool of PI(4,5)P₂ and, especially, its distinction from the bulk PI(4,5)P₂ of the cleavage furrow has been challenging so far. Our new finding of a lipid kinase required to accomplish cytokinesis is a hint in this direction.

Accordingly, depletion of PIPK1 γ disorganized anillin and septins at the ICB (**fig. 3-3**). Anillin recruitment to the cleavage furrow relies predominantly on the binding of PI(4,5)P₂ (Piekny & Glotzer, 2008; Liu *et al*, 2012), and it is probable that also its post-furrowing deposition around the midbody requires PI(4,5)P₂. Thus, the dispersal observed in absence of PIPK1 γ may be caused by insufficient levels of this phosphoinositide at the midbody (**fig. 3-3-A**). 3D-SIM imaging has revealed that membranous tubules containing anillin and septins are extruded during the maturation of the ICB (Amine *et al*, 2013; Renshaw *et al*, 2014). This was likely the reason why only half of the ICBs displayed compact anillin in control cells. Nonetheless, depletion of PIPK1 γ led to a decrease of this percentage from 47% to 16,7% (**fig. 3-3-B**).

Depletion of PIPK1 γ also led to mislocalization of septins, which failed to relocate onto the acetylated tubulin bridge and accumulated at the flanking membranes of the nascent daughter cells (**fig. 3-3-C-D**). How the loss of a putative PI(4,5)P₂ pool can affect the translocation of septins onto MTs will be addressed in detail in section 4.5. Notably, neither depletion of PIPK1 α , nor of PIPK1 β , significantly affected the organization of anillin and septins at the ICB, hence confirming the unique role of PIPK1 γ at cytokinesis (**fig. 3-3**).

Xu and colleagues postulated that PIPK1 γ -i3 restricts centriole duplication at centrosomes (Xu *et al*, 2014). In our hands, depletion of PIPK1 γ led also to a five- and sixteen-fold increase in cells exhibiting a multipolar spindle and multipolar bridge, respectively. This could indeed be caused by centriole overduplication (**fig. 3-3-F-G**). However, as these abnormalities accounted for less than 1% of the total cell population, we suspect that this is not the major cause of the defects described here. Furthermore, also depletion of PIPK1 β resulted in a twofold increase of

multipolar spindles (**fig. 3-3-F**). Multipolar spindles (or bridges) may also derive from cytokinesis failure and consequent generation of tetraploid cells with exceeding centrosomes (Maiato & Logarinho, 2014). Thus, in our case, these abnormalities could be the consequence of furrow or bridge regression in absence of PIPKI β or of PIPKI γ , rather than a direct effect of centriole overduplication.

Another hallmark of cytokinesis failure is multinucleation. Indeed, depletion of PIPKI γ resulted in a significant increase of the percentage of multinucleated cells from 2,37% (in control cells) to 7,3% , while depletion of PIPKI β led only to an increased tendency of multinucleation (4,37%) (**fig. 3-4**). Multinucleation occurs when karyokinesis is not accompanied by successful cytokinesis (Normand & King, 2010). Such a scenario has been observed upon depletion of a wide range of proteins required for the maturation of the cleavage furrow and ICB, such as anillin, septins, centralspindlin, CIT-K, or PRC-1 (Estey *et al*, 2013; Liu *et al*, 2012; Mishima *et al*, 2002; Zhu *et al*, 2006; Gai *et al*, 2011). More importantly, multinucleation is also observed upon manipulation of PI(4,5)P₂ levels at the cleavage furrow (Field *et al*, 2005; Liu *et al*, 2012; Emoto *et al*, 2005; Abe *et al*, 2012). Interestingly, the increase in multinucleation we observed upon depletion of PIPKI γ is in the range of that caused by the depletion of septin paralogues (e.g. SEPT2) (Estey *et al*, 2010; Spiliotis *et al*, 2005; Kinoshita, 2003).

In sum, our findings point toward a major role of PIPKI γ during cytokinesis. PIPKI γ cooperates with PIPKI β during furrow ingression, but unequivocally emerges as the sole isozyme required for post-furrowing events.

4.1.3. The role of PIPKI γ during telophase is exerted by the septin-binding and catalytically active PIPKI γ -i3/i5 splice variants

We found that the post-furrowing function of PIPKI γ is exerted by the septin-binding isoforms PIPKI γ -i3 and i5. Indeed, selective depletion of these splice variants increased multinucleation, and disorganized anillin and septins to a similar degree as depletion of all PIPKI γ transcripts (compare **fig. 3-4** to **fig. 3-9** and **fig. 3-3** to **fig. 3-8**). This demonstrates that the major function of PIPKI γ during cytokinesis is exerted by only a minor pool of splice variants (Balla, 2013). Furthermore, the stable expression of PIPKI γ -i5 wild type, but not of septin binding-deficient (PIPKI γ -i5 Δ SB) or catalytically inactive (K188A) variants, rescued the ICB defects caused by PIPKI γ -

i3/i5 depletion (**fig. 3-10** and **fig. 3-14**). This unequivocally proves that PIPKI γ function during late cytokinesis requires catalytic activity. Additionally, the requirement of septin interaction supports a model according to which septins guide the deposition of PIPKI γ to the nascent midbody, as elaborated in paragraph 4.2.1. In line with this interpretation, PIPKI γ -i5 exhibited a marked colocalization with septins at the midbody ring (**fig. 3-7**), and PIPKI γ co-immunoprecipitated SEPT9, along with other midbody components, during cytokinesis (**fig. 3-12-B**).

Unfortunately, we were not able to carry out many experiments with a stable cell line expressing PIPKI γ -i3, since the expression of this isoform drastically dropped after each passage. However, preliminary results suggested rescues also by PIPKI γ -i3 (data not shown), thus indicating a redundant function of PIPKI γ -i3 and PIPKI γ -i5 during cytokinesis and the ability to compensate for each other loss.

4.2. Spatiotemporal regulation of PIPKI γ during cell division

Type I PIP-kinases are known to synthesize distinct PI(4,5)P₂ pools with well-defined spatio-temporal coordinates (Balla, 2013). This is achieved through the interaction of the lipid kinases with specific partners, which serve as recruiters to distinct subcellular compartments at the appropriate time (Choi *et al*, 2015). Active RhoA has been shown to interact with PIPKI β and PIPKI γ (Weernink *et al*, 2004b). This might, thus, contribute to the recruitment of these PIPKIs to the cleavage furrow. Indeed, PIPKI β colocalizes with RhoA at the cleavage furrow of CHO cells (Emoto *et al.*, 2005).

In this study, PIPKI γ -i5 was found enriched, along with anillin and septins, at the cleavage furrow and midbody ring (**fig. 3-7**), where active RhoA supposedly localizes too (Gai *et al*, 2011; Carim & Hickson, 2023). However, as the septin binding-deficient mutant PIPKI γ -i5 Δ SB was unable to rescue the defects imposed by depletion of PIPKI γ -i3/i5 at telophase, it is evident that RhoA-GTP alone is not sufficient to maintain PIPKI γ at the nascent ICB.

4.2.1. Putative molecular mechanisms underlying the interaction between PIPKI γ -i3/i5 and septins

We found that PIPKI γ -i3/i5 interact with septins through two aromatic residues (Y646 and W647) harbored in the 26-aa splice insert shared by the two isoforms (**fig. 3-5**). This interaction is crucial to exert PIPKI γ function at telophase, as the septin binding-deficient mutant of PIPKI γ -i5 (PIPKI γ -i5 Δ SB) failed to rescue the organization of the ICB and the accumulation of MKLP1 at the midbody (**fig. 3-10** and **fig. 3-14**).

Unfortunately, all attempts to generate antibodies selectively recognizing PIPKI γ i3/i5 failed. However, overexpressed PIPKI γ -i5 co-immunoprecipitated overexpressed septins from Hek cells lysate (**fig. 3-5-D-F**), and an antibody recognizing all PIPKI γ splice variants co-immunoprecipitated SEPT9 from mitotic, but not from interphase HeLa M lysates (**fig. 3-12-B**). Based on these observations, we propose that the expression of PIPKI γ isoforms and/or their interaction with septins may be subjected to mitotic regulation. Further experiments are required to address this question in more detail, for instance by applying select mitotic inhibitors. Nevertheless, **fig. 3-7** demonstrates that by the time that anillin and septins are enriched at the cleavage furrow, PIPKI γ -i5 starts to accumulate at the same site, and ultimately distributes around the midbody. Hence, septins may engage in PIPKI γ -i3/i5 binding during furrow ingression. Notably, this seems to be independent of anillin, as anillin failed to co-immunoprecipitate with PIPKI γ (**fig. 3-12-B**). Our data do not clearly prove a direct interaction between septins and PIPKI γ . In fact, septins might associate indirectly with PIPKI γ -i3/i5, for instance through F-actin, which is abundant at the cleavage furrow. However, we could demonstrate that the septin/PIPKI γ -i3/i5 interaction is also independent of actin, since in NRK cells (which exhibit a predominant association of septins with actin filaments, **fig. 3-6-A**), upon treatment with cytochalasin D actin and septins crumbled into separate rings, while PIPKI γ -i5 remained associated with septins (**fig. 3-6-B-C**). This was observed for PIPKI γ -i5 wild type and catalytically dead (PIPKI γ -i5 K188A) variants, suggesting that the interaction with septins is also independent of kinase activity.

The temporal switch allowing the binding of PIPKI γ -i3/i5 to septins at a certain stage during cytokinesis may consist in a post-translational modification. In line with this interpretation, Schill and colleagues have shown that the Y646 of PIPKI γ -i5 is phosphorylated by the Src tyrosine kinase, and that this modification affects the

interaction with SNX5 on endosomes (Schill *et al*, 2014). Since our data involve this particular residue also in septin binding, it is conceivable that such modification may modulate also the interaction with septins during cytokinesis. Of note, Src activity is required for furrow ingression and successful cytokinesis (Kasahara *et al*, 2007; Tominaga *et al*, 2000; Roche *et al*, 1995).

Phosphorylation by mitotic kinases may also play a regulatory role. For instance, Estey and colleagues have shown that a threonine residue common to SEPT9 long isoforms (T38 in SEPT9-i1) is phosphorylated by cyclin-dependent kinase 1 (Cdk1) (Estey *et al*, 2013). This modification is required for the interaction between SEPT9 and the peptidylprolyl isomerase Pin1, which in turn isomerizes the peptide bond between T38 and P39, thereby inducing a conformational change of the SEPT9 N-terminus (Estey *et al*, 2013). This process is required for abscission; however, the underlying molecular mechanism has remained elusive. Septin PTMs and/or conformational changes, as in the case of SEPT9, may modulate the interaction with PIPKI γ -i3/i5. Of note, several potential phosphorylation sites have been identified on mammalian septins, albeit experimental confirmations are still missing (Hall & Russell, 2004). Yeast and fungal septins are subjected to a wide range of PTMs that regulate their assembly into higher order structures (Hernández-Rodríguez & Momany, 2012). Similarly, during mammalian cytokinesis, PTM-induced septin oligomerization may increase the affinity for PIPKI γ -i3/i5.

It remains unclear whether PIPKI γ -i3/i5 interact with select septin paralogues and whether the interaction is direct. An intriguing possibility could be that the binding of PIPKI γ to adjacent septin paralogues in a septin filament, or bundle, may favor PIPKI γ homo-dimerization and boost its catalytic activity (Lacalle *et al*, 2015). Of note, Kumari and colleagues have recently shown that septins modulate the catalytic activity of a splice variant of dPIP5K, a *Drosophila* phosphatidylinositol 4-phosphate 5-kinase that, as mammalian PIPKI γ , has multiple isoforms and is predominantly expressed in the brain (Kumari *et al*, 2022; Chakrabarti *et al*, 2015). As highlighted in paragraph 1.2.3, distinct interaction partners of PIPKI γ splice variants are PI(4,5)P₂-effectors, hence resulting in the efficient coupling of PI(4,5)P₂ synthesis with its use. For instance, PIPKI γ -i2 contains a 28-aa splice insert that associates with the PI(4,5)P₂-effectors AP2 and talin (Di Paolo *et al*, 2002; Kahlfeldt *et al*, 2010). These interactions target PIPKI γ -i2 to sites of endocytosis and focal adhesions, respectively (Bairstow *et al*, 2006; Ling *et al*, 2002; Thieman *et al*, 2009).

PIP $\text{KI}\gamma$ -i5 instead localizes on endosomes and nascent autophagosomes based on the interaction with SNX5 and ATG14 (Tan *et al*, 2016; Sun *et al*, 2015). At these sites PIP $\text{KI}\gamma$ -i5 synthesizes PI(4,5)P $_2$ pools that serve to modulate the interaction of SNX5 with Hrs, and of ATG14 with VPS34 and Beclin, respectively. Hence, in all these cases, the recruitment of PIP $\text{KI}\gamma$ initiates a feed-forward loop to locally increase the PI(4,5)P $_2$ concentration, and, thus, potentiates effector retention at membrane surfaces (Tan *et al*, 2016; Sun *et al*, 2015). We hypothesize that septins similarly serve to recruit and maintain PIP $\text{KI}\gamma$ -i3/i5 at the ICB as the furrow completes constriction, and at the midbody. Of note, the binding of septins to PI(4,5)P $_2$ is known to regulate their oligomerization into high-order structures (Bertin *et al*, 2010b; Zhang *et al*, 1999), and to increase their capability to deform membranes, a process required for the maturation of the ICB (Tanaka-Takiguchi *et al*, 2009; Beber *et al*, 2019; Carim *et al*, 2020).

4.2.2. Additional tuning of PIP $\text{KI}\gamma$ activity at the midbody

Another key element that may potentially confer spatio-temporal regulation to PIP $\text{KI}\gamma$ -i3/i5 at cytokinesis is ARF6, which is known to bind PIP $\text{KI}\gamma$ and stimulate its activity (Krauss *et al*, 2003). Upon furrow closure, GTP-bound ARF6 binds MKLP1 and localizes to the midbody (Makyio *et al*, 2012). At this site, ARF6 aids the exocyst-mediated docking of recycling endosomes (**fig. 1-5**) and the anchoring of MTs to the PM (**fig. 1-4**), two processes that depend also on PI(4,5)P $_2$ (Mierzwa & Gerlich, 2014; Takahashi *et al*, 2011; Fielding *et al*, 2005). Hence, the localization and activity of PIP $\text{KI}\gamma$ -i3/i5 at the midbody may be further promoted by the local interaction with ARF6. Of note, similar to PIP $\text{KI}\gamma$ depletion, depletion of ARF6 leads to late cytokinetic defects and to a two- to threefold increase in multinucleation (Makyio *et al*, 2012; Schweitzer & Souza-schorey, 2005). Thus, ARF6 and PIP $\text{KI}\gamma$ -i3/i5 may be working within the same pathway to ensure PI(4,5)P $_2$ at the midbody. Additionally, MKLP1 and CIT-K co-immunoprecipitated with PIP $\text{KI}\gamma$ (**fig. 3-12-B**). The interaction with these midbody components may represent an additional mechanism to retain the kinase at the midbody and efficiently couple PI(4,5)P $_2$ synthesis with its usage.

But why would it be so important to ensure the anchoring of PIP $\text{KI}\gamma$ to the nascent midbody? Furrow constriction is accompanied by extrusion of plasmalemmal

tubules. These tubules serve to rapidly remove excess membrane and may contain PI(4,5)P₂, along with septins (**fig. 1-2-B-C**) (Carim *et al*, 2020; Renshaw *et al*, 2014). Therefore, the additional binding of the kinase to midbody components as the membrane narrows down around the ICB, may serve as an additional mechanism to retain PIPKI γ and replenish PI(4,5)P₂ loss.

4.3. PIPKI γ as a novel regulator of the midbody organelle

In this study we unveiled a novel and central role for PIPKI γ during cell division. It does not only synergize with PIPKI β during furrow ingression, but also emerges as the sole isozyme required for later stages of cytokinesis.

Our data suggest that a septin-PIPKI γ module acts as a regulator of midbody integrity. The establishment of the midbody is an important checkpoint during cytokinetic progression. This organelle serves to stably connect the ingressed cleavage furrow with the bundled MTs underneath, and initiates the recruitment of the abscission machinery (Addi *et al*, 2018; Karasmanis *et al*, 2019; Lekomtsev *et al*, 2012). Thus, the correct midbody assembly is of crucial importance for successful cytokinesis. We propose that upon septin-dependent recruitment of PIPKI γ to the forming midbody, PIPKI γ -i3/i5 provide a localized pool of PI(4,5)P₂, which locally enriches anillin and centralspindlin. Additionally, midbody-resident PIPKI γ -i3/i5 may aid the recruitment of recycling endosomes and post-Golgi vesicles that, by delivering selective cargos to the midbody and fusing in its proximity, aid the thinning of the ICB and the recruitment of the abscission machinery. This is schematized in **fig. 4-1** and described in the following paragraphs.

4.3.1. A septin-PIPKI γ -i3/i5 module to localize the synthesis of PI(4,5)P₂ at the midbody and locally retain centralspindlin

At telophase anillin localizes at the midbody and at its flanks (**fig. 1-3-A**) (Renshaw *et al*, 2014; Panagiotou *et al*, 2022). This organization was perturbed upon depletion of PIPKI γ -i3/i5, with a consequent decrease in the percentage of bridges displaying compact anillin (to about half in **fig. 3-8-C-D** or to a third in **fig. 3-10-A-B**). This phenotype was rescued by wild type PIPKI γ -i5, but not PIPKI γ -i5 K188A or PIPKI γ -

i5 Δ SB (**fig. 3-10-A-B**), suggesting that PIPKI γ -i5 synthesizes a pool of PI(4,5)P₂ required for anillin retention at the midbody. Co-depletion of OCRL together with PIPKI γ -i3/i5 rescued anillin compaction at the ICB (**fig. 3-11-A-B**). OCRL is a PI(4,5)P₂-5-phosphatase that is targeted to the ICB by active Rab35 (Dambournet *et al*, 2011), and its co-depletion with PIPKI γ -i3/i5 should ideally restore PI(4,5)P₂ levels at the bridge prior to abscission. This finding, thus, confirms the interpretation that the scattering of anillin was caused by a loss of PI(4,5)P₂ at the midbody (and in its proximity) (**fig. 4-1-A**).

PI(4,5)P₂ at the midbody plasmalemma is also required for the centralspindlin-dependent anchoring of bundled MTs to the ingressed cleavage furrow. Mechanistically, the motor component MKLP1 associates with MTs, while MgcRacGAP interacts with PI(4,5)P₂ (Pavicic-Kaltenbrunner Visnja *et al*, 2007; Lekomtsev *et al*, 2012). Notably, the exchange of MgcRacGAP with mutants incapable of PI(4,5)P₂ binding does not generally perturb the organization of the midzone and furrow constriction, but leads to a moderate widening of the ICB and cytokinesis failure (Lekomtsev *et al*, 2012). Based on this, we hypothesize that the PI(4,5)P₂ pool required for anchoring centralspindlin at the midbody is synthesized by septin-recruited PIPKI γ -i3/i5.

As described in paragraph 4.3.3, we were not able to compare PI(4,5)P₂ intensity around the midbody between control and PIPKI γ -i3/i5-depleted cells due to a redistribution of PI(4,5)P₂ over a broader area in the latter condition (**fig. 3-18**). Notably, however, such redistribution suggests a widening of the ICB, in line with an about 50% loss of both centralspindlin components upon depletion of PIPKI γ -i3/i5 (**fig. 3-13**), as confirmed by U-ExM (**fig. 3-16-A-C**). Specifically, by physical expanding the specimens prior to antibody labeling (Gambarotto *et al*, 2021), we were able to efficiently stain midbody-localized proteins, whose detection by conventional immunofluorescence is otherwise hampered due to their dense packing. In expanded samples, centralspindlin subunits colocalized at the center of the midbody where the antiparallel plus ends of bridge MTs overlapped, in accordance with literature (Hu *et al*, 2012a). In PIPKI γ -i3/i5-depleted bridges, the levels of both MKLP1 and MgcRacGAP were significantly reduced (**fig. 3-16-A**).

Of note, the intensity of MKLP1 was rescued by the expression of PIPKI γ -i5 wild type but not K188A (**fig. 3-14**). Together these data support the hypothesis that the PI(4,5)P₂ pool synthesized by PIPKI γ -i3/i5 is also required for centralspindlin

retention at the midbody (**fig. 4-1-B**), and the consequent anchoring of MTs to the PM. Also in this case, PIPKI γ -i5 Δ SB failed the rescue, consistent with a septin scaffold, guiding the deposition of PIPKI γ -i3/i5 to the nascent midbody. Additionally, the complex formation of both SEPT2 and PIPKI γ with MKLP1 and CIT-K (**fig. 3-12**), supports the hypothesis of a “septin-PIPKI γ module” that localizes at the midbody to ensure midbody integrity. Interestingly, depletion of SEPT2 reduced MKLP1 intensity to the same extent as depletion of PIPKI γ -i3/i5 (**fig. 3-15**). Further experiments are required to determine whether the role of septins is limited to the recruitment of PIPKI γ -i3/i5 to the midbody, or whether septins themselves additionally contribute to centralspindlin recruitment by acting as diffusion barriers, or by directly associating with centralspindlin. Qiu and colleagues have shown that SEPT7 interacts with MKLP2/KIF20A, a mitotic kinesin required for the correct localization of Aurora B, and knockout of SEPT7 depletes MKLP2 from the ICB of neural progenitor cells (Qiu *et al*, 2020; Wu *et al*, 2019). Therefore, it is not unlikely that septins may also directly regulate the localization of MKLP1, hence acting in concert with PIPKI γ -i3/i5 to stabilize centralspindlin.

In order to stably accumulate at the midbody, centralspindlin must multimerize into clusters and this process is spatially regulated (Hutterer *et al*, 2009). In the cytoplasm, 14-3-3 proteins bind MKLP1 and sequester centralspindlin heterodimers into an inactive form incapable of clustering (Douglas *et al*, 2010). Conversely, at the midbody, the interaction of MKLP1 with active ARF6 prevents 14-3-3 proteins from binding, hence allowing a stable association of centralspindlin clusters to the midbody (Joseph *et al*, 2012). Interestingly, in Joseph *et al.*, a mutant of MKLP1 incapable of ARF6 binding exhibited a decreased intensity at the midbody, similarly to what we observed for endogenous MKLP1 upon depletion of PIPKI γ -i3/i5 or SEPT2. Hence, the septin-PIPKI γ -i3/i5 module may contribute to centralspindlin maintenance at the midbody by favoring its clustered conformation. This may be achieved also by fueling a positive feedback loop that maintains ARF6 active (hence capable of binding MKLP1) (**fig. 4-1-B-C**). Of note, the ARF6-specific GEF, EFA6, binds PI(4,5)P₂ and is further activated by this phosphoinositide (Macia *et al*, 2008; Makyio *et al*, 2012; Ueda *et al*, 2013).

Interestingly, depletion of PIPKI γ -i3/i5 did not affect the localization or abundance of CIT-K (**fig. 3-13**). Upon furrow closure, CIT-K is deposited at the midbody in a KIF-14-dependent manner and, at this site, it stabilizes anillin via a direct interaction and

by additionally maintaining active RhoA (Gai *et al*, 2011; Watanabe *et al*, 2013). The observed complex formation between PIPKI γ and CIT-K during mitosis (**fig. 3-12-B**) may indicate an additional mechanism by which CIT-K could regulate anillin retention at the midbody. Surprisingly, however, depletion of PIPKI γ -i3/i5 caused an extensive scattering of anillin (**fig. 3-8-C-D**), despite CIT-K remained in place (**fig. 3-13-A-B**). Furthermore, Watanabe and colleagues have shown that depletion of CIT-K in HeLa cells did not alter MKLP1 localization at the midbody (Watanabe *et al*, 2013) while, as shown here, depletion of PIPKI γ -i3/i5 (and septins) did (**fig. 3-15**). Hence, the septin-PIPKI γ module identified in this study likely represents a novel and independent mechanism to ensure the deposition of PI(4,5)P₂ effectors (anillin and centralspindlin) at the midbody.

4.3.2. PIPKI γ may contribute to abscission by orchestrating vesicle delivery to the midbody

Multinucleation is a hallmark of cytokinesis failure that occurs when the ICB fails to mature, and as a consequence the ingressed cleavage furrow regresses (Emoto *et al*, 2005; Field *et al*, 2005; Liu *et al*, 2012; Lekomtsev *et al*, 2012; Gai *et al*, 2011). Depletion of PIPKI γ (and of PIPKI γ -i3/i5) led to a four-fold increase in the percentage of multinucleated cells (from ~2% in control, to ~8%) (**fig. 3-4** and **fig. 3-9**). This is consistent with the observed defects in midbody integrity, which could ultimately cause defective anchoring of the cleavage furrow and regression of the bridge.

Additionally, depletion of PIPKI γ was accompanied by a two-fold increase in the percentage of cells displaying an acetylated tubulin bridge (**fig. 3-1-B/E**), hence stalled at late telophase. This suggests a defect also in the process of abscission. Indeed, daughter cells that mature an ICB but fail to abscise, often remain connected through a long-lasting cytokinetic bridge that eventually breaks under mechanical strain (Gromley *et al*, 2005; Estey *et al*, 2010). An abscission defect in absence of PIPKI γ is plausible because the midbody organelle does not only stabilize the cleavage furrow but also subsequently orchestrates abscission (as introduced in paragraph 1.1.4, see also Mierzwa & Gerlich, 2014). In particular, MKLP1 binds and recruits CEP55 (Zhao *et al*, 2007). CEP55 in turn mediates the accumulation of ALIX and TSG101 (Hyung *et al*, 2008) to ultimately foster the

recruitment of ESCRT-III components (Christ *et al*, 2016; Addi *et al*, 2020). Therefore, by maintaining centralspindlin at the midbody, the PIPKI γ -i3/i5-septin module identified in this study may additionally/indirectly also regulate the molecular cascade underlying ESCRT-III-mediated abscission.

Successful abscission requires also the delivery of Golgi-derived exocytic vesicles and recycling endosomes that dock at the midbody and fuse at its proximity (Schiel *et al*, 2013; Goss & Toomre, 2008). Localized vesicle fusion may physically contribute to cortical actin destabilization and thinning of the ICB (Gromley *et al*, 2005). Recycling endosomes support abscission also by transporting relevant cargos (Frémont & Echard, 2018). For instance, Rab11-FIP3-positive endosomes prevent F-actin polymerization at the ICB by delivering RhoGAP50, a GAP for RhoA (Schiel *et al*, 2012). At later points, Rab35 and PI(3)P-positive endosomes (with their cargos) aid lipid conversion and the assembly of the ESCRT-III complex at the secondary ingression site, respectively (Dambournet *et al*, 2011; Sagona *et al*, 2010).

Docking of many vesicles relies on the exocyst complex, whose subunits localize in a ring-like structure at the midbody (Gromley *et al*, 2005). The interactions with midbody components also provide temporal and spatial regulation to vesicle recruitment (**fig. 1-5**). For instance, MgcRacGAP and MKLP1-bound ARF6 become available for the interaction with FIP3 at telophase, when RhoGAP50 has to be delivered in order to downregulate RhoA and to prepare the bridge for abscission (Takahashi *et al*, 2011; Schweitzer & D'Souza-Schorey, 2002; Simon *et al*, 2008). Less clear remains the mechanism of accumulation of Rab35 and PI(3)P-positive endosomes at the ICB (Iannantuono & Emery, 2021; Frémont & Echard, 2018). Nevertheless, by maintaining centralspindlin, and centralspindlin-bound ARF6 at the midbody, PIPKI γ -i3/i5 and septins likely support the delivery and fusion of at least a subset of vesicles to the maturing ICB (**fig. 4-1-F**).

Localized synthesis of PI(4,5)P₂ by PIPKI γ -i3/i5 may also support the accumulation of the exocyst complex (**fig. 4-1-D**). Indeed, the assembly of exocyst requires the binding of PI(4,5)P₂ by the Exo70 and Sec3 subunits (Mei & Guo, 2018), and PIPKI γ interacts directly with Exo70 (Xiong *et al*, 2012). Of note, it has been shown that E-cadherin-bound or talin-bound PIPKI γ targets exocyst at forming adherent junctions in polarizing epithelia, or at the leading edge of migrating cells, respectively (Xiong *et al*, 2012; Thapa *et al*, 2012). Therefore, a similar model could apply for

centralspindlin- and septin-interacting PIPKI γ -i3/i5. Previous studies have already described the requirement of MKLP1 and SEPT9 to localize exocyst at the midbody (Gromley *et al*, 2005; Estey *et al*, 2010); PIPKI γ -i3/i5 and PIPKI γ -i3/i5-derived PI(4,5)P₂ may function as an additional cue to guide exocyst localization during cytokinesis.

In a recent work Maib and colleagues have shown that ARF6 recruits PIPKI γ on vesicles close to the PM (Maib & Murray, 2022). PIPKI γ in turn synthesizes a vesicular pool of PI(4,5)P₂ required for exocyst-mediated tethering. According to this model, Sec3 and Exo70 bind PI(4,5)P₂ in a trans configuration. Hence PI(4,5)P₂ must be present on both PM and on the vesicles about to fuse (Maib & Murray, 2022). It is therefore plausible that midbody-resident PIPKI γ -i3/i5 may also mediate a lipid conversion on PI(4)P-containing vesicles arriving at the midbody, and thereby ensure their tethering. In this scenario, depletion of PIPKI γ -i3/i5 would affect docking and fusion of post-Golgi exocytic vesicles and of certain types of endosome. This in turn could hamper the thinning of the ICB and the delivery of relevant cargoes for cytokinesis, such as RhoGAP50. Interestingly, we observed that PIPKI γ -i3/i5-depleted cytokinetic cells displayed excessive F-actin at the midzone (**fig. 3-S1**), in agreement with prolonged RhoA activity at the ICB.

As mentioned above, SEPT9 is required for the localization of the exocyst complex at the midbody, but it remains unclear how (Estey *et al*, 2010). Depletion of SEPT9 leads to a ~ 3,5 fold increase in the percentage of cells exhibiting a cytokinetic bridge (Estey *et al*, 2010), whereas, in this study, depletion of PIPKI γ led to a two-fold increase of the same phenotype (**fig. 3-1-E**). This suggests that the recruitment of PIPKI γ -i3/i5 may function during the SEPT9-dependent exocyst retention at the midbody, although other molecular processes may concur (Safavian *et al*, 2023).

In conclusion, by potentially regulating midbody integrity, midbody tethering to the PM and vesicle docking, PIPKI γ -i3/i5 could represent a novel and important element of coordination between the stabilization of the ingressed cleavage furrow and the initiation of the final phase of abscission (**fig. 4-1**).

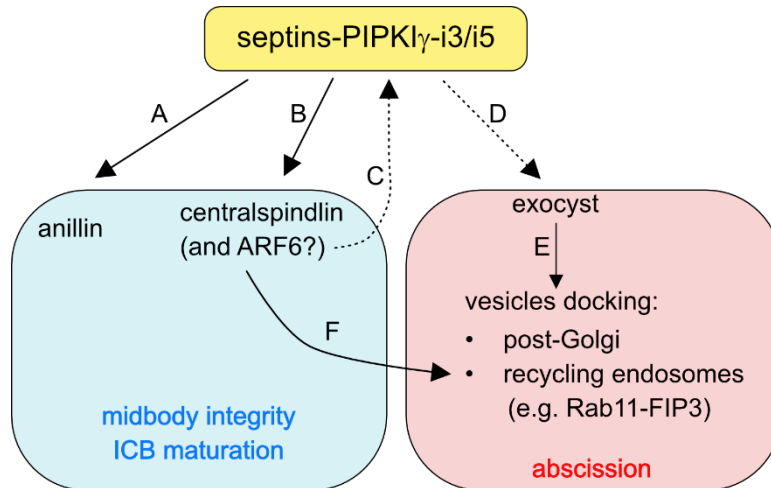


Figure 4-1. Diagram summarizing the contribution of the septin-PIP1 γ -i3/i5 module to midbody assembly and initiation of abscission. (A) Localized synthesis of PI(4,5)P₂ by septin-associated PIP1 γ -i3/i5 contributes to anillin retention at the ICB, (B) and to centralspindlin stabilization at the midbody. Septins may additionally facilitate centralspindlin recruitment by acting as diffusion barriers, or by directly associating with centralspindlin. Furthermore, localized PI(4,5)P₂ synthesis may help maintaining the activity of ARF6 (through its GEF, EFA6). (C) Active ARF6, in turn, may enhance PIP1 γ -i3/i5 activity at the midbody. A correct assembly of the midbody is necessary for the anchoring of bridge MTs to the ingressed cleavage furrow and for the maturation of the ICB. (D) PIP1 γ -i3/i5 possibly contribute to abscission by participating in the SEPT9-dependent targeting of the exocyst complex to the midbody. (E) Exocyst, in turn, enables local docking of vesicles that, upon fusion near the midbody, destabilize cortical actin and narrow the ICB. (F) Centralspindlin and ARF6 play a role in the docking of specific recycling endosomes, such as the Rab11-FIP3 positive ones (that carry RhoGAP50 and thereby promote the local inactivation of Rho). Centralspindlin further contributes to abscission by initiating the cascade of events to recruit ESCRT-III (not shown). Dashed arrows and the question mark indicate speculations. ICB: intercellular bridge.

4.3.3. Putative mechanisms underlying the redistribution of PI(4,5)P₂ across the midbody in absence of PIP1 γ -i3/i5

Previous studies successfully visualized enriched PI(4,5)P₂ at the cleavage furrow through the expression of the PH domain of PLC δ 1 fused to a fluorescent protein (Emoto *et al*, 2005; Field *et al*, 2005; Liu *et al*, 2012). Aiming at identifying the PI(4,5)P₂ pool required for midbody stability, we took advantage of the same probe and stably expressed it in eGFP-SEPT6 knock-in cells. Then, we compared the enrichment of the probe between the furrows of control and PIP1 γ -i3/i5-depleted cells at telophase, when the midbody is formed (hence when PIP1 γ -i3/i5 is presumably required) (**fig. 3-17-A**). In both control and PIP1 γ -i3/i5-depleted cells, eGFP-SEPT6 outlined the midbody. Additionally, in control cells eGFP-SEPT6 faintly marked the two sides of the ring, indicating the initiation of septin translocation onto MTs, as observed previously (**fig. 3-7**). The PH domain, instead, localized over a broader area contouring the midbody. However, its abundance at the furrow (or

within a ROI defined by CIT-K, hence marking the midbody ring, not shown) remained unchanged between control and PIPKI γ -i3/i5-depleted cells, suggesting a failure in the identification of the desired lipid pool (**fig. 3-17-B**). This is in line with other studies that encountered difficulties in the identification of PI(4,5)P₂ pools at sites of PIPKI γ activity (e.g. at focal adhesions or on endosomes) when expressing the PH-PLC δ 1 domain (Sun *et al*, 2007, 2013; Thapa *et al*, 2012; Ling *et al*, 2002). As pointed out by Sun and colleagues (Sun *et al*, 2013), this could be due to the low abundance of the respective pool, or to the local enrichment of lipid effectors that compete with the PH domain for PI(4,5)P₂ binding (**fig. 1-6**). In mitotic cells PIPKI γ interacts with septins and centralspindlin (**fig. 3-12-B**) and, especially the latter, could compete with the probe for the binding of PI(4,5)P₂ at the nascent midbody. Thus, the enriched PH domain in **fig. 3-17-A** rather labeled the bulk PI(4,5)P₂, which builds up during furrow constriction, and ends up in membrane protrusions which extend outside of the midbody ring, hence conferring to the probe a broader distribution compared to SEPT6.

During the maturation of the ICB, daughter cells grow apart, while excess membrane is extruded (Carim *et al*, 2020), in addition OCRL depletes PI(4,5)P₂ at the flanks of the midbody (Dambournet *et al*, 2011). Therefore, we hypothesized that the PI(4,5)P₂ remaining at the midbody by the onset of telophase would be exclusively the one synthesized by PIPKI γ -i3/i5 after furrow ingression. Interestingly, at this stage, the PH domain was poorly enriched at the bridge (not shown), suggesting that the bulk PI(4,5)P₂ deriving from the cleavage furrow was mostly depleted, as expected. Therefore, we opted for the staining of PI(4,5)P₂ with an antibody (**fig. 3-18**).

Under control conditions, we could occasionally spot PI(4,5)P₂ enrichment at the midbody (**fig. 3-18-A**, last two rows), in coincidence with MgcRacGAP. In PIPKI γ -i3/i5-depleted bridges, MgcRacGAP intensity was markedly dim, in accordance with the shown defect in centralspindlin maintenance (**fig. 3-15**). PI(4,5)P₂ instead was predominantly localized at membrane protrusions, possibly filopodia, and appeared sparse within the bridge, making it difficult to identify the edges of the bridge cortex (**fig. 3-18-A**). To gain insights in the distribution of PI(4,5)P₂ around the midbody, we measured its intensity over a line across the bridge, and centered on MgcRacGAP (which was still visible in knock-down samples upon boosting the contrast) (**fig. 3-18-B**). The resulting intensity profile exhibited two peaks, the height

of which was not affected by kinase depletion. However, in PIPKI γ -i3/i5-depleted cells the two peaks were further apart as compared to control cells. This might, if the peaks align with the bridge cortex, suggest that depletion of PIPKI γ -i3/i5 leads to a wider ICB, in line with reduced centralspindlin levels, and a consequent defect in the anchorage of PM to MTs (Lekomtsev *et al*, 2012). Alternatively, the two peaks may represent PI(4,5)P₂ residing in membrane protrusions. In this case the average intensity of PI(4,5)P₂ at the bridge cortex itself would be represented by the valley between the two peaks, and would therefore be lower than under control conditions. Based on our observation we cannot discriminate between both options. For instance, mass-spectrometry-based lipidomic analysis could be used to assess the phosphoinositide composition of purified midbodies upon depletion of PIPKI γ -i3/i5 (Posor *et al*, 2022; Atilla-Gokcumen *et al*, 2014; Cheung *et al*, 2021; Li, 2021).

4.3.4. Putative mechanisms underlying the morphological changes of the ICB in absence of PIPKI γ -i3/i5

Our data provide solid evidence that depletion of PIPKI γ -i3/i5 is accompanied by profound morphological changes at the ICB: the ICB is shorter, possibly wider, and spreads into membrane protrusions that resemble filopodia. This is also evidenced by the localization of stably transfected mCherry-PIPKI γ -i5 wild type as compared to PIPKI γ -i5 mutants in rescue experiments (**fig. 3-10-A/C** and **fig. 3-14-A**). Upon depletion of endogenous PIPKI γ -i3/i5, PIPKI γ -i5 Δ SB and K188A were not closely aligned with the ICB and midbody, unlike the wild-type kinase, but appeared rather scattered along the PMs of the two nascent daughter cells in areas neighboring the ICB, and, possibly, within a multitude of filopodia. This suggests that confined kinase localization not only requires the capability to associate with septins, but may also depend on local PI(4,5)P₂ production. We propose that the spatiotemporal control of PI(4,5)P₂ synthesis by PIPKI γ -i3/i5 is not only essential to sequester PI(4,5)P₂ effectors (like centralspindlin, anillin, and septins themselves) within the ICB and at the midbody, but also fuels a proofreading, feed-forward loop to maintain the kinase at these locales.

3D-SIM microscopy by Renshaw and colleagues has shown that the elongation of the ICB is driven by anillin and septins that form a transient collar of circular filaments decorating the ICB, and drive the wrapping of the PM around MT bundles (as

schematized in **fig. 1-2-B**) (Renshaw *et al*, 2014). This essentially depends on anillin's capability to associate with septins. Our data reveal a potential explanation for this phenomenon: PI(4,5)P₂ synthesis by septin-bound PIPK1 γ -i3/i5 is required to support the transient organization of anillin and septins in rings along the ICB. By contrast, the absence of septins (Estey *et al*, 2010), of PIPK1 γ -i3/i5, or the presence of an anillin mutant that cannot associate with septins (Renshaw *et al*, 2014; Panagiotou *et al*, 2022), hampers the maturation of the ICB.

A shorter ICB and excess of filopodia may also result from ectopic activity of Rac1 and Cdc42, caused by reduced levels of MgcRacGAP at the midbody in absence of PIPK1 γ -i3/i5 (see paragraph 4.5.3). Abnormally active GTPases may also stimulate the catalytic activity of other type I PIP-kinases, leading to a mislocalized synthesis of PI(4,5)P₂ at the bridge membrane (Weernink *et al*, 2004b). This could explain why the PI(4,5)P₂ peaks across the bridge of control and PIPK1 γ -i3/i5-depleted cells exhibited comparable amplitude (**fig. 3-18-B**).

4.4. PIPK1 γ regulates the subcellular localization of septins

PIPK1 γ -i3/i5 catalytic activity is ultimately required for the translocation of septins to bridge MTs. Interestingly, also interphase cells depleted of PIPK1 γ -i3/i5 exhibited a defect in the association of septins with MTs, and this was accompanied by reduced MT bundling, and by reorganization of actin. Based on our data, and on data of others, we advance the hypothesis that cytokinesis could serve the generation of a pool of septin filaments capable of guiding the cytoskeletal organization of daughter cells. Although further experiments are required to validate this hypothesis, our data point at PIPK1 γ as a novel regulator of septin subcellular redistribution and, thus, of more global septin functions.

4.4.1. PIPK1 γ -i3/i5 promote the localization of septins to bridge MTs

To follow septin remodeling during cytokinesis we generated a heterozygous gene-edited cell line expressing eGFP-SEPT6 from its endogenous promoter (**fig. 3-19-A-B**). EGFP-SEPT6 colocalized and interacted with the other members of the canonic septin octamer (SEPT2-SEPT7 and SEPT9), demonstrating that the tagged variant is successfully incorporated into filaments (Steffen Restel bachelor thesis).

This validation prompted us to study the behavior of eGFP-SEPT6 as a means to follow the reorganization of the septin cytoskeleton during cell division by live cell imaging (**fig. 3-19-C**).

During cytokinesis of control cells, septins first accumulated at the cleavage furrow. As the ICB emerged (~ 30 minutes later), septins redistributed into long sinuous fibers, resembling MTs, which extended in both directions towards the nascent daughter cells (red arrowheads in **fig. 3-19-C**). Depletion of PIPKI γ -i3/i5 clearly abolished the generation of those fibers, hence suggesting septin failure to associate with the MTs of the cytokinetic bridge. This observation was supported by additional data obtained in parental cells.

First, in absence of PIPKI γ -i3/i5, the percentage of SEPT2 localizing at the acetylated tubulin bridge was reduced by half (**fig. 3-8-E-F**). In contrast, SEPT2 exhibited a patchy distribution at the flanking PMs of the newly forming daughter cells, at sites adjacent to the ICB. The same was observed for immunostained endogenous SEPT6 (**fig. 3-8-C**), SEPT7 and SEPT9 (not shown), suggesting that scattered septins remained in a hetero-oligomeric state. Second, U-ExM confirmed such predominant association of septins with MTs in the bridges of control cells (**fig. 3-16-D/F**). Moreover, septins were absent from the midbody, but formed rings at both flanks, juxtaposed to the secondary ingression sites (**fig. 3-16-D**), in agreement with findings by Karasmanis *et al.*, 2019. By contrast, in PIPKI γ -i3/i5-depleted cells, septins were mostly dispersed from bridge MTs, and rather formed short, often curved, rods or rings (green and red arrowheads in **fig. 3-16-D**) near the cytokinetic bridge. We do not know the nature of these structures. However, part of them seemed to outline the PMs of the forming daughter cells adjacent to the bridge. Of note, reports by others have shown that the curved appearance of membrane-associated septins is dictated by their preferential accumulation at sites of micron-scale positive curvature, such as the base of membrane ruffles, lamellipodia and filopodia (Bridges *et al*, 2016; Kim & Cooper, 2018). The septin rods and rings observed by us may therefore demarcate the base of membrane protrusions, such as filopodia, which appear numerous at the ICB of PIPKI γ -i3/i5-depleted cells (**fig. 3-18-A**).

U-ExM further revealed that depletion of PIPKI γ -i3/i5 did not substantially affect the formation of septin rings at the midbody flanks (**fig. 3-16-E**). Thus, we conclude that

PIPKI γ -i3/i5 regulate only a subset of septins that redistribute onto MTs within the cytokinetic bridge.

The percentage of SEPT2 localizing at the acetylated tubulin bridge was rescued by PIPKI γ -i5 wild type but not K188A or Δ SB (**fig. 3-10-C-D**). Thus, the catalytic activity of PIPKI γ -i5 and its ability to associate with septins are essential for the translocation of septins onto bridge MTs.

4.4.2. The PIPKI γ -i3/i5-dependent relocation of septins to bridge MTs may regulate the length of the cytokinetic bridge

Depletion of PIPKI γ -i3/i5 led to 25% shorter acetylated tubulin bridges during cytokinesis (**fig. 3-8-E/G**), and this phenotype was rescued by PIPKI γ -i5 wild type, but not by K188A or Δ SB mutants (**fig. 3-10-C/E**). U-ExM also confirmed shorter MT bundles at the bridge of PIPKI γ -i3/i5-depleted cells. In particular, the U-ExM protocol used in this study included a longer denaturation step at 95°C that allowed the efficient staining of dense MT arrays, while practically destroying the thinner ones. In **fig. 3-16** both control and knock-down samples exhibited bundles of antiparallel MTs whose plus ends overlapped at the midbody. However, PIPKI γ -i3/i5-depleted cytokinetic bridges were consistently shorter, thus suggesting a defect in MT bundling, which remained confined to the midbody proximity.

Cytokinetic bridge formation is accompanied by progressive bundling of MTs while the cleavage furrow ingresses and the ICB matures (Fededa & Gerlich, 2012). Upon activation at anaphase, PRC1 moves toward the plus ends of the spindle MTs in a KIF4A-dependent manner, oligomerizes and crosslinks MTs, thereby promoting their bundling throughout furrow ingression (Zhu *et al*, 2006). As the PM converges to enwrap the midbody, septins translocate onto cytokinetic bridge MTs. This process initiates at the flanks of the midbody, and subsequently spreads toward the minus ends of bridge MTs (Surka *et al*, 2002) (**fig. 3-7**). By doing so, septins may propagate MTs bundling at distal sites from the midbody, in accordance with the ability of SEPT9-i1-containing filaments to bind and bundle MTs (Bai *et al*, 2013). Of note, HeLa cells express predominantly SEPT9-i1 (Kuzmić *et al*, 2022). Therefore, a failure in septins translocation and spreading along the cytokinetic bridge, as observed in absence of PIPKI γ -i3/i5 (**fig. 3-19-C**), may impair MTs bundling, and result in a shorter acetylated tubulin bridge. The requirement of septins for the

elongation of the cytokinetic bridge emerges also from **fig. 3-S5-A/C**: disruption of septin filaments via depletion of SEPT7 led to a phenocopy of the acetylated tubulin bridge shortage.

Immunoprecipitation assays revealed complex formation between SEPT2 and PRC1 (**fig. 3-S2-A**). Therefore, septins may reinforce MT bundling also by interacting and stabilizing PRC1 along the bridge. Indeed, in control cells PRC1 extended at the two flanks of the midbody while, upon depletion of PIPKI γ -i3/i5, it was confined to a narrower area (**fig. 3- S2-B-C**). Additionally, we frequently observed that in absence of PIPKI γ -i3/i5 the region of overlapping MTs at the midbody appeared broader or dimmer as compared to control cells (**fig. 3-16**), suggesting a possible defect in MTs organization and bundling at this site, in accordance with reduced MKLP1 levels (Mishima *et al*, 2002).

Taken together, we propose that PIPKI γ -i3/i5 control the length of the tubulin bridge, and MTs bundling, by regulating the translocation of septins onto bridge MTs.

4.4.3. Via septins, PIPKI γ may provide daughter cells with instructions on how to organize their cytoskeleton

Cells depleted of PIPKI γ (or PIPKI γ -i3/i5) displayed an altered septin cytoskeleton also at interphase (**fig. 3-4-A** and **fig. 3-9-A**). Confocal imaging of wild-type and genome-edited cells revealed that, in control conditions, septins associated poorly with actin, but formed prominent perinuclear fibers aligning with bundled MTs (**fig. 3-20-A-B**, **fig. 3-21-A**). On the contrary, in cells depleted of PIPKI γ -i3/i5, septins rather colocalized with actin stress fibers, while the association with MTs was poor, as at cytokinesis (see also **fig. 3-21-B**). This resulted in profound alterations in the appearance of the MT and the actin cytoskeleton. Upon PIPKI γ -i3/i5 depletion MTs failed to assemble ordered perinuclear bundles, and appeared entangled (**fig. 3-20-A-B**, **fig. 3-21-A** and **fig. 3-S4**). Actin stress fibers, on the other hand, were mostly found in the cell periphery in control cells, whereas upon PIPKI γ -i3/i5-depletion, they distributed also toward and across the cell center, together with focal adhesions (**fig. 3-20-A-B**, **fig. 3-21-A** and **fig. 3-S3**).

In the recent years, septins have emerged as important regulators of the MT cytoskeleton (Spiliotis & Nakos, 2021) (**Fig. 1-10**). Septins not only bundle MTs (Bai *et al*, 2013; Bowen *et al*, 2011; Kuzmić *et al*, 2022), but also promote their nucleation

(Chen *et al*, 2021; Song *et al*, 2019; Omrane *et al*, 2019), regulate their growth (Nakos *et al*, 2019b, 2019a) and steer their trajectories (Bowen *et al*, 2011).

Subconfluent MDCK cells exhibit perinuclear MT bundles that, as in HeLa M, colocalize with sinuous septin fibers (Bowen *et al*, 2011; Spiliotis *et al*, 2008). Through live cell imaging approaches, Bowen and colleagues have shown that septins provide trajectories along which MT plus-ends, emerging from the perinuclear centrosomal area, move anterogradely. Septins also capture neighboring MTs, and direct their growth along the forming bundle (Bowen *et al*, 2011). Thus, when the septin cytoskeleton is destroyed, or the interaction with MTs is perturbed, MTs become highly entangled and poorly bundled (Bai *et al*, 2013; Bowen *et al*, 2011).

These defects resemble those observed in this study in interphase cells: septin-free MTs appeared as a tangled web, suggesting extensive bending, and loss of directionality (**fig. 3-20-A-B**, **fig. 3-21-A** and **fig. 3-S4**). This was accompanied by a tendency of decrease in total acetylated tubulin (**fig. 3-20-C-D**), indicating a defect in MTs bundling and stability. Based on this, we speculate that such defects could result from a loss of PIPKI γ -i3/i5-dependent subcellular organization of septins that, having lost the association with MTs, fail to regulate them.

As indicated in more detail below, inhibiting cytokinesis by depletion of MKLP1 or MgcRacGAP triggered a similar redistribution of septins away from MTs to actin stress fibers, and, also in this case, cells lost prominent perinuclear MT bundles (**fig. 3-21**). Therefore, cytokinesis may serve to generate a pool of MT-associated septin filaments that is inherited by daughter cells, and has a role in instructing future MTs organization. Notably, septin filaments exhibit a slower subunit turnover as compared to other cytoskeletal components (Hagiwara *et al*, 2011; Hu *et al*, 2008; Spiliotis & McMurray, 2020). In accordance to this hypothesis, live cell imaging of the eGFP-SEPT6 throughout cytokinesis showed that, upon localizing to the cytokinetic bridge, septins form sinuous fibers extending toward the perinuclear area of daughter cells (**fig. 3-19-C**). These fibers seem to be inherited by daughter cells, and possibly converge into their already existing MT-associated septin pool. As HeLa M, also other cell types that exhibit septins association with MTs at interphase, display a prominent association of septins with bridge MTs at cytokinesis (Kuzmić *et al*, 2022; Karasmanis *et al*, 2019; Nagata *et al*, 2003). Therefore, in other words, the cytokinetic bridge may serve as a “collection point”, where septin filaments are

gathered, “primed” to associate with MTs (e.g. through PTMs- see below), and subsequently redistributed among daughter cells.

Bridge MTs-derived septins may also assist organelles positioning and integrity in daughter cells. For instance, septins have recently emerged as regulators of Golgi integrity and function (Song *et al*, 2019; Omrane *et al*, 2019). During mitosis, the Golgi complex is disassembled into vesicular and tubular fragments, to be partitioned between daughter cells (Mascanzoni *et al*, 2022). At telophase, parts of these fragments reassemble at the two sides of the cytokinetic bridge into minor Golgi clusters (Gaietta *et al*, 2006). Therefore, bridge-derived septin filaments may engage these clusters, and aid their reassembly and coalescence with the major Golgi ribbon forming at the peri-centriolar area.

Septins also extensively regulate the actin cytoskeleton (Spiliotis & Nakos, 2021) (**fig.1-9**). Septin filaments associate directly and indirectly with stress fibers, provide them with mechanical support and anchor them to PM (Martins *et al*, 2023; Calvo *et al*, 2015; Joo *et al*, 2007; Smith *et al*, 2015). In addition, septins promote the cross-linking of dorsal stress fibers with transversal arcs (Dolat *et al*, 2014), and may directly support the generation of new ventral stress fibers (Spiliotis, 2018). Hence, the increase in ventral stress fibers observed in PIPKI γ -i3/i5-depleted cells may be potentiated by septin relocalization at actin sites, as a consequence of their lost association with MTs.

Furthermore, it has been reported that MTs disruption stimulates the formation of actin stress fibers (Enomoto, 1996). Meiri and colleagues have shown that the Rho-GEF GEF-H1 is sequestered in an inactive state on MTs, and, when MTs depolymerize, it is relieved from inhibition (Meiri *et al*, 2012). Active GEF-H1 then activates RhoA and thereby enhances stress fibers formation (Krendel *et al*, 2003). Septin association with MTs reduces MTs plus-end catastrophes (Bowen *et al*, 2011). Therefore, the dissociation of septins from MTs, observed upon depletion of PIPKI γ -i3/i5, may enhance MTs depolymerization and, as a consequence, induce stress fibers also through the GEF-H1-dependent activation of RhoA.

In sum, PIPKI γ -i3/i5 emerges as a novel regulator of the septin cytoskeleton that, by promoting septin translocation onto bridge MTs, contributes to the propagation of a MT-binding and -regulating septin pool.

4.5. Putative mechanisms underlying the PIPKI γ -dependent translocation of septins to bridge MTs

4.5.1. Centralspindlin promotes spatial proximity between furrow membrane and bridge MTs

It remains unclear how a PI(4,5)P₂ pool synthesized by PIPKI γ -i3/i5 at the PM surrounding the midbody could mediate the translocation of septins onto bridge MTs. A major regulator is probably centralspindlin itself. A very straightforward explanation might be the close vicinity between PM and bridge MTs as established by centralspindlin at telophase (**fig. 4-2-A**). As highlighted in paragraph 1.3.4, it has been proposed that the physical proximity between subcellular compartments facilitates the redistribution of septins between them (**fig. 1-11**) (Spiliotis, 2018; Spiliotis & McMurray, 2020). For example, the association of septins with PI(3,5)P₂-rich endo-lysosomes at the peripheral lamellae of epithelial cells regulates also the association of septins with local stress fibers (Dolat & Spiliotis, 2016). Similarly, during cytokinesis, the translocation of septins from cell cortex to bridge MTs may be triggered by the vicinity of these two compartments. Indeed, septin redistribution takes place at telophase (when the furrow membrane has become sufficiently close to the bridge MTs) and emanates from the two flanks of the midbody, which is the site of closest proximity between furrow membrane and MT bundles (**fig. 3-7**, SEPT2 staining). Hence, PIPKI γ -i3/i5 may regulate the translocation of septins on bridge MTs by maintaining centralspindlin at the midbody.

Importantly, depletion of MKLP1 or of MgcRacGAP phenocopied the redistribution of septins from bundled MTs to actin stress fibers observed at interphase in absence of PIPKI γ -i3/i5 (**fig. 3-21**). Knock-down of each of the centralspindlin components resulted in ~ 50% of multinucleated cells (not shown). However, contrary to PIPKI γ -i3/i5, upon depletion of MKLP1 or MgcRacGAP only few cells reached telophase, thus suggesting a cytokinesis failure at an earlier stage, probably at anaphase, in line with centralspindlin's role to recruit and activate Ect2 at the cell equator (Yüce *et al*, 2005). Therefore, on the one hand, the results in **fig. 3-21** support the hypothesis that the septin feature to associate with MTs is established during cell division. But, on the other hand, further experiments are needed to assess whether this association depends on the centralspindlin-mediated anchoring of MTs to the

midbody cortex. For instance, testing whether a MgcRacGAP mutant incapable of PI(4,5)P₂ binding would be able to rescue the association of septins with bridge MTs upon depletion of endogenous MgcRacGAP, may clarify this point. Indeed, as shown previously, such mutant does not hamper cytokinetic progression until telophase (Lekomtsev *et al*, 2012). In mammalian cells in fact, contrary for instance to *C. elegans* embryos, the PI(4,5)P₂ binding property of MgcRacGAP is dispensable at anaphase (Basant *et al*, 2015).

Mitotic inhibitors may be further used to confirm that septin association with MTs depends on the capability of cells to undergo cytokinesis.

4.5.2. PTMs may modulate the affinity of septins for bridge MTs

PTMs may contribute at regulating the subcellular localization of septins during cytokinesis (Sharma & Menon, 2023). SEPT9 is the only septin paralogue for which direct MT binding has been demonstrated, and consistently, only SEPT9-i1-containing filaments co-align with MTs in cells (Bai *et al*, 2013; Kuzmić *et al*, 2022; Martins *et al*, 2023). According to Kuzmić and colleagues, the MT binding domain (MBD) of SEPT9 resides within the first 25 amino acids of SEPT9-i1. Additionally, the previously described (Bai *et al*, 2013) repeated motives (K/R-R/x-x-E/D) shared by the N-terminus of long SEPT9 isoforms, have recently been shown to regulate MBD availability to MTs lattice (Kuzmić *et al*, 2022). Therefore, PTMs at the N-terminus of SEPT9-i1, such as the phosphorylation by Cdk-1 on T38, and the consequent Pin-1-induced conformational change (see above, section 4.2.1) (Estey *et al*, 2013), may modulate septin affinity for bridge MTs.

Ribet and colleagues have shown that human septins harbor several sumoylation sites, and that the expression of non-sumoylatable SEPT7 or SEPT11 mutants induces a marked accumulation of septins along the ICB (Ribet *et al*, 2017). This indicates that a modulation of septin sumoylation may also regulate the association of septin filaments with bridge MTs.

It remains unknown whether and how PIPK1 γ -i3/i5 could regulate septin PTMs at the cleavage furrow. One possibility could be through the PIPK1 γ -, exocyst-, and centralspindlin-dependent delivery of vesicle to the ICB (paragraph 4.3.2) (Maib & Murray, 2022). Those vesicles may contain enzymes responsible for PTMs, which would be delivered to septins upon fusion to the ingressed cleavage furrow (**fig. 4-**

2-B). Analyzing and comparing the PTMs profile of septins, and in particular of SEPT9, in control and PIPKI γ -i3/i5-depleted cells may help to elucidate this point.

4.5.3. Rho GTPases contribute to cytoskeletal remodeling during cytokinesis and beyond

Another possible explanation for the PIPKI γ -i3/i5-dependent translocation of septins onto bridge MTs might involve Rho GTPases signaling cascades, in particular through Cdc42 (Russo & Krauss, 2021). During interphase, the Cdc42 effector BORG2 (and possibly BORG3) links septins to actin stress fibers (Calvo *et al*, 2015; Farrugia & Calvo, 2016; Salameh *et al*, 2021). BORG3 also links septins to the cortical actomyosin of amoeboid melanoma cells, which is a highly contractile network, similar to the actomyosin ring of dividing cells (Farrugia *et al*, 2020). Salameh and colleagues have shown that the acute inactivation of Cdc42 triggers the release from actin filaments, and proteasomal degradation of BORGs. This, in turn, causes a redistribution of septins from actin stress fibers onto MTs (Salameh *et al*, 2021). Based on these observations it is tempting to speculate that septin translocation to bridge MTs at telophase might be triggered by the inactivation of Cdc42 that, in turn, would be expected to relieve the BORG-dependent retention of septins on cortical actin filaments (**fig. 4-2-C**). Of note, pulldown assays of Cdc42-GST and FRET-analysis throughout mitosis have shown that Cdc42 activity transiently peaks at metaphase, and subsequently declines to reach its lowest point at telophase (Yoshizaki *et al*, 2003; Ocegüera-Yanez *et al*, 2005).

It is now established that the centralspindlin's GAP activity at the cell equator is directed toward Rac1 (Wadsworth, 2021; Bastos *et al*, 2012; Müller *et al*, 2020). However, several evidences support a regulatory role also on Cdc42. For instance, MgcRacGAP exhibits *in vitro* GAP activity toward both Rac1 and Cdc42 (and to a minor extend also toward RhoA) (Jantsch-Plunger *et al*, 2000; Hirose *et al*, 2001; Kawashima *et al*, 2000; Touré *et al*, 1998). Furthermore, Ocegüera-Yanez and colleagues have shown that MgcRacGAP suppresses Cdc42 activity at prometaphase (Ocegüera-Yanez *et al*, 2005). At metaphase, MgcRacGAP is bound and inhibited by PRC1 at the midzone, and consequently Cdc42 activity rises (Ban *et al*, 2004). Of note, overexpression of an MgcRacGAP mutant incapable of PRC1 binding causes spindle aberrations, in line with a defect in the Cdc42-mediated regulation of the spindle architecture (Yasuda *et al*, 2004; Ban *et al*, 2004). Then,

by the time that the Cdc42 activity declines again, MgcRacGAP is phosphorylated by Aurora B (Ban *et al*, 2004; Minoshima *et al*, 2003). This modification counteracts PRC1 binding, hence suggesting that the downregulation of Cdc42 during telophase may depend again on MgcRacGAP (Ban *et al*, 2004). In this scenario, a reduced level of centralspindlin at the midbody, caused by PIPKI γ -i3/i5 depletion, could result in prolonged Cdc42 activity at the ICB and, consequently, in BORG-dependent retention of septins at the cell cortex (**fig. 3-8-E-F**).

Excessive Cdc42 activity may also be the cause of the filopodia observed at the ICB of PIPKI γ -i3/i5-depleted cells (**fig. 3-18-A**) (Ridley, 2015). Moreover, hyperactivation of Cdc42 in interphase may explain the emergence of ventral septin-positive actin stress fibers in PIPKI γ -i3/i5- and in centralspindlin-depleted cells (**fig. 3-21**). Conclusively, such cytoskeletal organization, typical of the endothelial to mesenchymal transition (EMT), can be triggered by the overexpression of BORGs (Calvo *et al*, 2015). The inheritance of activated BORGs by daughter cells, could potentially explain how a defect in Cdc42 downregulation at telophase may propagate beyond cytokinesis.

MgcRacGAP restricts also Rac1 activity at the midzone to locally prevent the formation of cell adhesions that would otherwise restrain furrow ingression and ICB maturation (Chircop, 2014). Therefore, we expected the depletion of PIPKI γ -i3/i5 to result also in the abnormal activity of Rac1 at the ingressed furrow. Indeed, PIPKI γ -i3/i5 depleted cells exhibited excessive membrane spreading underneath and at the side of the forming ICB, as suggested by the broad distribution of disorganized SEPT2 and F-actin between their membranes (**fig. 3-S1**). Accordingly, a punctate vinculin pattern indicates the presence of focal adhesions in this area. In contrast, control daughter cells exhibited only few protrusions near the ICB, and appeared well separated from one another by a septin-positive cytokinetic bridge.

Further analyses are required to confirm ectopic activity of Rac1 at the midzone of PIPKI γ -i3/i5-depleted cells. However, in line with this scenario, Bastos and colleagues showed that dividing cells lacking centralspindlin GAP activity were more adherent to the growth surface, exhibited increased vinculin at the furrow, and failed to mature an ICB (Bastos *et al*, 2012).

Like Cdc42 and Rac1, also RhoA has to be downregulated at the ICB to allow for F-actin clearance and to permit access to the abscission machinery (Echard, 2012). As highlighted in paragraph 4.3.2, PIPKI γ -i3/i5 may be involved, together with

centralspindlin, in the delivery of RhoGAP50 to the midbody. Therefore, depletion of PIPK1 γ -i3/i5 could result also in prolonged RhoA activity and consequent excess of F-actin at the midzone (**fig. 3-S1**). Excessive actomyosin at the ICB may, in turn, increase the affinity of septins for the cell cortex (Joo *et al*, 2007), and thus contribute at hindering septins translocation to bridge MTs in PIPK1 γ -i3/i5-depleted cells. Cortex-localized septins may further prolong RhoA activity by promoting its association with GEF-H1, which stimulates RhoA activity during furrow ingression (Fu *et al*, 2023; Birkenfeld *et al*, 2007).

RhoA has a direct role in promoting the formation of actin stress fibers (Tojkander *et al*, 2012), in agreement with the increase in ventral stress fibers observed upon depletion of PIPK1 γ -i3/i5.

Interestingly, more actin stress fibers have been observed also in MDCK cells depleted of PIPK1 γ (Ling *et al*, 2007), while Mao and colleagues reported increased actin polymerization and a 6-fold increase in RhoA-GTP in PIPK1 γ knock-out macrophages (Mao *et al*, 2009). These data suggest that PIPK1 γ has a role in downregulating RhoA, in contrast with the generally accepted notion that PIPKs act downstream of Rho-GTPases. Aside from MgcRacGAP, the activity of RhoGTPases is controlled by a plethora of GAPs and GEFs (Bos *et al*, 2007; Müller *et al*, 2020), some of them containing PI(4,5)P₂ binding domains (Singh *et al*, 2021). This suggests a sophisticated and tight regulation of Rho GTPases beyond cytokinesis, dependent on localized lipid pools.

Clearly, more experiments are required to understand the impact of PIPK1 γ -i3i5 on Rho GTPases activity, and to elucidate the molecular mechanisms underlying the cytoskeletal remodeling described in this study.

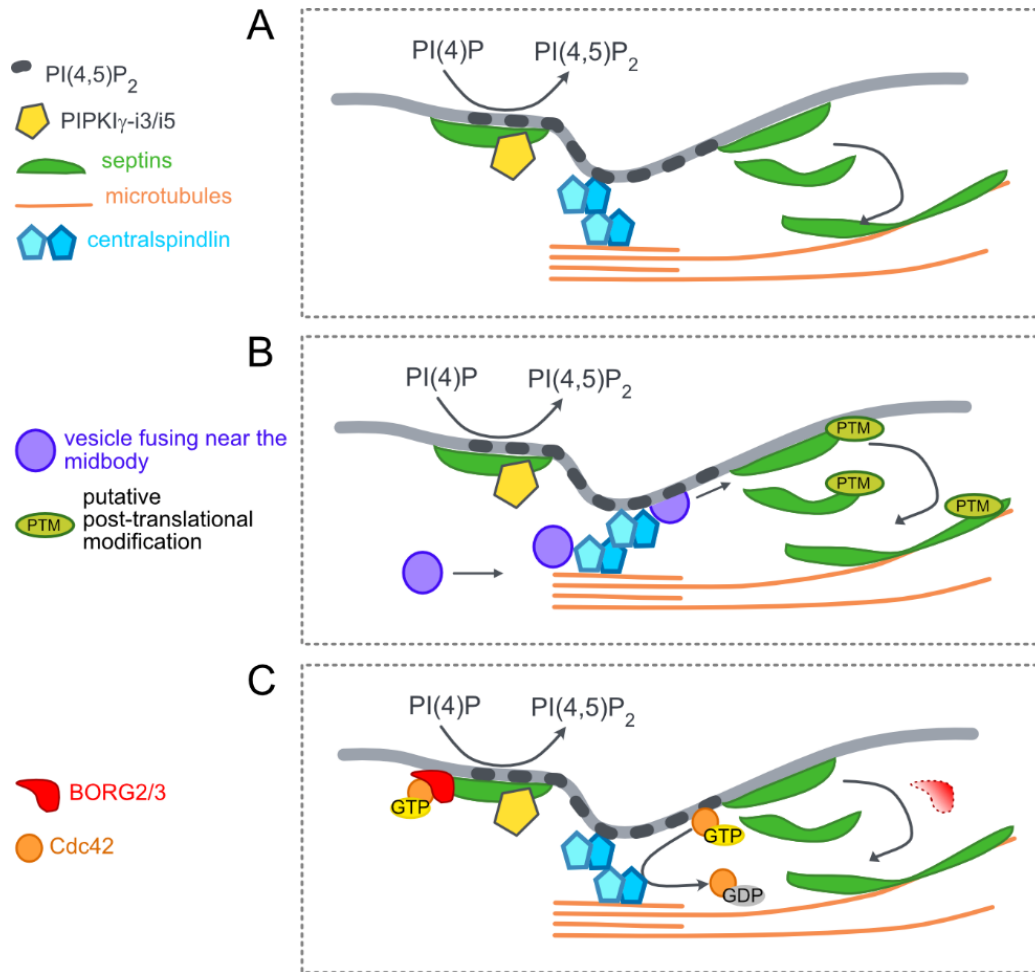


Figure 4-2. Potential mechanisms underlying the translocation of septins to bridge MTs. (A) Septin translocation to MTs may be facilitated by the spatial vicinity between the furrow membrane and the cytokinetic bridge, achieved through centralspindlin-dependent anchorage of the midbody at them PM. **(B)** Vesicles fusing at the midbody upon centralspindlin and exocyst (not shown)-dependent docking, may deliver enzymes that could modify septins, and thereby increase their affinity for MTs. **(C)** At telophase, the centralspindlin-dependent inactivation of Cdc42 may lead to BORGs degradation, consequent release of septins from the bridge cortex and translocation to MTs. Note that these mechanisms may also cooperate, and that centralspindlin has an essential role in all scenarios.

4.6. Working model

Based on our data and on how discussed so far, we propose the following cascade of events (**fig. 4-3**). At the constricting furrow PIPKI β and PIPKI γ synthesize bulk PI(4,5)P₂, which is required to recruit anillin. Anillin, in turn, recruits septins and stabilizes the actomyosin ring, thereby promoting cleavage furrow ingression (**fig. 4-3-A**). During ingression, septins interact with PIPKI γ -i3/i5 and recruit them to the furrow (**fig. 4-3-B**). PIPKI γ -i3/i5 synthesize a *de novo* pool of PI(4,5)P₂ essential to retain septins, anillin and centralspindlin at the nascent midbody. This pool mediates the centralspindlin-dependent anchorage of bridge MTs to the PM. Enriched centralspindlin at the midbody supports the relocalization of septins onto bridge MTs (**fig. 4-3-C**). At this location, septins contribute to MTs bundling, and thereby facilitate the elongation of the cytokinetic bridge, while the ICB matures around it (**fig. 4-3-D**).

Depletion of PIPKI γ -i3/i5 hampers the localized synthesis of PI(4,5)P₂ at the nascent midbody so that centralspindlin cannot efficiently associate with the PM and fails to accumulate (**fig. 4-3-E**). Consequently, septins fail to translocate to bridge MTs, and, together with anillin, scatter away from the midbody to form aberrant clusters in regions of the PMs of daughter cells adjacent to the midbody (**fig. 4-3-F**). Concomitantly, the ICB undergoes a change in morphology, possibly also caused by ectopic activity of Rho-GTPases, which may trigger the mislocalized synthesis of PI(4,5)P₂ by remaining type I PIP-kinases. Mislocalized PI(4,5)P₂ may facilitate clustering of anillin and septins at sites apart from the ICB.

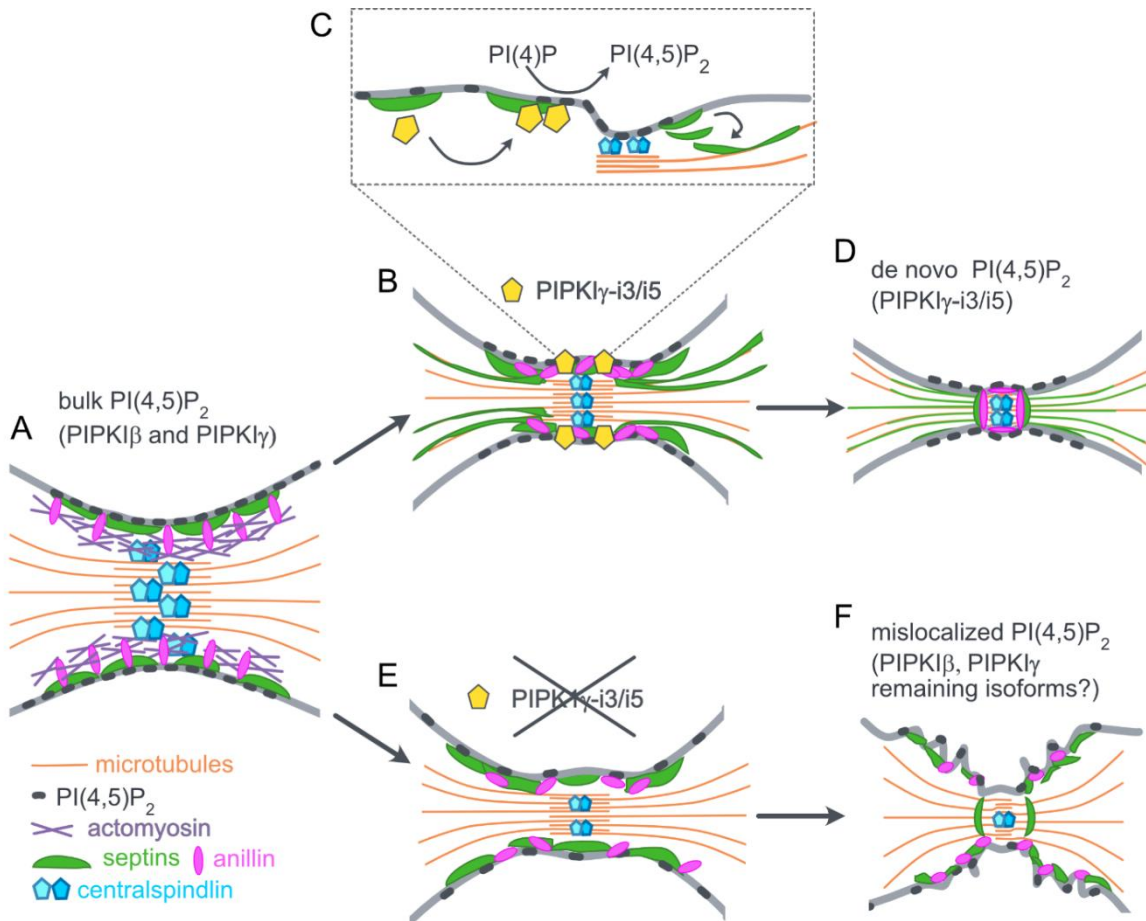


Figure 4-3. Hypothetical model illustrating PIPKI γ contributions during cytokinesis. (A) Anillin (pink) and septins (green) are enriched at the cleavage furrow, where they sustain actomyosin-mediated constriction. PIPKI β and PIPKI γ synthesize the PI(4,5)P $_2$ required for this step. (B) Through interaction with septins, PIPKI γ -i3/i5 (yellow pentagons) are recruited to the furrow, where they generate a novel local pool of PI(4,5)P $_2$. This pool is required for the maintenance of anillin, septins and centralspindlin (turquoise) at the nascent midbody. (C) The centralspindlin-mediated tethering of the furrow membrane to MTs is one of the possible mechanisms that facilitates the translocation of septins onto bridge MTs. (D) Presence of septins on bridge MTs favors their bundling, while the ICB matures. (E) Depletion of PIPKI γ -i3/i5 disrupts the localized synthesis of PI(4,5)P $_2$ at the nascent midbody, impairing centralspindlin local enrichment and septins translocation to MTs. (F) Mislocalized synthesis of PI(4,5)P $_2$ by remaining PIPKIs may contribute to the scattering of anillin and septins. Disorganized septins (and anillin) fail to assist bridge MTs bundling and maturation of the ICB

4.7. Are septins PI(4,5)P₂ effectors?

The hypothesized mechanisms according to which PIPK1 γ -i3/i5 catalytic activity only indirectly regulates the subcellular localization of septins, raise the question of whether septins are direct PI(4,5)P₂ effectors.

4.7.1. The co-depletion of OCRL with PIPK1 γ -i3/i5 did not rescue septin relocalization to bridge MTs

Contrary to anillin, septin disorganization was not rescued by the co-depletion of OCRL along with PIPK1 γ -i3/i5 (**fig. 3-11**). Indeed, although SEPT2 was occasionally found enriched at the midbody together with compact anillin, its percentage at the cytokinetic bridge remained significantly low compared to control conditions (**fig. 3-11-A/C**). This indicates that, while septin localization at the cleavage furrow relies entirely on anillin (Renshaw *et al*, 2014; Liu *et al*, 2012), upon furrow closure septins segregate into different pools: a sub-fraction still interacts with anillin, while another translocates to bridge MTs in an anillin-independent, but PIPK1 γ -i3/i5-dependent manner.

PIPK1 γ presumably becomes essential for cytokinetic progression shortly after furrow closure, when active ARF6, which localizes at the midbody (Makyio *et al*, 2012), stimulates its activity. OCRL, on the other hand, depletes PI(4,5)P₂ at a later stage of cytokinesis, when the ICB needs to be cleared of F-actin to prepare abscission (Dambournet *et al*, 2011). It is thus possible that OCRL arrives too late to really compensate for the loss of PI(4,5)P₂ arising from PIPK1 γ -i3/i5 depletion.

Furthermore, OCRL is predominantly delivered to the ICB as a cargo by fusion of Rab35-positive endosomes (Klinkert & Echard, 2016), and ARF6 may preclude OCRL from the nascent midbody. Indeed, as shown for clathrin coated pits, ARF6-GTP antagonizes Rab35 activity by recruiting the RabGAP EPI64B (Chesneau *et al*, 2012). A similar mechanism may take place at the plasmalemma of the nascent midbody in order to “protect” the PI(4,5)P₂ pool newly synthesized by PIPK1 γ -i3/i5.

For these reasons, the co-depletion of OCRL may not compensate the decrease of PI(4,5)P₂ caused by PIPK1 γ -i3/i5 depletion promptly after furrow closure.

In light of this, the rescue of anillin organization suggests that its scattering is reversible, or that it occurs progressively over time due to prolonged absence of PI(4,5)P₂ from the midbody in absence of PIPK1 γ -i3/i5. Monitoring the organization

of anillin by live cell imaging may help to clarify this point. On the contrary, septin translocation to the cytokinetic bridge could be strictly time-dependent so that the replenishment of PI(4,5)P₂ prior to abscission would not be sufficient to reverse septin disorganization. Indeed, contrary to anillin organization, septin translocation to bridge MTs might not depend directly on PI(4,5)P₂ binding, but could be promoted by centralspindlin, as hypothesized in section 4.5. If this hypothesis is true, then the co-depletion of OCRL with PIPKI γ -i3/i5 should not rescue the decrease of centralspindlin. Of note, centralspindlin stabilization at the midbody requires PI(4,5)P₂, but already at telophase (Lekomtsev *et al*, 2012).

4.7.2. Septins mostly “shape” PI(4,5)P₂ pools rather than acting as effectors

Septins paralogues belonging to the septin subgroup 2, 3 and 7 interact with PI(4,5)P₂ through a stretch of basic residues, similar to the PI(4,5)P₂-binding site of gelsolin, profilin and G-protein-coupled receptor kinases (Zhang *et al*, 1999). In vitro studies have also shown that the presence of PI(4,5)P₂ on lipid membranes facilitates the polymerization of yeast and mammalian septin complexes into filaments and higher order structures that, in turn, may modulate septin function (Bertin *et al*, 2010a; Tanaka-Takiguchi *et al*, 2009). However, septins are capable of interacting with cellular membranes through other means besides the binding of PI(4,5)P₂, such as the interaction with other negatively charged lipids, the insertion of amphipathic helices at sites of micron-scale curvatures, or the association with membrane-bound proteins (Szuba *et al*, 2021; Benoit *et al*, 2023; Omrane *et al*, 2019; Bridges *et al*, 2016).

In fact, despite the accumulation of PI(4,5)P₂ at the cleavage furrow, septin recruitment to the cell equator relies uniquely on anillin (Carim & Hickson, 2023; Renshaw *et al*, 2014; Liu *et al*, 2012). Indeed, the substitution of endogenous anillin with a chimera carrying a PH domain capable of binding PI(4,5)P₂ but not septins, impairs septin recruitment to the cleavage furrow (Renshaw *et al*, 2014; Liu *et al*, 2012).

Upon furrow closure, in certain cell types (as observed here in HeLa M), septins and anillin segregate from one-another, supporting the hypothesis that they respond to different spatial cues, with anillin being retained at the midbody cortex by PI(4,5)P₂, and septins localizing predominantly onto MTs (**fig. 3-7**) (Russo & Krauss, 2021;

Karasmanis *et al*, 2019). A portion of septins additionally redistributes together with anillin in a double ring flanking the midbody (Renshaw *et al*, 2014; Karasmanis *et al*, 2019; Panagiotou *et al*, 2022). Interestingly, this reorganization seems to be primarily driven by septins (Renshaw *et al*, 2014), but the molecular mechanism underlying it remains unknown. Karasmanis and colleagues provided evidence that these septin rings are membrane-bound. However, depletion of PIPK1 γ -i3/i5 did not impair their formation (**fig. 3-16-D-E**), thus suggesting that they may not require local enrichment of PI(4,5)P₂.

Budding yeast septins also reassemble into a double ring perpendicular to the mother-bud axis (Vrabiou & Mitchison, 2006). Beber and colleagues proposed a theoretical model predicting such reorganization, based on septin sensitivity and affinity for microscale membrane curvature (Beber *et al*, 2019). The organization of mammalian septins into rings flanking the midbody may similarly depend on membrane curvature and/or additional molecular cues, such as the presence of myosin II, at the secondary ingression sites (Wang *et al*, 2019; Joo *et al*, 2007).

Therefore, at cytokinesis, septins rather “shape” PI(4,5)P₂ pools, instead of acting as PI(4,5)P₂ effectors. At the cleavage furrow septins recruit PIPK1 γ -i3/i5, while the septin double ring may serve to restrict PI(4,5)P₂ diffusion from the midbody (Pacheco *et al*, 2023). This is similar to the proposed role of septins during SOCE (store operated calcium entry), where septins organize PI(4,5)P₂ microdomains at the PM and thereby support the formation of transient junctions with the endoplasmic reticulum (Sharma *et al*, 2013).

Nevertheless, in this study the high overexpression levels of PIPK1 γ -i5 led to a dramatic reorganization of septins into rings that partially colocalized with the overexpressed kinase, and possibly outlined intracellular vesicles (**fig. 3-24-A-C**). This was observed with PIPK1 γ -i5 wild type and septin binding deficient, but not upon overexpression of PIPK1 γ -i5 catalytically dead (**fig. 3-24-D**), thus suggesting that septin reorganization was primarily driven by the local synthesis of PI(4,5)P₂.

Ectopic accumulation of septins at PI(4,5)P₂-rich endomembranes has been reported before upon overexpression of ARF6 or Rab35 mutants. ARF6 and Rab35 respectively enhance (by recruiting PIPKs) or reduce (by recruiting OCRL) PI(4,5)P₂ on cellular membranes during vesicles internalization and recycling (Krauss *et al*, 2003; Cauvin *et al*, 2016; Maib & Murray, 2022; Klinkert & Echard, 2016; Brown *et al*, 2001). Therefore, the overexpression of constitutive active ARF6

or constitutive inactive Rab35 leads to the formation of PI(4,5)P₂-rich vacuoles, and septins accumulate there independently of F-actin (Chesneau *et al*, 2012; Kouranti *et al*, 2006). Similarly, overexpressed PIPK1 γ -i5 may be recruited to endosomal membranes and synthesize excessive PI(4,5)P₂, which in turn could ectopically recruit septins (Schill *et al*, 2014; Baba *et al*, 2019; Sun *et al*, 2013). This supports the notion that mammalian septins are capable of binding to PI(4,5)P₂, and to reorganize on PI(4,5)P₂-enriched membranes, as yeast orthologues (Bertin *et al*, 2010a). However, further studies are required to clarify whether their subcellular localization and function could be primarily driven by the recognition of specific PI(4,5)P₂ pools also during physiological processes.

4.8. Peculiar function of the SEPT6 paralogue during cytokinesis

The specific downregulation of SEPT6 observed upon depletion of PIPK1 γ led us to hypothesize that the regulatory role of PIPK1 γ -i3/i5 on the septin cytoskeleton could be exerted through this specific paralogue. However, depletion of SEPT6 did not fully phenocopy PIPK1 γ -i3/i5 depletion. Additionally, contrary to other septin paralogues, knock-down of SEPT6 led to a wider acetylated tubulin bridge, without affecting MKLP1 intensity at the midbody. Based on this, we speculate that SEPT6 may play a specific role during cytokinesis outside the canonical septin filaments, as a single paralogue, or as a member of a subset of filaments that are dispensable for the retention of centralspindlin at the midbody.

4.8.1. Hypothesized mechanism of SEPT6-specific downregulation upon depletion of PIPK1 γ

We hypothesize that the retention of septins at the bridge cortex, and their failure to re-localize onto MTs in absence of PIPK1 γ -i3/i5 could be also caused by a change in the protein levels of selected septin paralogues, such as a downregulation of SEPT9. Thus, we compared the protein levels of septin paralogues (against which antibodies were available) between control and PIPK1 γ -i3/i5-depleted cells (**fig. 3-22-A**). Surprisingly, we found that depletion of PIPK1 γ -i3/i5 led to a decrease of

about 50% of SEPT6, while SEPT2, SEPT7 and SEPT9 did not change significantly compared to control (**fig. 3-22-B**). This was observed also upon knock-down with a siRNA targeting all PIPKI γ isoforms (not shown).

The molecular mechanism driving the downregulation of SEPT6 in absence of PIPKI γ is unknown. Compared to other cell lines, HeLa express high levels of SEPT6 (Kuzmić *et al*, 2022). SEPT6 expression can be induced by the transcription factor snail (Simi *et al*, 2018), which plays important roles during cancer progression, and is expressed in HeLa cells under basal conditions (Mianem *et al*, 2008; Nieto, 2002). In epithelial cells undergoing EMT, the complex formed by PIPKI γ -i2 and talin at integrin-mediated adhesions sustains PI3K/AKT signaling, which, in turn, stabilizes snail by preventing its proteasomal degradation (Thapa *et al*, 2017). Although HeLa cells are a different system compared to transitioning epithelial cells, the possible downregulation of the PIPKI γ /talin complex, following PIPKI γ depletion, may reduce the basal levels of snail and consequently affect SEPT6 expression. Of note, PIPKI γ -i3 shares the splice insert of PIPKI γ -i2 that binds the FERM domain of talin (**fig. 3-5-A**) and is indeed capable of interacting with talin (**fig. 3-5-B**). Therefore, also a selective depletion of PIPKI γ -i3/i5 may affect in part PIPKI γ /talin complexes.

However, we do not know whether the decrease of SEPT6 protein levels is caused by a reduced expression of the SEPT6 gene or by a reduced protein stability. Quantitative PCR analysis, and western blotting in presence of translation inhibitors may help to clarify this point.

4.8.2. SEPT6 plays a role outside of the septin-PIPKI γ -i3/i5 module during cytokinesis

Few pieces of evidence suggest that SEPT6 may contribute to septin association with MTs, and/or to modulation of MT dynamics. In cultured hippocampal neurons SEPT6 localizes to MTs at the base of dendritic spines (Moon *et al*, 2013), and SEPT2/SEPT6/SEPT7 complexes interact with MTs and regulate their growth *in vitro*, in absence of SEPT9 (Nakos *et al*, 2019a). Therefore, we asked whether the loss of SEPT6 could be the cause of the septin mislocalization at the cleavage furrow in absence of PIPKI γ (**fig. 3-23**).

SiRNA-mediated depletion of SEPT6 led to undetectable levels of SEPT6 as assessed by western blotting (**fig. 3-23-A**). However, depletion of SEPT6 did not reduce the abundance of SEPT2 at the acetylated tubulin bridge, or the length of the acetylated tubulin bridge further than depletion of PIPKI γ -i3/i5 (**fig. 3-23-B-D**), as it would be expected if these phenotypes were exclusively caused by SEPT6 decrease. Hence, the defects in septin localization and bridge maturation caused by PIPKI γ -i3/i5 depletion are not primarily driven by reduced SEPT6 levels, although a decrease of SEPT6 may still contribute to them. Assessing the degree of rescue of these phenotypes by re-introduction of SEPT6 upon depletion of PIPKI γ -i3/i5 may help to clarify the contribution of this paralogue.

Importantly, depletion of SEPT6 did not affect MKLP1 enrichment at the bridge (**fig. 3-23-F-G**). This indicates that SEPT6, contrary to SEPT2 (**fig. 3-15**), is dispensable for the stabilization of centralspindlin at the midbody, hence it may not participate to the recruitment of PIPKI γ -i3/i5. Depletion of SEPT6 instead led to a small, albeit significant, increase of the width of the acetylated tubulin bridge, contrary to depletion of PIPKI γ -i3/i5 and other septin paralogues (**fig. 3-23-E** and **fig. 3-S5-D**). Thus, SEPT6 may play a specific role in narrowing the cytokinetic bridge.

Whether individual septin paralogues play specific roles outside of the hetero-oligomeric complex remains elusive and difficult to assess, as the loss of a distinct septin may compromise the integrity of the oligomer to which it belongs to (Benoit *et al*, 2023; Kinoshita *et al*, 2002; Kremer *et al*, 2005).

Contrary to cytokinesis, our attempts to assess the impact of SEPT6 depletion on the septin cytoskeleton during interphase yielded inconsistent results, with varying degree of septin filaments loss (as visualized through SEPT2 staining) across different experiments (not shown). Accordingly, SEPT6 colocalizes and forms complexes with other septin paralogues, and this also applies for SEPT6 remaining after depletion of PIPKI γ -i3/i5 (Steffen Restel bachelor thesis). Yet, we cannot exclude the existence of a SEPT6 pool playing a specific function outside of the canonical complex at cytokinesis.

It was found recently that the presence of specific septin paralogues defines distinct septin filaments with different roles at the ICB. In particular, Panagiotou and colleagues suggest that the presence of SEPT11 or SEPT9 is mutually exclusive, and that anillin interacts directly with SEPT11-containing complexes through its PH domain, and indirectly with SEPT9 through the binding of the adaptor protein CIN85

(Panagiotou *et al*, 2022). The SEPT11-based filaments, which presumably contain SEPT2 and surely SEPT7, are required for furrow maturation. Indeed these paralogues, when depleted, caused a more profound multinucleation than SEPT6 or SEPT9 (Estey *et al*, 2010).

According to the “Kinoshita hypothesis”, SEPT6 could be present within the SEPT9-containing filaments in place of SEPT11 (Kinoshita, 2003). Contrary to SEPT6, depletion of SEPT2 and SEPT7 caused MKLP1 decrease at the cytokinetic bridge (**fig. 3-15** and **fig. 3-S5-A-B**). Testing the effect of SEPT9 and SEPT11 depletion on midbody integrity may help to understand whether a specific filament type takes part in the septin-PIPKI γ -i3/i5 module stabilizing centralspindlin at the midbody. Yet, it is difficult to hypothesize the outcome of these experiments because the two types of septin filaments proposed by Panagiotou *et al.* may act upstream or downstream of PIPKI γ -i3/i5. For instance, SEPT2/7/11-based filaments could recruit PIPKI γ -i3/i5 to the midbody, while SEPT9-containing rings may cooperate with PIPKI γ -i3/i5 in recruiting the exocyst complex and in enriching the midbody pool of PI(4,5)P₂ by creating a diffusion barrier (Safavian *et al*, 2023; Pacheco *et al*, 2023; Estey *et al*, 2010). In sum, further studies are required to determine the precise role of SEPT6 and the types of septin filaments it forms.

Kremer and colleagues showed that SEPT6, in a complex with SEPT2 and SEPT7, retains the actin regulator NCK in the cytoplasm. Consequently, depletion of SEPT6 causes NCK translocation to the nucleus, and fragmentation of actin-stress fibers (Kremer *et al*, 2007a). On the contrary, depletion of PIPKI γ -i3/i5 enhanced ventral-stress fibers in interphase, despite reducing SEPT6 levels (**fig. 3-21-A** and **fig. 3-S3**). This suggests once again that the regulatory role of PIPKI γ -i3/i5 on the cytoskeleton is not exerted through SEPT6.

4.9. Conclusions and outlook

In this study we have unveiled the contributions of type I PIP-kinases to cytokinesis, and PIPKI γ has emerged as the sole isozyme required for the maturation of the ICB. Specifically, we have identified a septin-PIPKI γ module orchestrating midbody integrity. A well-assembled midbody is crucial for securing the tethering of the ingressed cleavage furrow to the underneath MTs bundles and, only if this happens, the ICB can mature toward abscission (Lekomtsev *et al*, 2012; Mierzwa & Gerlich, 2014). Therefore, the correct functioning of the septin-PIPKI γ module is essential for passing an important checkpoint during telophase. This module relies on PIPKI γ -i3/i5 septin-binding capability and on kinase activity to ensure kinase recruitment to the nascent midbody and *de novo* synthesis of a pool of PI(4,5)P₂ at this locale. This pool is essential for the enrichment of centralspindlin and, consequently, for the translocation of septins to bridge MTs to further promote their bundling.

PIPKI γ -i3/i5 might additionally foster cytokinesis by aiding in the septin-dependent assembly of the exocyst complex at the midbody (Estey *et al*, 2010). Notably, exocyst assembly requires the binding of PI(4,5)P₂ by the Exo70 and Sec3 subunits (Mei & Guo, 2018), and Exo70 interacts directly with PIPKI γ (Xiong *et al*, 2012). Future experiments should test this hypothesis.

It remains unknown whether the septin-PIPKI γ -i3i5 interaction occurs at subcellular locations other than the cleavage furrow. Understanding the molecular basis and the spatiotemporal regulation of this interaction may help to clarify this point. Nevertheless, previous findings suggest that the septin-PIPKI γ module may indeed play a role in other cellular processes. Similar to cytokinesis, during ciliogenesis, SEPT9 coordinates the activation and assembly of the exocyst complex at the basal body of the cilium (Estey *et al*, 2010; Safavian *et al*, 2023; Hu *et al*, 2010). At this site, exocyst promotes the delivery of post-Golgi vesicles carrying the cargoes required for the assembly of the transition zone (TZ) (Safavian *et al*, 2023). Interestingly, also PIPKI γ localizes at the basal body, and its kinase activity is required for the assembly of the TZ and for the maturation of the axoneme (Xu *et al*, 2016). It is therefore tempting to speculate that PIPKI γ may be recruited by septins and participate to the SEPT9-dependent mechanism of exocyst assembly. Remarkably, the cilium and the ICB share structural similarities: both contain parallel MTs and rely on exocyst-mediated vesicle delivery for maturation. Therefore, while

in proliferating cells the septin-PIPKI γ module contributes to the maturation of the cytokinetic bridge, in quiescent cells it may promote ciliogenesis. The PIPKI γ isoform active at the cilium is presumably the septin-binding PIPKI γ -i3, as it localizes to the centrosome during G1, S and G2 phases in proliferating cells (Xu *et al*, 2014).

PIPKI γ -i5 also localizes to endosomes, where its kinase activity is crucial for the ESCRT-dependent sorting of EGFR into intraluminal vesicles (Sun *et al*, 2013). Specifically, PIPKI γ -i5 synthesizes a pool of PI(4,5)P₂ that modulates the interaction between SNX5 and the ESCRT-0 protein, Hrs. This interaction prevents the degradation of Hrs, allowing it to bind ubiquitinated EGFR and initiate its sorting (Sun *et al*, 2013). Interestingly, Traikov and colleagues have shown that AP3-positive endosomes localize to actin filaments decorated by septins (Traikov *et al*, 2014). Depletion of SEPT6 or SEPT7 hampers the targeting of TSG101 to these endosomes and impairs the biogenesis of multivesicular bodies (Traikov *et al*, 2014). Therefore, it is tempting to speculate that septins and PIPKI γ may participate in the same pathway assisting cargo sorting on endosomal membranes.

Septin-dependent recruitment of PIPKI γ may secure localized PI(4,5)P₂ synthesis also at transient ER-PM contact sites, as described in Appendix A. In particular, septins shape plasmalemmal PI(4,5)P₂ microdomains around STIM1-Orai1 junctions (Katz *et al*, 2019; Sharma *et al*, 2013) and this may be achieved through the recruitment of PIPKI γ -i3/i5.

In conclusion, future research should investigate whether the septin-PIPKI γ module identified in this study plays a role in contexts beyond cytokinesis, especially considering the numerous subcellular localizations of septins (Benoit *et al*, 2023; Spiliotis & Nakos, 2021; Song *et al*, 2016)

5. Bibliography

- Abe M, Makino A, Hullin-Matsuda F, Kamijo K, Ohno-Iwashita Y, Hanada K, Mizuno H, Miyawaki A & Kobayashi T (2012) A Role for Sphingomyelin-Rich Lipid Domains in the Accumulation of Phosphatidylinositol-4,5-Bisphosphate to the Cleavage Furrow during Cytokinesis. *Mol Cell Biol* 32: 1396–1407
- Achildiev Cohen H, Zomot E, Nataniel T, Militsin R & Palty R (2023) The SOAR of STIM1 interacts with plasma membrane lipids to form ER-PM contact sites. *Cell Rep* 42: 112238
- Addi C, Bai J & Echard A (2018) Actin, microtubule, septin and ESCRT filament remodeling during late steps of cytokinesis. *Curr Opin Cell Biol* 50: 27–34
- Addi C, Presle A, Frémont S, Cuvelier F, Rocancourt M, Milin F, Schmutz S, Chamot-Rooke J, Douché T, Duchateau M, *et al* (2020) The Flemmingsome reveals an ESCRT-to-membrane coupling via ALIX/syntenin/syndecan-4 required for completion of cytokinesis. *Nat Commun* 11: 1–15
- Ageta-Ishihara N, Miyata T, Ohshima C, Watanabe M, Sato Y, Hamamura Y, Higashiyama T, Mazitschek R, Bito H & Kinoshita M (2013) Septins promote dendrite and axon development by negatively regulating microtubule stability via HDAC6-mediated deacetylation. *Nat Commun* 4: 1–11
- Ahmad M, Narayanasamy S, Ong HL & Ambudkar I (2022) STIM Proteins and Regulation of SOCE in ER-PM Junctions. *Biomolecules* 12
- Akil A, Peng J, Omrane M, Gondeau C, Desterke C, Marin M, Tronchère H, Taveneau C, Sar S, Briolotti P, *et al* (2016) Septin 9 induces lipid droplets growth by a phosphatidylinositol-5-phosphate and microtubule-dependent mechanism hijacked by HCV. *Nat Commun* 7
- Albarran L, Lopez JJ, Amor N Ben, Martin-Cano FE, Berna-Erro A, Smani T, Salido GM & Rosado JA (2016) Dynamic interaction of SARAF with STIM1 and Orai1 to modulate store-operated calcium entry. *Sci Rep* 6: 1–11
- Albarran L, Lopez JJ, Jardin I, Sanchez-Collado J, Berna-Erro A, Smani T, Camello PJ, Salido GM & Rosado JA (2018) EFHB is a novel cytosolic Ca²⁺ sensor that modulates STIM1-SARAF interaction. *Cell Physiol Biochem* 51: 1164–1178
- Amcheslavsky A, Wood ML, Yeromin A V., Parker I, Freites JA, Tobias DJ & Cahalan MD (2015) Molecular biophysics of Orai store-operated Ca²⁺ channels. *Biophys J* 108: 237–246
- Amine N El, Kechad A, Jananji S & Hickson GRX (2013) Opposing actions of septins and Sticky on Anillin promote the transition from contractile to midbody ring. *J Cell Biol* 203: 487–504
- Atilla-Gokcumen GE, Muro E, Relat-Goberna J, Sasse S, Bedigian A, Coughlin ML, Garcia-Manyes S & Eggert US (2014) Dividing cells regulate their lipid composition and localization. *Cell* 156: 428–439

- Baba T, Toth DJ, Sengupta N, Kim YJ & Balla T (2019) Phosphatidylinositol 4,5-bisphosphate controls Rab7 and PLEKHM 1 membrane cycling during autophagosome–lysosome fusion. *EMBO J* 38: 1–18
- Bai X, Bowen JR, Knox TK, Zhou K, Pendziwiat M, Kuhlenbäumer G, Sindelar C V. & Spiliotis ET (2013) Novel septin 9 repeat motifs altered in neuralgic amyotrophy bind and bundle microtubules. *J Cell Biol* 203: 895–905
- Bairstow SF, Ling K, Su X, Firestone AJ, Carbonara C & Anderson RA (2006) Type I γ 661 phosphatidylinositol phosphate kinase directly interacts with AP2 and regulates endocytosis. *J Biol Chem* 281: 20632–20642
- Balla T (2013) Phosphoinositides: Tiny lipids with giant impact on cell regulation. *Physiol Rev* 93: 1019–1137
- Balla T, Gulyas G, Kim YJ & Pemberton J (2021) PHOSPHOINOSITIDES AND CALCIUM SIGNALING. A MARRIAGE ARRANGED IN ER-PM CONTACT SITES. *Curr Opin Physiol*: 149–157
- Ban R, Irino Y, Fukami K & Tanaka H (2004) Human Mitotic Spindle-associated Protein PRC1 Inhibits MgcRacGAP Activity toward Cdc42 during the Metaphase. *J Biol Chem* 279: 16394–16402
- Banko M, Mucha-Kruczynska I, Weise C, Heyd F & Ewers H (2019) A homozygous genome-edited Sept2-EGFP fibroblast cell line. *Cytoskeleton* 76: 73–82
- Barisic M, Rajendraprasad G & Steblyanko Y (2021) The metaphase spindle at steady state – Mechanism and functions of microtubule poleward flux. *Semin Cell Dev Biol* 117: 99–117
- Barlan K & Gelfand VI (2017) Microtubule-based transport and the distribution, tethering, and organization of organelles. *Cold Spring Harb Perspect Biol* 9
- Basant A, Lekomtsev S, Tse YC, Zhang D, Longhini KM, Petronczki M & Glotzer M (2015) Aurora B Kinase Promotes Cytokinesis by Inducing Centralspindlin Oligomers that Associate with the Plasma Membrane. *Dev Cell* 33: 204–215
- Bastos RN, Penate X, Bates M, Hammond D & Barr FA (2012) CYK4 inhibits Rac1-dependent PAK1 and ARHGEF7 effector pathways during cytokinesis. *J Cell Biol* 198: 865–880
- Beber A, Taveneau C, Nania M, Tsai FC, Di Cicco A, Bassereau P, Lévy D, Cabral JT, Isambert H, Mangenot S, *et al* (2019) Membrane reshaping by micrometric curvature sensitive septin filaments. *Nat Commun* 10
- Benoit B, Poüs C & Baillet A (2023) Septins as membrane influencers: direct play or in association with other cytoskeleton partners. *Front Cell Dev Biol* 11: 1–10
- Berridge MJ (2012) Calcium signalling remodelling and disease. *Biochem Soc Trans* 40: 297–309
- Berridge MJ, Bootman MD & Roderick HL (2003) Calcium signalling: Dynamics, homeostasis and remodelling. *Nat Rev Mol Cell Biol* 4: 517–529

- Bertin A, McMurray MA, Thai L, Garcia G, Votin V, Grob P, Allyn T, Thorner J & Nogales E (2010a) Phosphatidylinositol-4,5-bisphosphate Promotes Budding Yeast Septin Filament Assembly and Organization. *J Mol Biol* 404: 711–731
- Bertin A, McMurray MA, Thai L, Iii GG, Votin V, Grob P, Allyn T, Thorner J & Nogales E (2010b) Budding Yeast Septin Filament Assembly and Organization. *J Mol Biol* 404: 711–731
- Bhardwaj R, Müller HM, Nickel W & Seedorf M (2013) Oligomerization and Ca²⁺/calmodulin control binding of the ER Ca²⁺ -sensors STIM1 and STIM2 to plasma membrane lipids. *Biosci Rep* 33
- Bian X, Saheki Y & De Camilli P (2018) Ca²⁺ releases E-Syt1 autoinhibition to couple ER -plasma membrane tethering with lipid transport . *EMBO J* 37: 219–234
- Birkenfeld J, Nalbant P, Bohl BP, Pertz O, Hahn KM & Bokoch GM (2007) GEF-H1 Modulates Localized RhoA Activation during Cytokinesis under the Control of Mitotic Kinases. *Dev Cell* 12: 699–712
- Bjursell G & Reichard P (1973) Effects of thymidine on deoxyribonucleoside triphosphate pools and deoxyribonucleic acid synthesis in Chinese hamster ovary cells. *J Biol Chem* 248: 3904–3909
- Bolz S, Kaempf N, Puchkov D & Perrais D (2023) Report Synaptotagmin 1-triggered lipid signaling facilitates coupling of exo- and endocytosis Report Synaptotagmin 1-triggered lipid signaling facilitates coupling of exo- and endocytosis. *Neuron* 111: 1–10
- Bos JL, Rehmann H & Wittinghofer A (2007) GEFs and GAPs: Critical Elements in the Control of Small G Proteins (DOI:10.1016/j.cell.2007.05.018). *Cell* 130: 385
- van den Bout I & Divecha N (2009) PIP5K-driven PtdIns(4,5)P₂ synthesis: Regulation and cellular functions. *J Cell Sci* 122: 3837–3850
- Bowen JR, Hwang D, Bai X, Roy D & Spiliotis ET (2011) Septin GTPases spatially guide microtubule organization and plus end dynamics in polarizing epithelia. *J Cell Biol* 194: 187–197
- Bradford MM (1976) A Rapid and Sensitive Method for the Quantitation of Microgram Quantities of Protein Utilizing the Principle of Protein-Dye Binding. *Anal Biochem* 72: 248–254
- Bridges AA, Jentsch MS, Oakes PW, Occhipinti P & Gladfelter AS (2016) Micron-scale plasma membrane curvature is recognized by the septin cytoskeleton. *J Cell Biol* 213: 23–32
- Brown FD, Rozelle AL, Yin HL, Balla T & Donaldson JG (2001) Phosphatidylinositol 4,5-bisphosphate and Arf6-regulated membrane traffic. *J Cell Biol* 154: 1007–1017
- Bulinski JC, Richards JE & Piperno G (1988) Posttranslational Modifications of ct Tubulin : Detyrosination and Acetylation Differentiate Populations of Interphase

- Microtubules in Cultured Cells. 106: 1213–1220
- Bulley SJ, Clarke JH, Droubi A, Giudici ML & Irvine RF (2015) Exploring phosphatidylinositol 5-phosphate 4-kinase function. *Adv Biol Regul* 57: 193–202
- Bultsma Y, Keune WJ & Divecha N (2010) PIP4K β interacts with and modulates nuclear localization of the high-activity PtdIns5 P-4-kinase isoform PIP4K α . *Biochem J* 430: 223–235
- Caldieri G, Barbieri E, Nappo G, Raimondi A & Bonora M (2017) Reticulon3-dependent ER-PM contact sites control EGFR non-clathrin endocytosis. *Science (80-)* 356: 617–624
- Calloway N, Owens T, Corwith K, Rodgers W, Holowka D & Baird B (2011) Stimulated association of STIM1 and Orai1 is regulated by the balance of PtdIns(4,5)P₂ between distinct membrane pools. *J Cell Sci* 124: 2602–2610
- Calvo F, Ranftl R, Hooper S, Farrugia AJ, Moeendarbary E, Bruckbauer A, Batista F, Charras G & Sahai E (2015) Cdc42EP3/BORG2 and Septin Network Enables Mechano-transduction and the Emergence of Cancer-Associated Fibroblasts. *Cell Rep* 13: 2699–2714
- Canman JC, Lewellyn L, Laband K, Smerdon SJ, Desai A, Bowerman B & Oegema K (2008) Inhibition of Rac by the GAP Activity of Centralspindlin Is Essential for Cytokinesis. *Science (80-)*: 1543–1546
- Cannon KS, Woods BL, Crutchley JM & Gladfelter AS (2019) An amphipathic helix enables septins to sense micrometer-scale membrane curvature. *J Cell Biol* 218: 1128–1137
- Carim SC & Hickson GRX (2023) The Rho1 GTPase controls anillo-septin assembly to facilitate contractile ring closure during cytokinesis. *iScience*: 106903
- Carim SC, Kechad A & Hickson GRX (2020) Animal Cell Cytokinesis: The Rho-Dependent Actomyosin-Anilloseptin Contractile Ring as a Membrane Microdomain Gathering, Compressing, and Sorting Machine. *Front Cell Dev Biol* 8: 1–26
- Carrasco S & Meyer T (2011) STIM proteins and the endoplasmic reticulum-plasma membrane junctions. *Annu Rev Biochem* 80: 973–1000
- Cauvin C & Echard A (2015) Phosphoinositides: Lipids with informative heads and mastermind functions in cell division. *Biochim Biophys Acta - Mol Cell Biol Lipids* 1851: 832–843
- Cauvin C, Rosendale M, Gupta-Rossi N, Rocancourt M, Larraufie P, Salomon R, Perrais D & Echard A (2016) Rab35 GTPase Triggers Switch-like Recruitment of the Lowe Syndrome Lipid Phosphatase OCRL on Newborn Endosomes. *Curr Biol* 26: 120–128
- Cavini IA, Leonardo DA, Rosa H V.D., Castro DKSV, D’Muniz Pereira H, Valadares NF, Araujo APU & Garratt RC (2021) The Structural Biology of Septins and

Their Filaments: An Update. *Front Cell Dev Biol* 9: 1–25

Chakrabarti P, Kolay S, Yadav S, Kumari K, Nair A, Trivedi D & Raghu P (2015) A dPIP5K Dependent Pool of Phosphatidylinositol 4,5 Bisphosphate (PIP₂) Is Required for G-Protein Coupled Signal Transduction in Drosophila Photoreceptors. *PLoS Genet* 11

Chang C, Hsieh T, Yang TT, Rothberg KG, Azizoglu DB, Volk E, Liao J & Liou J (2013) Feedback Regulation of Receptor-Induced Ca²⁺ Signaling Mediated by E-Syt1 and Nir2 at Endoplasmic Reticulum-Plasma Membrane Junctions. *CellReports* 5: 813–825

Chang CL & Liou J (2015) Phosphatidylinositol 4, 5-bisphosphate homeostasis regulated by Nir2 and Nir3 proteins at endoplasmic reticulum-plasma membrane junctions. *J Biol Chem* 290: 14289–14301

Cheffings TH, Burroughs NJ & Balasubramanian MK (2016) Actomyosin Ring Formation and Tension Generation in Eukaryotic Cytokinesis. *Curr Biol* 26: R719–R737

Chen TY, Lin TC, Kuo PL, Chen ZR, Cheng H ling, Chao YY, Syu JS, Lu FI & Wang CY (2021) Septin 7 is a centrosomal protein that ensures S phase entry and microtubule nucleation by maintaining the abundance of p150glued. *J Cell Physiol* 236: 2706–2724

Chen YJ, Chang CL, Lee WR & Liou J (2017) RAS SF4 controls SOCE and ER-PM junctions through regulation of PI(4,5)P₂. *J Cell Biol* 216: 2011–2025

Chesneau L, Dambournet D, MacHicoane M, Kouranti I, Fukuda M, Goud B & Echard A (2012) An ARF6/Rab35 GTPase cascade for endocytic recycling and successful cytokinesis. *Curr Biol* 22: 147–153

Cheung HYF, Coman C, Westhoff P, Manke M, Sickmann A, Borst O, Gawaz M, Watson SP, Heemskerk JWM & Ahrends R (2021) Targeted Phosphoinositides Analysis Using High-Performance Ion Chromatography-Coupled Selected Reaction Monitoring Mass Spectrometry. *J Proteome Res* 20: 3114–3123

Chircop M (2014) Rho GTPases as regulators of mitosis and cytokinesis in mammalian cells. *Small GTPases* 5

Choi S, Thapa N, Tan X, Hedman AC & Anderson RA (2015) PIP kinases define PI_{4,5}P₂ signaling specificity by association with effectors. *Biochim Biophys Acta - Mol Cell Biol Lipids* 1851: 711–723

Christ L, Wenzel EM, Liestøl K, Raiborg C, Campsteijn C & Stenmark H (2016) ALIX and ESCRT-I/III function as parallel ESC RT-III recruiters in cytokinetic abscission. *J Cell Biol* 212: 499–513

Chung J, Torta F, Masai K, Lucast L, Czaplá H, Tanner LB, Narayanaswamy P, Wenk MR, Nakatsu F & De Camilli P (2015) PI₄P/phosphatidylserine countertransport at ORP5- and ORP8-mediated ER - Plasma membrane contacts. *Science (80-)* 349: 428–432

- Clapham DE (2007) Calcium Signaling. *Cell* 131: 1047–1058
- Dagan I & Palty R (2021) Regulation of store-operated Ca^{2+} entry by saraf. *Cells* 10
- Dambournet D, MacHicoane M, Chesneau L, Sachse M, Rocancourt M, El Marjou A, Formstecher E, Salomon R, Goud B & Echard A (2011) Rab35 GTPase and OCRL phosphatase remodel lipids and F-actin for successful cytokinesis. *Nat Cell Biol* 13: 981–988
- Deb BK, Chakraborty P, Gopurappilly R & Hasan G (2020) SEPT7 regulates Ca^{2+} entry through Orai channels in human neural progenitor cells and neurons. *Cell Calcium* 90: 102252
- Deb BK & Hasan G (2016) Regulation of store-operated Ca^{2+} entry by septins. *Front Cell Dev Biol* 4: 1–7
- Deb BK, Pathak T & Hasan G (2016) Store-independent modulation of Ca^{2+} entry through Orai by Septin 7. *Nat Commun* 7
- Diesenberg K, Beerbaum M, Fink U, Schmieder P & Krauss M (2015) SEPT9 negatively regulates ubiquitin-dependent downregulation of EGFR. *J Cell Sci* 128: 397–407
- Dolat L, Hunyara JL, Bowen JR, Karasmanis EP, Elgawly M, Galkin VE & Spiliotis ET (2014) Septins promote stress fiber-mediated maturation of focal adhesions and renal epithelial motility. *J Cell Biol* 207: 225–235
- Dolat L & Spiliotis ET (2016) Septins promote macropinosome maturation and traffic to the lysosome by facilitating membrane fusion. *J Cell Biol* 214: 517–527
- Dong R, Saheki Y, Swarup S, Lucast L, Harper JW & De Camilli P (2016) Endosome-ER Contacts Control Actin Nucleation and Retromer Function through VAP-Dependent Regulation of PI4P. *Cell* 166: 408–423
- Dong R, Zhu T, Benedetti L, Gowrishankar S, Deng H, Cai Y, Wang X, Shen K & De Camilli P (2018) The inositol 5-phosphatase INPP5K participates in the fine control of ER organization. *J Cell Biol* 217: 3577–3592
- Doughman RL, Firestone AJ & Anderson RA (2003) Phosphatidylinositol phosphate kinases put PI4,5P2 in its place. *J Membr Biol* 194: 77–89
- Douglas ME, Davies T & Joseph N (2010) Aurora B and 14-3-3 Coordinately Regulate Clustering of Centralspindlin during Cytokinesis. *Curr Biol* 20: 927–933
- Echard A (2012) Phosphoinositides and cytokinesis: The ‘PIP’ of the iceberg. *Cytoskeleton* 69: 893–912
- Emoto K, Inadome H, Kanaho Y, Narumiya S & Umeda M (2005) Local change in phospholipid composition at the cleavage furrow is essential for completion of cytokinesis. *J Biol Chem* 280: 37901–37907
- Enomoto T (1996) Microtubule Disruption Induces the Formation of Actin Stress

Fibers and Focal Adhesions in Cultured Cells : Possible Involvement of the Rho Signal Cascade. 326: 317–326

Estey MP, Di Ciano-Oliveira C, Froese CD, Bejide MT & Trimble WS (2010) Distinct roles of septins in cytokinesis: SEPT9 mediates midbody abscission. *J Cell Biol* 191: 741–749

Estey MP, Di Ciano-Oliveira C, Froese CD, Fung KYY, Steels JD, Litchfield DW & Trimble WS (2013) Mitotic regulation of SEPT9 protein by cyclin-dependent kinase 1 (Cdk1) and pin1 protein is important for the completion of cytokinesis. *J Biol Chem* 288: 30075–30086

Fan W, Nassiri A & Zhong Q (2011) Autophagosome targeting and membrane curvature sensing by Barkor/Atg14(L). *Proc Natl Acad Sci U S A* 108: 7769–7774

Farrugia AJ & Calvo F (2016) The Borg family of Cdc42 effector proteins Cdc42EP1-5. *Biochem Soc Trans* 44: 1709–1716

Farrugia AJ, Rodríguez J, Orgaz JL, Lucas M, Sanz-Moreno V & Calvo F (2020) CDC42EP5/BORG3 modulates SEPT9 to promote actomyosin function, migration, and invasion. *J Cell Biol* 219

Fededa JP & Gerlich DW (2012) Molecular control of animal cell cytokinesis. *Nat Cell Biol* 14: 440–447

Field SJ, Madson N, Kerr ML, Galbraith KAA, Kennedy CE, Tahiliani M, Wilkins A & Cantley LC (2005) PtdIns(4,5)P₂ Functions at the Cleavage Furrow during Cytokinesis. *Curr Biol* 15: 1407–1412

Fielding AB, Schonteich E, Matheson J, Wilson G, Yu X, Hickson GRX, Srivastava S, Baldwin SA, Prekeris R & Gould GW (2005) Rab11-FIP3 and FIP4 interact with Arf6 and the Exocyst to control membrane traffic in cytokinesis. *EMBO J* 24: 3389–3399

Fish KN (2009) Total Internal Reflection Fluorescence (TIRF) Microscopy. *Curr Protoc Cytom* Vol.22: 273–275

Ford SK & Pringle JR (1991) Cellular morphogenesis in the *Saccharomyces cerevisiae* cell cycle: Localization of the CDC11 gene product and the timing of events at the budding site. *Dev Genet* 12: 281–292

Frémont S & Echard A (2018) Membrane Traffic in the Late Steps of Cytokinesis. *Curr Biol* 28: R458–R470

Froidevaux-Klipfel L, Targa B, Cantaloube I, Ahmed-Zaïd H, Poüs C & Baillet A (2015) Septin cooperation with tubulin polyglutamylation contributes to cancer cell adaptation to taxanes. *Oncotarget* 6: 36063–36080

Fu L, Xiaoyan W, Ying Y, Mingzhe M & XingZhong W (2023) Septin11 promotes hepatocellular carcinoma cell motility by activating RhoA to regulate cytoskeleton and cell adhesion. *Cell Death Dis*

- Gai M, Camera P, Dema A, Bianchi F, Berto G, Scarpa E, Germena G & Di Cunto F (2011) Citron kinase controls abscission through RhoA and anillin. *Mol Biol Cell* 22: 3768–3778
- Gaietta GM, Giepmans BNG, Deerinck TJ, Smith WB, Ngan L, Llopis J, Adams SR, Tsien RY & Ellisman MH (2006) Golgi twins in late mitosis revealed by genetically encoded tags for live cell imaging and correlated electron microscopy. *Proc Natl Acad Sci U S A* 103: 17777–17782
- Gambarotto D, Hamel V & Guichard P (2021) Ultrastructure expansion microscopy (U-ExM). *Methods Cell Biol* 161: 57–81
- Gambarotto D, Zwettler FU, Le Guennec M, Schmidt-Cernohorska M, Fortun D, Borgers S, Heine J, Schloetel JG, Reuss M, Unser M, *et al* (2019) Imaging cellular ultrastructures using expansion microscopy (U-ExM). *Nat Methods* 16: 71–74
- Ghossoub R, Hu Q, Failler M, Rouyez MC, Spitzbarth B, Mostowy S, Wolfrum U, Saunier S, Cossart P, Nelson WJ, *et al* (2013) Septins 2, 7 and 9 and MAP4 colocalize along the axoneme in the primary cilium and control ciliary length. *J Cell Sci* 126: 2583–2594
- Giordano F, Saheki Y, Idevall-Hagren O, Colombo SF, Pirruccello M, Milosevic I, Gracheva EO, Bagriantsev SN, Borgese N & De Camilli P (2013) PI(4,5)P2-Dependent and Ca²⁺-Regulated ER-PM interactions mediated by the extended synaptotagmins. *Cell* 153: 1494
- Glotzer M (2009) The 3Ms of central spindle assembly: Microtubules, motors and MAPs. *Nat Rev Mol Cell Biol* 10: 9–20
- Goliand I, Adar-Levor S, Segal I, Nachmias D, Dadosh T, Kozlov MM & Elia N (2018) Resolving ESCRT-III Spirals at the Intercellular Bridge of Dividing Cells Using 3D STORM. *Cell Rep* 24: 1756–1764
- Goss JW & Toomre DK (2008) Both daughter cells traffic and exocytose membrane at the cleavage furrow during mammalian cytokinesis. *J Cell Biol* 181: 1047–1054
- Gromley A, Yeaman C, Rosa J, Redick S, Chen CT, Mirabelle S, Guha M, Sillibourne J & Doxsey SJ (2005) Centriolin anchoring of exocyst and SNARE complexes at the midbody is required for secretory-vesicle-mediated abscission. *Cell* 123: 75–87
- Gudlur A, Zeraik AE, Hirve N & Hogan PG (2020) STIM calcium sensing and conformational change. *J Physiol* 2: 1–17
- Gudlur A, Zeraik AE, Hirve N, Rajanikanth V, Bobkov AA, Ma G, Zheng S, Wang Y, Zhou Y, Komives EA, *et al* (2018) Calcium sensing by the STIM1 ER-luminal domain. *Nat Commun* 9
- Gulluni F, Prever L, Li H, Krafcikova P, Corrado I, Lo T, Margaria JP, Chen A, Santis MC De, Cnudde SJ, *et al* (2022) PI(3,4)P2-mediated cytokinetic abscission prevents early senescence and cataract formation. *Science* (80-) 374

- Gurung R, Tan A, Ooms LM, McGrath MJ, Huysmans RD, Munday AD, Prescott M, Whisstock JC & Mitchell CA (2003) Identification of a novel domain in two mammalian inositol-polyphosphate 5-phosphatases that mediates membrane ruffle localization: The inositol 5-phosphatase SKIP localizes to the endoplasmic reticulum and translocates to membrane ruffles following epide. *J Biol Chem* 278: 11376–11385
- Haarer BK & Pringle JR (1987) Immunofluorescence localization of the *Saccharomyces cerevisiae* CDC12 gene product to the vicinity of the 10-nm filaments in the mother-bud neck. *Mol Cell Biol* 7: 3678–3687
- Hagiwara A, Tanaka Y, Hikawa R, Morone N, Kusumi A, Kimura H & Kinoshita M (2011) Submembranous septins as relatively stable components of actin-based membrane skeleton. *Cytoskeleton* 68: 512–525
- Hall PA & Russell SEH (2004) The pathobiology of the septin gene family. *J Pathol* 204: 489–505
- Halstead JR, Savaskan NE, Van Den Bout I, Van Horck F, Hajdo-Milasinovic A, Snell M, Keune WJ, Ten Klooster JP, Hordijk PL & Divecha N (2010) Rac controls PIP5K localisation and PtdIns(4,5)P2 synthesis, which modulates vinculin localisation and neurite dynamics. *J Cell Sci* 123: 3535–3546
- Hammond GRV & Balla T (2015) Polyphosphoinositide binding domains: Key to inositol lipid biology. *Biochim Biophys Acta - Mol Cell Biol Lipids* 1851: 746–758
- Hartwell LH (1971) Genetic control of the cell division cycle in yeast: IV. Genes controlling bud emergence and cytokinesis. *Exp Cell Res* 69: 265–276
- He B, Xi F, Zhang X, Zhang J & Guo W (2007) Exo70 interacts with phospholipids and mediates the targeting of the exocyst to the plasma membrane. *EMBO J* 26: 4053–4065
- Hernández-Rodríguez Y & Momany M (2012) Posttranslational modifications and assembly of septin heteropolymers and higher-order structures. *Curr Opin Microbiol* 15: 660–668
- Hilary Russell SE & Hall PA (2011) Septin genomics: a road less travelled. *Biol Chem* 392: 763–767
- Hirose K, Kawashima T, Iwamoto I, Nosaka T & Kitamura T (2001) MgcRacGAP Is Involved in Cytokinesis through Associating with Mitotic Spindle and Midbody. *J Biol Chem* 276: 5821–5828
- Holder J, Poser E & Barr FA (2019) Getting out of mitosis: spatial and temporal control of mitotic exit and cytokinesis by PP1 and PP2A. *FEBS Lett* 593: 2908–2924
- Honda A, Nogami M, Yokozeki T, Yamazaki M, Nakamura H, Watanabe H, Kawamoto K, Nakayama K, Morris AJ, Frohman MA, *et al* (1999) Phosphatidylinositol 4-phosphate 5-kinase α is a downstream effector of the small G protein ARF6 in membrane ruffle formation. *Cell* 99: 521–532

- Hu C-K, Coughlin M & Mitchison TJ (2012a) Midbody assembly and its regulation during cytokinesis.
- Hu J, Bai X, Bowen JR, Dolat L, Korobova F, Yu W, Baas PW, Svitkina T, Gallo G & Spiliotis ET (2012b) Septin-driven coordination of actin and microtubule remodeling regulates the collateral branching of axons. *Curr Biol* 22: 1109–1115
- Hu Q, Milenkovic L, Jin H, Scott MP, Nachury M V., Spiliotis ET & Nelson WJ (2010) A septin diffusion barrier at the base of the primary cilium maintains ciliary membrane protein distribution. *Science* (80-) 329: 436–439
- Hu Q, Nelson WJ & Spiliotis ET (2008) Forchlorfenuron Alters Mammalian Septin Assembly , Organization , and Dynamics. 283: 29563–29571
- Hutterer A, Glotzer M & Mishima M (2009) Clustering of Centralspindlin Is Essential for Its Accumulation to the Central Spindle and the Midbody. *Curr Biol* 19: 2043–2049
- Hyung HL, Elia N, Ghirlando R, Lippincott-Schwartz J & Hurley JH (2008) Midbody targeting of the ESCRT machinery by a noncanonical coiled coil in CEP55. *Science* (80-) 322: 576–580
- Iannantuono NVG & Emery G (2021) Rab11FIP1 maintains Rab35 at the intercellular bridge to promote actin removal and abscission. *J Cell Sci* 134
- Idevall-Hagren O, Lü A, Xie B & De Camilli P (2015) Triggered Ca²⁺ influx is required for extended synaptotagmin 1-induced ER-plasma membrane tethering . *EMBO J* 34: 2291–2305
- Iv F, Martins CS, Castro-Linares G, Taveneau C, Barbier P, Verdier-Pinard P, Camoin L, Audebert S, Tsai FC, Ramond L, *et al* (2021) Insights into animal septins using recombinant human septin octamers with distinct SEPT9 isoforms. *J Cell Sci* 134: 1–19
- Ivanov AI, Le HT, Naydenov NG & Rieder F (2021) Novel Functions of the Septin Cytoskeleton: Shaping Up Tissue Inflammation and Fibrosis. *Am J Pathol* 191: 40–51
- Jantsch-Plunger V, Gönczy P, Romano A, Schnabel H, Hamill D, Schnabel R, Hyman AA & Glotzer M (2000) CYK-4: A Rho family GTPase activating protein (GAP) required for central spindle formation and cytokinesis. *J Cell Biol* 149: 1391–1404
- Jardín I, Albarran L, Salido GM, López JJ, Sage SO & Rosado JA (2018) Fine-tuning of store-operated calcium entry by fast and slow Ca²⁺-dependent inactivation: Involvement of SARAF. *Biochim Biophys Acta - Mol Cell Res* 1865: 463–469
- Jha A, Ahuja M, Maléth J, Moreno Claudia C, Yuan Joseph J, Kim MS & Muallem S (2013) The STIM1 CTID domain determines access of SARAF to SOAR to regulate Orai1 channel function. *J Cell Biol* 202: 71–78
- Jinek M, Chylinski K, Fonfara I, Hauer M, Doudna JA & Charpentier E (2012) A

Programmable Dual-RNA – Guided. *Science (80-)* 337: 816–822

Joberty G, Perlungher RR, Sheffield PJ, Kinoshita M, Noda M, Haystead T & Macara IG (2001) Borg proteins control septin organization and are negatively regulated by Cdc42. *Nat Cell Biol* 3: 861–866

Johannes A.G. Rhodin (1974) *Histology; a Text and Atlas*

Joo E, Surka MC & Trimble WS (2007) Mammalian SEPT2 Is Required for Scaffolding Nonmuscle Myosin II and Its Kinases. *Dev Cell* 13: 677–690

Joseph N, Hutterer A, Poser I & Mishima M (2012) ARF6 GTPase protects the post-mitotic midbody from 14-3-3-mediated disintegration. *EMBO J* 31: 2604–2614

Kahlfeldt N, Vahedi-Faridi A, Koo SJ, Schäfer JG, Krainer G, Keller S, Saenger W, Krauss M & Haucke V (2010) Molecular basis for association of PIPKly-p90 with clathrin adaptor AP-2. *J Biol Chem* 285: 2734–2749

Kang F, Zhou M, Huang X, Fan J, Wei L, Boulanger J, Liu Z, Salamero J, Liu Y & Chen L (2019) E-syt1 Re-arranges STIM1 Clusters to Stabilize Ring-shaped ER-PM Contact Sites and Accelerate Ca²⁺ Store Replenishment. *Sci Rep* 9: 1–11

Karasmanis EP, Hwang D, Nakos K, Bowen JR, Angelis D & Spiliotis ET (2019) A Septin Double Ring Controls the Spatiotemporal Organization of the ESCRT Machinery in Cytokinetic Abscission. *Curr Biol* 29: 2174-2182.e7

Kasahara K, Nakayama Y, Nakazato Y, Ikeda K, Kuga T & Yamaguchi N (2007) Src signaling regulates completion of abscission in cytokinesis through ERK/MAPK activation at the midbody. *J Biol Chem* 282: 5327–5339

Katja Schmidt & Benjamin J. Nichols (2004) A Barrier to Lateral Diffusion in the Cleavage Furrow of Dividing Mammalian Cells. *Curr Biol* 14: ARTMED1118

Katz ZB, Zhang C, Quintana A, Lillemeier BF & Hogan PG (2019) Septins organize endoplasmic reticulum-plasma membrane junctions for STIM1-ORAI1 calcium signalling. *Sci Rep* 9: 1–17

Kawashima T, Hirose K, Satoh T, Kaneko A, Ikeda Y, Kaziro Y, Nosaka T & Kitamura T (2000) MgcRacGAP is involved in the control of growth and differentiation of hematopoietic cells. *Blood* 96: 2116–2124

Kim J & Cooper JA (2018) Septins regulate junctional integrity of endothelial monolayers. *Mol Biol Cell* 29: 1693–1703

Kim J & Cooper JA (2021) Junctional Localization of Septin 2 Is Required for Organization of Junctional Proteins in Static Endothelial Monolayers. *Arterioscler Thromb Vasc Biol* 41: 346–359

Kim YJ, Guzman-Hernandez ML, Wisniewski E & Balla T (2015) Phosphatidylinositol-Phosphatidic Acid Exchange by Nir2 at ER-PM Contact Sites Maintains Phosphoinositide Signaling Competence. *Dev Cell* 33: 549–561

- Kinoshita M (2003) Assembly of Mammalian Septins. *J Biochem* 134: 491–496
- Kinoshita M, Field CM, Coughlin ML, Straight AF & Mitchison TJ (2002) Self- and Actin-Templated Assembly of Mammalian Septins. *Dev Cell* 3: 791–802
- Kirchhausen T, Macia E & Pelish HE (2004) USE OF DYNASORE, THE SMALL MOLECULE INHIBITOR OF DYNAMIN, IN THE REGULATION OF ENDOCYTOSIS. *Brain Lang* 88: 1–20
- Von Kleist L, Stahlschmidt W, Bulut H, Gromova K, Puchkov D, Robertson MJ, MacGregor KA, Tomlin N, Pechstein A, Chau N, *et al* (2011) Role of the clathrin terminal domain in regulating coated pit dynamics revealed by small molecule inhibition. *Cell* 146: 471–484
- Klinkert K & Echard A (2016) Rab35 GTPase: A Central Regulator of Phosphoinositides and F-actin in Endocytic Recycling and Beyond. *Traffic* 17: 1063–1077
- Korzeniowski MK, Popovic MA, Szentpetery Z, Varnai P, Stojilkovic SS & Balla T (2009) Dependence of STIM1/Orai1-mediated calcium entry on plasma membrane phosphoinositides. *J Biol Chem* 284: 21027–21035
- Kotýnková K, Su KC, West SC & Petronczki M (2016) Plasma Membrane Association but Not Midzone Recruitment of RhoGEF ECT2 Is Essential for Cytokinesis. *Cell Rep* 17: 2672–2686
- Kouranti I, Sachse M, Arouche N, Goud B & Echard A (2006) Rab35 Regulates an Endocytic Recycling Pathway Essential for the Terminal Steps of Cytokinesis. *Curr Biol* 16: 1719–1725
- Krauss M, Kinuta M, Wenk MR, De Camilli P, Takei K & Haucke V (2003) ARF6 stimulates clathrin/AP-2 recruitment to synaptic membranes by activating phosphatidylinositol phosphate kinase type I γ . *J Cell Biol* 162: 113–124
- Krauss M, Kukhtina V, Pechstein A & Haucke V (2006) Stimulation of phosphatidylinositol kinase type I-mediated phosphatidylinositol (4,5)-bisphosphate synthesis by AP-2 μ -cargo complexes. *Proc Natl Acad Sci U S A* 103: 11934–11939
- Kremer BE, Adang LA & Macara IG (2007a) Septins Regulate Actin Organization and Cell-Cycle Arrest through Nuclear Accumulation of NCK Mediated by SOCS7. *Cell* 130: 837–850
- Kremer BE, Adang LA & Macara IG (2007b) Septins Regulate Actin Organization and Cell-Cycle Arrest through Nuclear Accumulation of NCK Mediated by SOCS7. *Cell* 130: 837
- Kremer BE, Haystead T & Macara IG (2005) Mammalian septins regulate microtubule stability through interaction with the microtubule-binding protein MAP4. *Mol Biol Cell* 16
- Krendel M, Zenke FT & Bokoch GM (2003) Nucleotide exchange factor GEF-H1 mediates cross-talk between microtubules and the actin cytoskeleton. 4

- Kumari A, Ghosh A, Kolay S & Raghu P (2022) Septins tune lipid kinase activity and PI(4,5)P₂ turnover during G-protein-coupled PLC signalling in vivo. *Life Sci Alliance* 5: 1–14
- Kuzmić M, Linares GC, Fialová JL, Iv F, Salaün D, Llewellyn A, Gomes M, Belhabib M, Liu Y, Asano K, *et al* (2022) Septin-microtubule association via a motif unique to isoform 1 of septin 9 tunes stress fibers. *J Cell Sci* 135
- Lacalle RA, De Karam JC, Martínez-Muñoz L, Artetxe I, Peregil RM, Sot J, Rojas AM, Goñi FM, Mellado M & Mañes S (2015) Type I phosphatidylinositol 4-phosphate 5-kinase homoand heterodimerization determines its membrane localization and activity. *FASEB J* 29: 2371–2385
- Laemmli UK (1970) 227680a0. *Nature* 227: 680–685
- Le OTT, Cho OY, Tran MH, Kim JA, Chang S, Jou I & Lee SY (2015) Phosphorylation of phosphatidylinositol 4-phosphate 5-kinase γ by Akt regulates its interaction with talin and focal adhesion dynamics. *Biochim Biophys Acta - Mol Cell Res* 1853: 2432–2443
- Leipe DD, Wolf YI, Koonin E V. & Aravind L (2002) Classification and evolution of P-loop GTPases and related ATPases. *J Mol Biol* 317: 41–72
- Lekomtsev S, Su KC, Pye VE, Blight K, Sundaramoorthy S, Takaki T, Collinson LM, Cherepanov P, Divecha N & Petronczki M (2012) Centralspindlin links the mitotic spindle to the plasma membrane during cytokinesis. *Nature* 492: 276–279
- Leonardo DA, Cavini IA, Sala FA, Mendonça DC, Rosa H V.D., Kumagai PS, Crusca E, Valadares NF, Marques IA, Brandão-Neto J, *et al* (2021) Orientational Ambiguity in Septin Coiled Coils and its Structural Basis. *J Mol Biol* 433
- Lera-Ramirez M, Nédélec FJ & Tran PT (2022) Microtubule rescue at Midzone edges promotes overlap stability and prevents spindle collapse during anaphase B. *Elife* 11: 1–36
- Li C, Qian T, He R, Wan C, Liu Y & Yu H (2021) Endoplasmic Reticulum–Plasma Membrane Contact Sites: Regulators, Mechanisms, and Physiological Functions. *Front Cell Dev Biol* 9
- Li P (2021) Isomer Selective Comprehensive Lipidomics Analysis of Phosphoinositides in Biological Samples by Liquid Chromatography with Data Independent Acquisition Tandem Mass Spectrometry. *Anal Chem* 93: 9583–9592
- Li Z, Lu J, Xu P, Xie X, Chen L & Xu T (2007) Mapping the interacting domains of STIM1 and Orai1 in Ca²⁺ release-activated Ca²⁺ channel activation. *J Biol Chem* 282: 29448–29456
- Ligasová A & Koberna K (2021) Strengths and weaknesses of cell synchronization protocols based on inhibition of dna synthesis. *Int J Mol Sci* 22
- Ling K, Bairstow SF, Carbonara C, Turbin DA, Huntsman DG & Anderson RA (2007)

- Type I γ phosphatidylinositol phosphate kinase modulates adherens junction and E-cadherin trafficking via a direct interaction with μ 1B adaptin. *J Cell Biol* 176: 343–353
- Ling K, Doughman RL, Firestone AJ, Bunce MW & Anderson RA (2002) Type I γ phosphatidylinositol phosphate kinase targets and regulates focal adhesions. *Nature* 420: 89–93
- Ling K, Doughman RL, Iyer V V., Firestone AJ, Bairstow SF, Mosher DF, Schaller MD & Anderson RA (2003) Tyrosine phosphorylation of type I γ phosphatidylinositol phosphate kinase by Src regulates an integrin-talin switch. *J Cell Biol* 163: 1339–1349
- Liou J, Fivaz M, Inoue T & Meyer T (2007) Live-cell imaging reveals sequential oligomerization and local plasma membrane targeting of stromal interaction molecule 1 after Ca²⁺ store depletion. *Proc Natl Acad Sci U S A* 104: 9301–9306
- Liou J, Kim Lyang M & Heo W Do (2005) STIM Is a Ca²⁺ Sensor Essential for Ca²⁺-Store-Depletion- Triggered Ca²⁺ Influx. *Curr Biol* 23: 1–7
- Liou J & Meyer T (2013) Septins Set the Stage for Orai1 to Bind STIM1 at ER-PM Junctions. *Dev Cell* 26: 116–118
- Liu J, Fairn GD, Ceccarelli DF, Sicheri F & Wilde A (2012) Cleavage furrow organization requires PIP 2-mediated recruitment of anillin. *Curr Biol* 22: 64–69
- Macia E, Partisani M, Favard C, Mortier E, Zimmermann P, Carlier MF, Gounon P, Luton F & Franco M (2008) The pleckstrin homology domain of the Arf6-specific exchange factor EFA6 localizes to the plasma membrane by interacting with phosphatidylinositol 4,5-bisphosphate and F-actin. *J Biol Chem* 283: 19836–19844
- Maiato H & Logarinho E (2014) Mitotic spindle multipolarity without centrosome amplification. *Nat Cell Biol* 16: 386–394
- Maib H & Murray DH (2022) A mechanism for exocyst-mediated tethering via Arf6 and PIP5K1C-driven phosphoinositide conversion. *Curr Biol* 32: 2821-2833.e6
- Makyio H, Ohgi M, Takei T, Takahashi S, Takatsu H, Katoh Y, Hanai A, Ueda T, Kanaho Y, Xie Y, *et al* (2012) Structural basis for Arf6-MKLP1 complex formation on the Flemming body responsible for cytokinesis. *EMBO J* 31: 2590–2603
- Mal  th J, Choi S, Muallem S & Ahuja M (2014) Translocation between PI(4,5)P 2 -poor and PI(4,5)P 2 -rich microdomains during store depletion determines STIM1 conformation and Orai1 gating. *Nat Commun* 5: 1–10
- Mao YS, Yamaga M, Zhu X, Wei Y, Sun HQ, Wang J, Yun M, Wang Y, Di Paolo G, Bennett M, *et al* (2009) Essential and unique roles of PIP5K- γ and - α in Fc γ receptor-mediated phagocytosis. *J Cell Biol* 184: 281–296
- Martins CS, Taveneau C, Castro-Linares G, Baibakov M, Buzhinsky N, Eroles M,

- Milanović V, Omi S, Pedelacq J-D, Iv F, *et al* (2023) Human septins organize as octamer-based filaments and mediate actin-membrane anchoring in cells. *J Cell Biol* 222
- Mascanzoni F, Iannitti R & Colanzi A (2022) Functional Coordination among the Golgi Complex, the Centrosome and the Microtubule Cytoskeleton during the Cell Cycle. *Cells* 11
- Matsumura F (2005) Regulation of myosin II during cytokinesis in higher eukaryotes. *Trends Cell Biol* 15: 371–377
- McNally FJ & Roll-Mecak A (2018) Microtubule-severing enzymes: From cellular functions to molecular mechanism. *J Cell Biol* 217: 4057–4069
- Mei K & Guo W (2018) The exocyst complex. *Curr Biol* 28: R922–R925
- Meiri D, Marshall CB, Greeve MA, Kim B, Balan M, Suarez F, Bakal C, Wu C, Larose J, Fine N, *et al* (2012) Mechanistic Insight into the Microtubule and Actin Cytoskeleton Coupling through Dynein-Dependent RhoGEF Inhibition. *Mol Cell* 45: 642–655
- Mendonça DC, Macedo JN, Guimarães SL, Barroso da Silva FL, Cassago A, Garratt RC, Portugal R V. & Araujo APU (2019) A revised order of subunits in mammalian septin complexes. *Cytoskeleton* 76: 457–466
- Menon MB, Sawada A, Chaturvedi A, Mishra P, Schuster-Gossler K, Galla M, Schambach A, Gossler A, Förster R, Heuser M, *et al* (2014) Genetic deletion of SEPT7 reveals a cell type-specific role of septins in microtubule destabilization for the completion of cytokinesis. *PLoS Genet* 10: 1–12
- Mianem S, Ling S, Tong Z, G.Yancey G & Richard S. J (2008) The Role of DDX3 in Regulating Snail. *Bone* 23: 1–7
- Mierzwa B & Gerlich DW (2014) Cytokinetic Abscission: Molecular Mechanisms and Temporal Control. *Dev Cell* 31: 525–538
- Mierzwa BE, Chiaruttini N, Redondo-Morata L, Moser Von Filseck J, König J, Larios J, Poser I, Müller-Reichert T, Scheuring S, Roux A, *et al* (2017) Dynamic subunit turnover in ESCRT-III assemblies is regulated by Vps4 to mediate membrane remodelling during cytokinesis. *Nat Cell Biol* 19: 787–798
- Miller AL & Bement WM (2009) Regulation of cytokinesis by Rho GTPase flux. *Nat Cell Biol* 11: 71–77
- Minoshima Y, Kawashima T, Hirose K, Tonozuka Y, Kawajiri A, Bao YC, Deng X, Tatsuka M, Narumiya S, May WS, *et al* (2003) Phosphorylation by Aurora B converts MgcRacGAP to a RhoGAP during cytokinesis. *Dev Cell* 4: 549–560
- Mishima M, Kaitna S & Glotzer M (2002) Central spindle assembly and cytokinesis require a kinesin-like protein/RhoGAP complex with microtubule bundling activity. *Dev Cell* 2: 41–54
- Mishima M, Pavicic V, Grüneberg U, Nigg EA & Glotzer M (2004) Cell cycle

- regulation of central spindle assembly. *Nature* 430: 908–913
- Moon IS, Lee H & Walikonis RS (2013) Septin 6 localizes to microtubules in neuronal dendrites. *Cytotechnology* 65: 179–186
- Mostowy S & Cossart P (2012) Septins: The fourth component of the cytoskeleton. *Nat Rev Mol Cell Biol* 13: 183–194
- Müller PM, Rademacher J, Bagshaw RD, Wortmann C, Barth C, van Unen J, Alp KM, Giudice G, Eccles RL, Heinrich LE, *et al* (2020) Systems analysis of RhoGEF and RhoGAP regulatory proteins reveals spatially organized RAC1 signalling from integrin adhesions. *Nat Cell Biol* 22: 498–511
- Mullins FM, Yen M & Lewis RS (2016) Orai1 pore residues control CRAC channel inactivation independently of calmodulin. *J Gen Physiol* 147: 137–152
- Nagata K ichi, Kawajiri A, Matsui S, Takagishi M, Shiromizu T, Saitoh N, Izawa I, Kiyono T, Itoh TJ, Hotani H, *et al* (2003) Filament formation of MSF-A, a mammalian septin, in human mammary epithelial cells depends on interactions with microtubules. *J Biol Chem* 278: 18538–18543
- Nakano-Kobayashi A, Yamazaki M, Unoki T, Hongu T, Murata C, Taguchi R, Katada T, Frohman MA, Yokozeki T & Kanaho Y (2007) Role of activation of PIP5K γ 661 by AP-2 complex in synaptic vesicle endocytosis. *EMBO J* 26: 1105–1116
- Nakatsu F, Baskin JM, Chung J, Tanner LB, Shui G, Lee SY, Pirruccello M, Hao M, Ingolia NT, Wenk MR, *et al* (2012) Ptdins4P synthesis by PI4KIII α at the plasma membrane and its impact on plasma membrane identity. *J Cell Biol* 199: 1003–1016
- Nakos K, Radler MR & Spiliotis ET (2019a) Septin 2/6/7 complexes tune microtubule plus-end growth and EB1 binding in a concentration- And filament-dependent manner. *Mol Biol Cell* 30: 2913–2928
- Nakos K, Rosenberg M & Spiliotis ET (2019b) Regulation of microtubule plus end dynamics by septin 9. *Cytoskeleton* 76: 83–91
- Nezis IP, Sagona AP, Schink KO & Stenmark H (2010) Divide and ProsPer: The emerging role of PtdIns3P in cytokinesis. *Trends Cell Biol* 20: 642–649
- Nieto MA (2002) The snail superfamily of zinc-finger transcription factors. *Nat Rev Mol Cell Biol* 3: 155–166
- Nishihama R, Onishi M & Pringle JR (2011) New Insights into the Phylogenetic Distribution and Evolutionary Origins of the Septins. *Biol Chem* 392: 681
- Normand G & King RW (2010) Understanding cytokinesis failure. *Adv Exp Med Biol* 675: 27–55
- Oceguera-Yanez F, Kimura K, Yasuda S, Higashida C, Kitamura T, Hiraoka Y, Haraguchi T & Narumiya S (2005) Ect2 and MgcRacGAP regulate the activation and function of Cdc42 in mitosis. *J Cell Biol* 168: 221–232

- Omrane M, Camara AS, Taveneau C, Benzoubir N, Tubiana T, Yu J, Guérois R, Samuel D, Goud B, Poüs C, *et al* (2019) Septin 9 has Two Polybasic Domains Critical to Septin Filament Assembly and Golgi Integrity. *iScience* 13: 138–153
- Pacheco J, Cassidy AC, Zewe JP, Wills RC & Hammond GR V (2023) PI (4 , 5) P 2 diffuses freely in the plasma membrane even within high-density effector protein complexes. *J Cell Biol* 222
- Padrón D, Wang YJ, Yamamoto M, Yin H & Roth MG (2003) Phosphatidylinositol phosphate 5-kinase I β recruits AP-2 to the plasma membrane and regulates rates of constitutive endocytosis. *J Cell Biol* 162: 693–701
- Palty R, Raveh A, Kaminsky I, Meller R & Reuveny E (2012) SARAF inactivates the store operated calcium entry machinery to prevent excess calcium refilling. *Cell* 149: 425–438
- Panagiotou TC, Chen A & Wilde A (2022) An anillin-CIN85-SEPT9 complex promotes intercellular bridge maturation required for successful cytokinesis. *Cell Rep* 40: 111274
- Di Paolo G, Moskowitz HS, Gipson K, Wenk MR, Voronov S, Obayashi M, Flavell R, Fitzsimonds RM, Ryan TA & De Camilli P (2004) Impaired PtdIns(4,5)P2 synthesis in nerve terminals produces defects in synaptic vesicle trafficking. *Nature* 431: 415–422
- Di Paolo G, Pellegrini L, Letinic K, Cestra G, Zoncu R, Voronov S, Chang S, Guo J, Wenk MR & De Camilli P (2002) Recruitment and regulation of phosphatidylinositol phosphate kinase type 1 γ by the FERM domain of talin. *Nat* 2002 4206911 420: 85–89
- Pavicic-Kaltenbrunner Visnja, Mishima Masanori & Glotzer M (2007) Cooperative Assembly of CYK-4/MgcRacGAP and ZEN-4/MKLP1 to Form the Centralspindlin Complex. *Mol Biol Cell* 18: 3250–3263
- Pfzner AK, Mercier V, Jiang X, Moser von Filseck J, Baum B, Šarić A & Roux A (2020) An ESCRT-III Polymerization Sequence Drives Membrane Deformation and Fission. *Cell* 182: 1140-1155.e18
- Piekny A, Werner M & Glotzer M (2005) Cytokinesis: Welcome to the Rho zone. *Trends Cell Biol* 15: 651–658
- Piekny AJ & Glotzer M (2008) Anillin Is a Scaffold Protein That Links RhoA, Actin, and Myosin during Cytokinesis. *Curr Biol* 18: 30–36
- Piekny AJ & Maddox AS (2010) The myriad roles of Anillin during cytokinesis. *Semin Cell Dev Biol* 21: 881–891
- Posor Y, Jang W & Haucke V (2022) Phosphoinositides as membrane organizers. *Nat Rev Mol Cell Biol* 0123456789
- Poüs C, Klipfel L & Baillet A (2016) Cancer-related functions and subcellular localizations of septins. *Front Cell Dev Biol* 4: 1–8

- Preußner M, Goldammer G, Neumann A, Haltenhof T, Rautenstrauch P, Müller-McNicoll M & Heyd F (2017) Body Temperature Cycles Control Rhythmic Alternative Splicing in Mammals. *Mol Cell* 67: 433-446.e4
- Qiu R, Runxiang Q, Geng A, Liu J, Xu CW, Menon MB, Gaestel M & Lu Q (2020) SEPT7 Interacts with KIF20A and Regulates the Proliferative State of Neural Progenitor Cells during Cortical Development. *Cereb Cortex* 30: 3030–3043
- Ran FA, Hsu PD, Wright J, Agarwala V, Scott DA & Zhang F (2013) Genome engineering using the CRISPR-Cas9 system. *Nat Protoc* 8: 2281–2308
- Renshaw MJ, Liu J, Lavoie BD & Wilde A (2014) Anillin-dependent organization of septin filaments promotes intercellular bridge elongation and Chmp4B targeting to the abscission site. *Open Biol* 4
- Ribet D, Boscaini S, Cauvin C, Siguier M, Mostowy S, Echard A & Cossart P (2017) SUMOylation of human septins is critical for septin filament bundling and cytokinesis. *J Cell Biol* 216: 4041–4052
- Ridley AJ (2015) Rho GTPase signalling in cell migration. *Curr Opin Cell Biol* 36: 103
- Roche S, Fumagalli S & Courtneidge SA (1995) Requirement for Src family protein tyrosine kinases in G2 for fibroblast cell division. *Science (80-)* 269: 1567–1569
- Rogers TB, Inesi G, Wade R & Lederer WJ (1995) Use of thapsigargin to study Ca²⁺ homeostasis in cardiac cells. *Biosci Rep* 15: 341–349
- Roubinet C, Decelle B, Chicanne G, Dorn JF, Payrastre B, Payre F & Carreno S (2011) Molecular networks linked by Moesin drive remodeling of the cell cortex during mitosis. *J Cell Biol* 195: 99–112
- Russo G & Krauss M (2021) Septin Remodeling During Mammalian Cytokinesis. *Front Cell Dev Biol* 9: 1–6
- Saarikangas J, Zhao H & Lappalainen P (2010) Regulation of the actin cytoskeleton-plasma membrane interplay by phosphoinositides. *Physiol Rev* 90: 259–289
- Safavian D, Kim MS, Xie H, El-Zeirry M, Palander O, Dai L, Collins RF, Froese C, Shannon R, Nagata K, *et al* (2023) Septin-mediated RhoA activation engages the exocyst complex to recruit the cilium transition zone. *J Cell Biol* 222
- Sagona AP, Nezis IP, Pedersen NM, Liestøl K, Poulton J, Rusten TE, Skotheim RI, Raiborg C & Stenmark H (2010) PtdIns(3)P controls cytokinesis through KIF13A-mediated recruitment of FYVE-CENT to the midbody. *Nat Cell Biol* 12: 362–371
- Sagona AP & Stenmark H (2010) Cytokinesis and cancer. *FEBS Lett* 584: 2652–2661
- Saheki Y, Bian X, Schauder CM, Sawaki Y, Surma MA, Klose C, Pincet F, Reinisch KM & De Camilli P (2016) Control of plasma membrane lipid homeostasis by the extended synaptotagmins. *Nat Cell Biol* 18: 504–515

- Salameh J, Cantaloube I, Benoit B, Poüs C & Baillet A (2021) Cdc42 and its BORG2 and BORG3 effectors control the subcellular localization of septins between actin stress fibers and microtubules. *Curr Biol*: 1–16
- Santarius M, Lee CH & Anderson RA (2006) Supervised membrane swimming: Small G-protein lifeguards regulate PIPK signaling and monitor intracellular PtdIns(4,5)P₂ pools. *Biochem J* 398: 1–13
- Sarkes D & Rameh LE (2010) A novel HPLC-based approach makes possible the spatial characterization of cellular PtdIns5P and other phosphoinositides. *Biochem J* 428: 375–384
- Sasaki J, Sasaki T, Yamazaki M, Matsuoka K, Taya C, Shitara H, Takasuga S, Nishio M, Mizuno K, Wada T, *et al* (2005) Regulation of anaphylactic responses by phosphatidylinositol phosphate kinase type I α . *J Exp Med* 201: 859–870
- Schauder CM, Wu X, Saheki Y, Narayanaswamy P, Torta F, Wenk MR, De Camilli P & Reinisch KM (2014) Structure of a lipid-bound extended synaptotagmin indicates a role in lipid transfer. *Nat Lett* 510: 552–555
- Schiel JA, Childs C & Prekeris R (2013) Endocytic transport and cytokinesis: From regulation of the cytoskeleton to midbody inheritance. *Trends Cell Biol* 23: 319–327
- Schiel JA, Simon GC, Zaharris C, Weisz J, Castle D, Wu CC & Prekeris R (2012) FIP3-endosome-dependent formation of the secondary ingression mediates ESCRT-III recruitment during cytokinesis. *Nat Cell Biol* 14: 1068–1078
- Schill NJ & Anderson RA (2009) Two novel phosphatidylinositol-4-phosphate 5-kinase type I γ splice variants expressed in human cells display distinctive cellular targeting. *Biochem J* 422: 473–482
- Schill NJ, Hedman AC, Choi S & Anderson RA (2014) Isoform 5 of PIPK1 γ regulates the endosomal trafficking and degradation of E-cadherin. *J Cell Sci* 127: 2189–2203
- Schweitzer JK & D'Souza-Schorey C (2002) Localization and activation of the ARF6 GTPase during cleavage furrow ingression and cytokinesis. *J Biol Chem* 277: 27210–27216
- Schweitzer JK & Souza-schorey CD (2005) A requirement for ARF6 during the completion of cytokinesis. *Exp Cell Res* 311: 74–83
- Sharma K & Menon MB (2023) Decoding post-translational modifications of mammalian septins. *Cytoskeleton*: 169–181
- Sharma S, Quintana A, Findlay GM, Mettlen M, Baust B, Jain M, Nilsson R, Rao A & Hogan PG (2013) An siRNA screen for NFAT activation identifies septins as coordinators of store-operated Ca²⁺ entry. *Nature* 499
- Sheffield PJ, Oliver CJ, Kremer BE, Sheng S, Shao Z & Macara IG (2003) Borg/Septin interactions and the assembly of mammalian septin heterodimers, trimers, and filaments. *J Biol Chem* 278: 3483–3488

- Simi AK, Anlaş AA, Stallings-Mann M, Zhang S, Hsia T, Cichon M, Radisky DC & Nelson CM (2018) A soft microenvironment protects from failure of Midbody abscission and multinucleation downstream of the EMT-promoting transcription factor snail. *Cancer Res* 78: 2277–2289
- Simon GC, Schonteich E, Wu CC, Piekny A, Ekiert D, Yu X, Gould GW, Glotzer M & Prekeris R (2008) Sequential Cyk-4 binding to ECT2 and FIP3 regulates cleavage furrow ingression and abscission during cytokinesis. *EMBO J* 27: 1791–1803
- Singh N, Reyes-Ordoñez A, Compagnone MA, Moreno JF, Leslie BJ, Ha T & Chen J (2021) Redefining the specificity of phosphoinositide-binding by human PH domain-containing proteins. *Nat Commun* 12: 1–13
- Sinha S, Elbaz-Alon Y & Avinoam O (2022) Ca²⁺ as a coordinator of skeletal muscle differentiation, fusion and contraction. *FEBS J* 289: 6531–6542
- Sirajuddin M, Farkasovsky M, Hauer F, Kühlmann D, Macara IG, Weyand M, Stark H & Wittinghofer A (2007) Structural insight into filament formation by mammalian septins. *Nature* 449: 311–315
- Sirajuddin M, Marian Farkasovsky, Eldar Zent & Alfred Wittinghofer (2009) GTP-induced conformational changes in septins and implications for function
- Smith C, Dolat L, Angelis D, Forgacs E, Spiliotis ET & Galkin VE (2015) Septin 9 Exhibits Polymorphic Binding to F-Actin and Inhibits Myosin and Cofilin Activity. *J Mol Biol* 427: 3273–3284
- Sohn M, Korzeniowski M, Zewe JP, Wills RC, Hammond GRV, Humpolickova J, Vrzal L, Chalupska D, Veverka V, Fairn GD, *et al* (2018) PI(4,5)P₂ controls plasma membrane PI4P and PS levels via ORP5/8 recruitment to ER-PM contact sites. *J Cell Biol* 217: 1797–1813
- Song K, Gras C, Capin G, Gimber N, Lehmann M, Mohd S, Puchkov D, Rödiger M, Wilhelmi I, Daumke O, *et al* (2019) A SEPT1-based scaffold is required for Golgi integrity and function. *J Cell Sci* 132
- Song K, Russo G & Krauss M (2016) Septins as modulators of endo-lysosomal membrane traffic. *Front Cell Dev Biol* 4: 1–5
- Soroor F, Kim MS, Palander O, Balachandran Y, Collins RF, Benlekbir S, Rubinstein JL & Trimble WS (2021) Revised subunit order of mammalian septin complexes explains their in vitro polymerization properties. *Mol Biol Cell* 32: 289–300
- de Souza LB, Ong HL, Liu X & Ambudkar IS (2021) PIP₂ and septin control STIM1/Orai1 assembly by regulating cytoskeletal remodeling via a CDC42-WASP/WAVE-ARP2/3 protein complex. *Cell Calcium* 99: 102475
- Spiliotis ET (2018) Spatial effects – site-specific regulation of actin and microtubule organization by septin GTPases. 1–10
- Spiliotis ET, Hunt SJ, Hu Q, Kinoshita M & Nelson WJ (2008) Epithelial polarity requires septin coupling of vesicle transport to polyglutamylated microtubules.

J Cell Biol 180: 295–303

Spiliotis ET, Kinoshita M & Nelson WJ (2005) A mitotic septin scaffold required for mammalian chromosome congression and segregation. *Science* (80-) 307: 1781–1785

Spiliotis ET & McMurray MA (2020) Masters of asymmetry-lessons and perspectives from 50 years of septins. *Mol Biol Cell* 31: 2289–2297

Spiliotis ET & Nakos K (2021) Cellular functions of actin- and microtubule-associated septins. *Curr Biol* 31: R651–R666

Stathopoulos PB & Ikura M (2009) Structurally delineating stromal interaction molecules as the endoplasmic reticulum calcium sensors and regulators of calcium release-activated calcium entry. *Immunol Rev* 231: 113–131

Stathopoulos PB, Zheng L, Li GY, Plevin MJ & Ikura M (2008) Structural and Mechanistic Insights into STIM1-Mediated Initiation of Store-Operated Calcium Entry. *Cell* 135: 110–122

Stefan CJ (2020) Endoplasmic reticulum–plasma membrane contacts: Principals of phosphoinositide and calcium signaling. *Curr Opin Cell Biol* 63: 125–134

Straight AF, Field CM & Mitchison TJ (2004) Anillin Binds Nonmuscle Myosin II and Regulates the Contractile Ring. *Mol Biol Cell* 15: 5318–5328

Su KC, Takaki T & Petronczki M (2011) Targeting of the RhoGEF Ect2 to the Equatorial Membrane Controls Cleavage Furrow Formation during Cytokinesis. *Dev Cell* 21: 1104–1115

Sun L, Guan R, Lee IJ, Liu Y, Chen M, Wang J, Wu JQ & Chen Z (2015) Mechanistic Insights into the Anchorage of the Contractile Ring by Anillin and Mid1. *Dev Cell* 33: 413–426

Sun Y, Hedman AC, Tan X, Schill NJ & Anderson RA (2013) Endosomal Type I γ PIP 5-Kinase Controls EGF Receptor Lysosomal Sorting. *Dev Cell* 25: 144–155

Sun Y, Ling K, Wagoner MP & Anderson RA (2007) Type I γ phosphatidylinositol phosphate kinase is required for EGF-stimulated directional cell migration. *J Cell Biol* 178: 297–308

Surka MC, Tsang CW & Trimble WS (2002) The Mammalian Septin MSF Localizes with Microtubules and Is Required for Completion of Cytokinesis. *Mol Biol Cell* 13: 3532

Szuba A, Bano F, Castro-Linares G, Iv F, Mavrikis M, Richter RP, Bertin A & Koenderink GH (2021) Membrane binding controls ordered self-assembly of animal septins. *Elife* 10: 1–35

Takahashi S, Takei T, Koga H, Takatsu H, Shin HW & Nakayama K (2011) Distinct roles of Rab11 and Arf6 in the regulation of Rab11-FIP3/arfophilin-1 localization in mitotic cells. *Genes to Cells* 16: 938–950

- Tan X, Thapa N, Choi S & Anderson RA (2015) Emerging roles of PtdIns(4,5)P₂ - beyond the plasma membrane. *J Cell Sci* 128: 4047–4056
- Tan X, Thapa N, Liao Y, Choi S & Anderson RA (2016) PtdIns(4,5)P₂ signaling regulates ATG14 and autophagy. *Proc Natl Acad Sci U S A* 113: 10896–10901
- Tanaka-Takiguchi Y, Kinoshita M & Takiguchi K (2009) Septin-Mediated Uniform Bracing of Phospholipid Membranes. *Curr Biol* 19: 140–145
- Targa B, Klipfel L, Cantaloube I, Salameh J, Benoit B, Poüs C & Baillet A (2019) Septin filament coalignment with microtubules depends on SEPT9_i1 and tubulin polyglutamylation, and is an early feature of acquired cell resistance to paclitaxel. *Cell Death Dis* 10
- Thapa N, Sun Y, Schramp M, Choi S, Ling K & Anderson RA (2012) Phosphoinositide Signaling Regulates the Exocyst Complex and Polarized Integrin Trafficking in Directionally Migrating Cells. *Dev Cell* 22: 116–130
- Thapa N, Tan X, Choi S, Wise T & Anderson RA (2017) PIPK γ and talin couple phosphoinositide and adhesion signaling to control the epithelial to mesenchymal transition. *Oncogene* 36: 899–911
- Thieman JR, Mishra SK, Ling K, Doray B, Anderson RA & Traub LM (2009) Clathrin regulates the association of PIPK γ 661 with the AP-2 adaptor β 2 Appendage. *J Biol Chem* 284: 13924–13939
- Thoresen SB, Pedersen NM, Liestøl K & Stenmark H (2010) A phosphatidylinositol 3-kinase class III sub-complex containing VPS15, VPS34, Beclin 1, UVRAG and BIF-1 regulates cytokinesis and degradative endocytic traffic. *Exp Cell Res* 316: 3368–3378
- Tojkander S, Gateva G & Lappalainen P (2012) Actin stress fibers - Assembly, dynamics and biological roles. *J Cell Sci* 125: 1855–1864
- Tominaga T, Sahai E, Chardin P, McCormick F, Courtneidge SA & Alberts AS (2000) Diaphanous-related formins bridge Rho GTPase and Src tyrosine kinase signaling. *Mol Cell* 5: 13–25
- Touré A, Dorseuil O, Morin L, Timmons P, Jégou B, Reibel L & Gacon G (1998) MgcRacGAP, a new human GTPase-activating protein for Rac and Cdc42 similar to *Drosophila* rotundRacGAP gene product, is expressed in male germ cells. *J Biol Chem* 273: 6019–6023
- Traikov S, Stange C, Wassmer T, Paul-Gilloteaux P, Salamero J, Raposo G & Hoflack B (2014) Septin6 and septin7 GTP binding proteins regulate AP-3- and ESCRT-dependent multivesicular body biogenesis. *PLoS One* 9: 1–12
- Ueda T, Hanai A, Takei T, Kubo K, Ohgi M, Sakagami H, Takahashi S, Shin HW & Nakayama K (2013) EFA6 activates Arf6 and participates in its targeting to the Flemming body during cytokinesis. *FEBS Lett* 587: 1617–1623
- Ugorets V, Mendez P, Zagrebina D, Russo G, Kerkhoff Y, Herpelinck T., Kotsaris G., Jatzlau J., Stricker S., Knaus P. (2023) Reorganization of Septin structures

regulates early myogenesis. *bioRxiv* 637

Várnai P, Lin X, Lee SB, Tuymetova G, Bondeva T, Spät A, Rhee SG, Czky GH & Balla T (2002) Inositol Lipid Binding and Membrane Localization of Isolated Pleckstrin Homology (PH) Domains: STUDIES ON THE PH DOMAINS OF PHOSPHOLIPASE C δ 1 AND p130. *J Biol Chem* 277: 27412–27422

Verdier-Pinard P, Salaun D, Bouguenina H, Shimada S, Pophillat M, Audebert S, Agavnian E, Coslet S, Charafe-Jauffret E, Tachibana T, *et al* (2017) Septin 9_i2 is downregulated in tumors, impairs cancer cell migration and alters subnuclear actin filaments. *Sci Reports* 2017 717: 1–18

Volpicelli-Daley LA, Lucast L, Gong LW, Liu L, Sasaki J, Sasaki T, Abrams CS, Kanaho Y & De Camilli P (2010) Phosphatidylinositol-4-phosphate 5-kinases and phosphatidylinositol 4,5-bisphosphate synthesis in the brain. *J Biol Chem* 285: 28708–28714

Vrabioiu AM & Mitchison TJ (2006) Structural insights into yeast septin organization from polarized fluorescence microscopy. *Nature* 443: 466–469

Wadsworth P (2021) The multifunctional spindle midzone in vertebrate cells at a glance. *J Cell Sci* 134: 1–8

Walsh CM, Chvanov M, Haynes LP, Petersen OH, Tepikin A V. & Burgoyne RD (2010) Role of phosphoinositides in STIM1 dynamics and store-operated calcium entry. *Biochem J* 425: 159–168

Wang K, Wloka C & Bi E (2019) Non-muscle Myosin-II Is Required for the Generation of a Constriction Site for Subsequent Abscission. *iScience* 13: 69–81

Wang Y, Chen X, Lian L, Tang T, Stalker TJ, Sasaki T, Brass LF, Choi JK, Hartwig JH & Abrams CS (2008) Loss of PIP5KI β demonstrates that PIP5KI isoform-specific PIP 2 synthesis is required for IP3 formation. *Proc Natl Acad Sci U S A* 105: 14064–14069

Wang Y, Lian L, Golden JA, Morrissey EE & Abrams CS (2007) PIP5KI γ is required for cardiovascular and neuronal development. *Proc Natl Acad Sci U S A* 104: 11748–11753

Wang YJ, Li WH, Wang J, Xu K, Dong P, Luo X & Yin HL (2004) Critical role of PIP5KI γ 87 in InsP3-mediated Ca²⁺ signaling. *J Cell Biol* 167: 1005–1010

Watanabe S, Ando Y, Yasuda S, Hosoya H, Watanabe N, Ishizaki T & Narumiya S (2007) mDia2 Induces the Actin Scaffold for the Contractile Ring and Stabilizes Its Position during Cytokinesis in NIH 3T3 Cells. *Mol Biol Cell* 18: 3250–3263

Watanabe S, Okawa K, Miki T, Sakamoto S, Morinaga T, Segawa K, Arakawa T, Kinoshita M, Ishizaki T & Narumiya S (2010) Rho and anillin-dependent control of mDia2 localization and function in cytokinesis. *Mol Biol Cell* 21: 3193–3204

Watanabe S, De Zan T, Ishizaki T & Narumiya S (2013) Citron kinase mediates

- transition from constriction to abscission through its coiled-coil domain. *J Cell Sci* 126: 1773–1784
- Watt SA, Kular G, Fleming IN, Downes CP & Lucocq JM (2002) Subcellular localization of phosphatidylinositol 4,5-bisphosphate using the pleckstrin homology domain of phospholipase C δ 1. *Biochem J* 363: 657–666
- Weernink PAO, Meletiadis K, Hommeltenberg S, Hinz M, Ishihara H, Schmidt M & Jakobs KH (2004a) Activation of Type I Phosphatidylinositol 4-Phosphate 5-Kinase Isoforms by the Rho GTPases, RhoA, Rac1, and Cdc42. *J Biol Chem* 279: 7840–7849
- Weernink PAO, Meletiadis K, Hommeltenberg S, Hinz M, Ishihara H, Schmidt M & Jakobs KH (2004b) Activation of Type I Phosphatidylinositol 4-Phosphate 5-Kinase Isoforms by the Rho GTPases, RhoA, Rac1, and Cdc42. *J Biol Chem* 279: 7840–7849
- Wenk MR, Pellegrini L, Klenchin VA, Di Paolo G, Chang S, Daniell L, Arioka M, Martin TF & De Camilli P (2001) PIP kinase I γ is the major PI(4,5)P₂ synthesizing enzyme at the synapse. *Neuron* 32: 79–88
- Wieffer M, Maritzen T & Haucke V (2009) SnapShot: Endocytic Trafficking. *Cell* 137: 382.e1-382.e3
- Wills RC & Hammond GR V (2022) PI(4,5)P₂ : signaling the plasma membrane. 0: 2311–2325
- Woods BL & Gladfelter AS (2021) The state of the septin cytoskeleton from assembly to function. *Curr Opin Cell Biol* 68: 105–112
- Wu W Da, Yu KW, Zhong N, Xiao Y & She ZY (2019) Roles and mechanisms of Kinesin-6 KIF20A in spindle organization during cell division. *Eur J Cell Biol* 98: 74–80
- Xia Y, Irvine RF & Giudici ML (2011) Phosphatidylinositol 4-phosphate 5-kinase I γ _v6, a new splice variant found in rodents and humans. *Biochem Biophys Res Commun* 411: 416–420
- Xiong X, Xu Q, Huang Y, Singh RD, Anderson R, Leof E, Hu J & Ling K (2012) An association between type I γ PI4P 5-kinase and Exo70 directs E-cadherin clustering and epithelial polarization. *Mol Biol Cell* 23: 87–98
- Xu Q, Zhang Y, Wei Q, Huang Y, Hu J & Ling K (2016) Phosphatidylinositol phosphate kinase PIPKI γ and phosphatase INPP5E coordinate initiation of ciliogenesis. *Nat Commun* 7: 1–12
- Xu Q, Zhang Y, Xiong X, Huang Y, Salisbury JL, Hu J & Ling K (2014) PIPKI targets to the centrosome and restrains centriole duplication. *J Cell Sci* 127: 1293–1305
- Yasuda S, Ocegüera-Yanez F, Kato Takayuti, Okamoto Muneo, Yonemura Shigenobu, Yasuhiko T, Ishizaki T & Narumiya S (2004) Cdc42 and mDia3 regulate microtubule attachment to kinetochores. *Nature* 1: e0039

- Yasunori Saheki and Pietro De Camilli (2018) The Extended-Synaptotagmins. *Biochim Biophys Acta* 176: 139–148
- Yeung PSW, Yamashita M & Prakriya M (2020) Molecular basis of allosteric Orai1 channel activation by STIM1. *J Physiol* 598: 1707–1723
- Yoshizaki H, Ohba Y, Kurokawa K, Itoh RE, Nakamura T, Mochizuki N, Nagashima K & Matsuda M (2003) Activity of Rho-family GTPases during cell division as visualized with FRET-based probes. *J Cell Biol* 162: 223–232
- Yuan JP, Zeng W, Dorwart MR, Choi Y, Paul F & Muallem S (2009) SOAR and the polybasic STIM1 domains gate and regulate the Orai channels. *Nat Cell Biol* 11: 337–343
- Yüce Ö, Piekny A & Glotzer M (2005) An ECT2-centralspindlin complex regulates the localization and function of RhoA. *J Cell Biol* 170: 571–582
- Zent E & Wittinghofer A (2014) Human septin isoforms and the GDP-GTP cycle. *Biol Chem* 395: 169–180
- Zhang J, Kong C, Xie H, McPherson PS, Grinstein S & Trimble WS (1999) Phosphatidylinositol polyphosphate binding to the mammalian septin H5 is modulated by GTP. *Curr Biol* 9: 1458–1467
- Zhang W, Muramatsu A, Matsuo R, Teranishi N, Kahara Y, Takahara T, Shibata H & Maki M (2020) The penta-ef-hand alg-2 protein interacts with the cytosolic domain of the soce regulator saraf and interferes with ubiquitination. *Int J Mol Sci* 21: 1–21
- Zhang Y, Sugiura R, Lu Y, Asami M, Maeda T, Itoh T, Takenawa T, Shuntoh H & Kuno T (2000) Phosphatidylinositol 4-phosphate 5-kinase its3 and calcineurin Ppb1 coordinately regulate cytokinesis in fission yeast. *J Biol Chem* 275: 35600–35606
- Zhao W, Seki A & Fang G (2007) Cep55, a Microtubule-bundling Protein, Associates with Centralspindlin to Control the Midbody Integrity and Cell Abscission during Cytokinesis. *Mol Biol Cell* 18: 986–994
- Zhou Y, Srinivasan P, Razavi S, Seymour S, Meraner P, Gudlur A, Stathopoulos PB, Ikura M, Rao A & Hogan PG (2013) Initial activation of STIM1, the regulator of store-operated calcium entry. *Nat Struct Mol Biol* 176: 100–106
- Zhu C, Lau E, Schwarzenbacher R, Bossy-Wetzler E & Jiang W (2006) Spatiotemporal control of spindle midzone formation by PRC1 in human cells. *Proc Natl Acad Sci* 103: 6196–6201
- Zhuravlev Y, Hirsch SM, Jordan SN, Dumont J, Shirasu-Hiza M & Canman JC (2017) CYK-4 regulates Rac, but not Rho, during cytokinesis. *Mol Biol Cell* 28: 1258–1270
- Zuvanov L, Mota DMD, Araujo APU & DeMarco R (2019) A blueprint of septin expression in human tissues. *Funct Integr Genomics* 19: 787–797

6. Appendix A: putative role of septin-binding PIPKI γ isoforms in ER-PM contact sites

6.1. Introduction

6.1.1. Store-operated Ca²⁺ entry (SOCE)

Calcium ion (Ca²⁺) is an essential second messenger involved in the regulation of several cellular processes ranging from differentiation to cell death (Berridge, 2012). Under steady state conditions, cytoplasmic Ca²⁺ concentration is kept at a low level (0.1 to 0.2 μ M), while in the extracellular space it ranges between 1 and 3 mM (Clapham, 2007).

Ca²⁺ signaling is initially supported by the mobilization of Ca²⁺ from its primary reservoir, the endoplasmic reticulum (ER), and subsequently by the process of SOCE, which further elevates cytoplasmic Ca²⁺ levels, while aiding the replenishment of Ca²⁺ stores (Stefan, 2020). The release of Ca²⁺ from the ER can be triggered by extracellular signals that engage the phospholipase C (PLC) pathway (**fig. 6.1-1-A**) (Clapham, 2007). In particular, activation of G protein-coupled receptors and/or of receptors tyrosine kinases by extracellular stimuli results in the stimulation of PLC activity at the PM. PLC hydrolyzes PI(4,5)P₂ into diacylglycerol (DAG) and inositol 1,4,5-triphosphate (IP₃). IP₃, in turn, binds and activates the ligand-gated Ca²⁺ channel inositol triphosphate receptor (IP₃R) located at cortical ER, thereby inducing the release of Ca²⁺ from this organelle (Clapham, 2007).

Ca²⁺ release from the ER triggers the process of SOCE, which culminates in a sustained Ca²⁺ influx from the extracellular space to the cytosol (Stefan, 2020). This is achieved through the formation of the calcium release-activated calcium (CRAC) channels at preexisting sites of contacts between ER and PM. Canonical CRAC channels are formed by the transmembrane pore subunit Orai1 and by the stromal interaction molecule 1 (STIM1), which acts as a sensor of free Ca²⁺ in the ER, and activates Orai1 at the PM (Carrasco & Meyer, 2011). STIM1 is an ER-resident, single pass, transmembrane protein. Its N-terminal luminal portion contains an EF-hand adjacent to a sterile alpha motif (SAM), while the cytoplasmic portion harbors the SOAR (STIM1 Orai activating region), a minimum region capable of gating

Orai1, and a C-terminal polybasic sequence (**fig. 6.1-1-B**) (Stathopoulos & Ikura, 2009).

At resting conditions, STIM1 forms dimers, whose luminal domains are loaded with Ca^{2+} , while the cytoplasmic portions are folded close to the ER. Following the activation of IP_3R , the dissociation of Ca^{2+} from the EF-SAM domains triggers a conformational change within the dimer resulting into the extension and exposition of the cytoplasmic regions toward the PM (Gudlur *et al*, 2018, 2020; Stathopoulos *et al*, 2008). Activated STIM1 dimers oligomerize and cluster at nearby ER-PM junctions to eventually recruit and activate Orai1, via exposed SOAR domains (Yuan *et al*, 2009; Liou *et al*, 2007). A functional CRAC channel is composed by six Orai1 subunits that coordinate selective Ca^{2+} influx (Amcheslavsky *et al*, 2015). The stabilization of STIM1 oligomers at ER-PM junctions is mediated by both SOAR domain and the C-terminal polybasic sequence that, upon exposure, bind negatively charged phosphoinositides, at the inner leaflet of the PM (Achiliev Cohen *et al*, 2023; Bhardwaj *et al*, 2013).

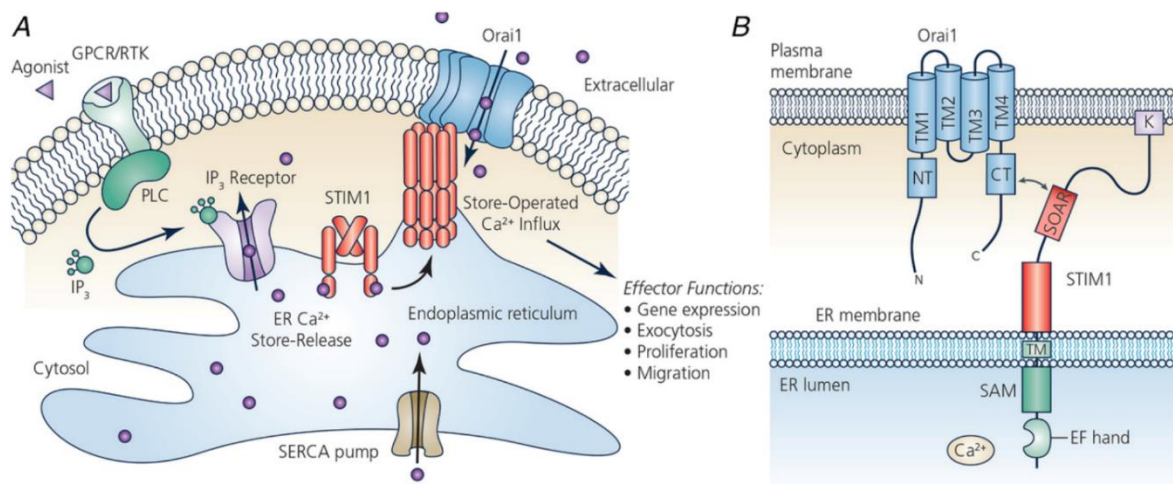


Figure 6.1-1. Molecular mechanism of SOCE. (A) Stimulation of surface receptors results in the activation of PLC and consequent generation of IP_3 . IP_3 , in turn, binds IP_3 receptors and thereby promotes Ca^{2+} exit from the ER. Ca^{2+} decrease in the ER lumen leads to the activation, oligomerization, and translocation of STIM1 to ER-PM junctions. At these sites, STIM1 oligomers interact and gate plasmalemmal Orai1 channels, leading to Ca^{2+} influx from the extracellular space. Elevated cytoplasmic Ca^{2+} levels initiate various downstream responses. The ER Ca^{2+} store is replenished through the SERCA pump activity. **(B)** STIM1 senses the decrease of Ca^{2+} concentration in the ER lumen through multiple Ca^{2+} binding sites within the EF-hand and SAM domains. Activated STIM1 engages Orai1 through the exposed cytoplasmic SOAR domain. The polybasic sequence ("K"), but also the SOAR domain (although not shown in the figure), interacts with phosphoinositides at the PM. Modified from Yeung *et al.*, 2020.

To counterbalance excessive Ca^{2+} influx, CRAC current undergoes two distinct forms of Ca^{2+} -dependent inactivation (CDI), fast (FCDI) and slow (SCDI) (Jardín *et al*, 2018). FCDI operates rapidly within milliseconds, and results from a conformational change within the CRAC channel induced by the binding of Ca^{2+} to Orai1 specific sites (Mullins *et al*, 2016). Conversely, SCDI is initiated tens of seconds after Orai1 activation, and is mediated by the SOCE-associated regulatory factor (SARAF), an ER membrane protein capable of interacting with the SOAR domain of STIM1 (Jardín *et al*, 2018; Jha *et al*, 2013). At resting condition, this interaction prevents oligomerization and spontaneous activation of STIM1 (Palty *et al*, 2012). Following ER Ca^{2+} depletion, STIM1 and SARAF transiently dissociate, but quickly regain and increase their interaction after the binding of STIM1 to Orai1 (Albarran *et al*, 2016). The binding of SARAF to SOAR under high levels of cytosolic Ca^{2+} inhibits CRAC channels, but the detailed molecular mechanism remains unclear so far (Dagan & Palty, 2021). Proposed models postulate the cooperation of SARAF with Ca^{2+} -binding proteins (such as ALG-2 or EFHB), or a Ca^{2+} -dependent conformational change of STIM1 that, in presence of SARAF, enables CRAC channel inhibition (Albarran *et al*, 2018; Zhang *et al*, 2020; Dagan & Palty, 2021; Jha *et al*, 2013). Importantly, Maléth and colleagues showed that SCDI by SARAF occurs at membrane microdomains rich in $\text{PI}(4,5)\text{P}_2$ (Maléth *et al*, 2014), as further described in paragraph 6.1.4.

6.1.2. The extended synaptotagmins (E-Syts)

E-Syts are ER-resident proteins that promote the tethering of this organelle to the PM, and transport glycerolipids between the two compartments (Yasunori Saheki and Pietro De Camilli, 2018).

They share partial domain similarity with the synaptotagmins (Syts), with both families containing an N-terminal lipid anchor, and C2 domains exposed to the cytosol (**fig. 6.1-2**). However, E-Syts differs from Syts in localization and function (Giordano *et al*, 2013). Mammals express three E-Syts: E-Syt1, E-Syt2 and E-Syt3. These proteins insert into the ER membrane through a hydrophobic hairpin at their N-terminus (Giordano *et al*, 2013). Downstream of the hairpin follow cytoplasmic domains consisting of a synaptotagmin-like mitochondrial lipid-binding protein (SMP) domain, responsible for lipid transport, and a variable number of C2 domains. E-Syt2 and E-Syt3 exhibit three C2 domains (C2A, C2B and C2B), while E-Syt1

possesses five (from C2A to C2E) (**fig. 6.1-2**) (Giordano *et al*, 2013; Schauder *et al*, 2014). The C2C domains of E-Syt1/2/3, and the C2E domain of E-Syts1 bind plasmalemmal PI(4,5)P₂ and thereby tether the ER to the PM (Idevall-Hagren *et al*, 2015; Giordano *et al*, 2013). E-Syt2 and E-Syt3 act as constitutive tethers, while E-Syt1 requires Ca²⁺ binding to its C2A and C2C domains to relieve its autoinhibitory conformation and enable the interaction with the PM (Bian *et al*, 2018). E-Syts can form homo and heterodimers, with tethering properties dependent on the specific type of E-Syts forming the complex (Giordano *et al*, 2013).

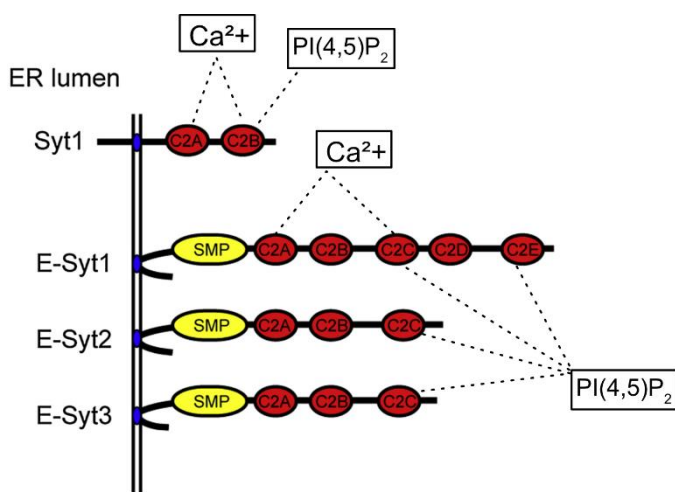


Figure 6.1-2. Domain structure of synaptotagmin 1 (Syt1) and extended synaptotagmins (E-Syts). The C2C domain of E-Syt1/2/3 and the C2E domain of E-Syt1 bind PI(4,5)P₂. The interaction of E-Syt1 with plasmalemmal PI(4,5)P₂ is promoted by the binding of C2A and C2C to Ca²⁺. Notably, the C2A domain of E-Syt2/3 is also capable of Ca²⁺-binding (not shown). However, unlike E-Syt1, the interaction of E-Syt2/3 with the PM is Ca²⁺-independent. Modified from Giordano *et al.*, 2013.

The concentration of Ca²⁺ required for the association of E-Syt1 to the PM is within the low micromolar range, and can be reached during SOCE (Idevall-Hagren *et al*, 2015). During this process, the initial depletion of Ca²⁺ from the ER leads to STIM1 translocation to the PM and activation of Orai1. Subsequently, Ca²⁺ influx via CRAC channels triggers E-Syt1 recruitment to the PM (Idevall-Hagren *et al*, 2015).

Accordingly, knock-down of STIM1 hampered E-Syt1 recruitment to the PM (Idevall-Hagren *et al*, 2015). While the co-depletion of E-Syt1/2/3 reduced ER-PM contacts, it did not affect SOCE, suggesting that E-Syts are not necessary for STIM1 and Orai1 junctions, which can still form in part at remaining contacts provided by other molecular tethers (Giordano *et al*, 2013; Saheki *et al*, 2016; Li *et al*, 2021).

Upon recruitment to the PM, E-Syt1 reshapes membrane contact sites (MCS) and facilitates the replenishment of the ER Ca²⁺ store, possibly by enhancing the activity of the sarco-endoplasmic reticulum Ca²⁺ ATPase (SERCA) pump, which is responsible for transporting Ca²⁺ from the cytoplasm back into the ER lumen (Kang *et al*, 2019).

Furthermore, Saheki and colleagues proposed a role for E-Syts in shuttling the excess of DAG from the PM to ER, following PLC activation (**fig. 6.1-3**) (Saheki *et al*, 2016). This pathway likely acts in parallel with the conversion of DAG into phosphatidic acid (PA), and subsequent Nir2-mediated transfer of PA from the PM to the ER (Saheki *et al*, 2016; Kim *et al*, 2015).

E-Syt1 and STIM1-Orai1 junctions have been observed at the same MCS (Idevall-Hagren *et al*, 2015; Kang *et al*, 2019), and few lines of evidence suggest that E-Syt1 may play a role in the inactivation of STIM1 by restoring the local lipid homeostasis downstream of Ca²⁺ signaling (see paragraph 6.1.4) (Mal  th *et al*, 2014; Ahmad *et al*, 2022; Chang *et al*, 2013).

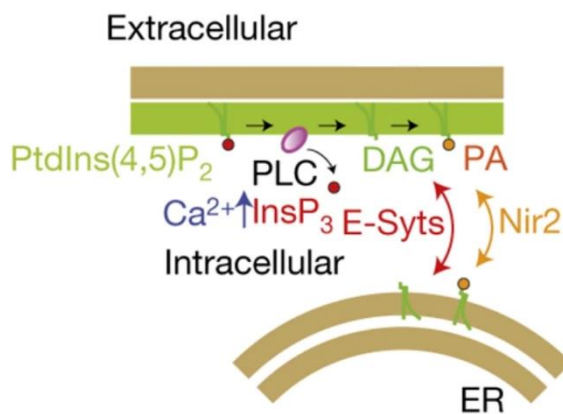


Figure 6.1-3. Proposed contribution of E-Syts in restoring lipid homeostasis downstream of PLC activation.

E-Syts facilitate the removal of DAG from the PM by transporting it to the ER. This process operates alongside the Nir2-mediated transfer of PA, a DAG derivative. Modified from Saheki *et al*, 2016

6.1.3. The role of septins during SOCE

In a genome-wide screen, Sharma and colleagues identified septin paralogues belonging to the septin 2 subgroup as positive regulators of SOCE (Sharma *et al*, 2013). In particular, they showed that treatment with a siRNA (“siSEPT”) targeting SEPT4, SEPT5, and to a lesser extent SEPT2, reduced SOCE to a similar degree as depletion of STIM1 in HeLa and Jurkat cells.

Total internal reflection fluorescence (TIRF) microscopy and super-resolution imaging further revealed that, upon Ca²⁺ store depletion, fluorescently labeled SEPT4 and SEPT5 reorganized at ER-PM junctions, and surrounded forming STIM1-Orai1 contact sites (Sharma *et al*, 2013; Katz *et al*, 2019). Importantly, septins did not colocalize with STIM1-Orai1 clusters but localized in their proximity/at their rims, and, by the time that Orai1 intensity peaked, septins intensity was already decreased (Sharma *et al*, 2013; Katz *et al*, 2019). Still, co-depletion of SEPT4 and SEPT5 hampered STIM1 clustering and, particularly, the stable

recruitment of Orai1 (Sharma *et al*, 2013; Katz *et al*, 2019). Together these data led to the conclusion that SEPT4 and SEPT5 do not form part of STIM1-Orai1 complexes, but rather organize them, and “prime” ER-PM junctions for a stable STIM1-Orai1 engagement (Katz *et al*, 2019; Sharma *et al*, 2013; Liou & Meyer, 2013).

Sharma and colleagues additionally showed that during SOCE, PI(4,5)P₂ accumulated around forming Orai1 clusters, similar to SEPT4. By contrast, siSEPT-treated cells exhibited a homogenous distribution of PI(4,5)P₂, while Orai1 clustering was hampered (Sharma *et al*, 2013). This let the authors hypothesize that septins could regulate SOCE by organizing PI(4,5)P₂ microdomains at ER-PM junctions. Septins may likely exert this function since they act as potent PI(4,5)P₂ diffusion barriers. Indeed, Pacheco and colleagues recently showed that, among a wide range of tested proteins (including E-Syt1, clathrin, actin and actin-binding proteins), only septins and spectrins were capable of significantly restricting free PI(4,5)P₂ diffusion at the PM (Pacheco *et al*, 2023).

The positive contribution of septin 2 paralogues to SOCE was confirmed by Deb and colleagues in *drosophila* neurons (Deb *et al*, 2016). Furthermore, the authors observed that heterozygous SEPT7 knockout neurons exhibited Orai1-mediated Ca²⁺ entry under basal conditions, hence without former stimulation (Deb *et al*, 2016). This was subsequently observed also in human neural progenitor cells (Deb *et al*, 2020). Based on this, it was proposed that SEPT7 could serve as a molecular brake to avoid Ca²⁺ uptake in unstimulated cells (Deb *et al*, 2016, 2020). However, this finding is hard to reconcile with the previously shown role of septins as positive regulators of SOCE.

Deb and colleagues proposed that in unstimulated cells, membrane-associated septins restrict Orai1 mobility, and thereby the probability to encounter STIM1 occasionally bound to the PM (Deb *et al*, 2020). Conversely, the reorganization of septins that follow ER store Ca²⁺ depletion allows STIM1 and Orai1 co-clustering possibly by easing Orai1 diffusion and by rearranging lipid domains at ER-PM junctions. Importantly, treating the cells with forchlorfenuron (FCF, a drug perturbing septin dynamics (Hu *et al*, 2008)) abolished SOCE (Sharma *et al*, 2013; Deb *et al*, 2016), supporting the idea that the spatial reorganization of septins at ER-PM contact sites is indeed required for SOCE.

Considering that SEPT7 is the only member of its subgroup (Mostowy & Cossart, 2012), a reduction of SEPT7 levels is expected to lead to a corresponding reduction of septin filaments/complexes. At resting conditions, such scenario may reduce Orai1 confinement and thereby facilitate the interaction with STIM1 occasionally localized at the PM.

In principle, depletion of septin 2 subgroup members should also hamper septin filaments and facilitate SOCE. However, the pan-siRNA used by Sharma and colleagues displayed only limited efficiency toward the abundant SEPT2 (Sharma *et al*, 2013), potentially still allowing filament formation, and restriction of Orai1 diffusion. Furthermore, though expressed at low levels in most cell lines and tissues SEPT1 (another member of the septin 2 subgroup) may substitute for SEPT4 and SEPT5 in filament assembly. SEPT4 and SEPT5 might instead promote SOCE through specific interaction with a molecular partner that, in turn, regulates ER-PM junctions. This specific function of SEPT4 and SEPT5 may be exerted within the filament, implying different roles for SEPT2 and SEPT4/5-containing filaments, or outside of the filament. Notably, during myogenic differentiation (where Ca^{2+} signaling through sarcoplasmic reticulum stores plays a central role, Sinha *et al*, 2022), SEPT4 expression increases, while the expression of all other septins decreases (Ugorets *et al*, 2023).

Interestingly, De Souza and colleagues have recently proposed a model wherein, upon ER store Ca^{2+} depletion, SEPT4 and PI(4,5)P₂ rearrange at ER-PM junctions and recruit CDC42 that, in turn, promotes the reorganization of cortical actin around forming STIM1 clusters (**fig. 6.1-4**) (de Souza *et al*, 2021). Such actin architecture favors the aggregation of STIM1 and the consequent stable engagement of Orai1. Accordingly, depletion of CDC42, or latrunculin treatment hampered SOCE (de Souza *et al*, 2021).

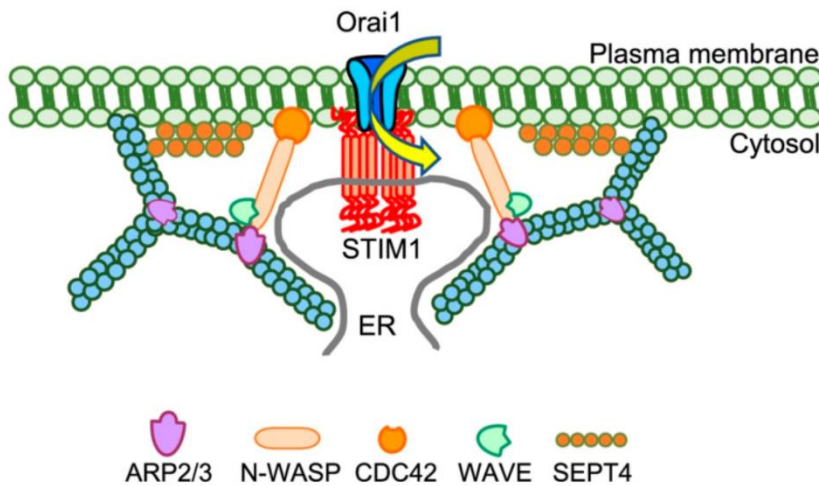


Figure 6.1-4. Proposed model of SEPT4-mediated stabilization of STIM1-Orai1 junctions. SEPT 4 and PI(4,5)P₂ promote the recruitment of CDC42 at ER-PM contact sites. CDC42, in turn, orchestrates actin remodeling around nascent STIM1-Orai1 junctions. Modified from Ahmad et al., 2022

6.1.4. The role of PI(4,5)P₂ during SOCE

Several authors have previously proposed that the polybasic sequence at the C-terminus of STIM1 serves the binding of PI(4,5)P₂ at the PM, and thereby promotes the stable positioning of STIM1 at ER-PM junctions (Liou *et al*, 2007; Li *et al*, 2007; Walsh *et al*, 2010; Zhou *et al*, 2013). Although there is still agreement that PI(4,5)P₂ plays a regulatory role during SOCE, the underlying mechanism seems more intricate than previously thought.

The binding of PI(4,5)P₂ by the STIM1 polybasic sequence is indeed weak (Zhou *et al*, 2013), and a recent study has identified a lysine-rich stretch within the SOAR domain as the primary stabilizer of STIM1 oligomers at the PM (Achildiev Cohen *et al*, 2023). Contrary to the polybasic sequence, SOAR binds several phosphoinositide species, including PI(4)P, which is emerging as a novel regulator of STIM1-dependent activation of Orai1 (Balla *et al*, 2021; Achildiev Cohen *et al*, 2023). Indeed, depletion of PI4P, pharmacological inhibition or genetic deletion of PI4KA (phosphatidylinositol 4-kinase type III α) reduced STIM1 clustering at the PM, and SOCE (Korzeniowski *et al*, 2009; Nakatsu *et al*, 2012). In contrast, depletion of plasmalemmal PI(4,5)P₂ yielded disparate effects on SOCE across different studies, hence challenging the notion of PI(4,5)P₂ as an unequivocal positive regulator of STIM1-Orai1 junctions (Korzeniowski *et al*, 2009; de Souza *et al*, 2021; Mal  th *et al*, 2014; Walsh *et al*, 2010).

Chen and colleagues identified the RAS association domain family 4 (RASSF4), as a positive regulator of SOCE and of membrane contact site formation (Chen *et al*, 2017). RASSF4 activates ARF6 at the PM, and the consequent type I PIP-kinase-

dependent synthesis of PI(4,5)P₂ (Chen *et al*, 2017). Plasmalemmal PI(4,5)P₂ is indeed required for the establishment of steady state membrane contact sites (e.g. by E-Syt2 and E-Syt3) that act as molecular platforms for the recruitment of STIM1 in case of Ca²⁺ store depletion. However, Calloway and colleagues found that PI(4,5)P₂ pools synthesized by distinct type I PIP-Kinase isozymes exert different effects on SOCE (Calloway *et al*, 2011). Specifically, STIM1-Orai1 association upon Ca²⁺ release from the ER was enhanced by PIPKI β overexpression, but inhibited by PIPKI γ overexpression. This was attributed to the finding that PIPKI γ synthesizes PI(4,5)P₂ at disordered plasmalemmal lipid domains, which hinder the engagement of Orai1 by STIM1 (Calloway *et al*, 2011). STIM1-Orai1 junctions instead form at ordered microdomains, which are populated by PIPKI β (Calloway *et al*, 2011). Also the amount of PI(4,5)P₂ within the membrane domain plays a role in the dynamic of STIM1-Orai1 junctions. In particular, Mal  th and colleagues found that depletion of plasmalemmal PI(4,5)P₂ or deletion of the STIM1 polybasic sequence inhibited SARAF-mediated SCDI, hence suggesting a role for PI(4,5)P₂ in the inhibition of SOCE (Mal  th *et al*, 2014). Accordingly, the authors proposed a model wherein STIM1-Orai1 junctions form at PM microdomains characterized by a poor content of PI(4,5)P₂. There, STIM1 holds a conformation that promotes the maximal activation of Orai1 and a minimal interaction with SARAF. Subsequently, STIM1-Orai1 complexes migrate to membrane microdomains with high PI(4,5)P₂ content, where the conformation of STIM1 becomes favorable for the binding of SARAF and subsequent SCDI (fig. 6.1-5).

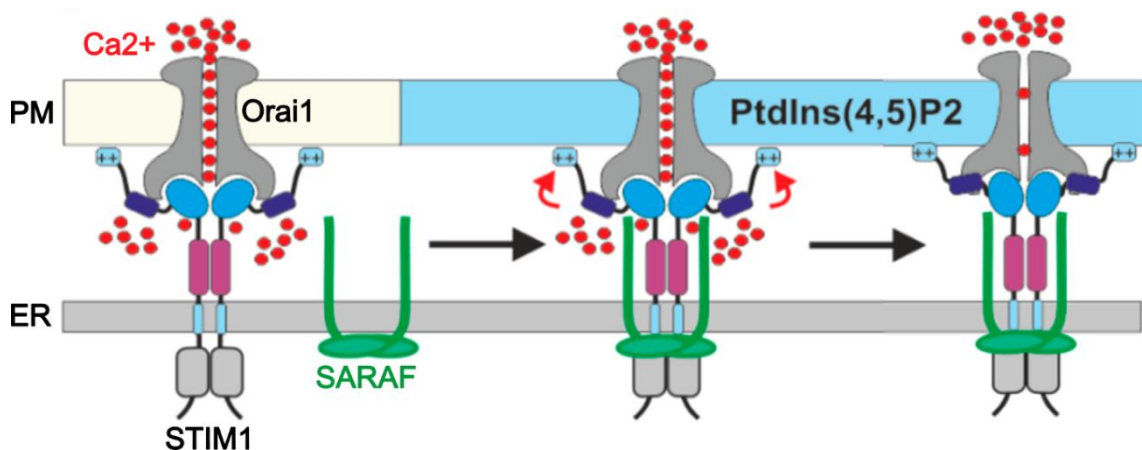


Figure 6.1-5. The plasmalemmal content of PI(4,5)P₂ regulates the turnover of STIM1-Orai1 junctions. STIM1 engages Orai1 at PM microdomains characterized by a low content of PI(4,5)P₂. At these sites the interaction with SARAF is minimal. Then, STIM1-Orai1 complexes relocate to PI(4,5)P₂-rich microdomains where STIM1 possibly adopts a new conformation enabling the association with SARAF and the consequent SCDI. Modified from Dagan & Palty, 2021.

Importantly, depletion of E-Syt1 did not affect the activation of Orai1 channels but hampered the interaction of STIM1 with SARAF, thus suggesting a role for E-Syt1 in defining ER-PM microdomains with high PI(4,5)P₂ content.

After signaling-induced release of Ca²⁺ from the ER, E-Syt1 contributes to the replenishment of plasmalemmal PI(4,5)P₂ by enhancing the connection between ER and PM and thereby facilitating the recruitment of the lipid transporter Nir2 (Chang *et al*, 2013). Nir2, in turn, transfers PA from the PM to the ER, and PI (phosphatidylinositol) in the opposite direction, and thus fuels the local re-synthesis of PI(4,5)P₂ (Chang & Liou, 2015).

Septins, instead, may contribute to the initial shaping of PI(4,5)P₂-poor microdomains by creating a diffusion barrier that excludes PI(4,5)P₂ from nascent STIM1-Orai1 junctions (Pacheco *et al*, 2023). Indeed, upon ER store Ca²⁺ depletion, fluorescently labeled SEPT4 and SEPT5 did not colocalize with STIM1-Orai1 junctions, but reorganized in a ring like structure around them (Sharma *et al*, 2013; Katz *et al*, 2019). When overexpressed, the PH domain was found distributed in a very similar pattern, hence suggesting a spatial segregation between contact sites and septins/PI(4,5)P₂ (Sharma *et al*, 2013). Of note, septin intensity around ER-PM junctions decreased by the time that Orai1 was fully recruited, perhaps to allow the diffusion of PI(4,5)P₂ across contact sites, and the transition of STIM1-Orai1 into a PI(4,5)P₂-rich microdomain.

6.1.5. Aim of this study

Previous data from our laboratory showed that E-Syts bind PIPKI γ . Furthermore, the depletion of the two septin-binding isoforms, PIPKI γ -i3/i5, resulted in an enhanced and prolonged association of E-Syt1 with the PM (Claudia Gras PhD thesis). These data pointed toward a role for these isoforms during SOCE. In light of these findings, we aimed at gaining insights into the dynamics and spatial distribution of E-Syt1-dependent contact sites. Particularly, we aimed at identifying the origin and localization of PI(4,5)P₂ at these junctions, and at elucidating the molecular mechanism underlying the observed regulatory role of PIPKI γ -i3/i5 at ER-PM contact sites.

6.2. Results

6.2.1. E-Syt1-dependent contact sites insert between cortical septin and actin filaments, and actin may regulate their dynamics

The translocation of E-Syt1 to the PM can be induced by suppressing the activity of the SERCA pump with thapsigargin (TG) (Giordano *et al*, 2013). At resting conditions, SERCA actively transports cytosolic Ca^{2+} into the ER lumen, thus counterbalancing the passive efflux of Ca^{2+} from this compartment (Clapham, 2007). Therefore, TG treatment leads to a reduction in ER Ca^{2+} concentration, resulting from unhindered passive Ca^{2+} efflux from the ER (Rogers *et al*, 1995). Reciprocally, the Ca^{2+} concentration in the cytoplasm rises. This, in turn, triggers the formation of STIM1-Orai1 complexes and subsequent cytosolic Ca^{2+} influx via SOCE (Liou *et al*, 2005). The binding of Ca^{2+} to E-Syt1 relieves E-Syt1 from auto-inhibition and enables its binding to plasmalemmal PI(4,5)P₂ (Bian *et al*, 2018).

As a first step to gain insight into the architecture of E-Syt1-dependent contact sites, we sought to investigate their cortical distribution in relation to other cytoskeletal components. Notably, septin and actin filaments localize around STIM1-Orai1 clusters and regulate the spatial distribution and dynamics of these clusters (de Souza *et al*, 2021; Ahmad *et al*, 2022). Therefore, we asked whether a similar scenario may apply to E-Syt1 junctions. To this end, HeLa M cells were transfected with a plasmid encoding fluorescently tagged E-Syt1 (eGFP-E-Syt1), and incubated for 180 seconds with thapsigargin (TG), in presence of calcium. Then, the cells were fixed and immunostained for SEPT2, as a marker of endogenous septin filaments. Samples were subsequently imaged with TIRF (total internal reflection) microscopy, which enables a selective focus on the basal PM (Fish, 2009) (**fig. 6.2-1**).

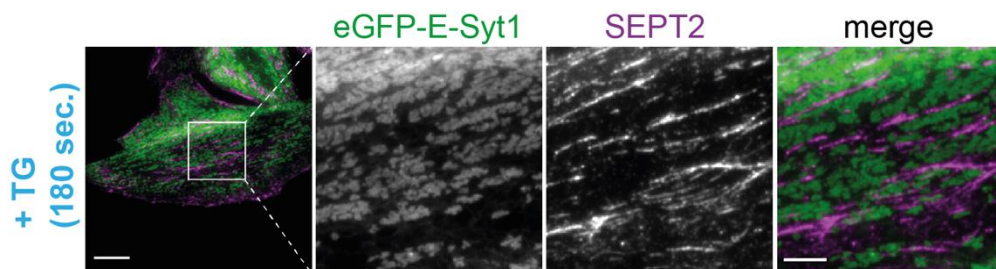


Figure 6.2-1. E-Syt1-dependent contact sites insert between cortical septin filaments. Representative TIRF images of HeLa M cells expressing eGFP-E-Syt1. After 180 seconds of incubation with 1 μM thapsigargin (TG) in presence of extracellular Ca^{2+} (1,3 mM), cells were fixed and immunostained for SEPT2. Scale bar: 10 μm , scale bar of inset: 3 μm .

After 180-seconds exposure to TG, eGFP-E-Syt1 puncta were visible within the TIRF field, but did not colocalize with SEPT2 (**fig. 6.2-1**). Rather, eGFP-E-Syt1 puncta localized between septin filaments. Similarly, it was shown that STIM1-Orai1 junctions do not colocalize with septins, but form at membrane microdomains spatially demarcated by them (Sharma *et al*, 2013). Our result suggests that this may apply to E-Syt1 too, supporting the notion that septins contribute to contact sites formation without being integral part of these molecular complexes.

According to de Souza and colleagues, the septin-mediated reshaping of PI(4,5)P₂ at membrane contact sites serves the reorganization of cortical actin around forming STIM1-Orai1 junctions (de Souza *et al*, 2021; Katz *et al*, 2019). Hence, we further assessed the localization of eGFP-E-Syt1 junctions in relation to actin, which was visualized through the calponin homology domain of utrophin (CHUtrophin), an F-actin reporter (Dong *et al*, 2016). This strategy allowed to perform TIRF imaging on live samples. Also in this case, eGFP-E-Syt1 puncta distributed between actin filaments, without colocalizing with them (**fig. 6.2-2**).

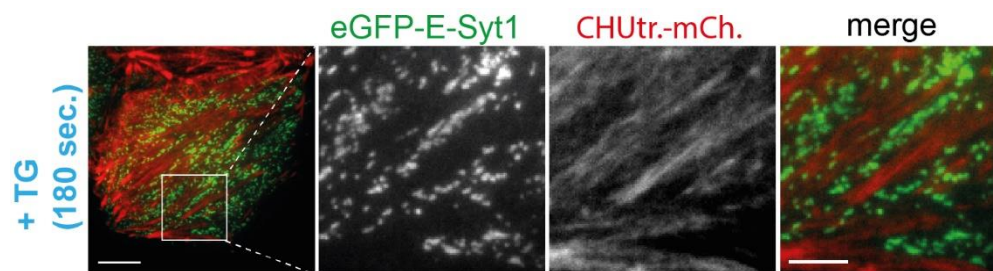


Figure 6.2-2. E-Syt1-dependent contact sites insert between cortical actin filaments. Representative TIRF images of HeLa M cells expressing eGFP-E-Syt1 and CHUtrophin-mCherry. Cells were incubated for 180 seconds with 1 μ M TG in presence of extracellular Ca²⁺ (1,3 mM) before acquisition. Scale bar: 10 μ m, scale bar of inset: 4 μ m.

Then, to gain insight into the dynamics of cortical actin and E-Syt1 contact sites, we monitored the change in fluorescence intensity of eGFP-E-Syt1 and CHUtrophin-mCherry at the PM of TG-stimulated cells. To this end, we focused on cells expressing CHUtrophin at low level, to minimize actin hindrance (**fig. 6.2-3**).

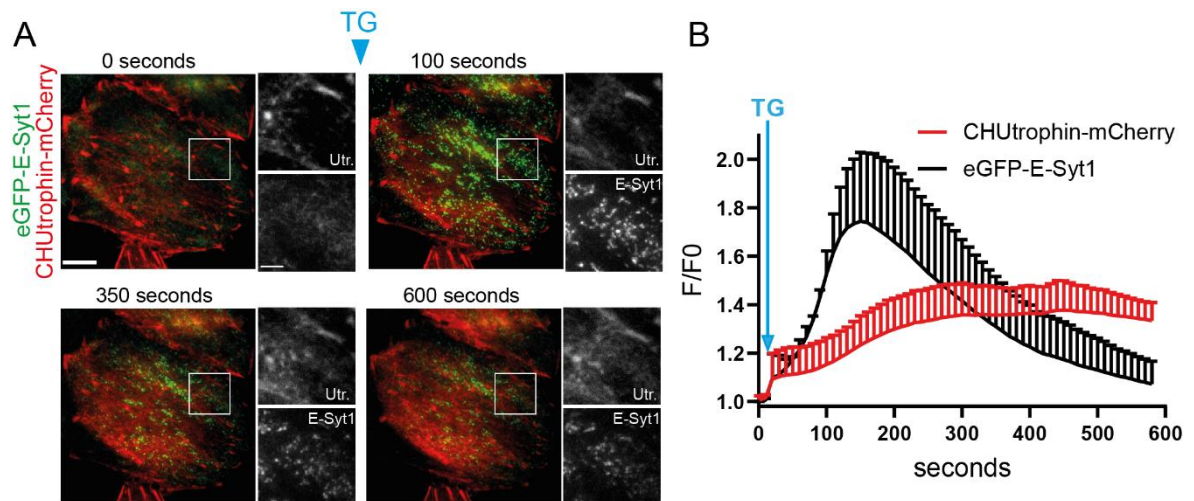


Figure 6.2-3. Dynamics of E-Syt1 and actin at the PM during TG-induced SOCE. (A) Representative frames from live TIRF imaging of HeLa M cells expressing eGFP-E-Syt1 and CHUtrophin-mCherry before and during 1 μ M TG stimulation in presence of extracellular Ca²⁺ (1,3mM). Images were acquired every 10 seconds and TG was added after the first image. Scale bar: 10 μ m, scale bar of inset: 3 μ m. **(B)** Time course of normalized eGFP-E-Syt1 and CHUtrophin-mCherry fluorescence within the TIRF field during the experiment described in (A). Data are represented as mean \pm SD (n=2). Between 5 and 10 cells were imaged per experiment.

The fluorescence intensity of eGFP-E-Syt1 within the TIRF field increased rapidly after TG was applied, to reach a maximum at 150 seconds of recording, before declining again to basal level (**fig. 6.2-3-B**). A similar dynamics was described previously for overexpressed E-Syt1 in response of TG (Giordano et al., 2013). In contrast, actin intensity increased gradually to reach a plateau after 200 seconds, at a phase where E-Syt1 contact sites were dissociating already (**fig. 6.2-3-B**). The inversely correlated trend of E-Syt1 and actin emerges also from the insets in **fig. 6.2-3-A**. While the eGFP-E-Syt1 dots fade between 100 and 350 seconds, CHUtrophin-mCherry increases in intensity and acquires a more homogeneous distribution within the TIRF field. This observation suggests that cortical actin remodeling may promote the dissociation of E-Syt1-contact sites.

To test this hypothesis, we destabilized actin filaments by treating the cells for 10 minutes with 5 μ M latrunculin A. Subsequently, we monitored the recruitment of eGFP-E-Syt1 to the PM in response to TG (**fig. 6.2-4**).

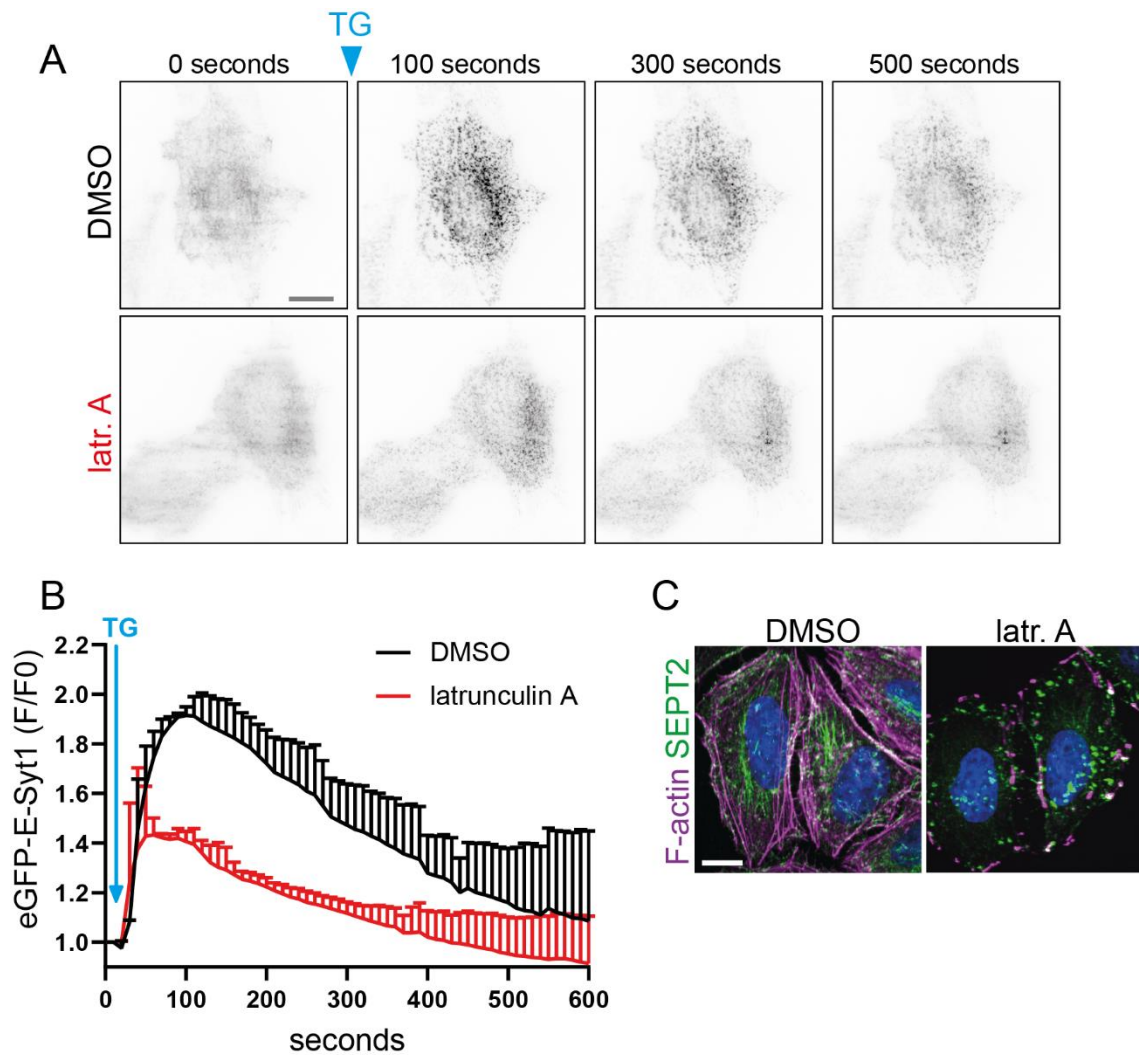


Figure 6.2-4. Formation of E-Syt1-dependent contact sites requires intact actin filaments. (A) Representative frames from live TIRF imaging of HeLa M cells expressing eGFP-E-Syt1 before and during 1 μ M TG stimulation in presence of extracellular Ca²⁺ (1,3mM). Cells were incubated for 10 minutes with 5 μ M latrunculin A or DMSO before imaging. Images were acquired every 10 seconds and TG was added after the first image. Scale bar: 10 μ m. **(B)** Time course of normalized eGFP-E-Syt1 fluorescence within the TIRF field during the experiment described in (A). Data are represented as mean \pm SD (n=2). Between 5 and 10 cells were imaged per condition and experiment. **(C)** Confocal images of HeLa M cells treated for 10 minutes with 5 μ M latrunculin A or DMSO and stained for SEPT2 and F-actin (phalloidin). Scale bar: 15 μ m.

Contrary to what was expected, we did not observe persistent eGFP-E-Syt1 puncta in latrunculin A-treated cells (**fig. 6.2-4-A**). Rather, eGFP-E-Syt1 exhibited a weak and brief recruitment to the PM, followed by dissociation after 100 seconds of recording (**fig. 6.2-4-B**). This indicates a defect in the recruitment and/or stabilization of E-Syt1 at the PM, a scenario that could occur in case of hampered SOCE. Indeed, latrunculin A treatment resulted also in the disruption of septin filaments; therefore, it likely hindered the septin-dependent regulation and stabilization of STIM1-Orai1 junctions (**fig. 6.2-4-C**). In conclusion, further analyses are required to clarify the role of actin in the dynamics of E-Syt1 association with the PM.

6.2.2. The recruitment of E-Syt1 to the PM may occur at membrane microdomains with a “poor” content of PI(4,5)P₂

STIM1-Orai1 junctions form at membrane microdomains with a poor PI(4,5)P₂ content, and subsequently relocate to PI(4,5)P₂-rich microdomains (Mal  th *et al*, 2014). In these PI(4,5)P₂-rich microdomains, STIM1 adopts a conformation that enhances its interaction with SARAF, and the SCDI process initiates (Dagan & Palty, 2021; Mal  th *et al*, 2014). In line with this model, Sharma and colleagues observed that upon TG stimulation, Orai1 and the PI(4,5)P₂ sensor - the PH-PLC  1 domain - acquired an inversely correlated distribution, with the PH domain surrounding Orai1 clusters without co-localizing with them (Sharma *et al*, 2013). Conversely, in absence of SEPT4 and SEPT5, PI(4,5)P₂ maintained a uniform distribution, and was not cleared from Orai1 puncta, supporting a role for septins in reshaping PI(4,5)P₂ microdomains at the PM (Sharma *et al*, 2013).

Like STIM1, also E-Syt1 binds plasmalemmal PI(4,5)P₂ (Giordano *et al*, 2013) and positions in between septin filaments (**fig. 6.2-1**). Therefore, we sought to investigate the distribution of E-Syt1 puncta in relation to PI(4,5)P₂. To this end, we co-expressed the PH domain of PLC   1 fused to eGFP along with mCherry-tagged E-Syt1 (**fig. 6.2-5**). After 180 seconds of incubation with TG, mCh-E-Syt1 puncta became visible within the TIRF field (**fig. 6.2-5-A**). The intensity profile along a 10   m line revealed mild drops in fluorescence intensity of the PH domain coinciding with E-Syt1 puncta (**fig. 6.2-5-B**).

In contrast, prior to stimulation, or after 500 sec. of TG stimulation (when the mCh.-E-Syt1 puncta were decreasing again) the intensity of the PH domain along the same line was more uniform (**fig. 6.2-5-B**, dashed traces). This suggests that, when E-Syt1 reaches the PM, the PH domain distributes outside of the puncta and spreads again when E-Syt1 dissociates.

In case the distribution of the PH domain mirrors that of PI(4,5)P₂, our observations could support a model according to which also E-Syt1 junctions form at PI(4,5)P₂-poor microdomains, and dissociate when PI(4,5)P₂ repopulates these areas. Also in this case, septins may serve as diffusion barriers that modulate the PI(4,5)P₂ content around forming E-Syt1 junctions.

Nevertheless, further analyses are necessary to determine whether this is the case or if the inversely correlated distribution of the PH domain with E-Syt1 simply derives from their competition for binding to PI(4,5)P₂.

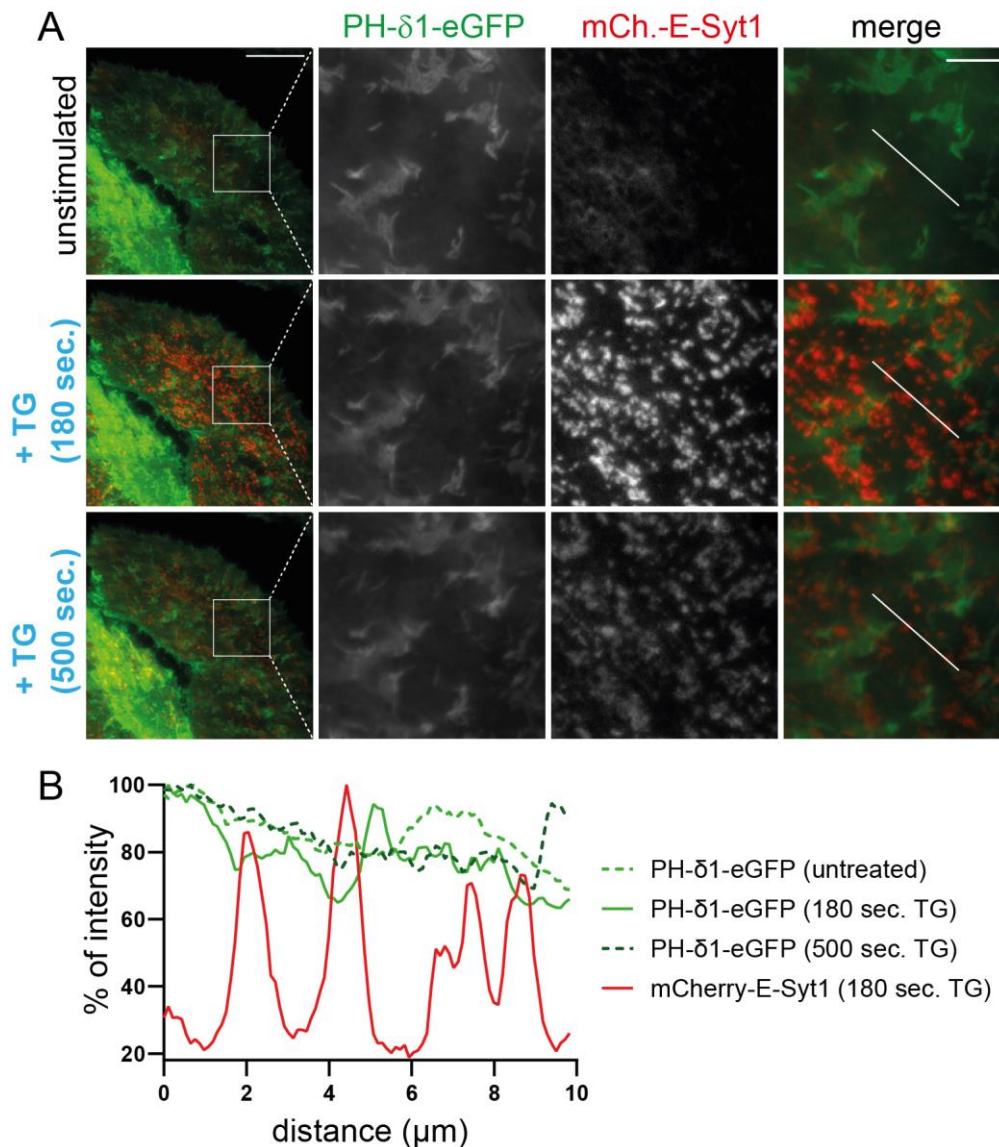


Figure 6.2-5. The PI(4,5)P₂ sensor, the PH-PLC δ 1 domain, acquires an inversely-correlated distribution with E-Syt1 puncta at the PM. (A) Representative frames from live TIRF imaging of HeLa M cells expressing mCherry-E-Syt1 and the PH domain of PLC δ 1 (PH- δ 1-eGFP) before, and after 180 and 500 seconds of incubation with 1 μ M TG in presence of extracellular Ca²⁺ (1,3mM). Scale bar: 20 μ m, scale bar of the inset: 5 μ m. **(B)** Peak normalized intensity profiles of mCherry-E-Syt1 and PH- δ 1-eGFP along the 10 μ m line in (A), after 180 seconds of TG stimulation (solid traces), or before and after 500 seconds of TG stimulation (dashed traces, only for PH- δ 1-eGFP).

6.2.3. PIPKI γ -i5 negatively regulates the recruitment of E-Syt1 to the PM

The recruitment of E-Syt1 to the PM requires the binding of its C2C and C2E domains to PI(4,5)P₂ (Idevall-Hagren *et al*, 2015). Therefore, it may appear counterintuitive that a microdomain enriched in PI(4,5)P₂ would promote the dissociation of E-Syt1 from the PM. However, previous experiments from our laboratory have shown that E-Syts interact with PIPKI γ , and that the depletion of the

septin binding isoforms, PIPKI γ -i3/i5, led to increased and prolonged recruitment of E-Syt1 to the PM in response to TG treatment (Claudia Gras PhD thesis). These data suggest a role for these two kinase isoforms in regulating the dissociation of E-Syt1, and possibly also of STIM1-Orai1 junctions, from the PM.

To further investigate this hypothesis, we monitored the recruitment of eGFP-E-Syt1 when co-expressed along with mCherry-PIPKI γ -i5 (**fig. 6.2-6**). To our surprise, the formation of eGFP-E-Syt1 puncta at the PM was completely abolished, and no increase in eGFP-E-Syt1 fluorescence was detected over time in presence of mCherry-PIPKI γ -i5 (**fig. 6.2-6-A**). Interestingly, already before TG stimulation, eGFP-E-Syt1 was visible within the TIRF field and outlined ER tubules in close proximity to the PM (**fig. 6.2-6-B**).

The failure of eGFP-E-Syt1 to form puncta visible within the TIRF field suggests that the overexpression of PIPKI γ -i5 abolished eGFP-E-Syt1 recruitment to the PM. In principle, this observation is consistent with the earlier finding of enhanced and prolonged E-Syt1 puncta in absence of PIPKI γ -i3/i5.

Nevertheless, it is important to consider that the overexpression of PIPKI γ -i5 may also interfere with the establishment of STIM1-Orai junctions. Indeed it may saturate the PM with PI(4,5)P₂ and impede the generation of PI(4,5)P₂-poor microdomains that allow the interaction between STIM1 and Orai1 (Mal  th *et al*, 2014).

Furthermore, as described in Calloway *et al.*, PIPKI γ , unlike its isozyme PIPKI β , exclusively generates PI(4,5)P₂ within disordered lipid domains, and an elevated concentration of PI(4,5)P₂ in these regions negatively impacts the formation of STIM1-Orai1 junctions (Calloway *et al*, 2011). Indeed, in this study, the overexpression of PIPKI γ -i1 inhibited the TG-dependent association of STIM1 and Orai1.

Hence, considering that the recruitment of E-Syt1 to the PM is Ca²⁺-dependent, the lack of eGFP-E-Syt1 puncta in **fig. 6.2-6** may have derived from an inadequate initiation of SOCE following TG treatment. Conversely, the overexpression-induced excess of PI(4,5)P₂ might have promoted the calcium-independent anchoring of endogenous E-Syt2 and E-Syt3, thereby explaining the close proximity of the ER to the PM before stimulation.

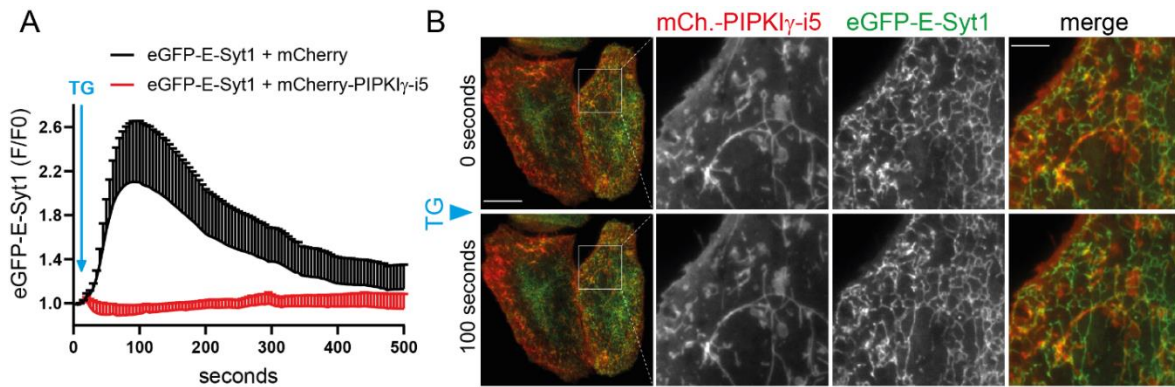


Figure 6.2-6. The overexpression of PIPK1 γ -i5 abolishes the formation of eGFP-E-Syt1-dependent contact sites. (A) Time course of normalized eGFP-E-Syt1 fluorescence within the TIRF field in HeLa M cells co-expressing mCherry or mCherry-PIPK1 γ -i5. Images were acquired every 10 seconds and TG was added after the first image. Data are represented as the mean \pm SD of values obtained from 5 (eGFP-E-Syt1 + mCherry) or 8 (eGFP-E-Syt1+ mCherry-PIPK1 γ -i5) imaged cells (n=1). **(B)** Representative TIRF frames of cells co-expressing eGFP-E-Syt1 and mCherry-PIPK1 γ -i5 from the experiment described in (A). Scale bar: 20 μ m.

6.2.4. Distinct PIPK1 γ Isoforms may differentially modulate E-Syt1 dynamics via direct binding of the E-Syt1 C2E domain

Previous experiments conducted in our laboratory showed that the binding of E-Syts to PIPK1 γ occurs through the C2C domain of E-Syt2 (Bolz *et al*, 2023) and E-Syt3, and the C2E domain of E-Syt1. To further test whether the interaction between E-Syt1 and PIPK1 γ is direct, we assessed the binding capability of recombinant proteins. Indeed, the GST-tagged C2E domain successfully pulled down purified His-tagged PIPK1 γ -i3, thus confirming a direct interaction (**fig. 6.2-7-A**).

Next, we asked whether this interaction could serve the stimulation of PIPK1 γ catalytic activity. In particular, we hypothesized that PIPK1 γ -i3/i5 might be delivered by septins to ER-PM contact sites. There, E-Syt1 could stimulate kinase activity and promote the synthesis of a pool of PI(4,5)P₂ serving the dissociation of ER-PM junctions. However, we did not detect any significant increase in the activity of recombinant PIPK1 γ -i3 in presence of the GST-C2E domain in *in vitro* enzymatic assays (not shown).

We further proceeded with mapping the interaction site of PIPK1 γ on the C2E domain. To this end, we aligned the C2 domains of E-Syt1 (C2A to C2E) with the C2C domains of E-Syt2 and E-Syt3 (**fig. 6.2-7-B**). The PIPK1 γ -binding domains exhibited four basic residues (highlighted in red) that were absent from the non-binding domains, and were distributed across two potential interaction sites. To test whether these sites were indeed involved in kinase binding, we generated several

C2E mutants carrying an alanine and/or a glutamic acid in place of the basic residue in one of the two sites. None of these GST-tagged C2E mutants was able to pull down endogenous PIPKI γ from mouse brain lysate (**fig. 6.2-7-C**), thus suggesting that both sites of basic residues are indispensable for kinase binding.

Finally, we investigated how the binding of PIPKI γ impacts the dynamics of recruitment and dissociation of E-Syt1 at the PM. In particular, we hypothesized that if PIPKI γ plays a role in the dissociation of ESyt1 (and/ or of STIM1-Orai1 junctions) from the PM, the E-Syt1 mutants deficient of PIPKI γ binding, should exhibit a slower or hindered dissociation from the PM. Thus, we expressed an eGFP-E-Syt1 double mutant (residues K1018A/R1020A within the C2E domain) or eGFP-E-Syt1 R1052A single mutant in HeLa M cells and tracked their association with the PM upon addition of TG (**fig. 6.2-7-D-E**).

Interestingly, eGFP-E-Syt1 K1018A/R1020A was not recruited to the PM, whereas the eGFP-E-Syt1 R1052A exhibited a similar kinetics of recruitment as the eGFP-E-Syt1 WT, albeit with a slightly slower dissociation phase.

It is possible that E-Syt1 interacts with different PIPKI γ isoforms. In light of this, the kinetics of E-Syt1 R1052A, similar to that of E-Syt1 WT, could result from the simultaneous partial loss of interaction with different PIPKI γ isoforms that play distinct roles at MCS. For instance, the septin-binding isoforms PIPKI γ -i3/i5 might be involved in the dissociation of E-Syt1 puncta from the PM, while PIPKI γ -i1 and its pool of PI(4,5)P₂ might facilitate the initial stabilization of E-Syt1 at the PM. Of note, PIPKI γ -i1 is the major contributor to the synthesis of plasmalemmal PI(4,5)P₂ that supports the G protein-coupled receptor-mediated Ca²⁺ signaling (Wang *et al*, 2004). Additionally, the difference between E-Syt1 R1052A and E-Syt1 K1018A/R1020A could stem from the single mutant potentially still retaining a limited binding capacity to PIPKI γ , whereas the double mutant might have lost it completely. In fact, E-Syt1 K1018A/R1020A might have also lost the ability to bind PI(4,5)P₂ and might therefore not be recruited to the PM at all. Of note, although the PI(4,5)P₂ binding sites of E-Syt1 reside within both the C2C and C2E domains (Idevall-Hagren *et al.*, 2015), an E-Syt1 mutant carrying a second C2C domain in place of C2E failed to be recruited to the PM (not shown).

Ultimately, the dimerization of E-Syt1 R1052A with endogenous E-Syts could have also mitigated the effect of the loss of interaction with PIPKI γ .

In conclusion, further experiments are required to assess the real impact of each PIPKI γ isoform on the kinetics of recruitment and dissociation of E-Syt1 to the PM.

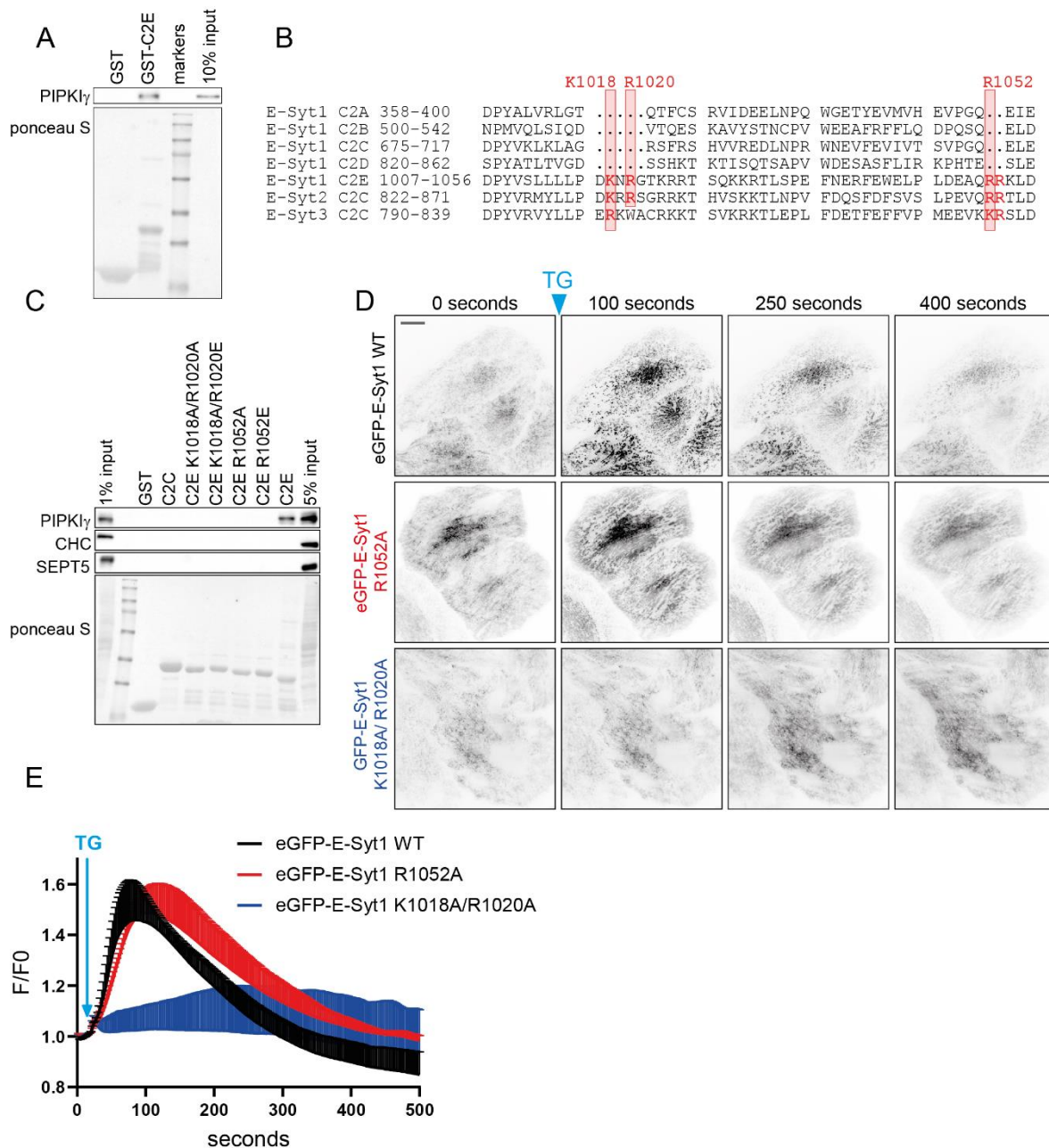


Figure 6.2-7. E-Syt1 directly binds PIPKI γ , and this interaction may regulate both the formation and dissociation of E-Syt1-dependent contact sites. (A) Immunoblot analysis showing successful *in vitro* pull-down of affinity purified His₁₀-PIPKI γ -i3 by the GST-tagged C2E domain of E-Syt1. (B) Primary sequence alignment of PIPKI γ -binding vs. non-binding C2 domains reveals putative E-Syt1 interaction sites, as highlighted in red (residues: K1018, R1020, R1052, R1053). Red rectangles highlight the amino acids mutated in the following screening. (C) Immunoblot analysis of material affinity-purified from mouse brain extracts on GST-fused C2E domain wild type or mutants (as indicated). The mutant C2E domains failed to associate with PIPKI γ . (D) Representative frames from live TIRF imaging of HeLa M cells expressing eGFP-E-Syt1 wild type or the PIPKI γ binding deficient mutants (eGFP-E-Syt1 K1018A/R1020A; eGFP-E-Syt1 R1052A) before and during 1 μ M TG stimulation in presence of extracellular Ca²⁺ (1,3mM). Images were acquired every 10 seconds and TG was added after the first image. Scale bar: 15 μ m. (E) Normalized fluorescence of eGFP-E-Syt1 wild type and mutants over time, measured within the TIRF field during the experiment described in (D). Data are represented as mean \pm SD (n=3). Between 5 and 10 cells were imaged per condition and experiment

6.2.5. Confocal imaging reveals colocalization between TG-induced E-Syt1 puncta and PI(4,5)P₂

The recruitment of E-Syt1 to the PM requires the binding of PI(4,5)P₂ by C2C and C2E domains (Idevall-Hagren *et al*, 2015). However, when the PI(4,5)P₂ reporter - the PH domain of PLC δ 1 - was co-expressed along with eGFP-E-Syt1, no colocalization could be revealed. Instead, following TG stimulation, they acquired an inversely-correlated distribution within the TIRF field. This may arise from the displacement of the PH domain from the PM by E-Syt1. Alternatively, it may reflect the complex scenario where, albeit the recruitment of E-Syt1 to the PM requires the binding of PI(4,5)P₂, it takes place at PI(4,5)P₂-poor microdomains, as suggested for STIM1-Orai1 junctions (Mal  th *et al*, 2014).

To better assess the localization of E-Syt1 in relation to PI(4,5)P₂, we changed strategy and stained PI(4,5)P₂ with an antibody in fixed cells. Therefore, cells expressing eGFP-E-Syt1 were incubated for 200 seconds with TG, fixed, and subsequently immunostained. Then, samples were analyzed by confocal microscope in order to be able to set the focus on different planes (**fig. 6.2-8**).

At the basal plane, PI(4,5)P₂ was enriched at the cell edge (corresponding to the PM), while eGFP-E-Syt1 delineated the ER, spanning most of the cell, in both unstimulated and stimulated cells (**fig. 6.2-8-A**). Additionally, upon stimulation, eGFP-E-Syt1 formed clusters potentially in contact with the PM situated in a different plane, either above or below the focal point.

When we focused on the middle plane of the cell (1,2 μ m up), we found e-GFP-E-Syt1 and PI(4,5)P₂ distributed in a rim around the nucleus, and occasionally colocalizing in presence of TG (**fig. 6.2-8-B**).

The outer border of this rim should align with the PM. However, in **fig. 6.2-8-B** example 1, eGFP-E-Syt1 and PI(4,5)P₂ displayed colocalization as punctate structures resembling endosomes (pink arrowheads). In example 2, instead, eGFP-E-Syt1 and PI(4,5)P₂ exhibited colocalization along tubular patterns, resembling the ER (pink arrowheads).

This suggests the intriguing possibility that the dissociation of E-Syt1 from the PM could be facilitated by PI(4,5)P₂ pools localized on different subcellular compartments, namely endosomes or the ER. These compartments may sequester mature E-Syt1 puncta from the PM and thereby facilitate their detachment. Further

analyses are required to characterize the identity of these subcellular compartments.

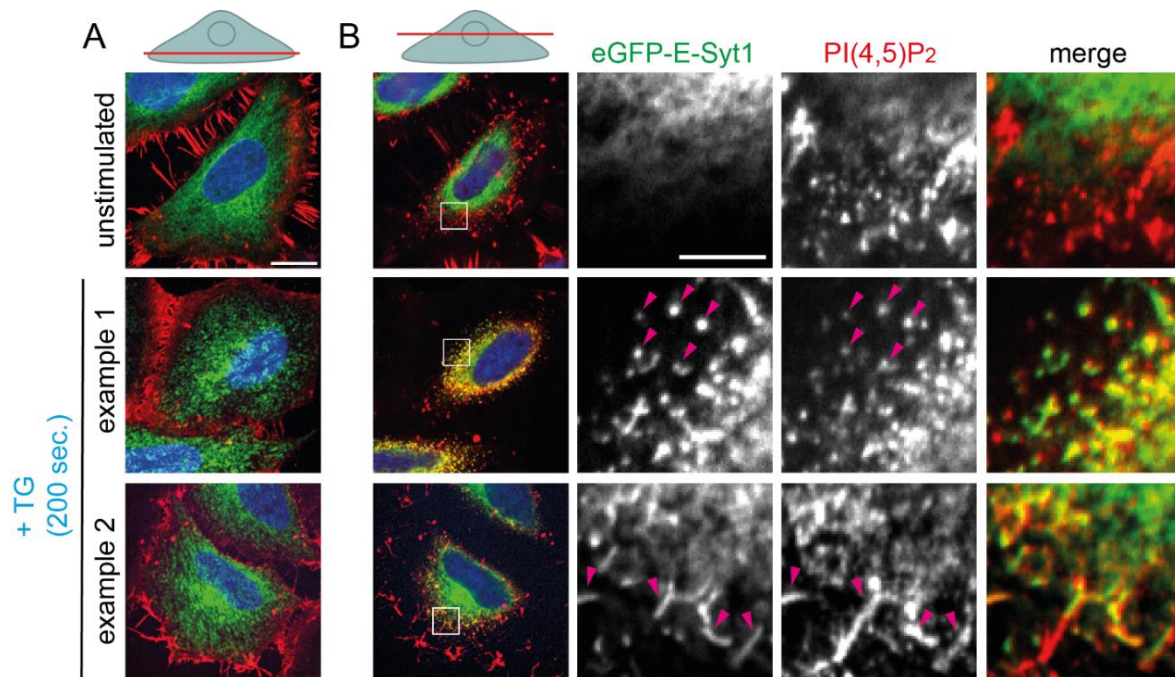


Figure 6.2-8. TG-induced E-Syt1 puncta colocalize with putative intracellular PI(4,5)P₂ pools. (A) Representative confocal images of HeLa M cells expressing eGFP-E-Syt1 and immunostained for PI(4,5)P₂. Cells were left untreated or were incubated for 200 seconds with 1 μM thapsigargin (TG) in presence of extracellular Ca²⁺ (1,3 mM) before fixation. While acquiring these pictures, the focus was kept on the cell basal plane. (B) Confocal images of the same cells shown in (A), acquired by shifting the focus 1,2 μm above the basal plane. Scale bar: 20 μm, scale bar of the inset: 5 μm. Pink arrowheads point at examples of colocalization sites between e-GFP-E-Syt1 and PI(4,5)P₂.

6.2.6. A putative pool of PI(4,5)P₂ synthesized at the ER may compete with the binding of E-Syt1 to the PM

Upon TG treatment a portion of E-Syt1 puncta co-localized with PI(4,5)P₂-containing subcellular compartments resembling vesicles (fig. 6.2-8-B, example 1, pink arrowheads). Given the presence of PI(4,5)P₂, these structures could potentially represent clathrin coated pits or plasmalemma-derived tubular invaginations responsible for clathrin-independent endocytosis. Of note, RTN3, a peripheral ER protein, participates in clathrin-independent endocytosis of EGFR by interacting with such invaginations and exerting the necessary pulling force until dynamin-dependent scission occurs (Caldieri *et al*, 2017). Based on this, we hypothesized that also E-Syt1 might transiently interact with early PI(4,5)P₂-containing endocytic compartments, whose subsequent internalization could facilitate the dissociation of E-Syt1 from the PM.

Hence, we assessed whether interfering with endocytosis could impact the kinetics of E-Syt1 recruitment to, and dissociation from, the PM. To this end, we pre-treated cells with pitstop 2 and dynasore. Pitstop 2 is an inhibitor of clathrin mediated endocytosis that blocks the interaction of the N-terminal domain of clathrin heavy chain with accessory proteins (Von Kleist *et al*, 2011). Dynasore is a dynamin inhibitor, and thus, an inhibitor of clathrin-dependent and clathrin-independent endocytosis (Kirchhausen *et al*, 2004; Wieffer *et al*, 2009). After the treatment, cells were subjected to TG stimulation, and TIRF imaging was employed to monitor the dynamics of eGFP-E-Syt1 junctions (**fig. 6.2-9**).

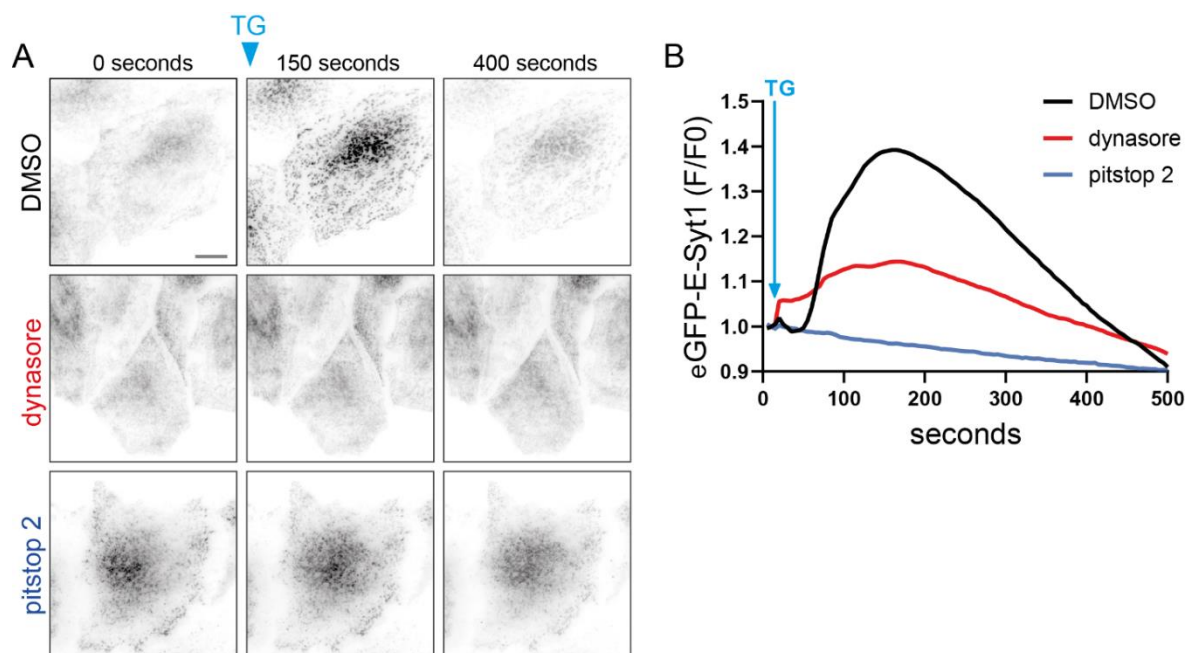


Figure 6.2-9. Dynasore inhibits the formation of E-Syt1-dependent contact sites while pitstop 2 induces constitutive E-Syt1 puncta. (A) Representative frames from live TIRF imaging of HeLa M cells expressing eGFP-E-Syt1 before and during 1 μ M TG stimulation in presence of extracellular Ca²⁺ (1,3mM). Before imaging, cells were incubated for 30 minutes with either dynasore (80 μ M), pitstop 2 (30 μ M), or DMSO. Images were acquired every 10 seconds and TG was added after the first image. Scale bar: 15 μ m. **(B)** Time course of normalized eGFP-E-Syt1 fluorescence within the TIRF field during the experiment described in (A). Data are represented as the mean of values obtained from 10 to 20 imaged cells per condition (n=1).

Cells treated with pitstop 2 displayed few puncta within the TIRF field already before TG stimulation (**fig. 6.2-9-A**), and TG only slightly enhanced eGFP-E-Syt1 recruitment (**fig. 6.2-9-B**). As a mere hypothesis, the presence of eGFP-E-Syt1 clusters at the PM already under resting conditions could be caused by stalled clathrin-coated pits, thus indicating a potential binding of E-Syt1 to these structures. However, if this were the case, a similar outcome should have been observed following dynasore treatment. In this case, however, eGFP-E-Syt1 recruitment was

completely abolished (**fig. 6.2-9**). Therefore, we speculate that pitstop 2 induces constitutive E-Syt1 puncta through a different mechanism that, perhaps, alters cytoplasmic Ca^{2+} levels.

As eGFP-E-Syt1 and $\text{PI}(4,5)\text{P}_2$ exhibited co-localization along tubular patterns resembling the ER (**fig. 6.2-8-B**, example 2, pink arrowheads) we speculated that the $\text{PI}(4,5)\text{P}_2$ -rich microdomains, with which E-Syt1 potentially interacts in order to dissociate from the PM, may be localized on the ER. Intriguingly, the $\text{PI}(4,5)\text{P}_2$ 5-phosphatase INPP5K (inositol polyphosphate-5-phosphatase K) predominantly localizes on the ER, thus suggesting that a small and transient pool of $\text{PI}(4,5)\text{P}_2$ may exist on this organelle (Dong *et al*, 2018; Gurung *et al*, 2003). To investigate the role of this hypothesized pool in ER-PM contact sites, we depleted INPP5K (ideally aiming at increasing $\text{PI}(4,5)\text{P}_2$ on the ER) and monitored the dynamics of eGFP-E-Syt1 at the PM following TG stimulation (**fig. 6.2-10**). Efficient depletion of INPP5K was achieved through 72h of siRNA-mediated knock-down (**fig. 6.2-10-C**). 48h after the treatment with siRNA, cells were transfected with the plasmid encoding eGFP-E-Syt1 and imaged with the TIRF microscope one day later.

INPP5K-depleted cells exhibited a reduced recruitment of eGFP-E-Syt1 to the PM as compared to control cells. This is evident from the F/F0 intensity profile in **fig. 6.2-10-B**, as well as from the reduced intensity of eGFP-E-Syt1 puncta exhibited by knock-down cells compared to control upon a 150-second treatment with TG (representative snapshots, **fig. 6.2-10-A**). This result indeed supports the hypothesis that $\text{PI}(4,5)\text{P}_2$ at the ER may counteract the binding of E-Syt1 to the PM, and thereby aid the dissociation of ER-PM contact sites.

Specifically, INPP5K may hydrolyze $\text{PI}(4,5)\text{P}_2$ at the ER, making E-Syt1 available for binding to the PM in a trans configuration. Conversely, $\text{PIP}K\text{I}\gamma\text{-i3i5}$ may synthesize $\text{PI}(4,5)\text{P}_2$ on the ER, to thus promote the cis binding of E-Syt1 to this organelle and its consequent dissociation from the PM.

Further experiments are required to validate this hypothesis and to elucidate the molecular mechanisms governing the temporal and spatial regulation of these enzymes during the formation and dissociation of ER-PM contact sites.

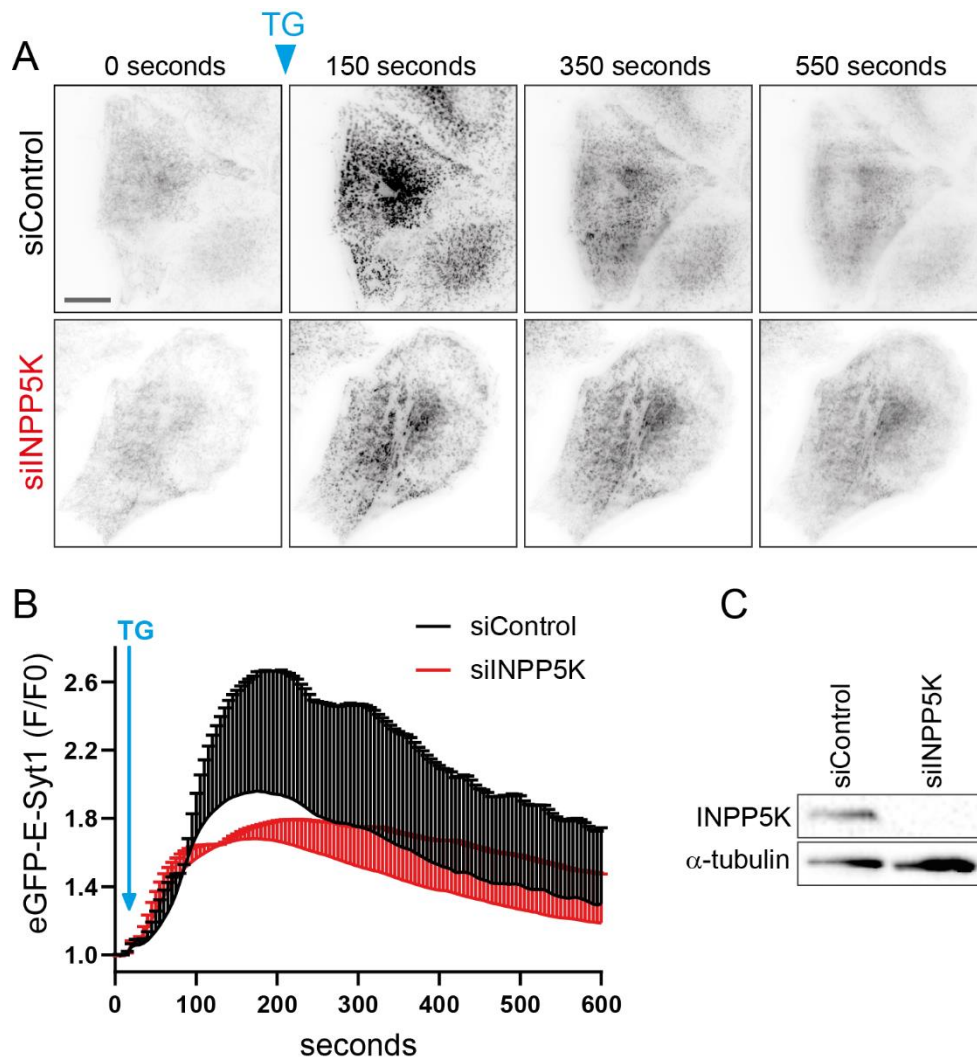


Figure 6.2-10. Depletion of INPP5K reduces the formation of E-Syt1 puncta at the PM. (A) Representative TIRF frames of HeLa M cells treated with siRNA control or targeting INPP5K, and expressing eGFP-E-Syt1, before and during 1 μ M TG stimulation in presence of extracellular Ca²⁺ (1,3mM). During live imaging, pictures were acquired every 10 seconds and TG was added after the first image. Scale bar: 15 μ m. (B) Time course of normalized eGFP-E-Syt1 fluorescence within the TIRF field during the experiment described in (A). Data are represented as mean \pm SD (n=2). Between 5 and 10 cells were imaged per condition and experiment. (C) Western blot analysis of HeLa M cell lysates showing efficient depletion of INPP5K upon 72h of siRNA mediated knock-down.

6.2.7. Generation and analysis of a genome-engineered knock-in cell line expressing eGFP-E-Syt1 from its endogenous locus

To study the dynamics of E-Syt1-dependent contact sites, and to avoid artifacts imposed by exogenous overexpression, we aimed at tagging the endogenous E-Syt1 protein via CRISPR-Cas9 technology, as done previously by Saheki and colleagues (Saheki *et al*, 2016). We introduced a sequence encoding for eGFP (without the stop codon), and a 15 amino acids linker immediately before the start codon of the E-Syt1 gene (fig. 6.2-11-A). Successful knock-in HeLa M clones were validated by Western blotting (fig. 6.2-11-B). The total cell lysate of clone 22

exhibited a band immunoreactive toward both anti-GFP and anti-E-Syt1 antibodies. The molecular size matched the expected size of eGFP-E-Syt1.

The anti-E-Syt1 antibody identified two additional bands at a molecular weight corresponding to E-Syt1. These two bands were also present in HeLa M wild-type lysate, indicating that clone 22 is a heterogeneous knock-in clone. Of note, human E-Syt1 has two isoforms that differ by just 11 residues within exon 14, and cannot be distinguished by Western blot analysis (Saheki *et al*, 2016). Therefore, of the two bands identified by the anti-E-Syt1 antibody, we hypothesize that one was a non-specific, or represented a post-translational modification.

In Saheki *et al.*, the kinetics of endogenous eGFP-E-Syt1 was similar to that of the overexpressed protein. However, in our genome-edited cell line, TG-induced eGFP-E-Syt1 puncta remained detectable within the TIRF field throughout imaging (**fig. 6.2-11-C**), and the F/F0 intensity of endogenous eGFP-E-Syt1 did not exhibit the significant rise and decline over time, as seen for exogenously overexpressed eGFP-E-Syt1 (**fig. 6.2-3/4/6/7/9/10**). Instead, despite some fluctuations, it continued to rise over the course of the 500 seconds of imaging (**fig. 6.2-11-D**), indicating that eGFP-E-Syt1 remained associated with the PM. A similar behavior was observed for other clones obtained in parallel to clone 22 (not shown). We speculated that the difference to Saheki *et al.*, might be caused by a slightly different linker sequence inserted between eGFP and E-Syt1. In particular, we used SGLGSEFDIQHSGGR, whereas Saheki and colleagues inserted SGLRSRAQASNSAVD.

However, also a second batch of clones entirely lacking the linker sequence formed persistent puncta at the PM following TG treatment (not shown), thus suggesting that the linker had no impact on endogenous eGFP-E-Syt1 dynamics. We thus speculated that a possible cause of discrepancy with Saheki and colleagues might lie in different expression patterns of E-Syt paralogs in different HeLa clones used. Nevertheless, due to this unexpected difference we did not use our knock-in cell line for further investigations.

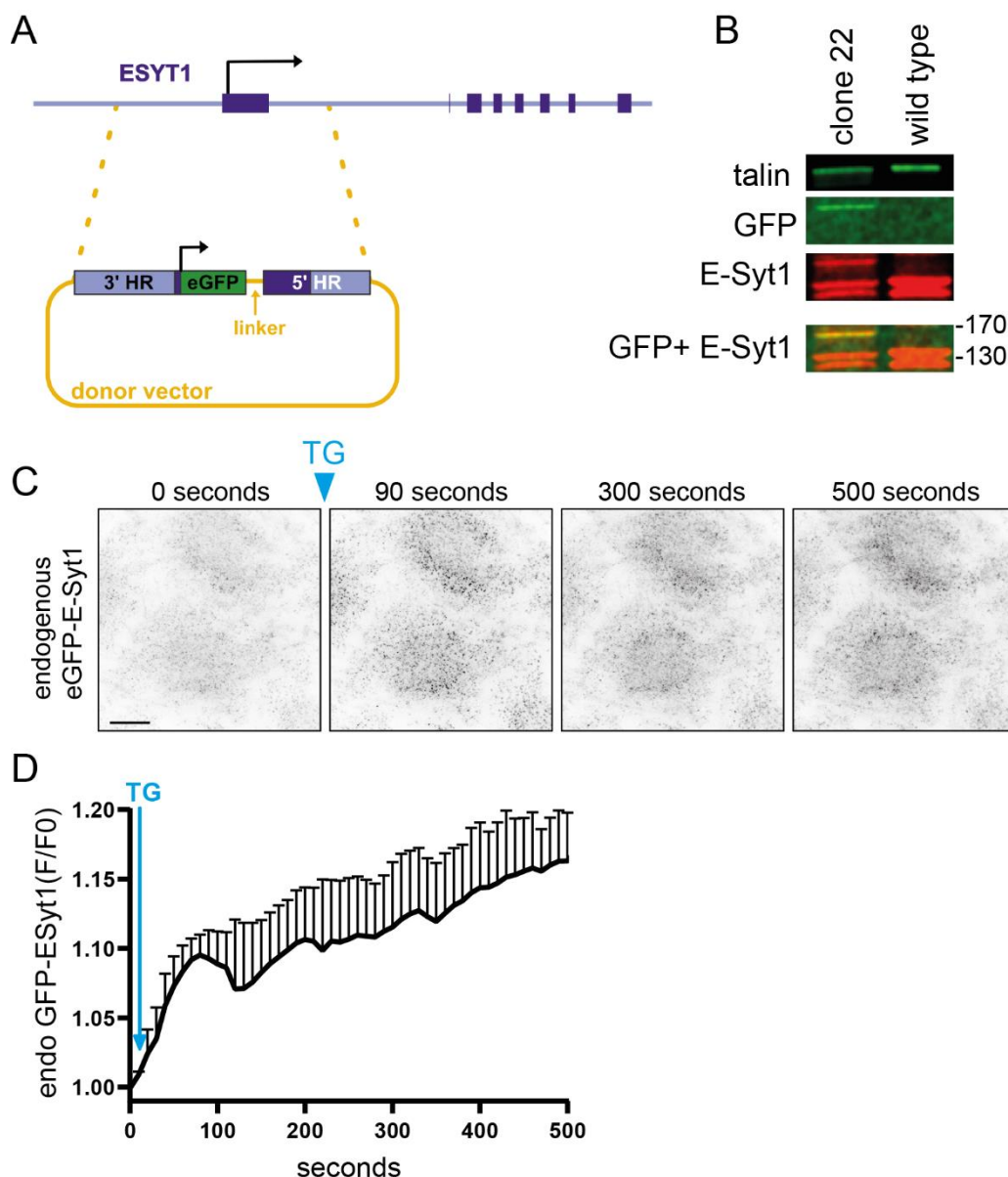


Figure 6.2-11. Generation and time lapse TIRF imaging of an eGFP-E-Syt1 knock-in HeLa M cell line. (A) Scheme of the first part of the E-Syt1 gene (purple: exons, light purple: introns) and of the donor vector used to tag the N-terminus of E-Syt1 with eGFP via the CRISPR-Cas9 based gene editing. The cDNA sequence of eGFP (without the stop codon) was inserted between homology regions (HR). The 5' HR anneals with 975 bp of genomic sequence upstream the E-Syt1 start codon, while the 3' HR anneals with 868 bp downstream (and including) the E-Syt1 start codon. A linker encoding for SGLGSEFDIQHSGGR was inserted between eGFP and the 3'HR. (B) Western blot analysis comparing the immunoreactivity for anti-GFP and anti-E-Syt1 antibodies of cell lysates derived from a selected heterozygous knock-in clone (#22) and parental HeLa M cell line. (C) Representative TIRF frames of knock-in clone #22 before and during 1 μ M TG stimulation in presence of extracellular Ca²⁺ (1,3mM). During live imaging, pictures were acquired every 10 seconds and TG was added after the first image. Scale bar: 15 μ m. (D) Time course of normalized fluorescence of endogenous eGFP-E-Syt1 within the TIRF field during the experiment described in (C). Data are represented as mean \pm SD (n=3). Between 5 and 10 cells were imaged per experiment.

6.3. Discussion

6.3.1. The formation and dissociation of E-Syt1-mediated contact sites may occur at different plasmalemmal microdomains characterized by low and high PI(4,5)P₂ content, respectively

Following ER-Ca²⁺ store depletion, STIM1-Orai1 junctions form at specific membrane microdomains, whose properties are established by septins (Liou & Meyer, 2013; Deb & Hasan, 2016). Septins organize around newly forming STIM1-Orai1 junctions and, possibly by acting as diffusion barriers, restrict the diffusion of PI(4,5)P₂ (Sharma *et al*, 2013; Katz *et al*, 2019; Pacheco *et al*, 2023). This leads to the retention of PI(4,5)P₂ around STIM1-Orai1 junctions, and leaves these contact sites within membrane regions containing low levels of PI(4,5)P₂. At these sites, STIM1 adopts a conformation that maximizes the interaction with Orai1, while minimizing the binding of SARAF (Maléth *et al*, 2014). Additionally, SEPT4 promotes the CDC42-mediated remodeling of actin around STIM1 clusters, thus further supporting the assembly of STIM1-Orai1 complexes (de Souza *et al*, 2021).

STIM1-Orai1 junctions and E-Syt1-mediated ER-PM contact sites are functionally distinct, but act in concert. Following receptor-mediated activation of PLC, and subsequent hydrolysis of PI(4,5)P₂ into DAG and IP₃, STIM1-Orai1 clusters form to mediate SOCE (Carrasco & Meyer, 2011). E-Syt1 contacts form subsequently, as a response to elevated cytoplasmic Ca²⁺ levels, and promote the maintenance of plasmalemmal lipid homeostasis (Yasunori Saheki and Pietro De Camilli, 2018).

In particular, E-Syt1 transports excess DAG from the PM to the ER, and facilitates the recruitment of Nir2 (Saheki *et al*, 2016; Chang *et al*, 2013). Nir2, in turn, shuttles PA from the PM to the ER, and PI in the opposite direction, thus enabling the re-synthesis of PI(4,5)P₂ at the PM (Kim *et al*, 2015; Chang & Liou, 2015).

Considering that E-Syt1 populates STIM1-Orai1 contact sites (Idevall-Hagren *et al*, 2015; Kang *et al*, 2019), we hypothesized that the same membrane characteristics that favor the generation of STIM1-Orai1 complexes may also favor the recruitment of E-Syt1 to the PM. In line with this hypothesis, upon TG-mediated induction of SOCE, eGFP-E-Syt1 contact sites formed between septin and actin filaments (**fig. 6.2-1** and **fig. 6.2-2**). Additionally, when both actin and septin fibers were disrupted by latrunculin A, the recruitment of eGFP-E-Syt1 to the PM was hampered (**fig. 6.2-**

4). These results indicate that the cortical cytoskeleton indeed plays a role in positioning and stabilizing E-Syt1 junctions.

We further asked whether these junctions also form at membrane microdomains characterized by a specific organization of PI(4,5)P₂. Sharma and colleagues previously used the fluorescently labeled PH domain of PLCδ1 to track the distribution of PI(4,5)P₂ relative to Orai1 puncta during SOCE (Sharma *et al*, 2013). We adopted the same approach, and co-expressed mCherry-E-Syt1 with eGFP-PH-δ1 and monitored their distribution through live TIRF imaging (**fig. 6.2-5-A**). Similar to what was previously observed with Orai1 puncta, in our case, at the point when E-Syt1 contact sites formed within the TIRF field, the PH domain moved away from them. Later, when E-Syt1 dissociated, the PH domain partially redistributed across the membrane (**fig. 6.2-5-B**).

In principle, this result may indicate that also E-Syt1 puncta form at membrane microdomains characterized by a lower content of PI(4,5)P₂. Such property may be imposed, once again, by septins creating a diffusion barrier around forming E-Syt1 contacts. Of note, Pacheco *et al.*, showed that the free diffusion of PI(4,5)P₂ is impeded by septins, but not by E-Syt1 puncta (Pacheco *et al*, 2023).

Given the E-Syt1 role in restoring the lipid balance at the PM, it is possible that E-Syt1 junctions initially form at microdomains characterized by a low content of PI(4,5)P₂ (possibly the same where STIM1-Orai1 junctions form). Then, at these sites, E-Syt1 favors the replenishment of PI(4,5)P₂ (Chang *et al*, 2013). This, together with the redistribution of septins away from established contact sites (Sharma *et al*, 2013), likely contributes to the elevation of PI(4,5)P₂ levels at mature E-Syt1 contacts. Accordingly, Maléth and colleagues found that E-Syt1 is required for the establishment of PI(4,5)P₂-rich microdomains where SARAF-induced SCDI occurs (Maléth *et al*, 2014).

Of note, the gradual increase and stabilization of the actin-sensor, UTHrophin-mCherry, at the PM as E-Syt1 dissociates may be caused by PI(4,5)P₂-induced actin polymerization events taking place at mature ER-PM contact sites (Ahmad *et al*, 2022; Wills & Hammond, 2022) (**fig. 6.2-3**). Nevertheless, the data in **fig. 6.2-5**, must be interpreted with caution, because the distribution of the PH domain might not accurately represent the actual distribution of PI(4,5)P₂. Specifically, E-Syt1 and the PH domain may compete for the binding to PI(4,5)P₂, so that the PH domain is displaced when E-Syt1 arrives to the PM.

6.3.2. Putative role of the interaction of E-Syt1 with PIPKI γ

Following the activation of PLC, E-Syt1 aids the restoration of plasmalemmal PI(4,5)P₂ levels by promoting the Nir2-dependent transport of its precursor, PI, to the PM (Chang *et al*, 2013). Nevertheless, repetitive contact site formation, as occurring during Ca²⁺ oscillations under certain signaling conditions (Berridge *et al*, 2003), might require additional mechanisms ensuring a fast, local re-synthesis of PI(4,5)P₂.

The C2E domain of E-Syt1 and the C2C domains of E-Syt2 and E-Syt3 bind PIPKI γ (**fig. 6.2-7**) (Bolz *et al*, 2023). Furthermore, depletion of the septin-binding isoforms, PIPKI γ -i3/i5, led to enhanced and prolonged association of E-Syt1 with the PM during SOCE (Claudia Gras PhD thesis). Conversely, the overexpression of PIPKI γ -i5 abolished the recruitment of E-Syt1 to the PM (**fig. 6.2-6**).

These findings point to two potential scenarios. Either PIPKI γ -i3/i5 play a direct inhibitory role in the recruitment of E-Syt1 to the PM, or these isoforms negatively regulate STIM1-Orai1 junctions and the consequent process of SOCE. Indeed, the recruitment of E-Syt1 to the PM relies on SOCE (Idevall-Hagren *et al*, 2015). The increase in calcium influx upon depletion of PIPKI γ -i3/i5 or i5 alone, observed by Prof. Dr. Michael Krauß, points toward the second possibility.

Nevertheless, based on the requirement of E-Syt1 for the generation of PI(4,5)P₂-rich microdomains where the SCD1 process occurs (Maléth *et al*, 2014), it is tempting to speculate that, by simultaneously binding to PIPKI γ -i3/i5, E-Syt1 and septins could recruit these kinases to MCS. At these sites, PIPKI γ -i3/i5 may contribute to the restoration of local PI(4,5)P₂ levels, and to the consequent inactivation of STIM1-Orai1 complexes by SARAF (Maléth *et al*, 2014; Calloway *et al*, 2011).

We additionally hypothesized that kinase binding to E-Syt1 may potentially serve to enhance PIPKI γ activity. Therefore, after confirming the direct interaction between the C2E domain of E-Syt1 and PIPKI γ (**fig. 6.2-7-A**), we performed in vitro kinase assays. However, we did not find a significant increase in kinase activity when recombinant His₁₀-PIPKI γ -i3 was incubated with recombinant C2E domain (not shown). Nonetheless, PIPKI γ activity is known to be boosted by homodimerization (Lacalle *et al*, 2015). Considering that E-Syt1 forms dimers (Giordano *et al*, 2013), it is plausible that when it binds to PIPKI γ it could induce the kinase to dimerize too. However, since the dimerization of E-Syts occurs through the SMP domain

(Schauder *et al*, 2014), our in vitro assays involving only the purified C2E domain, could not have allowed such event to occur. Hence, the question of whether E-Syt1 enhances PIPKI γ activity remains unresolved.

We identified the binding sites for PIPKI γ on the C2E domain (**fig. 6.2-7-B**). These sites involve four basic residues organized into two pairs (K1018, R1020 and R1052, R1053), which are conserved across the C2 binding domains of E-Syts. A mutagenesis approach further confirmed the requirement of both binding sites for a successful interaction with PIPKI γ (**fig. 6.2-7-C**). In light of the putative negative regulatory role of PIPKI γ -i3/i5 during SOCE (or, simply, on E-Syt1-dependent contact sites), we hypothesized that E-Syt1 mutants unable to bind PIPKI γ would persist longer at the PM. Surprisingly, however, of the two tested mutants, the double mutant (eGFP-E-Syt1-K1018A/R1020A) showed no recruitment to the PM at all, while the single mutant (eGFP-E-Syt1-R1052A) exhibited only a slight delay in the dissociation from the PM, compared to eGFP-E-Syt1 WT (**fig. 6.2-7-D-E**). Given that the binding of E-Syt1 to PI(4,5)P₂ relies also on the C2E domain (Idevall-Hagren *et al*, 2015), it is possible that eGFP-E-Syt1-K1018A/R1020A lost the ability to bind the PM. This needs to be assessed in future experiments.

Alternatively, eGFP-E-Syt1 R1052A might show similar kinetics of membrane recruitment as eGFP-E-Syt1 WT, because of one or more of the following reasons: 1) eGFP-E-Syt1 R1052A may still retain some residual binding to PIPKI γ . 2) E-Syt1 may bind different PIPKI γ isoforms, which, in turn, could exert opposite regulatory roles on the interaction of E-Syt1 with the PM. For instance, PIPKI γ -i3/i5 may facilitate the dissociation of E-Syt1 contact sites, while other isoforms may provide the initial stabilization of E-Syt1 at the PM. In this case, a partial loss of interaction with all PIPKI γ isoforms, could result in an intermediate phenotype. 3) The dimerization of E-Syt1 R1052A mutant with endogenous wild type E-Syts could generate complexes still capable of recruiting PIPKI γ to MCS. To analyze this in more detail, the dynamics of eGFP-E-Syt1 R1052A should be assessed in combination with the depletion of, at least, endogenous E-Syt1.

6.3.3. The ER as a putative source of PI(4,5)P₂

Following TG stimulation, a fraction of eGFP-E-Syt1 exhibited colocalization with PI(4,5)P₂ on intracellular compartments resembling vesicles and ER-tubules (**fig. 6.2-8**). Based on this, we hypothesized that the binding of E-Syt1 to PI(4,5)P₂ pools

localized on compartments other than the PM, such as early endocytic or lysosomal compartments, could serve as a mechanism for E-Syt1 dissociation from the PM. Of note, PIPKI γ -i5 has been shown to populate endosomes, and autophagosomes (Sun *et al*, 2013; Schill *et al*, 2014; Tan *et al*, 2016). Hence, we assessed whether the inhibition of endocytosis would result in a prolonged association of E-Syt1 with the PM (**fig. 6.2-9**). However, treatment with two endocytic drugs, pitstop 2 and dynasore, yielded conflicting results. Therefore, we focused on the ER as a potential source of alternative PI(4,5)P₂ pools. In particular, Watt and colleagues provided evidence of small PI(4,5)P₂ pools within the ER using purified PLC δ 1-PH-GST applied to ultrathin cellular sections, followed by detection through immunogold labeling and electron microscopy imaging (Watt *et al*, 2002). Remarkably, they found that approximately 8% of the gold particles were concentrated within the ER (Watt *et al*, 2002). In addition, a PI(4,5)P₂ 5-phosphatase, INPP5K, resides on peripheral tubular ER, suggesting that a small portion of this phosphoinositide may indeed reside on this organelle (Gurung *et al*, 2003; Dong *et al*, 2018).

To artificially increase the putative PI(4,5)P₂ content on the ER, we depleted INPP5K, and subsequently monitored the dynamic of eGFP-E-Syt1 during SOCE (**fig. 6.2-10**). Cells depleted of INPP5K exhibited a small decrease in eGFP-E-Syt1 recruitment to the PM, suggesting that a second pool of PI(4,5)P₂, substrate to INPP5K, might indeed compete with the binding of E-Syt1 to the PM. Given the negative role of PIPKI γ -i3/i5 on E-Syt1-dependent MCSs, we hypothesize that these isoforms are indeed responsible for the synthesis of this ER-resident PI(4,5)P₂ pool. Notably, Tan and colleagues found PIPKI γ -i5 to synthesize PI(4,5)P₂ on nascent autophagosomes at the ER surface (Tan *et al*, 2016).

The substrate for PIPKI γ , PI(4)P, might be provided by the lipid transfer proteins ORP5 and ORP8 (oxysterol-binding protein–related protein 5 and 8) that transport PI(4)P from the PM to the ER at ER-PM contact sites (Chung *et al*, 2015). ORP8, in particular, is recruited to ER-PM junctions by increased plasmalemmal levels of PI(4,5)P₂ (Sohn *et al*, 2018). Hence, the generation of PI(4,5)P₂-rich microdomains at mature ER-PM contact sites (where SCID is initiated), may result in the synthesis of PI(4,5)P₂ on the ER, thus finally facilitating the dissociation of E-Syt1 from the PM.

This hypothetical mechanism would require tight spatiotemporal regulation. One might consider, for instance, that tubular ER is in close proximity to MTs, where also

septins localize (Barlan & Gelfand, 2017; Spiliotis & Nakos, 2021). Septins, in particular, not only colocalize with perinuclear MTs bundles, but also associate with and spatially organize- MTs plus ends nearby the PM (Bowen *et al*, 2011).

According to Sharma *et al.*, septins initially gather around forming STIM1-Orai1 complexes, but leave as these complexes mature (Sharma *et al*, 2013; Katz *et al*, 2019). It is possible that, at this point, cortical MTs-associated septins recruit PIPKI γ and bring it in proximity to tubular ER, where E-Syts could retain it. Then, local synthesis of PI(4,5)P₂ would facilitate the binding of E-Syt1 to the ER in cis, and the dissociation from the PM.

Finally, INPP5K, may deplete excess PI(4,5)P₂ to restore the “availability” of E-Syt1 to bind to the PM again for a next round of stimulation. Of note, like E-Syt1, also INPP5K localizes on tubular peripheral ER, and its phosphatase activity is required for regulating the ER shape (Dong *et al*, 2018).

6.3.4. Experimental considerations and limitations of this study

During our experiments we monitored exogenous eGFP-E-Syt1. However, the overexpression of this protein may induce artifacts. For instance, it may lead to the excessive tethering of the ER to the PM. Furthermore, given that E-Syt proteins form homo- and heterodimers, whose characteristics depend on the type of E-Syt present within the complex, an excess of E-Syt1 over E-Syt2 and E-Syt3 may increase the fraction of E-Syt complexes exhibiting calcium sensitivity (Giordano *et al*, 2013; Idevall-Hagren *et al*, 2015). This could eventually modify the formation of ER-PM contact sites in response to increased levels of cytoplasmic Ca²⁺.

Indeed, endogenously labeled eGFP-E-Syt1, as expressed by genome-edited cells, exhibited a different dynamics compared to the exogenous one upon stimulation with TG in presence of extracellular Ca²⁺ (**fig. 6.2-11-C-D**). Despite some fluctuations, its intensity at the PM continued to increase throughout the imaging period, indicating a more persistent association with the PM. This may reflect the behavior of heterodimers containing E-Syt2 and E-Syt3. On the contrary, the over-expressed eGFP-E-Syt1 has a high probability to homodimerize with itself; therefore, the resulting MCS likely exhibit the expected Ca²⁺ dependent dynamics of E-Syt1 homodimers.

Another issue arises from the reliance of E-Syt1 contact sites on the formation of STIM1-Orai1 complexes and SOCE. This dependency is evident from the fact that

the depletion of STIM1 impedes the recruitment of E-Syt1 to the PM (Idevall-Hagren *et al*, 2015). This complicates the understanding of whether a specific manipulation, leading to changes in E-Syt1 dynamics, directly influences E-Syt1 or, instead, has a primary impact on cytoplasmic calcium levels. This is the case of manipulations such as the knock-down and overexpression of PIPKI γ , knock-down of septins, and latrunculin A treatment. In the latter example, for instance, it is established that septins and actin are required for the stable association of STIM1 with Orai1 (de Souza *et al*, 2021; Sharma *et al*, 2013). Consequently, any alteration in the organization of septins and actin may influence the association of STIM1 to Orai1. Accompanying these experiments with measurements of Ca²⁺ levels may help to clarify such implications.

7. Appendix B

7.1. Abbreviations

AA	acrylamide
AH	anillin homology
ALIX	apoptosis-linked Gene 2 Interacting Protein X
ANOVA	analysis of variance
AP	alkaline phosphatase
APS	ammonium persulfate
ARF	ADP-ribosylation factor
ATCC	American type culture collection
ATG14	autophagy-related protein 14
ATP	adenosine triphosphate
BMM	bone marrow-derived macrophages
BORG	binder of Rho GTPase
BSA	bovine serum albumin
Ca ²⁺	calcium
CAF	cancer-associated fibroblasts
Cdc42EPs	Cdc42 effector proteins
CDK(s)	cyclin-dependent kinase(s)
CDP	cytidine diphosphate
CDS(s)	coding sequence(s)
CEP170	centrosomal protein 170
CEP55	centrosomal protein of 55 KDa
CHC	clathrin heavy chain
CHMP4B	charged multivesicular body protein 4B
CHUtrophin	calponin homology domain of utrophin
CIT-K	citron kinase
CLIP-170	cytoplasmic linker protein 70
CMV	cytomegalovirus
CRAC	calcium release-activated calcium
CRISPR	clustered regularly interspaced short palindromic repeats
Cas	CRISPR-associated systems
CTE	carboxyl-terminal extension
DAG	diacylglycerol
DAPI	4',6-diamidino-2-phenylindole
dCDP	deoxycytidine diphosphate
dCTP	deoxycytidine triphosphate
DMEM	Dulbecco's modified Eagle's medium

DMSO	dimethyl sulfoxide
DNA	deoxyribonucleic acid
dNTP	deoxynucleotide triphosphates
DPBS	Dulbecco´s phosphate-buffered saline
ΔSB	septin binding deficient
DSDB	donkey serum dilution buffer
dTTP	deoxythymidine triphosphate
ECT2	epithelial cell transforming sequence 2
EDTA	ethylenediaminetetraacetic acid
EGFR	epidermal growth factor receptor
EM	electron microscopy
EMT	endothelial to mesenchymal transition
ESCRT	endosomal sorting complexes required for transport
E-Syt(s)	extended synaptotagmin(s)
FAK	focal adhesion kinase
FBS	fetal bovine serum
FCDI	fast Ca ²⁺ -dependent inactivation
FCF	forchlorfenuron
FERM	four-point-one-protein/ezrin/radixin/moesin
FIP3	Rab11 family-interacting protein 3
FRET	förster resonance energy transfer
FYVE-CENT	FYVE domain-containing centrosomal protein
GA	glutaraldehyde
GAP	GTPase-activating protein
GAPDH	glyceraldehyde-3-phosphate dehydrogenase
GDP	guanosine diphosphate
GEF	guanine nucleotide exchange factor
GFP	green fluorescent protein
GS	goat serum
GSDB	goat serum dilution buffer
GST	glutathione S-transferases
GTP	guanosine triphosphate
GTP	guanosine-5´-triphosphate
GUV	giant unilamellar vesicle
H	Hour(s)
HA	Human influenza hemaagglutinin
HBS	HEPES-buffered saline
HDAC6	histone deacetylase 6
Hek	human embryonic kidney
HeLa	named after Henrietta Lacks
HEPES	4-(2-hydroxyethyl)-1-piperazineethanesulfonic acid

HHL16	human hepatocyte line 16
HR	homology region
HRP	horseradish peroxidase
HSP70	70 kilodalton heat shock protein
ICB	intercellular bridge
ICC	immunocytochemistry
ICC	immunocytochemistry
IgG/M	immunoglobulin G/M
INPP5K	inositol polyphosphate-5-phosphatase K
IP	immunoprecipitation
IP3	inositol 1,4,5-triphosphate
IP3R	inositol triphosphate receptor
IRES	internal ribosome entry site
JACoP	just another colocalization plugin
LB	lysogeny broth
MAP	MT-associated protein
MBD	microtubules binding domain
MCAK	mitotic centromere-associated kinesin
MCS	membrane contact sites
MDCK	madin-Darby Canine Kidney
MKLP1	mitotic kinesin-like protein 1
MKLP2	mitotic kinesin-like protein 2
mRNA	messenger RNA
MT(s)	Microtubule(s)
NCK	non-catalytic region of tyrosine kinase
NRK	normal rat kidney
NTE	amino-terminal extension
NTP	nucleotide triphosphate
OCRL	oculo-cerebro-renal-syndrome of Lowe
ORP5/8	oxysterol-binding protein-related protein 5/8
PA	phosphatidic acid
PBS	phosphate-buffered saline
PCR	polymerase chain reaction
Pen-Strep	penicillin-streptomycin
PFA	paraformaldehyde
PH	pleckstrin homology
PI	phosphatidylinositol
PI(3)P	phosphatidylinositol-3-phosphate
PI(3,4)P ₂	phosphatidylinositol-3,4-bisphosphate
PI(3,4,5)P ₃	phosphatidylinositol-3,4,5-triphosphate

PI(3,5)P ₂	phosphatidylinositol-3,5-bisphosphate
PI(4)P	phosphatidylinositol-4-phosphate
PI(4,5)P ₂	phosphatidylinositol-4,5-bisphosphate
PI(5)P	phosphatidylinositol-5-phosphate
PI3K-C2a	phosphatidylinositol-4-phosphate 3-kinase C2 domain-containing alpha
PI4KA	phosphatidylinositol 4-kinase type IIIa
PIC	protease inhibitor cocktail
PIPKI	phosphatidylinositol 4-phosphate 5-kinase type 1
PIPKI α	phosphatidylinositol 4-phosphate 5-kinase type 1 alpha
PIPKI β	phosphatidylinositol 4-phosphate 5-kinase type 1 beta
PIPKI γ	phosphatidylinositol 4-phosphate 5-kinase type 1 gamma
PIPKI γ -i3/i5	phosphatidylinositol 4-phosphate 5-kinase type 1 gamma isoform 3 and 5
PIP-kinases	phosphatidylinositol phosphate kinases
PLC	phospholipase C
PLK4	polo-like kinase 4
PM(s)	plasma membrane(s)
PMSF	phenylmethylsulphonyl fluoride
PRC1	protein regulator of cytokinesis
PTMs	post-translational modifications
RASSF4	RAS association domain family 4
RFP	red fluorescent protein
RNA	ribonucleic acid
ROCK	Rho-associated coiled-coiled-containing kinase
ROI(s)	region(s) of interest
RT	room temperature
RT-PCRs	reverse transcriptase-PCRs
SAM	sterile alpha motif
SARAF	SOCE-associated regulatory factor
SCDI	slow Ca ²⁺ -dependent inactivation
SDS(-PAGE)	Sodium dodecyl sulfate (-polyacrylamide gel electrophoresis)
SERCA	sarco-endoplasmic reticulum Ca ²⁺ ATPase
sgRNAs	single guide RNAs
siRNA	small interference RNA
SMP	synaptotagmin-like mitochondrial lipid-binding protein
SNX5	sorting nexin 5
SOAR	STIM1 Orai activating region
SOCE	store-operated calcium entry
SOCS7	suppressor of cytokine signaling 7
STIM1	stromal interaction molecule 1
SUE	septin unique element

TAE	Tris-Acetate-EDTA
TAU	tubulin-associated unit
TE	TRIS-EDTA
TEMED	tetramethylethylenediamine
TG	thapsigargin
TIRF	total internal reflection fluorescence
Tris	tris(hydroxymethyl)aminomethane
TSG101	tumor susceptibility gene 101
TTC19	tetratricopeptide repeat domain 19
U-ExM	ultrastructure expansion microscopy
VPS 36	vacuolar protein-sorting-associated protein 36
YAP1	yes-associated protein 1
3D-SIM	three-dimensional structured illumination microscopy

7.2. List of Figures and Tables

Figure 1-1. Positioning of the actomyosin ring	13
Figure 1-2. Cleavage furrow Ingression	15
Figure 1-3. Midbody maturation and abscission.....	18
Figure 1-4. The anchoring function of the midbody	19
Figure 1-5. The midbody is a docking station for recycling endosomes	20
Figure 1-6. The localized synthesis of PI(4,5)P ₂ by PIPKIs is linked to its usage.....	26
Figure 1-7. Scheme representing the human PIPK1 γ isoforms	29
Figure 1-8. Structure and assembly of mammalian septins	33
Figure 1-9. Actin-associated septins	36
Figure 1-10. MT-associated septins.....	39
Figure 1-11. Septins at the base-neck border of a cellular protrusion	40
Figure 3-1. Depletion of PIPK1 β or PIPK1 γ stalls cells at early stages of mitosis while exclusively PIP1 γ is required for mitotic progression after furrow ingression.....	82
Figure 3-2. Depletion of PIPK1 α , β or γ does not cause major changes in plasmalemmal PI(4,5)P ₂ 83	
Figure 3-3. Upon knock-down of PIPK1 γ , anillin is scattered and the fraction of SEPT2 at the cytokinetic bridge is reduced.....	85
Figure 3-4. Knock-down of PIPK1 γ leads to multinucleation	86
Figure 3-5. PIPK1 γ isoform 3 and 5 (i3/i5) interact with septins through two aromatic amino acids (W646 and Y647) harbored in their common splice insert	89
Figure 3-6. PIPK1 γ -i5 interacts with septins independently of actin and kinase activity	90
Figure 3-7. MCherry-PIPK1 γ -i5 progressively enriches at the ingressing cleavage furrow together with anillin and SEPT2	91
Figure 3-8. Selective knock-down of PIPK1 γ -i3/i5 affects the organization of anillin and SEPT2, and impairs the elongation of the cytokinetic bridge	93
Figure 3-9. Knock-down of PIPK1 γ -i3/i5 increases multinucleation	94
Figure 3-10. PIPK1 γ -i5 wild type, but not kinase dead or septin binding-deficient, rescues anillin compactness, septin accumulation at the bridge and the length of the acetylated tubulin bridge	97
Figure 3-11. Knock-down of OCRL rescues anillin scattering, but not septin enrichment at the bridge, in PIPK1 γ -i3/i5 depleted cells	99
Figure 3-12. Septins and PIPK1 γ form a complex with midbody components.....	100
Figure 3-13. Depletion of PIPK1 γ -i3/i5 selectively reduces the intensity of the centralspindlin component, MKLP1, at the midbody.....	101
Figure 3-14. PIPK1 γ -i5 wild type, but not kinase dead or septin binding-deficient mutants, rescues MKLP1 accumulation at the midbody	102
Figure 3-15. Depletion of SEPT2 phenocopies the loss of MKLP1 observed in absence of PIPK1 γ - i3/i5	103

Figure 3-16. Super-resolution of the cytokinetic bridge through ultrastructure expansion microscopy (U-ExM).....	106
Figure 3-17. Depletion of PIPK1 γ -i3/i5 does not obviously change PI(4,5)P ₂ levels at the cleavage furrow.....	108
Figure 3-18. Depletion of PIPK1 γ -i3/i5 alters the distribution of PI(4,5)P ₂ across the ICB.....	110
Figure 3-19. Generation and time lapse imaging of an eGFP-SEPT6 knock-in HeLa M cell line throughout cytokinesis	112
Figure 3-20. Upon knock-down of PIPK1 γ -i3/i5, septins relocate to actin filaments and MT bundling is impaired.....	114
Figure 3-21. Depletion of MKLP1 or MgcRacGAP phenocopies the relocalization of eGFP-SEPT6 from MTs to actin stress fibers observed in absence of PIPK1 γ -i3/i5.....	117
Figure 3-22. SEPT6 protein levels decrease upon knock-down of PIPK1 γ -i3/i5.....	119
Figure 3-23. Depletion of SEPT6 leads to only a partial phenocopy of PIPK1 γ -i3/i5 depletion.....	121
Figure 3-24. Septins reorganize into rings upon high-level overexpression of active PIPK1 γ -i5.....	123
Figure 3-S1. Depletion of PIPK1 γ -i3/i5 scatters F-actin at the flanking membranes of daughter cells	124
Figure 3-S2. PRC1 interacts with septins during mitosis, and depletion of PIPK1 γ -i3/i5 affects its distribution along the ICB	124
Figure 3-S3. Depletion of PIPK1 γ -i3/i5 enhances stress fibers across the cell and leads to a redistribution of focal adhesions from the periphery toward the center	125
Figure 3-S4. Depletion of PIPK1 γ -i3/i5 affects MTs organization	125
Figure 3-S5. Depletion of SEPT7 phenocopies the loss of MKLP1 and the shortening of the acetylated tubulin bridge.....	125
Figure 4-1. Diagram summarizing the contribution of the septin-PIPK1 γ -i3/i5 module to midbody assembly and initiation of abscission.....	140
Figure 4-2. Potential mechanisms underlying the translocation of septins to bridge MTs	154
Figure 4-3. Hypothetical model illustrating PIPK1 γ contributions during cytokinesis	156
Figure 6.1-1. Molecular mechanism of SOCE	192
Figure 6.1-2. Domain structure of synaptotagmin 1 (Syt1) and extended synaptotagmins (E-Syts)	194
Figure 6.1-3. Proposed contribution of E-Syts in re-storing lipid homeostasis downstream of PLC activation.....	195
Figure 6.1-4. Proposed model of SEPT4-mediated stabilization of STIM1-Orai1 junctions	198
Figure 6.1-5. The plasmalemmal content of PI(4,5)P ₂ regulates the turnover of STIM1-Orai1 junctions	199
Figure 6.2-1. E-Syt1-dependent contact sites insert between cortical septin filaments	201
Figure 6.2-2. E-Syt1-dependent contact sites insert between cortical actin filaments	202
Figure 6.2-3. Dynamics of E-Syt1 and actin at the PM during TG-induced SOCE	203

Figure 6.2-4. Formation of E-Syt1-dependent contact sites requires intact actin filaments. (A)
 Representative frames from live TIRF imaging of HeLa M cells expressing eGFP-E-Syt1 before
 204

Figure 6.2-5. The PI(4,5)P₂ sensor, the PH-PLC δ1 domain, acquires an inversely-correlated
 distribution with E-Syt1 puncta at the PM 206

Figure 6.2-6. The overexpression of PIPKI_γ-i5 abolishes the formation of eGFP-E-Syt1-dependent
 contact sites..... 208

Figure 6.2-7. E-Syt1 directly binds PIPKI_γ, and this interaction may regulate both the formation and
 dissociation of E-Syt1-dependent contact sites 210

Figure 6.2-8. TG-induced E-Syt1 puncta colocalize with putative intracellular PI(4,5)P₂ pools 212

Figure 6.2-9. Dynasore inhibits the formation of E-Syt1-dependent contact sites while pitstop 2
 induces constitutive E-Syt1 puncta 213

Figure 6.2-10. Depletion of INPP5K reduces the formation of E-Syt1 puncta at the PM..... 215

Figure 6.2-11. Generation and time lapse TIRF imaging of an eGFP-E-Syt1 knock-in HeLa M cell
 line 217

Table 2-1. Solutions and buffers for molecular biology methods 42

Table 2-2. Solutions and buffers for biochemistry methods 43

Table 2-3. Solutions and buffers for cell biology methods 45

Table 2-4. List of DNA oligonucleotides used in this study 46

Table 2-5. List of siRNA oligonucleotides used in this study 48

Table 2-6. List of expression constructs used in this study 49

Table 2-7. List of primary antibodies used in this study 51

Table 2-8. List of secondary antibodies used in this study 52

Table 2-9. List of software and databases used in this study 53

Table 2-10. ImageJ macro used for regular confocal images 54

Table 2-11. ImageJ macro used for confocal images derived from expanded samples 55

Table 2-12. ImageJ macro used to quantify the total amount of nuclei 55

Table 2-13. PCR programs..... 56

Table 2-14. SDS-PAGE recipes 62

7.3. Publications

Russo G., Hümpfer N., Criado Santos N., Restel S., Schmied C., Heyd F., Lehmann M., Haucke V., Ewers H., Krauss M., (2023). Centralspindlin maintenance at the midbody requires septin-dependent recruitment of PIPK1 γ splice variants. *In preparation*

Ugorets V., Mendez PL., Zagrebina D., **Russo G.**, Kerkhoff Y., Herpelinck T., Kotsaris G., Jatzlau J., Stricker S., Knaus P., (2023). Dynamic remodeling of Septin structures orchestrates early myogenesis. *iScience, in revision*

Bolz S., Kaempf N., Puchkov D., Krauss M., **Russo G.**, Soykan T., Schmied C., Lehmann M., Müller R., Schultz C., Perrais D., Maritzen T., Haucke V., (2023). Synaptotagmin 1-triggered lipid signaling facilitates coupling of exo- and endocytosis. *Neuron 111: 1-10*

Russo G. & Krauss M., (2021). Septin Remodeling During Mammalian Cytokinesis. *Front Cell Dev Biol. 9: 768309*

Meyer K., Kirchner M., Uyar B., Cheng JY., **Russo G.**, Hernandez-Miranda LR., Szymborska A., Zauber H., Rudolph IM., Willnow TE., Akalin A., Haucke V., Gerhardt H., Birchmeier C., Kühn R., Krauss M., Diecke S., Pascual JM., Selbach M., (2018). Mutations in Disordered Regions Can Cause Disease by Creating Dileucine Motifs. *Cell 175: 239–253*

Maani N., Sabha N., Rezai K., Ramani A., Groom L., Eltayeb N., Mavandadnejad F., Pang A., **Russo G.**, Brudno M., Haucke V., Dirksen RT., Dowling JJ. (2018) Tamoxifen therapy in a murine model of myotubular myopathy. *Nat Commun. 9:4849*

Song K., **Russo G.**, and Krauss M. (2016). Septins as modulators of endo-lysosomal membrane traffic. *Front Cell Dev Biol. 4: 124*